LBL-36900
UC-400

Lawrence Berkeley Laboratory
UNIVERSITY OF CALIFORNIA

EARTH SCIENCES DIVISION

Predicting the Transport Properties of Sedimentary Rocks from Microstructure

E.M. Schlueter
(Ph.D. Thesis)

January 1995

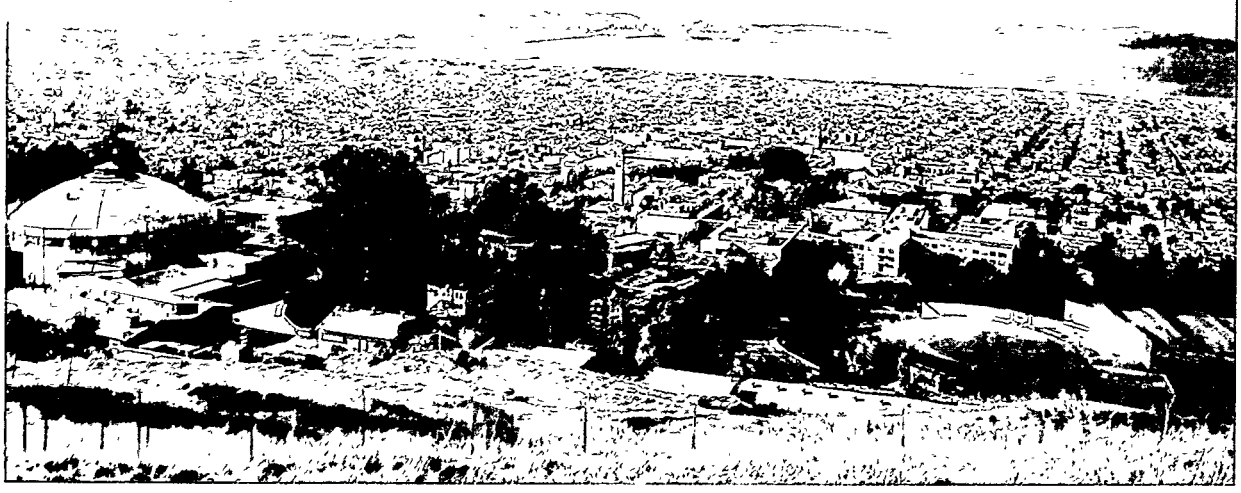

Prepared for the U.S. Department of Energy under Contract Number DE-AC03-76SF00098

Predicting the Transport Properties of Sedimentary Rocks from Microstructure*

Erika M. Schlueter

(Ph.D. Thesis)

Department of Materials Science and Mineral Engineering
University of California

and

Earth Sciences Division
Lawrence Berkeley Laboratory
University of California
Berkeley, California 94720

January 1995

---

*This research was supported by the U.S. Department of Energy through the Assistant Secretary for Fossil Energy, Bartlesville Project Office, Advanced Extraction Process Technology (AEPT), under contract No. DE-AC22-89BC14475, and by the Director, Office of Energy Research, Office of Basic Energy Sciences, Engineering and Geosciences Division, under Contract No. DE-AC03-76SF00098.

ABSTRACT

PREDICTING THE TRANSPORT PROPERTIES OF SEDIMENTARY ROCKS FROM MICROSTRUCTURE

by

Erika Manríquez Schlueter

Doctor of Philosophy in Engineering Science-
Materials Science and Mineral Engineering
University of California at Berkeley
Professor Paul A. Witherspoon, Chair

Understanding transport properties of sedimentary rocks, including permeability, relative permeability, and electrical conductivity, is of great importance for petroleum engineering, waste isolation, environmental restoration, and other applications. These transport properties are controlled to a great extent by the pore structure. How pore geometry, topology, and the physics and chemistry of mineral-fluid and fluid-fluid interactions affect the flow of fluids through consolidated/partially consolidated porous media are investigated analytically and experimentally. This understanding is important in characterizing porous media properties and heterogeneities before simulating and monitoring the progress of complex flow processes at the field scale in permeable media.

Hydraulic and electrical conductivity of sedimentary rocks are predicted from the microscopic geometry of the pore space. Cross-sectional areas and perimeters of individual pores are estimated from two-dimensional scanning electron microscope (SEM) photomicrographs of rock sections. Hydraulic and electrical conductances of the individual pores are determined from these geometrical parameters using Darcy's and Ohm's laws. Account is taken of random orientation of cross sections with respect to the channel axes, and for variation of cross-sectional area along pore length. The effective medium theory of solid-state physics is then used to determine an effective conductance of each pore. Finally, the pores are assumed to be arranged on a cubic lattice, which allows the calculation of overall macroscopic values for the permeability and the electrical conductivity. Results, using Berea, Boise, Massilon, and Saint-Gilles sandstones show close agreement between the predicted and measured permeabilities.

Good to fair agreement is found in the case of electrical conductivity. In particular, good agreement is found for a poorly cemented rock such as Saint-Gilles sandstone, whereas the agreement is not very good for well-cemented rocks. The possible reasons for this are investigated.

Experimentally the electrical conductivity of a partially saturated rock has been studied. The tests were conducted on Berea sandstone samples that had a formation factor of 15 and a porosity of 20%. The effective resistivities (formation factors) of the specimens, with an electrolyte solution in the pores that are not occupied by a wetting fluid (paraffin wax), were measured at different saturations, after solidifying the wetting fluid in place. The experimental data is studied in light of the role of the pore structure in the wetting fluid invasion process with the aid of fluid distributions at each saturation regime, a complete rock pore cast, and its associated rock section. The surface conductance contribution of clay minerals to the overall electrical conductivity is assessed. The effect of partial hydrocarbon saturation on overall rock conductivity, and on the Archie saturation exponent, is discussed. The electrical conductivity of Berea sandstone changes substantially with a relatively small addition of the insulating wetting fluid, suggesting that the electrolyte at the grain contacts may play an important role in the electrical properties, e.g., act as bottlenecks, in the electrical conduction process. The resistivity of the electrolyte at the grain contacts has to be added to the resistivity of the intergranular pore space (i.e., in between the grains) to accurately predict electrical conductivity of cemented rocks.

The region of validity of the well-known Kozeny-Carman permeability formulae for consolidated porous media and their relationship to the microscopic spatial variations of channel dimensions are established. It is found that the permeabilities predicted by the Kozeny-Carman equations are valid within a factor of three of the observed values. Even though the complete pore space system of most sandstones is strictly speaking inhomogeneous, the hydraulic active or 'principal' network approaches homogeneity. For highly inhomogeneous rock-pore-space systems, the critical path analysis for estimating the permeability of consolidated rocks is valid within limits.

Perimeter-area power-law relationships of pores in five sedimentary rocks are determined from SEM photomicrographs of thin sections. The perimeter-area power-law relationship of pores of four sandstones was found to lie between 1.43 and 1.49, while

that of an Indiana limestone was found to be 1.67. The perimeter-area power-law relationship of pores, along with a pore-size distribution and a classical model for permeability, is used to estimate the permeability.

Analytical calculations of the capillary pressure-saturation function are conducted, based on the distribution of pore hydraulic radii and the area-perimeter power-law relationship for pores. The geometrical quantities are estimated from two-dimensional SEM photomicrographs of rock sections. Experimental capillary pressure-saturation curves are obtained using alloy Wood's metal, which allows for direct examination of occupied pore space after the experiment. Model predictions are compared to empirical capillary pressure curves to calculate average pore body and pore throat sizes and aspect ratios, and these are compared to values estimated from photomicrographs. The resistance offered by the pore structure to various transport phenomena, i.e., permeability, is controlled by the pore throats.

Experiments to measure relative permeabilities of a partially saturated rock have been carried out in Berea sandstone using fluids that can be solidified in place. The effective permeability of the spaces not occupied by the wetting fluid (paraffin wax) or the nonwetting fluid (Wood's metal), have been measured at various saturations after solidifying each of the phases. The tests were conducted on Berea sandstone samples that had an absolute permeability of approximately 600 mD. The shape of the laboratory-derived relative permeability vs. saturation curves measured with the other phase solidified conforms well with typical curves obtained using conventional methods. The corresponding wetting and nonwetting fluid distributions at different saturations are presented and analyzed in light of the role of the pore structure in the invasion process, and their impact on relative permeability and capillary pressure. Irreducible wetting and nonwetting phase fluid distributions are studied. The effect of clay minerals on permeability is also assessed.

Predicting the Transport Properties of Sedimentary Rocks from Microstructure

by

Erika Manríquez Schlueter

With love, to

Javier, Caty, Emilia, Ross, Dietrich and Kurt

"I am part of all that I have met;
Yet all experience is an arch wherethrough
Gleams that untravelled world...
And this grey spirit yearning in desire
To follow knowledge like a sinking star
Beyond the utmost bound of human thought."

Quotation from Alfred Lord Tennyson's Ulysses.

Contents

1 INTRODUCTION AND BACKGROUND 1

1.1 Motivation for the present work 2

1.2 Transport properties 3

1.3 Other work on pore-level modeling of transport properties 5

1.3.1 Capillaric modeling 5

1.3.2 Percolation modeling 7

1.3.3 Network modeling 8

2 OVERVIEW AND ORGANIZATION 11

2.1 Approach 11

2.2 Objectives 15

2.3 Organization 16

3 PREDICTING PERMEABILITY OF SEDIMENTARY ROCKS FROM MICROSTRUCTURE 17

3.1 Discrete approach using individual conductances 18

3.1.1 Effective medium theory 19

3.1.1.1 Uniform field solution (external field) 20

3.1.1.2 Uniform field solution (local field) 20

3.1.2 Method of analysis 24

3.1.3 Effect of cross-sectional pore shape on permeability 39

3.1.3.1 Exact solution 39

3.1.3.2 Hydraulic radius approximation 40

3.1.3.3 Examples 41

3.1.4 Effect of pore orientation 46

3.1.4.1 Projected line 46

3.1.4.2 Projected area 48

3.1.4.3 Hydraulic radius 48

3.1.4.4 Hydraulic conductance 49

3.1.4.5 Tortuosity and projection 50

3.1.5 Pore body to pore throat aspect ratio dependence 52

3.1.6 Permeability calculation 54

3.1.7 Results and discussion 58

3.2 Statistical approach using the perimeter-area power-law relationship of pores 62

3.2.1 Perimeter-area power-law relationship of pores 64

3.2.2 Permeability implications 67

3.2.3 Effects of pore orientation and constrictivity 70

3.2.4 Results and discussion 70

3.3 Note on the validity of the Kozeny-Carman formulas for consolidated porous media 73

3.3.1 Region of validity of the effective medium theory 75

3.3.2 Numerical evaluation of conductances of large regular 3-D networks . . . 77

3.3.3 Region of validity of the critical path analysis 79

3.3.4 Region of validity of the Kozeny-Carman formulas and the microscopic spatial variations of channel dimensions 81

3.3.4.1 Parallel arrangement of the conductors 81

3.3.4.2 Series arrangement of the conductors 83

3.3.4.3 Simple cubic arrangement of the conductors 84

3.3.4.4 Results and discussion 85

3.4 Comparison of analytical and experimental results 86

4 PREDICTING ELECTRICAL CONDUCTIVITY OF SEDIMENTARY ROCKS FROM MICROSTRUCTURE 97

4.1 Analytical approach using individual conductances 97

4.1.1 Effect of cross-sectional pore shape 97

4.1.2 Effect of pore orientation 98

4.1.3 Effect of pore constrictivity 98

4.1.4 Effective medium theory 98
4.1.5 Results and discussion 101
4.2 Experimental approach using microscopic distribution of solid hydrocarbon (paraffin wax) in the pore space 102
4.2.1 Apparatus and procedure 104
4.2.2 Effect of hydrocarbon saturation 106
4.2.3 Effect of clay 109
4.2.4 Effect of surface conductance 109
4.2.5 Effect of pore structure and topology 115
4.2.6 The saturation exponent in Archie's law 121
4.2.7 Results and discussion 123
4.3 Comparison of analytical and experimental results 124

5 PREDICTING CAPILLARY PRESSURE OF BEREA SANDSTONE FROM MICROSTRUCTURE 125
5.1 Description of analytical model 125
5.1.1 Effect of cross-sectional pore shape 126
5.1.2 Capillary pressure analysis 127
5.1.1 Effect of pore orientation 129
5.2 Experimental imbibition with Wood's metal 129
5.2.1 Examination of Wood's metal distribution in the pore space 131
5.3 Comparison of analytical and experimental results 140

6 RELATIVE PERMEABILITY AND THE MICROSCOPIC DISTRIBUTION OF WETTING AND NONWETTING PHASES IN THE PORE SPACE OF BEREA SANDSTONE 145
6.1 Apparatus and procedure 147
6.2 Effect of wetting phase saturation 147
6.2.1 Effect of pore structure and topology 148
6.2.2 Irreducible wetting phase saturation 157
6.3 Effect of clay minerals 157

6.4 Effect of nonwetting phase saturation 163
6.4.1 Effect of pore structure and topology 164
6.4.2 Irreducible nonwetting phase saturation 167
6.5 Results and discussion 172

7 SUMMARY AND CONCLUSIONS 177

References 183

A EXPLORATORY SIMULATIONS OF GAS INJECTION TESTS IN AN UNDERGROUND ROCK LABORATORY 189
A.1 Introduction 191
A.2 Radial flow in a fracture with permeable rock matrix 192
A.3 Discussion and conclusions 193
References 194

B SENSITIVITY STUDIES ON PARAMETERS AFFECTING GAS RELEASE FROM AN UNDERGROUND ROCK CAVERN 209
B.1 Introduction 211
B.2 Model domain and computational grid 212
B.3 System behavior for the reference case 212
B.4 Sensitivity studies 213
B.4.1 Capillary pressure 214
B.4.2 Relative permeability 214
B.4.3 Absolute permeability 215
B.4.4 Porosity 215
B.5 Summary of multiphase effects 215
B.5.1 Capillary pressure 215
B.5.2 Relative permeability 216
B.5.3 Absolute permeability 216
B.5.4 Porosity 216

B.6 Conclusions 216

References 218

B-A GAS RELEASE RATES 219

B-B CAPILLARY PRESSURE FOR A FRACTURE WITH LOG-NORMAL APERTURE DISTRIBUTION 219

B-B.1 Function origin 219

B-B.2 Parameter adjustment 220

B-B.3 Numerical implementation 221

B-B.3.1 Inverse error function 221

B-B.3.2 Access procedure of erfi(x) on the Cray (Code Listing B-D.3) . . 222

B-B.3.3 Treatment of singularities 222

B-B.3.4 Test cases 222

B-B.3.5 P_c vs. S_l functions for different σ, $\bar{b}$ 223

B-C STRONG INTERFERENCE RELATIVE PERMEABILITY FUNCTIONS 224

B-D CODE LISTINGS 225

B-D.1 FORTRAN source code for calculating fracture capillary pressure (version 1).226

B-D.2 FORTRAN source code for calculating fracture capillary pressure (version 2).228

B-D.3 Access procedure for inverse error function from IMSLSFUN library. . . . 230

B-D.4 Coding for identifying the position of the gas saturation front. 231

B-D.5 Coding for relative permeability function with strong phase interference. . 233

B-D.6 Sample TOUGH2-input file for reference case. 235

List of Figures

3.1 Construction used in calculating the uniform field solution, in which the voltages increase by a constant amount, V_m, per row. 21

3.2 Construction used in calculating the voltage induced across one conductance, C_o, surrounded by a uniform medium (after Kirkpatrick, 1973). 21

3.3 Stereo SEM photomicrographs of a Berea sandstone pore cast. The pore space is partially impregnated with Wood's metal alloy and the quartz grains removed by hydrofluoric acid. 25

3.4 Stereo SEM photomicrographs of a Saint-Gilles sandstone pore cast. The pore space is partially impregnated with Wood's metal alloy and the quartz grains removed by hydrofluoric acid. 26

3.5a Typical SEM photomicrograph of Berea sandstone (Section B). The rock is composed mainly of quartz grains (dark gray), feldspar grains (medium gray), and products of grain dissolution (light gray) 29

3.5b Pore-space contours obtained from image analysis of the photomicrograph of Berea sandstone (Section B) shown in Fig. 3.5a. 29

3.6a Typical SEM photomicrograph of Berea sandstone (Section T). The rock is composed mainly of quartz grains (dark gray). The pore space is impregnated with epoxy (black). 31

3.6b Pore-space contours obtained from image analysis of the photomicrograph of Berea sandstone (Section T) shown in Fig. 3.6a. 31

3.7 Pore-space contours obtained from serial section of Massilon sandstone (after Koplik et al., 1984). 33

3.8a Typical SEM photomicrograph of Boise sandstone. The rock is composed mainly of quartz grains (dark gray). The pore space is impregnated with epoxy (black). 35

3.8b Pore-space contours obtained from image analysis of the photomicrograph of Boise sandstone shown in Fig. 3.8a. 35

3.9a Typical SEM photomicrograph of Saint-Gilles sandstone. The rock is composed mainly of quartz grains (dark gray). The pore space is impregnated with epoxy (black). 37

3.9b Pore-space contours obtained from image analysis of the photomicrograph of Saint-Gilles sandstone shown in Fig. 3.9a. 37

3.10 Mean projected length of a randomly oriented linear segment (after Underwood, 1970). 47

3.11 Relationship between area of a circular tube (area actual) and its projection onto a plane (area measured). 47

3.12 Construction used in calculating the tortuosity factor, τ, for randomly oriented cylindrical tubes in three dimensions. 51

3.13 Sinusoidal variation of the radius along the length of a tube used to calculate the constriction hydraulic factor. 51

3.14 Constriction factor for hydraulic flux as function of the ratio of the minimum pore radius to the maximum pore radius of an individual pore. 55

3.15 Microscopically inhomogeneous pore system and its skeleton (after Doyen, 1988). 56

3.16 Cubic lattice representation of the pore structure employed to calculate the permeability of sedimentary rocks with the effective medium theory. 56

3.17 Schematic drawing of a rough-walled tube (of radius R_0). Surface roughness does not have a strong effect on the overall fluid permeability of a tube, because a slightly smaller tube (of radius R_i) is known to have a comparable permeability (after Berryman and Blair, 1987). 63

3.18 Typical serial section of Saint-Gilles sandstone at 100x magnification. The mineral grains of different shades are quartz, carbonate, feldspar, and muscovite, whereas the darkest regions represent pore space. 63

3.19a Pore-space contours obtained from serial section of Massilon sandstone (after Koplik et al., 1984). 65

3.19b Perimeter-area power-law relationship for Massilon sandstone obtained from pore-space contours shown in Fig. 3.19a. 65

3.20a Pore-space contours obtained from image analysis of the photomicrograph of Berea sandstone (Section B) shown in Fig. 3.5a. 66

3.20b Perimeter-area power-law relationship of pores for Berea sandstone obtained from pore-space contours shown in Fig. 3.20a. 66

3.21 Pore-size distribution of Massilon sandstone obtained from pore-space contours shown in Fig. 3.19a. 69

3.22 Pore-size distribution of Berea sandstone obtained from pore-space contours shown in Fig. 3.20a. 69

3.23 Total conductance of a simple cubic network of conductances C_{ij} with binary disorder. Values of the conductances are 1 (with probability f) and $C_2 < 1$ (probability $1 - f$), assigned at random. 78

3.24 Symbols show total conductance of a simple cubic network of 15^3 nodes, with values of the conductances chosen at random from the distribution $f(C) = (2C \log A)^{-1}$ with conductances C_{ij}'s range from A^{-1} to A. 78

3.25 Conductance envelope. The plot shows the effective conductances of a parallel, simple cubic, and series networks of conductors, with values of the conductances chosen at random from the distribution $f(C)$ indicated. The critical path conductance and the total conductance of a simple cubic network from previous figure (data points) have also been plotted. 82

3.26 Dimensionless experimental mercury-porosimetry data and analytical curve of sandstone samples. A regular cubic lattice consisting of capillary tubes of angular cross section, at the intersection of which there are angular bulges, is introduced as a pore structure model. 88

4.1 Constriction factor for electric flux as function of the ratio of the minimum pore radius to the maximum pore radius of an individual pore 99

4.2 Schematic representation of the laboratory apparatus designed to simultaneously measure both electrical and hydraulic conductivity. 105

4.3 Experimental setup for one-dimensional paraffin impregnation. 107

4.4 Effective formation factor vs. hydrocarbon paraffin saturation for Berea sandstone. The pore space was partially saturated with hydrocarbon paraffin. The remaining portion of the pore space was filled with a 0.5-M zinc nitrate solution. 108

4.5 SEM photomicrographs of a Berea sandstone specimen showing the presence of fine-grained clay minerals (mainly kaolinite) partly filling pores. 110

4.6 X-ray spectrum of clay minerals coating Berea sandstone sample pores shown in figure 6.4. EDX analysis yielding nearly equal peak heights of Si and Al confirms the identification as kaolinite 111

4.7 Conductivity data of Berea sandstone at different electrolyte concentrations. Zinc nitrate electrolyte solutions with concentrations 0.005-0.5 M were used. 113

4.8 Mobility for kaolinite as a function of salt concentration and pH (after Williams and Williams, 1978). 114

4.9 SEM photomicrograph collage of a Berea sandstone specimen impregnated with approximately 20-30% paraffin. The actual width of field is about 6 mm. The gray phase is quartz grains, the white phase is. 116

4.10 SEM photomicrograph collage of a Berea sandstone specimen impregnated with approximately 40-50% paraffin. The actual width of field is about 6 mm. The gray phase is quartz grains, the white phase is. 117

4.11 SEM photomicrograph collage of a Berea sandstone specimen impregnated with approximately 60-70% paraffin. The actual width of field is about 6 mm. The gray phase is quartz grains, the white phase is. 118

4.12 SEM photomicrograph collage of a Berea sandstone pore cast. Actual width of field is about 6 mm. The rock pore space was completely filled with Wood's metal alloy and the quartz grains removed by. 119

4.13 SEM photomicrograph collage of a Berea sandstone sample fully impregnated with Wood's metal alloy. The actual width of field is about 3 mm. The gray phase is quartz grains and the white phase is. 120

4.14 Effective formation factor vs. electrolyte saturation for Berea sandstone (case B). The pore space was partially saturated with hydrocarbon paraffin with the remainder of the pore space filled with a 0.5-M zinc nitrate solution. 122

5.1 Experimental setup for three-dimensional Wood's metal imbibition. 130

5.2 Experimental capillary pressure function of Berea sandstone. The rock has been impregnated with a nonwetting fluid (Wood's metal) at different equilibrium pressures and solidified in place. 132

5.3 Experimental mercury porosimetry saturation curve of Berea sandstone (after Chatzis and Dullien, 1977). 132

5.4 Top and bottom axial quarter sections of Berea sandstone core partially saturated with a nonwetting fluid (Wood's metal) at different equilibrium pressures and solidified in place. The procedure allows for direct observation. 134

5.5 Top section of Berea sandstone core partially saturated with a nonwetting fluid (Wood's metal) at an equilibrium pressure of 6.8 psia and solidified in place. The procedure allows for direct observation. 135

5.6 Top section of Berea sandstone core partially saturated with a nonwetting fluid (Wood's metal) at an equilibrium pressure of 6.9 psia and solidified in place. The procedure allows for direct observation. 136

5.7 Top section of Berea sandstone core partially saturated with a nonwetting fluid (Wood's metal) at an equilibrium pressure of 7.2 psia and solidified in place. The procedure allows for direct observation. 137

5.8 SEM photomicrograph collage of a 1 in × 1 in Berea sandstone specimen partially saturated with approximately 50% Wood's metal at 8.5 psia equilibrium pressure. 138

5.9 SEM photomicrograph collage of an enlarged partial section obtained from a Berea sandstone sample partially saturated with approximately 50% Wood's metal. . . 139

5.10a Computerized analysis of Berea sandstone image shown in Fig. 3.5a display intergranular pore space contours from which hydraulic radius distribution and transport properties. 141

5.10b Pore hydraulic radii frequency distribution of Berea sandstone obtained from pore space contours shown in Fig. 5.10a. 141

5.11 Experimental vs. predicted capillary pressure function of Berea sandstone. To obtain the experimental capillary pressure function, the rock has been impregnated with a nonwetting fluid (Wood's metal) at. 142

5.12 Pore-size distribution representative of a consolidated porous medium (Berea sandstone). Pore throats are smaller than pore bodies. 144

6.1 Effective permeability vs. paraffin saturation for Berea sandstone. The pore space was partially saturated with hydrocarbon paraffin. The remaining portion of the pore space was filled with triple-distilled water. Cases A and B. 149

6.2 Effective permeability vs. paraffin wax saturation for Berea sandstone (case B). The pore space was partially saturated with hydrocarbon paraffin, with the remainder of the pore space filled with triple-distilled water. 150

6.3 SEM photomicrograph collage of a Berea sandstone specimen impregnated with approximately 20-30% paraffin. The actual width of field is about 6 mm. The gray phase represents quartz grains, the white phase. 152

6.4 SEM photomicrograph collage of a Berea sandstone specimen impregnated with approximately 40-50% paraffin. Actual width of field is about 6 mm. The gray phase represents quartz grains, the white phase. 153

6.5 SEM photomicrograph collage of a Berea sandstone specimen impregnated with approximately 60-70% paraffin. Actual width of field is about 6 mm. The gray phase represents quartz grains, the white phase. 154

6.6 SEM photomicrograph collage of a Berea sandstone pore cast. Actual width of field is about 6 mm. The rock pore space was completely filled with Wood's metal alloy and the quartz grains removed by hydrofluoric acid to allow. 155

6.7 Typical SEM photomicrograph collage of Berea sandstone showing pore-grain interface roughness. The rock is composed mainly of quartz grains (dark gray), feldspar grains (medium gray), and products of grain dissolution (light gray). . . 159

6.8 SEM photomicrographs of a Berea sandstone specimen showing the presence of fine-grained clay minerals (mainly kaolinite) partly filling pores between quartz grains. 160

6.9 SEM photomicrographs of a Berea sandstone specimen showing the presence of fine-grained clay minerals (mainly illite) partly filling pores between quartz grains. 161

6.10 SEM photomicrographs of a Berea sandstone specimen showing the presence of fine-grained clay minerals (mainly montmorillonite) partly filling pores between quartz grains. 162

6.11 Effective permeability vs. Wood's metal saturation for Berea sandstone. The pore space was partially saturated with Wood's metal at different pressures, with the remainder of the pore space filled with triple-distilled water. 165

6.12 Axial quarter sections of Berea sandstone core partially saturated with a nonwetting fluid (Wood's metal) at different equilibrium pressures, and solidified in place. The procedure allows for direct observation and. 168

6.13 SEM photomicrograph collage of a 1 in × 1 in Berea sandstone specimen partially saturated with approximately 30% Wood's metal at 7.3 psia. 169

6.14 SEM photomicrograph collage of an enlarged partial section obtained from a Berea sandstone sample partially saturated with approximately 30% Wood's metal (white phase) at 7.3 psia pressure. 170

6.15 Relative permeability vs. saturation curve for Berea sandstone using two fluids, serving as the wetting and nonwetting phases, that can be frozen in situ, one at a time. The effective permeability of the spaces not occupied by the. 174

6.16 Relative permeability vs. saturation curve for Berea sandstone measured by Corey and Rathjens (1956) using oil and gas. 175

A-1a Radial flow domain. 196

A-1b Radial flow griding. 197

A-2a Gas pressure vs. time at wellblock. 198

A-2b Gas saturation vs. time at wellblock. 199

A-3a Gas pressure profiles in fracture ($Q = 1 \times 10^{-4}$ kg/s). 200

A-3b Gas pressure profiles in fracture ($Q = 1 \times 10^{-5}$ kg/s). 201

A-3c Gas pressure recovery profiles in fracture ($Q = 0 \times 10^{-5}$ kg/s). 202

A-4 Gas saturation vs. time for different injection/recovery periods. 203

A-5a Gas saturation profiles in fracture ($Q = 1 \times 10^{-5}$ kg/s). 204

A-5b Gas saturation profiles in fracture ($Q = 1 \times 10^{-4}$ kg/s). 205

A-5c Gas saturation profiles in fracture ($Q = 0 \times 10^{-5}$ kg/s). 206

A-5d Saturation distribution at 7 days ($Q = 1 \times 10^{-5}$ kg/s). 207

B-1 Schematic of flow system for gas migration studies. 241

B-2 Capillary pressure of rough-walled fractures 242

B-3 Two-phase relative permeability curves (after Corey, 1954). 243

B-4 Simulated gas saturation in injection grid block for reference case. 244

B-5 Simulated gas pressure in injection grid block for reference case. 245

B-6 Simulated gas saturation profiles for the reference case at different times. 246

B-7 Gas pressure profiles for the reference case at different times. 247

B-8 Simulated advance of the gas front for the reference case. 248
B-9 Simulated rate of liquid outflow at the top of the column. 249
B-10 Capillary pressure functions used in sensitivity studies. 250
B-11 Sensitivity of gas pressures in injection block to variations in capillary. 251
B-12 Sensitivity of gas saturation in injection block to variations in capillary. 252
B-13 Advance of gas displacement front for different capillary pressures. 253
B-14 Grant's relative permeabilities compared with Corey's curves 254
B-15 Relative permeabilities with strong phase interference compared with Corey's. . 255
B-16 Sensitivity of gas pressures in injection block to variations in relative. 256
B-17 Sensitivity of gas saturations in injection block to variations in relative. 257
B-18 Sensitivity of gas front advance to variations in relative permeability. 258
B-19 Sensitivity of gas pressures in injection block to variations in absolute. 259
B-20 Sensitivity of gas front advance to variations in absolute permeability. 260
B-21 Sensitivity of gas saturations in injection block to variations in absolute. 261
B-22 Sensitivity of gas saturations in injection block to variations in porosity. 262
B-23 Sensitivity of gas pressures in injection block to variations in porosity. 263
B-24 Sensitivity of gas front advance to variations in porosity. 264
B-25 Fracture capillary pressures for log-normal aperture distribution. 265
B-26 Capillary pressure functions for three geologic media. 266
B-27 The error function. 267
B-28 Fracture capillary pressures for different values of variance σ. 268

List of Tables

3.1 Conductance data - Berea sandstone SEM section B. 30

3.2 Conductance data - Berea sandstone SEM section T. 32

3.3 Conductance data - Massilon sandstone SEM section. 34

3.4 Conductance data - Boise sandstone SEM section. 36

3.5 Conductance data - Saint-Gilles sandstone SEM section. 38

3.6 List of comparative values to show equivalence of the calculated permeabilities using the torsion analogy and the hydraulic radius approximation, respectively. . 45

3.7 Calculated permeability data - Berea sandstone SEM section B. 59

3.8 Calculated permeability data - Berea sandstone SEM section T. 59

3.9 Calculated permeability data - Massilon sandstone SEM section. 59

3.10 Calculated permeability data - Boise sandstone SEM section. 59

3.11 Calculated permeability data - Saint-Gilles sandstone SEM section. 59

3.12 Measured vs. predicted intrinsic permeabilities of four sedimentary rocks. 61

3.13 Perimeter-area power-law relationship γ parameter and correlation coefficient r measured from perimeter-area data of five sedimentary rocks. 64

3.14 Calculated permeability data - Massilon and Berea sandstones SEM photomicrographs. 71

3.15 Measured vs. predicted intrinsic permeabilities Massilon and Berea sandstones. . 71

3.16 Calculation of the mercury porosimetry curve of the Berea (BE-1) sandstone sample (after Chatzis and Dullien, 1985). 89

3.17 Calculated effective conductance data of various sandstones obtained from SEM 2-D sections (Chapter 3.1). 92

3.18 Calculated permeability data of two sandstones from rock microgeometry assuming a parallel pore model (Chapter 3.2). 92

4.1 Measured vs. predicted formation factors of four sedimentary rocks. 101

4.2 Formation factor data for Berea sandstone with a 0.5 M zinc nitrate solution used as electrolyte. 106

4.3 Resistivity data for Berea sandstone with zinc nitrate solution saturating the sample. 112

5.1 List of comparative values to show equivalence of the reciprocal hydraulic radius $(1/R_H)$ and the reciprocal mean radius of curvature $(1/r_1) + (1/r_2)$ 126

6.1 Effective (and absolute) permeability data (Case B) - Berea sandstone partially saturated with paraffin wax, with triple-distilled water used as permeant 148

6.2 Wetting fluid invasion and permeability. 156

6.3 Effective (and absolute) permeability data - Berea sandstone partially saturated with Wood's metal, with triple-distilled water used as permeant 164

6.4 Nonwetting fluid invasion and permeability 171

A-1 Initially specified parameters for the reference case. 195

B-1 Parameters for the reference case. 237

B-2 Sensitivity studies. 238

B-3 Results of sensitivity studies. 239

B-4a Behavior of fracture capillary pressure for $S_l \rightarrow 0$. 239

B-4b Behavior of fracture capillary pressure for $S_l \rightarrow 1$. 239

B-5 Numerical check of fracture capillary pressure function ($\beta = -.3341; \sigma = .43; \bar{b} = .2838\mu$m). 240

Index

A	area OR conductance span
$\bar{b}$	mean aperture
b_{ave}	mean aperture
b_p	cut-off aperture
c	constant that depends on pore shape
C_{AB}	conductance across A and B
C_c	critical conductance
C_e	electric conductance
C_{eff}	effective conductance
C_h	hydraulic conductance
D	diameter OR torsional rigidity
erf	error function
$erfi$	inverse error function
E	electric field
f	hydraulic constriction factor OR probability
F	formation factor
G	shear modulus
h	width
i_o	current intensity across A and B
j	current density
k	permeability

k_{r_g}	gas relative permeability
k_{r_l}	liquid relative permeability
l_c	characteristic length
L	length
L_t	total length
m	moles per molecule
M	molecular weight
n	number
N	number
p	fluid pressure
P	perimeter OR pressure
P_c	capillary pressure
P_{cap}	capillary pressure
P_g	gas pressure
P_l	liquid pressure
q	volumetric flow rate per unit area
Q_g	gas injection rate
r	tube radius
R	tube radius OR universal gas constant
R_H	hydraulic radius
s	specific surface area OR tube area
S_l	liquid saturation

S_{l_r}	liquid irreducible saturation
S_{s_r}	gas irreducible saturation
T	temperature
u	fluid velocity
v	fluid velocity
V	potential
V_{eff}	effective voltage
V_g	gas volume
V_o	voltage across A and B
w	angle of torsion
z	coordination number

Greek Symbols

β	distribution function
Γ	region in space
γ	slope of log A - log P plot
ϵ	constant that depends on the grid size
ζ	surface tension
κ	conductivity
κ_r	rock conductivity
κ_w	fluid conductivity
θ	contact angle

λ	wave length
μ	absolute viscosity
ρ	resistivity
ρ_r	rock resistivity
ρ_w	fluid resistivity
σ	variance
τ	shear stress OR tortuosity
ϕ	porosity
Ψ	stress function

Subscripts

ave	average
c	capillary OR critical
cap	capillary
e	electrical
eff	effective
g	gas
h	hydraulic
H	hydraulic
l	liquid
r	rock
t	total
w	water

ACKNOWLEDGMENTS

I would like to express my fondest appreciation to my thesis adviser and mentor Professor P. A. Witherspoon. I have been honored and privileged to be one of his students. Were it not for Professor Witherspoon's generous assurance and guidance during my stay at U.C. Berkeley, my dissertation and its results would have not been possible. I will always be grateful to Professor N. G. W. Cook and to Dr. L. R. Myer for guiding me in various phases of this thesis and for investing resources into my research. I am extremely thankful having been a student of Professor G. Sposito. His invaluable mentorship, exceptional academics, and unconditional support will ever be remembered as integral components of this work. I am very happy to acknowledge technical guidance from Dr. R. W. Zimmerman. His scientific input and advice were important elements in the creation and completion of this report. Special thanks to Professors A. Becker and S. Berger for their teaching excellence and for encouraging me to do my best. Thanks are due to Dr. K. Pruess for introducing me into the physics of two-phase flow and into the usage of the numerical simulator TOUGH. Thanks are also due to Dr. R. Lemmon, Dr. C. Trujillo, Dr. G. Bovardsson, Dr. S. Benson, Dr. J. Long, Dr. K. Karasaki, and D. Mangold for their support during critical periods of this research. I am indebted to C. Doughty and to Dr. P. Persoff for carefully reviewing many papers associated with this thesis.

Many thanks to the faculty of the Departments of Civil and Environmental Engineering of the University of Washington, Seattle, Professors M. Sherif, W.-S. Chu, R. Nece, and S. Burges, my Chilean professors and academic advisers Ing. E. Munizaga and Ing. E. Celedón, the faculty of the school of Civil Construction of the Universidad Católica de Chile, the Fulbright Commission for Educational Interchange between the U.S. and Chile, the Institute of International Education (I.I.E.), and the International Telephone and Telegraph Corporation (I.T.T.), for the confidence expressed in me.

I would be remiss not to acknowledge the profound and positive influence that Dr. and Ms. K. and R. Halbach, Dr. B. Kincaid, Ms. L. Geniesse and Dr. D. Attwood have had on my family and me during this very challenging period. Meeting and getting to know my colleagues C. Torres, R. Suarez, C. Doughty, L. Moreno, L. Cox, Y. Liu, K. Lee, A. Davey, A.M. Cook, Y.-S. Wu, T. Hadgu, K. Chapman, P. Kuzmenko,

C. Chan, B. Hilbert, S. Roy, G. Hesler, K. Nihei, S. Blair, Z. Aunzo, E. Karageorgi, S. Turek, D.-W. Chen, J. Jacobsen, C. Haukwa, B. Thapa, and many others with whom I could share some of my experiences in this endeavor has been a gift. I would like to thank very specially Ms. P. Bronnenberg, Ms. E. Klahn, Mr. R. Johnson, Ms. C. James, and Ms. W. Capece for their assistance and friendliness throughout this project. Finally, thanks are due to R. Curtis of Lawrence Berkeley Laboratory for exceptional technical support with the experimental equipment and to R. Wilson of U.C. Berkeley for superior expertise with the scanning electron microscope.

This work was supported by the Assistant Secretary for Fossil Energy, Bartlesville Project Office, Advanced Extraction Process Technology (AEPT), under U.S. Department of Energy Contract No. DE-AC22-89BC14475, and by the Director, Office of Energy Research, Office of Basic Energy Sciences, under U.S. Department of Energy Contract No. DE-AC03-76SF00098, in cooperation with the Swiss National Cooperative for the Storage of Nuclear Waste (NAGRA).

1 INTRODUCTION AND BACKGROUND

The properties of rocks are determined not only by the intrinsic properties of the constituent minerals but also by the microstructure of the rock and the interaction between the mineral phases and the pore fluids. Rocks are in general far more complex than most engineering composites, being composed of grains of different minerals, with various sizes and shapes, along with intergranular cementing material. Rocks also contain pores that allow the flow of fluids. The viscous nature of these fluids, along with chemical interactions between the fluid and the mineral phases, leads to behavior that involves a greater range of phenomena than is exhibited by man-made materials.

The flow of fluids through geological media is governed by a constitutive equation relating the volumetric flux to its driving force, the total head gradient. Traditionally, this relationship has also been assumed to be linear (i.e., Darcy's law). The constant of proportionality, the permeability coefficient, is determined by the sizes, shapes, and interconnectivity of the pores. Just as the flow of fluid through a rock is greatly dependent upon the geometry and the topology of the pore space, so is the conduction of electric current. Since the conductivities of many fluids that fill the pore spaces of rocks are many orders of magnitude greater than that of most rock-forming minerals, electrical current in a rock is essentially confined to the pore space. Hence, the overall electrical conductivity of a rock depends on the conductivity of the pore fluid and the interconnectivity of the pore space.

Although some progress has been made in relating permeability and electrical conductivity to pore structure, work has been hindered by a lack of knowledge of the detailed microstructure and the ability to model its intricacy, and a lack of understanding of the nature of the interactions between the rock matrix and the pore fluids. It has long been recognized that the important physical properties of rocks are related to each other in some definite matter. Much effort in the petroleum and well-logging industry, for instance, has been devoted to developing relationships between properties such as permeability and electrical conductivity or formation factor. Yet, the equations developed have been typically empirically-fitted curves which are usually valid for very narrow classes of rocks.

Constitutive relationships developed in the pages that follow are based on microstructural considerations. They display the dependence of constitutive parameters on pore and grain structure, and thereby reveal the nature of the interrelationship between the various coupled processes and properties. The main research goal has been to develop constitutive relations for various types of sedimentary rocks which reflect their actual nonlinear behavior. Rather than incorporating empirically derived phenomenological parameters, these constitutive equations contain parameters that explicitly depend on the rock fabric, microstrure, degree of cementation, etc.

1.1 Motivation for the present work

The precise definition of reservoir characteristics and structure on the scale of meters is key to the planning and control of successful complex flow processes in waste isolation and environmental restoration. Although this subject has received some attention in the past most major issues still remain unresolved.

Determination of subsurface hydrologic parameters that characterize fluid flow through porous media (e.g., permeability, relative permeability, and capillary pressure) is crucial to the understanding, monitoring, and simulation of complex flow problems in permeable media, including multiphase, multicomponent field scale processes as well as waste remediation and/or isolation. Results of numerical simulations quantifying the effects of the release and transport of noncondensible gas (Appendixes A and B) and nonaqueous phase liquids (NAPL's) in subsurface formations (Falta et al., 1992) highlight the impact of macroscopic transport and physical properties on multi-phase system behavior. For example, the parameters that were shown to have by far the largest impact on the particular two-phase system under isothermal conditions presented in Appendix B were relative and intrinsic permeability. Relative permeability was found to affect strongly both the gas pressure and the gas front displacement (Figs. B-16, B-17, and B-18). Intrinsic permeability was found to affect the gas pressure values (Fig. B-19) more than the displacement front speed (Fig. B-20). Indeed, these previous studies clearly show that simulation results depend heavily on the physical properties as defined, and that they are only as accurate as the underlying reservoir description.

The macroscopic transport properties of porous (and fractured) media depend critically upon processes at the pore level, which are controlled by the geometry and connectivity of the pore space. Consequently, there is a need for a first-principle understanding of how pore morphology and other related factors can be used to predict porous media macroscopic physical properties such as intrinsic permeability, formation factor, relative permeability, and capillary pressure. The ultimate aim is to distinguish physical properties of rocks with a resolution from the pore level to the laboratory and to the field scales. This understanding will be important in determining reservoir properties and heterogeneities before prediction of complex reservoir behavior. In this thesis, we tackle the first step: the relationship between rock microstructure and the laboratory measured transport properties and heterogeneities.

1.2 Transport properties

Our chief concern is the relationship between the transport properties such as intrinsic permeability and electrical conductivity, and the rock geometry and topology.

In the case of hydraulic flux, consider, for example, low Reynolds number flow of an incompressible viscous fluid through a porous medium. At the local scale of a fluid particle moving in the pore space, the flow is governed by the linearized Navier-Stokes equations and the continuity equation:

$$\mu \nabla^2 \vec{v} = \vec{\nabla} p \, ; \quad \vec{\nabla} \cdot \vec{v} = 0 \, ,$$

where μ is the absolute viscosity of the fluid, p the fluid pressure, and $\vec{v}$ the fluid velocity at a given point in the fluid. The boundary conditions require that the velocity vanishes at the pore-grain interface. At the macroscopic level, i.e., the scale of a macroscopically homogeneous isotropic rock sample whose size is large compared with the pore dimensions, the flow is governed by Darcy's law. The empirical Darcy's law states that the average volumetric flow rate per unit area $\vec{q}$ is proportional to the applied uniform average pressure gradient $\vec{\nabla} p$:

$$\vec{q} = \frac{-k}{\mu} \vec{\nabla} p \, ,$$

where k is the scalar intrinsic permeability that depends only upon the geometry of the porous medium under consideration.

In the case of electrical flux, consider, for example, the steady state (d.c.) conduction of electricity through a porous rock whose pore space is fully saturated with an electrolyte of conductivity κ_w. The grain phase is considered homogeneous with conductivity κ_g. The electrostatics equations governing the flow of current are:

$$\vec{j} = \kappa \vec{E} \; ; \quad \vec{E} = -\vec{\nabla} V \; ; \quad \vec{\nabla} \cdot \vec{j} = 0 \; ,$$

where $\vec{j}$, $\vec{E}$, and V are the current density, the electric field, and the potential at a point in the material where the conductivity κ is equal to κ_w or κ_g. At the macroscopic level of description, Ohm's law relates the average current density $\vec{j}$ to the applied uniform average voltage gradient $\vec{\nabla} V$:

$$\vec{j} = -\kappa \vec{\nabla} V \; ,$$

where κ is the d.c. electrical conductivity.

In principle, these properties may be calculated by solving the appropiate equation of motion, provided that the boundary conditions are specified. The complexity of these limiting conditions imposed at the very irregular pore surface, however, makes this approach unmanageable. In practice, the problem is approached by relating the transport properties to a small number of measurable parameters directly from microgeometry characterizing the microstructure of rocks.

The analogy between permeability and electrical conductivity is not a simple one-to-one relationship however, due to the lack of an electrostatic equivalent to the no-slip hydraulic boundary condition which applies at the grain surfaces.

1.3 Other work on pore-level modeling of transport properties

Muskat as early as 1937 suggested the importance of knowing the pore geometry of a reservoir rock before fluid movement through it could be rigorously analyzed. However, due to the complexity of porous media structure, assumptions must be made and models created. Moreover, it is the physically-grounded mathematical models, based on experimental observation of actual phenomena, that will ultimately provide not only a satisfactory explanation for the concept of transport properties but also for the dynamics of an entire reservoir.

1.3.1 Capillaric modeling

The early literature has been thoroughly reviewed by Scheidegger (1974). Much of that work, continuing to the present day, is based on capillary-tube models such as the Kozeny-Carman equivalent channel model. The cross section of this equivalent tube has a constant shape and an area proportional to the porosity of the sample. The permeability and the electrical conductivity are expressed by terms of the tortuosity $(L/L_t)^2$, the porosity ϕ, and the specific surface area s as:

$$k = c\left(\frac{L}{L_t}\right)^2 \frac{\phi^3}{s^2}\,,$$

$$\kappa_r = \kappa_w \left(\frac{L}{L_t}\right)^2 \phi\,,$$

where c is a constant that depends on the cross-sectional shape of the channel. The parallel-tube models may yield, in some instances, a satisfactory explanation of Darcy's law. However, these models are not physically similar to actual pore structures especially since they neglect the phenomena of pore coordination or connectivity. An improvement to the capillaric models are the branching models which take into account the fluid flow path branching and reconnecting.

Rose and Witherspoon (1956) discussed flow branching and reconnecting in the pore space. Various attempts to introduce the complexity of the pore space by making progressively more complex tube structures introduced a series of new adjustable

parameters into the basic tube relation. Many parameters were introduced to account for distribution of pore sizes, for tube shape variations, misalignment of tubes, etc. The generalized Kozeny-Carman equation obtained by Wyllie and Gardner (1958) implicitly contained twelve adjustable parameters. These parameters attempt to account for two factors; connectivity or coordination and the pore size. These early studies led to permeability expressions involving to some measure of the surface area and the porosity raised to a higher power such as four or six. These empirical permeability relations have been used until recently in log analysis (Dewan, 1983) although their accuracy is limited to an order of magnitude and there is no physical motivation for large powers of porosity.

Swanson (1981) made a conceptual advance recognizing that the fluid flow could be dominated by flow on a path of large pores. He provided an estimation of permeability based on its relationship to the mercury-capillary pressure curves. He used two adjustable parameters for taking into account different lithologies.

Wong et al. (1984) obtained an expression for the permeability in terms of macroscopic geometric parameters such as the porosity and the specific surface area. Their result is consistent with the Kozeny-Carman result.

Walsh and Brace (1984) modified the original Kozeny-Carman equivalent channel formula to obtain an expression in terms of the measurable parameters, the specific surface area, the porosity, and the formation factor. The permeability and the electrical conductivity of an equivalent single channel can readily be expressed in terms of the porosity, the specific surface area, and the tortuosity. By combining the permeability and electrical conductivity expressions for a single channel, the tortuosity can be eliminated, and the permeability expression that is obtained is dependent only on the surface area, the porosity, and the formation factor F. It is

$$k = \frac{\phi^2}{cFs^2} .$$

Berryman and Blair (1986) used the modified form of the Kozeny-Carman equivalent tube model by Walsh and Brace (1984) to make estimates of the permeability from microgeometry of Berea sandstone. Digitized scanning electron microscope (SEM) photomicrographs of rock thin sections were employed to estimate porosity

and specific surface area from measured two-point correlation functions. These parameters were then combined with known values of the electrical formation factor to predict permeability from Kozeny-Carman formulas. The specific surface area is directly proportional to the slope of the two-point correlation function evaluated at the origin (Matheron, 1967). Berryman and Blair (1986) change the magnification of the microscope to estimate the specific surface area of different samples, which makes the accuracy of their permeability estimates somewhat difficult to assess.

Doyen (1987) used an homogenized form of the pore space to estimate the permeability and electrical conductivity of Fontainebleau sandstone using the Kozeny-Carman formula. Pore-throat distribution data obtained from image analysis of digitized thin sections was introduced in the effective medium theory self-consistency equation (Kirkpatrick, 1973) to obtain a characteristic throat size that serves as input for the Kozeny-Carman formula. Doyen's estimates of transport properties were within a factor of three of the measured values.

1.3.2 Percolation modeling

We next briefly discuss the percolation approach to the transport properties. This method does not rely on specific pore-size distributions or lattice topologies and can be applied within limits for rocks that have pore sizes that are broadly distributed.

Ambegaokar, Halperin, and Langer (1971) showed in their work on electron hopping in amorphous semiconductors that transport in a random system with a broad distribution of conductances is dominated by those conductances with magnitudes greater than some characteristic value C_c. The characteristic conductance is the largest conductance such that the conductances field forms an infinite connected cluster. Transport in such a system reduces to a percolation problem with a threshold value.

Kirkpatrick (1979) set conductances with $C < C_c$ to zero and assigned all local conductances $C \geq C_c$ the value C_c. He arrived at an expression for the conductance of the form

$$C = aC_c[f(C_c) - f_c]^t \,,$$

where $f(C_c)$ is the probability for a given conductance to be greater or equal to C_c, a is a constant, and t is approximately 1.9 for three-dimensional distributions.

Katz and Thompson (1986) applied this percolation scheme to the permeability and electrical conductivity of porous rocks. For a very broad pore-size distributions they found the following relationship

$$k = \frac{l_c^2}{226}\left(\frac{\kappa_r}{\kappa_w}\right) ,$$

where l_c is the characteristic length defined by the threshold conductance C_c. The magnitude of the constant is a direct reflection of the different weighting of the flow paths for the hydraulic and electrical conductance problems; this observation reflects the difference, for example, between the hydraulic conductance of a tube of diameter and length l, which is proportional to l^3, and the electrical conductance of the same tube filled with an electrolyte solution, which is proportional to l.

1.3.3 Network modeling

A more accurate representation of the pore structure is a random network with varying coordination numbers and composed of tubes of different shapes and sizes which are distributed randomly along the connections. Using appropriate physical laws, network models can then be made to replicate measurements at the microscopic scale. It has been demonstrated by numerous researchers (Fatt, 1956a,b,c; Chatzis and Dullien, 1977; Dullien, 1979; Mohanty and Salter, 1982; Chatzis and Dullien, 1985; Tourboul et al., 1987; Lenormand et al., 1988) that network models do exhibit the observed properties of porous media.

Fatt (1956a,b,c) introduced the concept of modeling a porous medium by a pore network. He used a two-dimensional regular network of randomly-distributed capillary throats with nodes that had no volume. He employed both uncorrelated throat lengths and capillary throat lengths that were inversely proportional to their radii. Fatt utilized the Laplace and the Hagen-Poiseuille equations for the capillary pressure and the relative permeability calculations. He used an analog computer of resistors with the resistances determined from Ohm's law. Fatt's model qualitatively represented observed behavior of relative permeability, relative resistivity, saturation

exponent, and capillary pressure. He illustrated his model using square and single, double, and triple hexagonal patterns and found that the results were less affected by the pattern than they were by the throat radius distribution. Fatt demonstrated his network using only up to about 400 pore throats, since his calculations were done manually.

Chatzis and Dullien (1977) studied both two- and three-dimensional networks. They used the coordination number, which is the total number of pore throats (bonds) connected to one pore body (node), to characterize a network pattern. They obtained cumulative probability values for different network lengths until the critical probability was determined. The critical probabibity is that which would apply to a network of infinite length. They found that a network of about forty pore segments deep was sufficient to simulate an infinite-length network. Chatzis and Dullien concluded that two-dimensional networks could not be used to simulate three-dimensional networks because of their differing properties. One problem is that bicontinua cannot exist in a two-dimentional network. They also found that the best three-dimensional results were obtained when the volume fraction of pores of a certain size was proportional to the diameter of those pores. They noted that porosities in the 20% to 40% range could not be described if the pore throat lengths were made either directly or inversely proportional to their diameters.

Mohanty and Salter (1982) used a network model to calculate relative permeability, capillary pressure and dispersivity. They used a three-dimensional cubic arrangement of pore throats with pore bodies at the nodes. They used a Weibull distribution to determine pore throat and pore body radii. Pore body volumes were assumed to be proportional to the cube of their radii. Pore throat volumes were neglected in saturation calculations. Pore throat lengths were considered to be proportional to some power of the throat radii.

Koplik and Lasseter (1984, 1985) show that Fatt's analog resistor network procedures can be condensed into a two-step analog effective medium process. They consider one pore throat where all of the random conductances in the rest of the network have been changed to an effective conductance, C_{eff}. They calculate the pressure gradient across the one pore throat assuming its conductance is first C_{eff},

and then is random. Requiring that the pressure gradient for C_{eff} be equal to the average pressure gradient for C random gives (Kirkpatrick, 1973):

$$\left\langle \frac{C - C_{eff}}{C + \left(\frac{z}{2} - 1\right) C_{eff}} \right\rangle = 0 \,,$$

where z is the average coordination number and the brackets indicate the average over all possible values of C. They found that this approximation is good to $\pm 5\%$. They derived an equation estimating the average velocity. Macroscopic permeability was then calculated using this equation and Darcy's law.

Koplik, Lin, and Vermette (1984) used the effective medium theory of Kirkpatrick (1973) and similar techniques to calculate both permeability and conductivity. Using rock SEM photomicrographs of thin sections to get pore sizes, their results were off by a factor of 10 and 2, respectively. They attached this large difference principally to the sample size studied with rock thin sections. Their analysis requires calculation of a parameter t which is a function of the average number of branches of the pore space system intersecting a unit surface across the porous medium. The quantity t requires a large sample volume to be calculated accurately. Also, a term $\cos\theta$ (with angle θ given with respect to the direction of fluid flow) is not considered in their definition of t. Our modelling approach avoids the problem of evaluating the parameter t altogether.

2 OVERVIEW AND ORGANIZATION

The successful operation and monitoring of large scale complex transport processes in permeable media necessitates a first principle understanding of how rock pore morphology and minerology, physical and chemical properties, and fluid compositions can be used to predict basic transport properties, including absolute and relative permeability, electrical conductivity, capillarity and contact angles, etc. A significant limitation to our understanding of the dynamics of multi-phase fluids in porous media is the inability to connect the physics at the microscopic scale to the macroscopic phenomena observed in the laboratory and in the field. Within individual pores, the motion of the fluids and the meniscus can be discussed, at least approximately, in terms of the microgeometry and the physical characteristic of the fluid present. On the macroscopic scale, the multiphase Darcy equations are used. The connection between these two levels of description has never been clearly elucidated despite years of effort (Chapter 1.3). In consequence, it is difficult to predict the behavior of reservoirs in advance, and considerable waste of money, efforts, and resources can ensue.

2.1 Approach

Here we wish to investigate the microstructure (geometry and topology) of sedimentary rocks and its relationship to the transport properties such as hydraulic permeability and electrical conductivity which are important in understanding the flow of fluids in reservoirs and their displacement by other fluids. Wood's metal, an alloy of bismuth, lead, tin, and cadmium that melts at around 70 °C, has been used as the nonwetting phase in our experiments. As a wetting fluid, paraffin wax, a mixture of solid hydrocarbons of high molecular weight that melts at approximately 50 °C, has been employed. The advantage of using Wood's metal and paraffin wax is that after a particular flow test they can be solidified in place and the distribution of the occupied and unoccupied pore spaces can be studied under either a scanning electron microscope (SEM) or an optical microscope. Experimental studies have been accomplished aimed at studying permeability and electrical conductivity of a partially saturated rock. For this purpose, the relative and effective permeabilities and resistivities of the spaces not occupied by the wetting fluid (paraffin wax) have been

measured at various saturations, solidifying the phase in Berea sandstone samples having an absolute permeability of $\sim$ 600 mD, and a formation factor of 15. Relative and effective permeabilities of the pore spaces not occupied by the nonwetting fluid (Wood's metal) have also been measured. This technique allows post-experiment examination of the occupied pore space and yields results for Berea sandstone that agree with typical relative permeability and capillary pressure curves reported elsewhere using conventional methods. The experimental work provides theoretical basis for the macroscopic constitutive relationships that are developed herein.

The hydraulic permeability and electrical conductivity of sedimentary rocks are predicted from the microgeometry and connectivity of the pore space. 2-D SEM micrographs of rock cross sections are used to infer the hydraulic and electrical conductances of individual pores. The hydraulic conductance of each tube is estimated from its area and perimeter, using the hydraulic radius approximation, while the electrical conductance is related only to the cross-sectional area of the tube. It is assumed that the pores are cylindrical tubes of varying radius, and that they are arranged on a cubic lattice, so that the coordination number of the network is 6. A stereological correction is applied to account for the fact that the cross section slices each pore at a random angle to its axis. Account is also taken for possible variation of the cross-sectional area along the length of each tube. The effective medium theory of Kirkpatrick (1973) is then used to replace each individual conductance with an effective conductance. Finally, an extension of a unit cubic cell is used to relate the effective tube conductances (hydraulic or electrical) to the continuum values of the permeability and electrical conductivity. Results, using a Berea, Boise, Massilon, and Saint-Gilles sandstone, show close agreement between predicted and measured hydraulic permeabilities, with essentially no adjustable parameters in the model.

In particular, permeabilities of sandstones obtained with the cubic lattice-network model are in very good agreement with experimental data. This outcome confirms previous research by Chatzis and Dullien (1985), who found that the simple cubic network of angular pores yields good agreement with the observed data when modeling the mercury porosimetry curve for a variety of sandstones. These results are not surprising when one notes that the above properties are strong functions of the pore structure of the samples, which is in every case multiply connected.

The region of validity of the well-known Kozeny-Carman formulas based on a parallel arrangement of the pores is studied, as it relates to the microscopic spatial variation of channel dimensions. It is important to evaluate the extent to which the widely-used parallel pore structure moves away from the regular cubic model as the pore space becomes increasingly more inhomogeneous at the pore scale. A conductance plot has been developed using the effective medium theory of solid-state physics to allow the investigation of the accuracy of the Kozeny-Carman equations for the prediction of permeability of consolidated porous media. It is found that the permeabilities predicted by the Kozeny-Carman formulas are approximately valid within a factor of three of the observed values. This finding is a direct result of the various sandstones 'principal' network approaching microscopic homogeneity in channels dimensions. For highly inhomogeneous rock-pore-space systems, the critical path analysis of Ambegaokar et al. (1971), which focuses on the details of the critical paths along which much of the flow must occur, can be applied within limits for estimating the permeability of consolidated sandstones.

Perimeter-area relationships of a smooth representation of pores are estimated from scanning electron micrographs of thin sections of typical reservoir-type sedimentary rocks. Although some sandstones also exhibit roughness at scales much smaller than the average pore diameter, it is known that such roughness has little effect on hydraulic conductance (Berryman and Blair, 1987), and can therefore be ignored. The basic method to estimate the area-perimeter statistics involves counting size and perimeter grid (or pixel) units for every feature in a standard scanning electron micrograph of some fixed magnification. This method is used to estimate the area-perimeter statistics for group of pores in a rock-section. It is found that the perimeter-area relationship of such a representation of the true void/solid interface satisfies the perimeter-area power-law relationship: $A = mP^{\gamma}$, where $\log m$ is the intercept on the $\log A$ axis, and γ the slope of the $\log A - \log P$ plot. The constants m and γ are found by performing a linear regression on the $\log A - \log P$ data. From this analysis we find slopes ranging from 1.43 to 1.49 for the four sandstones examined, while that of an Indiana limestone is found to be 1.67, with correlation coefficients varying from 0.98 to 0.99. We show how the perimeter-area power-law relationship of a smooth representation of the pore space of a rock can be used, in conjunction

with the pore-size distribution function and a classical model for permeability, to yield reasonable estimates of absolute permeability. In the two-dimensional sections under consideration, however, the pore cross-sections are randomly oriented with respect to the channel axes. The orientation effect is taken into account by means of geometrical and stereological considerations. In addition, constrictions within the individual branch channels, i.e., pore necks and bulges, are taken into account using an analysis based on a sinusoidal variation of cross-section. The example is intended to be a plausible demonstration of the use of perimeter-area power-law information for making quantitative predictions of permeability.

We have employed a simple cubic lattice-network model of electrical conductivity utilizing a smooth representation of the intergranular pore space (e.g., in between the grains). With this model we have found that the same pore system is responsible for both electrical and hydraulic properties of a lightly consolidated rock such as Saint-Gilles sandstone. Moreover, for a heavily consolidated rock such as Berea sandstone, we found that the pore space responsible for hydraulic properties is not responsible alone for electrical properties. The results from the cubic lattice-effective medium model suggest that it is mainly the electrolyte presence at the contacts that is important and that the uniform coverage with electrolyte elsewhere on the grain surfaces has no part in determining electrical properties. The fact that the electrical properties of a consolidated rock such as Berea sandstone change substantially with the addition of only 20% of an insulating wetting fluid suggests that the electrolyte at the grain contacts may also play an important role in electrical properties e.g., act as bottlenecks, in the electrical conduction process of consolidated rocks. In order to accurately predict electrical conductivity or formation factor of sedimentary rocks from microgeometry one must rigorously superimpose the resistivity of the electrolyte at the grain contacts to the resistivity of the electrolyte in the intergranular pore space.

An analytical expression of the capillary pressure-saturation curve, based on pore microgeometry, has been obtained using a perimeter-area power-law relationship and a hydraulic radii distribution. Two-dimensional SEM photomicrographs of rock cross sections are employed to estimate areas, perimeters, and hydraulic radii of individual pores. The porous media is idealized as consisting of an assembly of capillaries of arbitrary cross-sections randomly oriented with respect to the channel axes in the

two-dimensional SEM photomicrographs; actual cross-sectional areas are calculated using a stereological correction. Model predictions are compared to empirical capillary pressure curves to calculate average pore body and pore throat sizes and aspect ratios, and compare these with values estimated from SEM micrographs.

In summary, our approach is to study through analysis and experiment how pore geometry, topology and the physics of mineral-fluid and fluid-fluid interactions affect both the flow of fluids through rocks and the relationship between the fluid transport properties and the electrical behavior and properties of the porous media under consideration. The theoretical analysis has been useful in defining and ranking needed experiments, and to successfully correlate measurements of important transport properties, such as permeability and electrical conductivity of consolidated/partially consolidated porous media, to the microgeometry of the pore space. On the other hand, the experimental work has provided valuable insights into the pore level complexity of the natural porous media. It is clear from this study that heterogeneity characterization at the scale of pores, conventional macroscopic flow theory, and fluid flow modeling will not only improve our understanding of the fluid dynamics in permeable media but also will enable us to better monitor, simulate, and predict complex flow processes at the field scale.

2.2 Objectives

The main purpose of the entire exercise is to investigate the missing link between the pore microstructure and the fluid presence, and the macroscopic transport properties of reservoir rocks. This principal aim may be subdivided into several objectives as follows:

1. to understand the microscopic geometry, topology and heterogeneity of the pore space of rocks by direct observation of pore casts and associated rock sections;
2. to comprehend the relationships between pore space microscopic geometry, topology, and heterogeneity and macroscopic transport properties for porous media;
3. to develop relations between pore microscopic geometry and topology to macroscopic transport properties of sedimentary rocks;

4. to measure transport properties of rocks using multiple fluid phases that can be solidified in place to allow direct visualization and analysis of the fluid distributions in the pore space;

5. to examine hydraulic and electrical conductivity data in terms of the role of the pore structure and heterogeneities on the observed fluid distributions at different saturations to provide theoretical basis for the macroscopic constitutive relationships that we develop;

6. to compare measured transport properties to existing data on sedimentary rocks obtained using conventional methods;

7. to evaluate hydraulic and electrical conductivity data in terms of the microphysics and microchemistry of the processes involved (i.e., effect of clay coatings on the pore walls);

8. to study the experimental data and fluid distributions of rocks at low wetting-phase and nonwetting-phase saturations, and near threshold saturation; and

9. to ultimately use true macroscopic transport properties to better understand, simulate, and monitor large scale transport processes in permeable media.

2.3 Organization

This report is comprised of seven main Chapters and two appendices. Chapter 3 describes the development of analytical models (discrete and statistical) for predicting the hydraulic permeability of sedimentary rocks from microstructure. The validity of the Kozeny-Carman formulas for the prediction of permeability of consolidated porous media is assessed. In Chapter 4, the analytical model for predicting electrical conductivity (formation factor) of sedimentary rocks is presented. Experimental results for the effective formation factors of Berea sandstone are introduced and compared to the analytical results. Chapter 5 presents analytical and experimental results on capillary pressure of Berea sandstone. The study of the microscopic distribution of wetting and nonwetting phases in the pore space of Berea sandstone and their relationship to relative permeability is presented in Chapter 6. Chapter 7 includes a summary and conclusions of work completed together with implications for future work.

3 PREDICTING PERMEABILITY OF SEDIMENTARY ROCKS FROM MICROSTRUCTURE

The concept of permeability allows a macroscopic description of the fluid flow phenomena in porous media under a regime of sufficiently low fluid velocities (Scheidegger, 1974). This property is linked to other properties of porous media such as capillary pressure and relative permeability. In order to understand the relationships, one has to understand how all those properties are conditioned by the connectivity and geometrical properties of the pore space. The simplest model that can be constructed is one representing a porous medium by a bundle of straight, parallel cylindrical capillaries of uniform diameter that go from one face of the porous medium to the other. Equations based on this type of 1-D model are called Kozeny-Carman equations. The opposite extreme of this parallel case would be to assume a serial model in which all the pores are connected in series. Obviously, for a natural porous medium, this model is as idealized as the parallel model, and a realistic model lies somewhere between these limits.

In this study, we look at a natural porous material which is defined as a two-phase material in which the interconnected pore space constitutes one phase and the solid matrix the other. A distinctive property of a natural porous medium is the irregular pore-size and pore-shape distributions. We consider here the pore scale and its extention to the laboratory scale which is of the order of tens to thousands times larger. The laboratory samples are considered homogeneous in the sense that the irregular pore structure reproduces itself in the various portions of the sample. In a typical fluid flow laboratory experiment, the rates of flow are measured over areas which intersect many pores. Space-averaged or macroscopic quantities such as permeability are the ones of interest in applications. The main aim of this Chapter is to develop equations relating a macroscopic property such as permeability to rock microstructure. A few methods have been used in the past in order to achieve this (See Chapter 1). Two basic averaging approaches have been employed here. In the first one, the discrete approach, a macroscopic variable such as effective conductance is determined as an appropiate mean over a sufficiently large representative elementary volume (r.e.v.) defined through the concept of porosity associated with it. The length scale of the

r.e.v. is larger than the size of a single pore so that it includes a sufficient number of pores to allow the meaningful statistical average required in the continuum concept. It is assumed that results concerning the macroscopic quantities are independent of the size of the r.e.v. In the second one, the statistical approach is related to the uncertainty of the spatial distribution of microscopic quantities such as pore-sizes and pore-shapes. The statistical averaging is carried out over one realization. The actual sample is one of the possible realizations of media of some gross features. But the inference of statistical information about the realization is based on the unique sample. This is possible only under restrictive conditions of statistical homogeneity (stationarity) which are similar in essence to those underlying the concept of r.e.v. As long as we limit ourselves to deriving relationships between space averaged quantities with no special concern as to their fluctuations, the results of the two approaches should be essentially the same.

3.1 Discrete approach to individual conductances

Consider an inhomogeneous, disordered, composite system (conductive/non-conductive) in which one can define locally a given property, e.g., conductance, which can be calculated from the geometry of the conductive element (e.g., the coefficient in Poiseuille's law for cylindrical tubes). This is possible as long as the dimensions of the local elements are large with respect to the scale of the conduction process involved (i.e., as long as the individual pores are wide enough so that fluid flow obeys the macroscopic Navier-Stokes equations, and is not dominated by surface effects). Such a medium can be approximated by a 3-D network with the same topology, in which all the conductances have a single effective value. The effective medium can be defined as one in which the macroscopic conductance is the same as for the heterogeneous system, and therefore the effective conductance can be considered as the mean value controlling the physical property of concern. Since we are concerned with a random medium, it is assued that no spatial correlation exists between the individual conductances. Details of the effective medium theory of solid state physics are given in Section 3.1.1.

For this study, rock cross sections have been prepared for imaging with the scanning electron microscope (SEM). The resulting 2-D SEM photomicrographs have been

employed to infer the hydraulic conductance of the individual pores. We assume that the pores are cylindrical tubes of varying radius, and that they are arranged on a cubic lattice, so that the coordination number of the network is 6. The hydraulic conductance of each tube is estimated from its area and perimeter, using the hydraulic radius approximation and the Hagen-Poiseuille equation. In the section under consideration, the pore cross sections are assumed to be randomly oriented with respect to the directions of the channel axes. The orientation effect has been corrected by means of geometrical and stereological considerations. Account is also taken for possible variation of the cross-sectional area along the length of each tube, e.g., pore necks and bulges. The effective-medium theory of solid-state physics is then used to replace each individual conductance with an effective average conductance. Finally, a unit cubic cell is extended to relate the effective-hydraulic-tube conductances to the continuum values of permeability. Preliminary results, using Berea, Boise, Massilon, and Saint-Gilles sandstone, yield very close agreement between the predicted and measured permeabilities, with essentially no arbitrary parameters in the model.

3.1.1 Effective medium theory

The objective of the effective medium theory (Kirkpatrick, 1973) is to infer an average conductance parameter for heterogeneous disordered media from the statistics of local conducting elements. Consider an inhomogeneous disordered continuous system in which one can define locally the conductance. Such a medium can be approximated by a 3-D network with a regular topology in which each bond is occuppied by a conductance C_i. According to Kirkpatrick (1973) it is possible to build a homogeneous network with the same topology but in which all conductances C_i have a single value C_{eff} which is an effective value controlling the physical property involved. The effective medium is by definition the homogeneous equivalent network for which the macroscopic conductance is the same as for the heterogeneous system. The idea then, is to represent the average effects of the random conductors by a homogeneous effective medium in which the total field inside is equal to the external field. As a criterion to fix C_{eff} it is required that the incremental voltages induced, where individual conductances C_i are replaced by C_{eff} in this medium, should average to zero.

The distribution of potentials in a random resistor network to which a voltage has been applied along one axis may be regarded as due to both (1) an external field which increases the voltage by a constant amount per row of nodes, and (2) a local fluctuating field whose average over a sufficiently large region is zero.

3.1.1.1 *Uniform field solution (external field)*

By introducing a regular cubic mesh of points r_i with spacing $\triangle r$ (Figure 3.1), and applying the principle of conservation of charge, one obtains a system of linear equations for the voltages $V_i = V_{r_i}$.

At point i,

$$\sum_j C_{ij}(V_i - V_j) = 0 \,, \tag{1}$$

where j is summed over all neighboring points.

Replacing the conductance C_{ij} with a constant effective conductance C_{eff}, gives at point A (refer to Figure 3.1)

$$C_{eff}([V + 2V_{eff}]4 - [V + 3V_{eff} + V + V_{eff} + V + 2V_{eff} + V + 2V_{eff}]) = 0 \,, \tag{2}$$

where all conductances C_{eff} have associated with them $\triangle V = V_{eff}$ per row.

3.1.1.2 *Fluctuating field solution (local field)*

To find a mathematical expression for the effective conductance, a classical self-consistent method can be employed in which a single conductance C_o is embedded in the homogeneous medium of similar topology. The inclusion of C_o in the effective medium disturbs locally the uniform solution for the field but the deviation is easily calculated since the effective network is homogeneous.

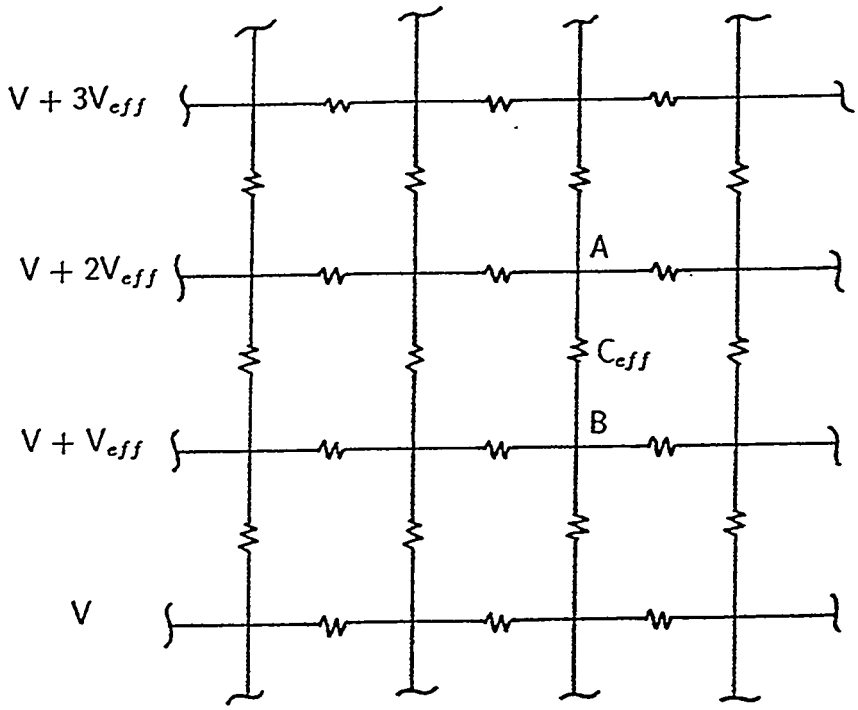

FIG. 3.1: Construction used in calculating the uniform field solution, in which the voltages increase by a constant amount, V_m, per row.

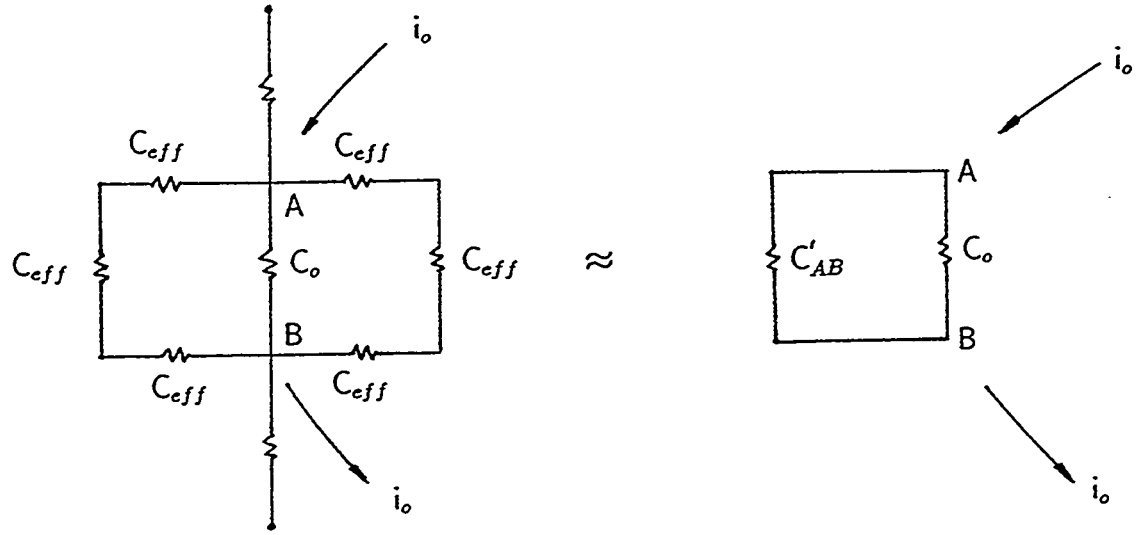

FIG. 3.2: Construction used in calculating the voltage induced across one conductance, C_o, surrounded by a uniform medium (after Kirkpatrick, 1973).

Consider one conductance having the value C_o surrounded by an otherwise uniform effective medium. The solution of the network Eq. (1) in the presence of C_o can be constructed by superposition (Figure 3.2). Far from C_o the field is uniform. To the uniform field solution given by Eq. (2), we add the effects of a fictitious current i_o introduced at A and extracted at B. Since the uniform solution fails to satisfy current conservation at A and B, the magnitude of i_o is chosen to correct for this.

At A,

$$V_{eff}(C_{eff} - C_o) = i_o \,. \tag{3}$$

The extra voltage, V_o, induced between A and B, is given by the conductance C'_{AB} of the network between points A and B when the perturbation is absent, i.e., when $C_o - C_{eff} = 0$:

$$V_o = \frac{i_o}{C_o + C'_{AB}} \,. \tag{4}$$

The current flowing through each of the z equivalent nodes at the point where the current enters is i_o/z so that a total current of $2i_o/z$ flows through the path AB. We then calculate the voltage developed across AB, the conductance across AB, $C_{AB} = (z/2)C_{eff}$, and $C'_{AB} = (z/2)C_{eff} - C_{eff}$.

Thus we can write

$$V_o = \frac{V_{eff}(C_{eff} - C_o)}{C_o + [z/2 - 1]C_{eff}} \,, \tag{5}$$

valid both in 2-D and 3-D.

The requirement that the average of V_o vanishes gives

$$\left\langle \frac{C_{eff} - C_i}{[(z/2) - 1]C_{eff} + C_i} \right\rangle = \sum_{i=1}^{N} \frac{C_{eff} - C_i}{[(z/2) - 1]C_{eff} + C_i} = 0 \,, \tag{6}$$

where the sum is taken over all N individual conductors.

Upper and lower bounds on the effective conductivity are found from the two limiting cases $z = 2$ and $z = \infty$. For $z = 2$, Eq. (6) can be solved for

$$C_{eff} = \frac{N}{\sum_{i=1}^{N} \frac{1}{C_i}} , \tag{7}$$

whereas for $z = \infty$, Eq. (6) can be solved for

$$C_{eff} = \frac{\sum_{i=1}^{N} C_i}{N} . \tag{8}$$

When the coordination number is 2, the tubes are arranged in series, and the effective conductance reaches its lowest possible value. On the other hand, when the coordination number is ∞, the tubes are arranged in parallel, and the effective conductance reaches its maximum value. The limiting values of both the effective conductance and the coordination number correspond to one-dimensional arrangements of the tubes. For a coordination number other than $z = 2$ or $z = \infty$, Eq. (6) must be solved numerically to find the effective conductance, given the individual conductances (See Code Listing 3.1).

The effective medium theory is expected to work best when spatial fluctuations of hydraulic (or current) flux are small in a relative scale. Our laboratory imbibition experiments in Berea sandstone, in combination with SEM analysis of the pore space, indicate that the distribution of pores and throats controlling permeability is narrow. Consequently, the effective medium theory is expected to, and does, give very good results in Berea sandstone. The effective medium theory coupled with a network of resistors has been used by Koplik et al. (1984) to predict permeability of Massilon sandstone, although the predicted value was ten times higher than that measured. Doyen (1988) calculated the transport properties of Fontainebleau sandstone, and predicted permeability within a factor of three of the measured value. These models do not account for the fact that the 2-D section under consideration slices each pore at a random angle to its axis or for the variation of the cross-sectional area along the length of each tube, both of which are significant effects. These effects are discussed below in sections 3.1.4 and 3.1.5, respectively.

3.1.2 Method of analysis

Figures 3.3 and 3.4, stereo SEM photomicrographs of pore casts of Berea sandstone and Saint-Gilles sandstone, respectively, reveal that the pore space is comprised of a three-dimensional network of irregularly shaped pores. Although an exact description of key pore space morphological characteristics is rather complex, it is possible to isolate three main features:

1. Multiple connectivity of the pore segments;
2. Converging-diverging cross sections of pores;
3. Roughness and irregularity of pore walls.

Since the actual rock geometry is too complex for any quantitative study, we have replaced it by a standard model geometry that preserves the main observed morphological features.

For the purposes of developing a network model for permeability, we need to know the volumetric flow through each pore. According to the Hagen-Poiseuille equation, the volumetric flux of fluid through a cylindrical pore of constant radius r is

$$q = \frac{\pi r^4}{8\mu} \nabla p \,, \tag{9}$$

where μ is the absolute viscosity, and ∇p is the pressure gradient. We now use the hydraulic radius concept to rewrite Eq. (9) in a form that is applicable to non-circular pores (See Section 3.1.3 for details).

The hydraulic radius R_H of the tube is defined as

$$R_H \equiv \frac{area}{wetted - perimeter} \,. \tag{10}$$

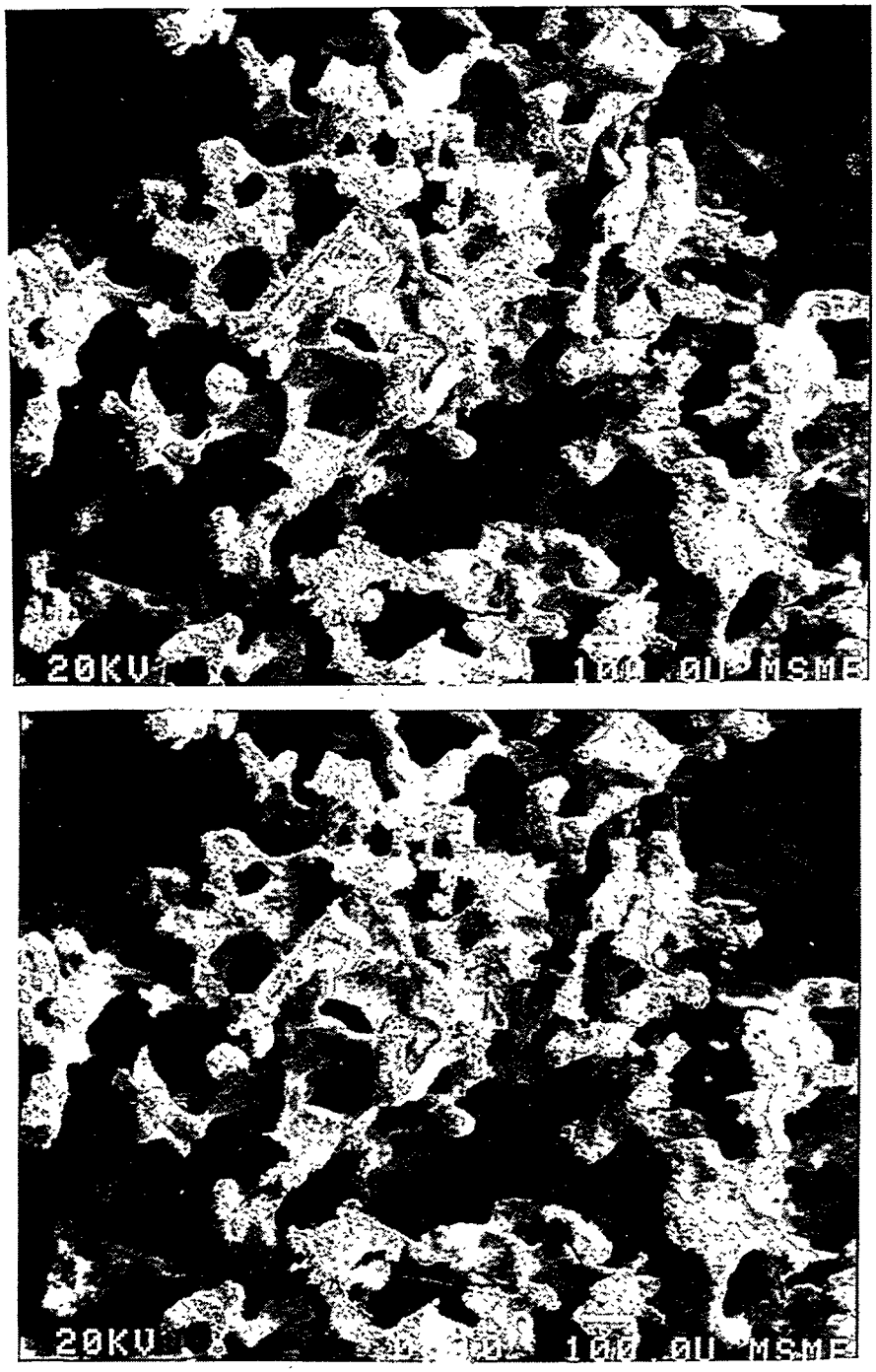

FIG. 3.3: Stereo SEM photomicrographs of a Berea sandstone pore cast. The pore space is partially impregnated with Wood's metal alloy and the quartz grains removed by hydrofluoric acid.

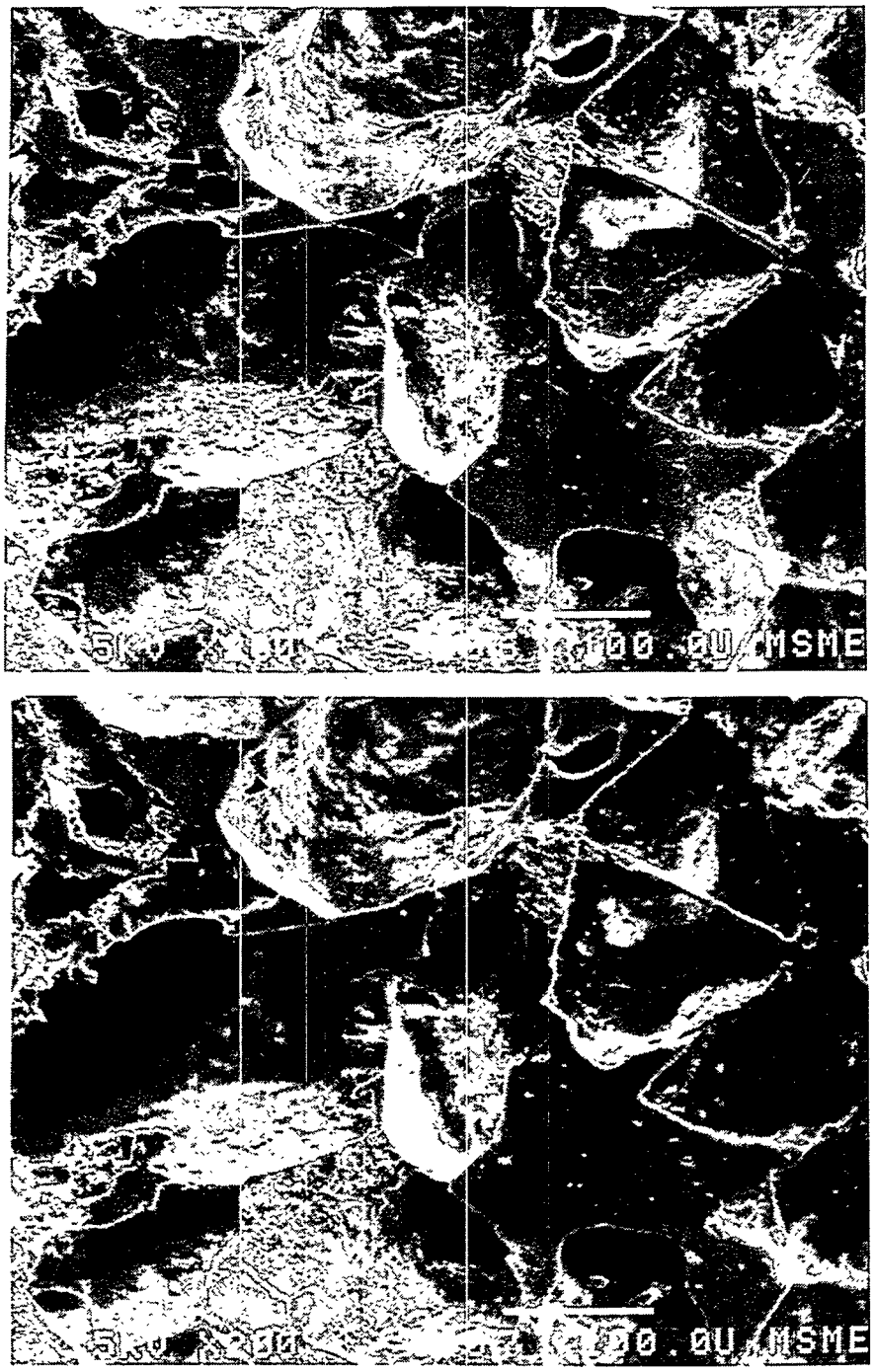

FIG. 3.4: Stereo SEM photomicrographs of a Saint-Gilles sandstone pore cast. The pore space is partially impregnated with epoxy and the quartz grains removed by hydrofluoric acid.

Using Eq. (10), we can rewrite Eq. (9) in terms of the hydraulic radius as

$$q = \frac{R_H^2 A}{2\mu} \nabla p \,, \tag{11}$$

where A is the area of the tube.

The conductance of a tube of area A and length l is given by $\sigma A/l$, where σ is the conductivity. The hydraulic conductance per unit length of each tube is therefore (aside from a length factor which eventually cancels out of the calculations) given by

$$C_i = \frac{R_H^2}{2} A \,. \tag{12}$$

The constant length of each tube assigned to all tubes in the model is assumed to be of the order of the correlation length characterizing the fluctuations of the channel cross-sectional dimensions. Measurements of two-point correlation functions (Berryman and Blair, 1986) show that the correlation length is of the order of the size of the grains in sandstone. Thus, the pore length can be assumed to be equal to the grain diameter. However, as mentioned earlier, the length does not need to appear explicitly in Eq. (6) where all conductances are proportional to L^{-1}. The local conductive elements have been obtained from 2-D SEM photomicrographs of rock sections. Figures 3.5a, 3.6a, 3.8a, and 3.9a show 2-D SEM photomicrographs of Berea sandstone (Sections B and T), Boise sandstone, and Saint-Gilles sandstone, respectively. Typical pore-space contours obtained from 2-D SEM photomicrographs of Berea, Massilon, Boise, and Saint-Gilles sandstones are shown in Figures 3.5b, 3.6b, 3.7, 3.8b, and 3.9b, respectively. The pore space contours are employed to estimate the area, perimeter, and individual conductance of each tube of varying radius using the hydraulic radius approximation and Poiseuille's law.

The basic method to calculate individual pore areas, perimeters, and hydraulic radii involves counting size and perimeter grid (or pixel) units for every feature in a standard scanning electron micrograph of some fixed magnification. The field imaged by each micrograph must contain a large enough number of pores to assure a statistically representative sample; we have found that 30-40 pores suffice for this purpose. The analysis was carried out using both a manual and an automated im-

age analysis procedure to verify the accuracy of the manual technique. The manual technique involved overlaying a square grid, with grid size of 2.54 mm, and visually counting the number of grid blocks occupied by the area of each pore, as well as the number of grid blocks that the perimeter passes through. Digital images with typical image sizes of 482 $\times$ 640 pixels, and 8 bits per pixel to quantify the darkness level, were used for studying the accuracy of the manual technique. The image analysis program sets a threshold level of darkness to distinguish between the pore contours and mineral grains. The digitized thin sections of Berea, Massilon, Boise, and Saint-Gilles sandstones (Figures 3.5b, 3.6b, 3.7, 3.8b, and 3.9b, respectively) then show pore space in white, and mineral grains in black. This method was used to estimate the area, perimeter, hydraulic radii, and hydraulic conductance of individual pores for each rock. Results for Berea (Sections B and T), Massilon, Boise, and Saint-Gilles sandstones are presented in Tables 3.1 to 3.5, respectively.

In the next section, the effect of pore shape on permeability will be studied: (1) to compare the exact permeabilities of various polygonal-shaped pores with the hydraulic-radius predictions, and (2) to calculate the error involved in using the hydraulic radius approximation and Poiseuille's law to estimate the individual pore conductances.

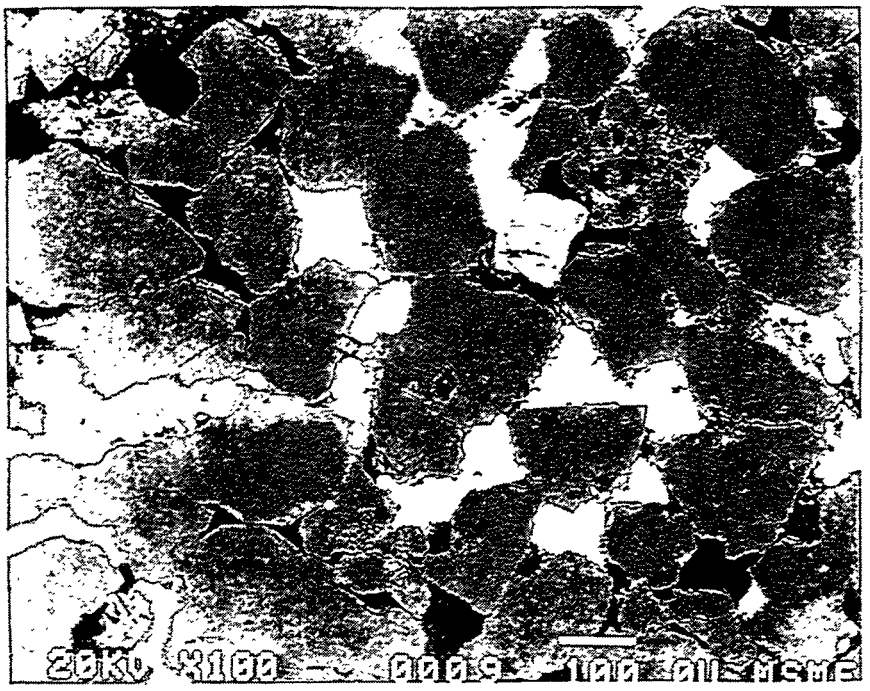

FIG. 3.5a: Typical SEM photomicrograph of Berea sandstone (Section B). The rock is composed mainly of quartz grains (dark gray), feldspar grains (medium gray), and products of grain dissolution (light gray). The pore space is impregnated with Wood's metal alloy (white), and epoxy (black). Actual width of field is about 1 mm.

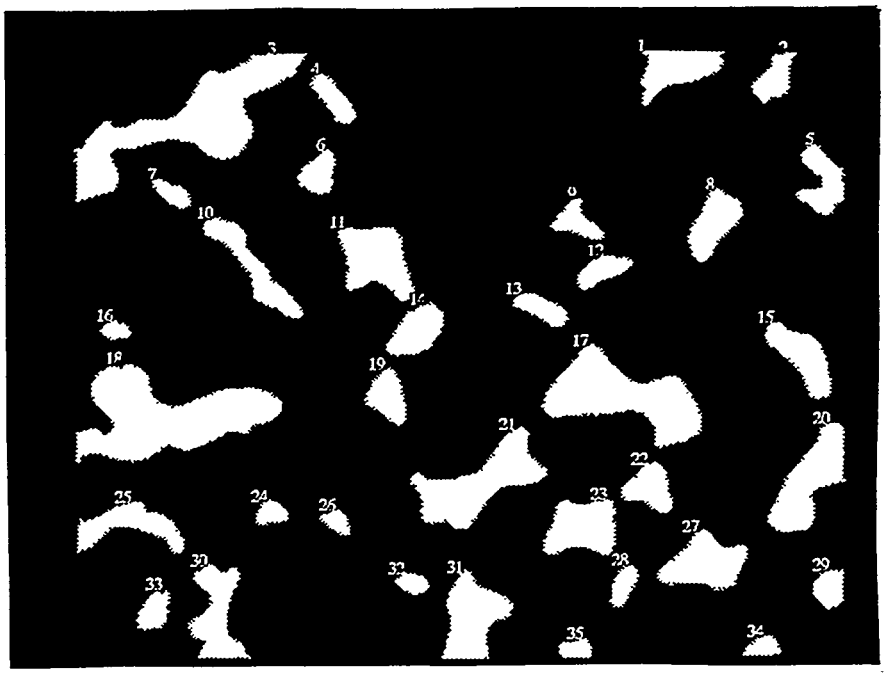

FIG. 3.5b: Pore-space contours obtained from image analysis of the photomicrograph of Berea sandstone (Section B) shown in Fig. 3.5a. The width of field is about 1 mm.

TABLE 3.1: Conductance data - Berea sandstone SEM section B.

N_i	A_i (units)	P_i (units)	A_i $\times 10^{-10}(\mathrm{m}^2)$	P_i $\times 10^{-5}$ (m)	R_{H_i} $\times 10^{-5}$(m)	C_i $\times 10^{-20}$ (m^4)
1	27	34	168.75	85.00	1.99	332.61
2	3	8	18.75	17.50	1.07	10.76
3	7	9	43.75	22.50	1.94	82.73
4	4	7	25.00	17.50	1.43	25.53
5	2	5	12.50	12.50	1.00	6.25
6	3	6	18.75	15.00	1.25	14.66
7	6	12	37.50	30.00	1.25	29.33
8	8	16	50.00	40.00	1.25	39.10
9	13	15	81.25	37.50	2.17	190.69
10	3	8	18.75	20.00	0.94	8.25
11	5	10	31.25	25.00	1.25	24.44
12	3	7	18.25	17.50	1.07	10.76
13	5	9	31.25	22.50	0.94	13.94
14	3	7	18.75	17.50	1.07	10.76
15	1	4	6.25	10.00	0.63	1.23
16	34	24	212.50	60.00	3.54	1332.80
17	4	8	25.00	20.00	1.25	19.55
18	24	24	150.00	60.00	2.50	468.75
19	7	12	43.75	30.00	1.46	46.55
20	7	14	43.75	35.00	1.25	34.21
21	2	5	12.50	12.50	1.00	6.25
22	2	5	12.50	12.50	1.00	6.25
23	18	21	112.50	52.50	2.14	258.30
24	4	9	25.00	22.50	1.11	15.45
25	10	14	62.50	35.00	1.79	99.69
26	10	13	62.50	32.50	1.92	115.56
27	2	6	12.50	15.00	0.83	4.34
28	9	16	56.20	40.00	1.41	55.58
29	1	4	6.25	10.00	0.63	1.23
30	12	10	75.00	25.00	3.00	337.50
31	2	5	12.50	12.50	1.00	6.25
32	8	13	50.00	32.50	1.54	59.20
33	2	4	12.50	10.00	1.25	9.78
34	1	3	6.25	7.50	0.83	2.14
35	2	3	12.50	7.50	1.67	17.36

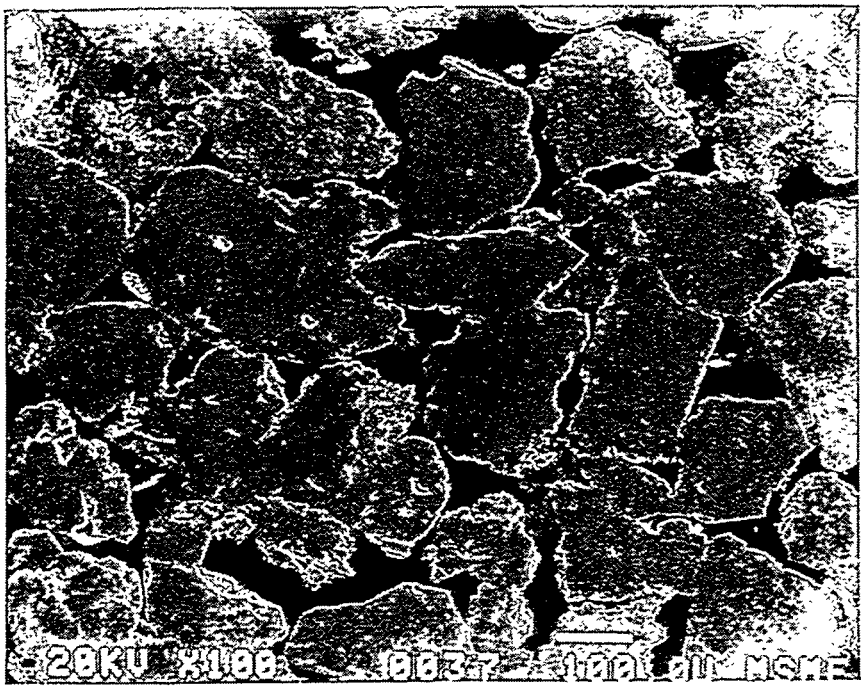

FIG. 3.6a: Typical SEM photomicrograph of Berea sandstone (Section T). The rock is composed of quartz grains (dark gray). The pore space is impregnated with epoxy (black). Actual width of field is about 1 mm.

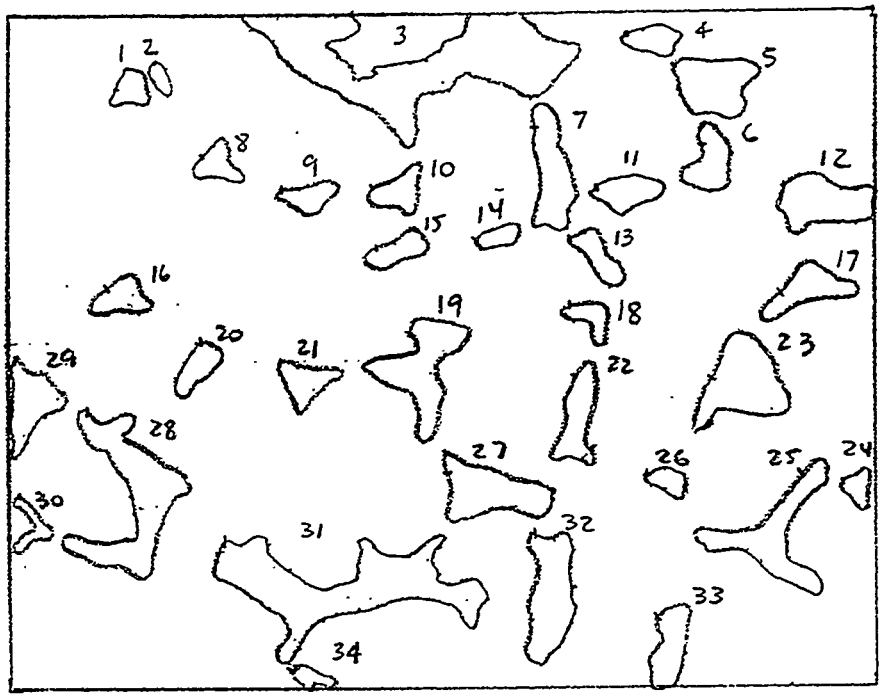

FIG. 3.6b: Pore-space contours obtained from computerized image analysis of the photomicrograph of Berea sandstone (Section T) shown in Fig. 3.6a. The width of field is about 1 mm.

TABLE 3.2: Conductance data - Berea sandstone SEM section T.

N_i	A_i (units)	P_i (units)	A_i $\times 10^{-10}(\mathrm{m}^2)$	P_i $\times 10^{-5}$ (m)	R_{H_i} $\times 10^{-5}$(m)	C_i $\times 10^{-20}(\mathrm{m}^4)$
1	3	7	18.75	17.50	1.07	10.76
2	1.5	6	9.38	15.00	0.63	1.83
3	45.5	56	284.38	140.00	2.03	586.67
4	3.5	9	21.88	22.50	0.97	10.34
5	9.5	15	59.38	37.50	1.58	74.42
6	5	12	31.25	30.00	1.04	16.96
7	9.5	18	59.38	45.00	1.32	51.68
8	2.5	10	15.63	25.00	0.63	3.05
9	3	9	18.75	22.50	0.83	6.51
10	3.5	11	21.88	27.50	0.80	6.92
11	5	11	31.25	27.50	1.14	20.18
12	11	17	68.75	42.50	1.62	89.95
13	4	11	25.00	27.50	0.91	10.33
14	2	8	12.50	20.00	0.63	2.44
15	3.5	9	21.88	22.50	0.97	10.34
16	4.5	10	28.13	25.00	1.13	17.80
17	6.5	15	40.63	37.50	1.08	23.84
18	2.8	11	17.19	27.50	0.63	3.36
19	12.5	24	78.73	60.00	1.30	66.23
20	3.8	10	23.44	25.00	0.94	10.30
21	4.5	12	28.13	30.00	0.94	12.36
22	5.5	16	34.38	40.00	0.86	12.69
23	13.5	19	84.38	47.50	1.78	133.11
24	2.5	7	15.63	17.50	0.89	6.23
25	13	3	81.25	75.00	1.08	47.68
26	2	7	12.50	17.50	0.71	3.19
27	10	18	62.50	45.00	1.39	60.28
28	20	35	125.00	87.50	1.43	127.57
29	7.5	14	46.88	35.00	1.34	42.04
30	2.5	11	15.63	27.50	0.57	2.53
31	36	47	225.00	117.50	1.92	412.52
32	13	18	81.25	45.00	1.81	132.44
33	6	14	37.50	35.00	1.07	21.53
34	1.5	7	9.38	17.50	0.54	1.35

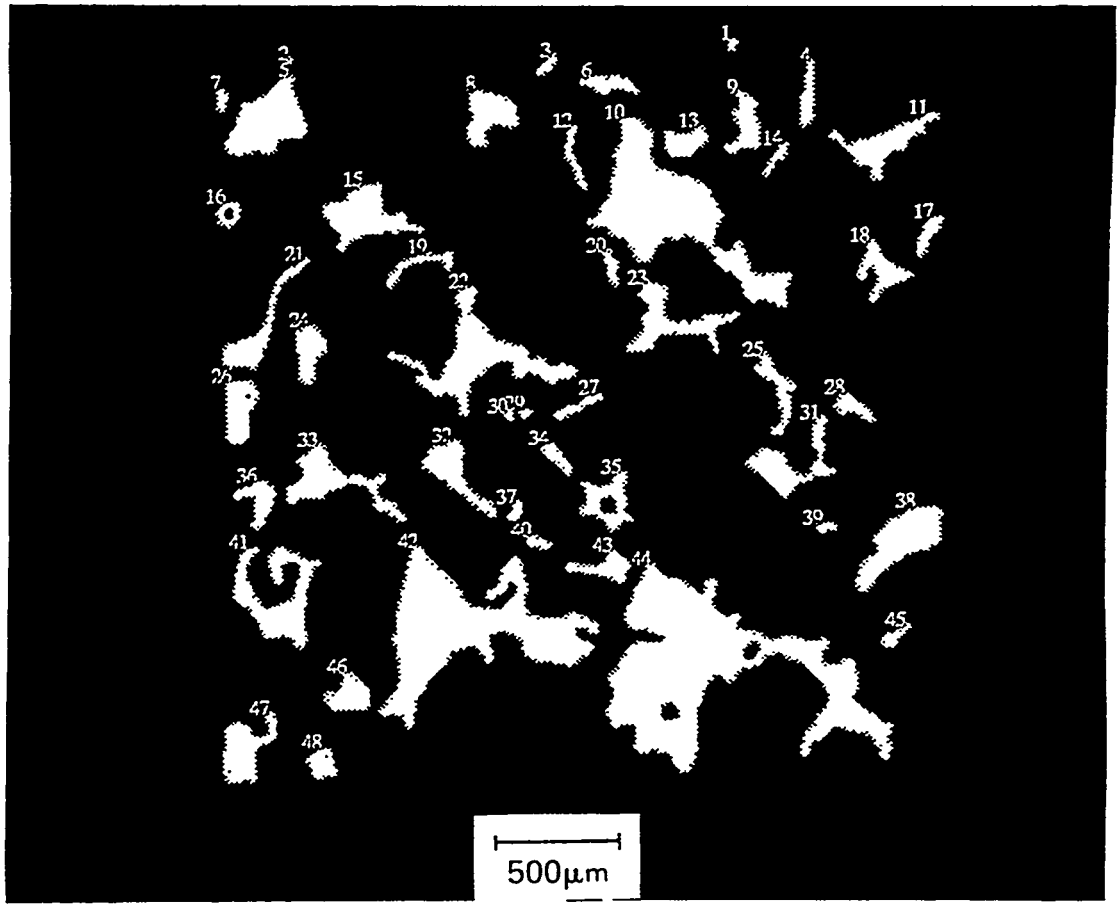

FIG. 3.7: Pore-space contours obtained from serial section of Massilon sandstone (after Koplik et al., 1984).

TABLE 3.3: Conductance data - Massilon sandstone SEM section.

N_i	A_i (units)	P_i (units)	A_i $\times 10^{-8}(\mathrm{m}^2)$	P_i $\times 10^{-4}$ (m)	R_{H_i} $\times 10^{-5}$(m)	C_i $\times 10^{-19}$ (m^4)
1	33	43	22.92	35.83	6.40	4687.54
2	54	62	37.50	51.67	7.26	9877.23
3	28	38	19.44	31.67	6.14	3665.33
4	14	36	9.72	30.00	3.24	510.50
5	8	15	5.56	12.50	4.45	548.83
6	10	14	6.94	11.67	5.95	1229.90
7	7	15	4.86	12.50	3.89	367.56
8	6	21	4.17	17.50	2.38	118.13
9	10	25	6.94	20.83	3.33	385.74
10	6	20	4.17	16.67	2.50	130.23
11	6	14	4.17	11.67	2.50	265.78
12	5	14	3.47	11.67	2.98	153.74
13	5	15	3.47	12.50	2.78	133.93
14	5	10	3.47	8.33	4.17	301.37
15	5	10	3.47	8.33	4.17	301.37
16	4	10	2.78	8.33	4.53	154.37
17	4	9	2.78	7.50	3.70	190.57
18	4	9	2.78	7.50	3.70	190.57
19	4	9	2.78	7.50	3.70	190.57
20	3	7	2.08	5.83	3.57	132.82
21	3	8	2.08	6.67	3.12	101.67
22	2	7	1.39	5.83	2.38	39.38
23	2	6	1.39	5.00	2.78	53.60
24	3	10	2.08	8.33	2.50	65.08
25	1.5	6	1.04	5.00	2.08	22.63
26	1.5	7	1.04	5.83	1.79	16.63
27	2	7	1.39	5.83	2.38	39.38
28	1.25	5	0.87	4.17	2.08	18.83
29	1.5	6	1.04	5.00	2.08	22.63
30	2	9	1.39	7.50	1.85	23.82
31	1.5	7	1.04	5.83	1.79	16.63
32	1	5	0.69	4.17	1.67	9.63
33	2	7	1.39	5.83	2.38	39.38
34	2	5	1.39	4.17	3.33	77.17
35	1	4	0.69	3.33	2.08	15.05
36	0.5	2	0.35	1.67	2.08	7.52
37	0.5	3	0.35	2.50	1.39	3.34
38	0.5	2.5	0.35	2.08	1.67	4.81
39	0.75	4	0.52	3.33	1.56	6.37
40	0.75	5	0.52	4.17	1.25	4.07
41	1	4	0.69	3.33	2.08	15.05
42	0.25	1.5	0.17	1.25	1.39	1.69
43	0.75	3	0.52	2.50	2.08	11.31
44	0.50	1.5	0.35	1.25	2.78	13.37
45	0.13	0.75	0.09	0.63	0.14	0.84
46	0.13	1	0.09	0.83	0.10	0.47
47	0.13	1	0.09	0.83	0.10	0.47
48	0.75	4	0.52	3.33	0.16	6.37

FIG. 3.8a: Typical SEM photomicrograph of Boise sandstone. The rock is composed mainly of quartz grains (dark gray). The pore space is impregnated with epoxy (black). Actual width of field is about 1 mm.

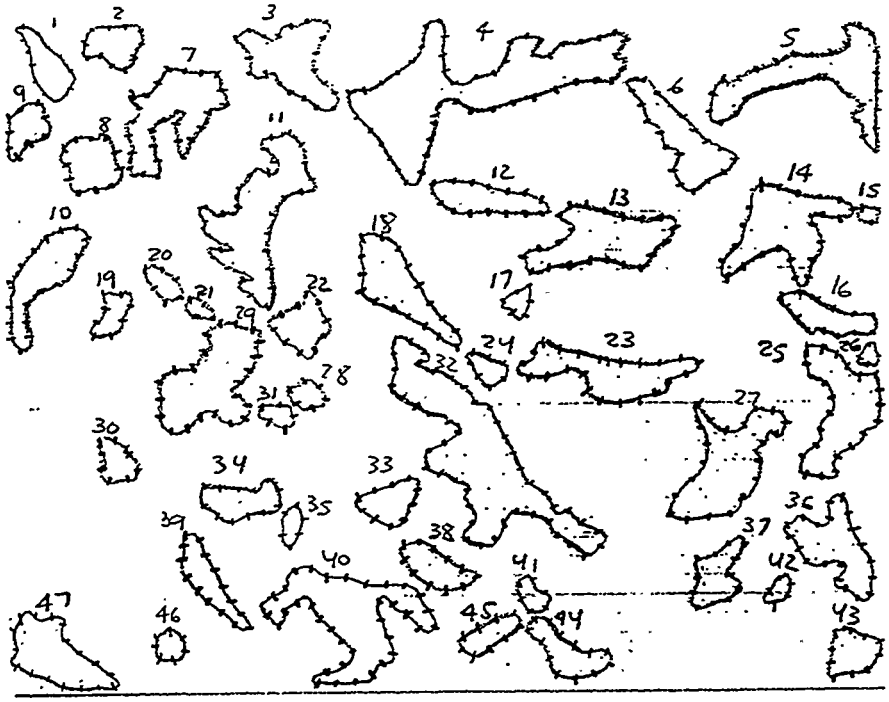

FIG. 3.8b: Pore-space contours obtained from image analysis of the photomicrograph of Boise sandstone shown in Fig. 3.8a. The width of field is about 1 mm.

TABLE 3.4: Conductance data - Boise sandstone SEM section.

N_i	A_i (units)	P_i (units)	A_i $\times 10^{-10}(m^2)$	P_i $\times 10^{-4}$ (m)	R_{H_i} $\times 10^{-6}$(m)	C_i $\times 10^{-20}$ (m^4)
1	5.5	12	34.38	3.00	11.46	22.57
2	5	11	31.25	2.75	11.36	20.18
3	12.5	21	78.13	5.25	14.88	86.50
4	40	47.5	250.00	11.88	21.04	554.02
5	18	31	112.50	7.75	14.52	118.53
6	12	19.5	75.00	4.88	15.37	88.76
7	16	27	100.00	6.75	14.82	109.74
8	7	11	43.75	2.75	15.91	55.37
9	4.5	9	28.13	2.25	12.50	21.97
10	11	18	68.75	4.50	15.28	80.24
11	22	30	137.50	7.50	18.33	231.08
12	8	14.5	50.00	3.63	13.77	47.56
13	16	21	100.00	5.25	19.05	181.41
14	17	22.5	106.25	5.63	18.87	189.55
15	1	3.5	6.25	0.88	7.10	1.59
16	6	12.5	37.50	3.13	11.98	27.00
17	1.5	6	9.38	1.50	6.25	1.83
18	12	17	75.00	4.25	17.65	116.78
19	3	8	18.75	2.00	9.38	8.24
20	2	6	12.50	1.50	8.33	4.34
21	1	4	6.25	1.00	6.25	1.22
22	6	10	37.50	2.50	15.00	42.19
23	13	22	81.25	5.50	14.77	88.66
24	2.5	6.5	15.63	1.63	9.59	7.22
25	15	23	93.75	5.75	16.30	124.61
26	1	3.5	6.25	0.88	7.10	1.59
27	18	21	112.50	5.25	21.43	258.29
28	2	6	12.50	1.50	8.33	4.34
29	17.5	22	109.38	5.50	19.88	216.27
30	3.5	7.5	21.88	1.88	11.64	14.89
31	1.5	5	9.38	1.25	7.50	2.64
32	35	47	218.75	11.75	18.62	379.09
33	5	10	31.25	2.50	12.50	24.41
34	6.5	12	40.63	3.00	13.54	37.25
35	2	6.5	12.50	1.63	7.67	3.70
36	11.5	19.5	71.88	4.88	14.73	78.12
37	6.5	12	40.63	3.00	13.54	37.25
38	5.5	11	34.38	2.75	12.50	26.86
39	7	14.5	43.75	3.63	12.05	31.86
40	23.5	36.5	146.88	9.13	16.09	190.26
41	2.5	6	15.63	1.50	10.42	8.48
42	2.5	5	15.63	1.25	12.50	12.21
43	5.75	10	35.94	2.50	14.38	37.13
44	6	13	37.50	3.25	11.54	24.96
45	3.5	9	21.88	2.25	9.72	10.34
46	2	6.5	12.50	1.63	7.67	3.70
47	12.5	17	78.13	4.25	18.38	132.00

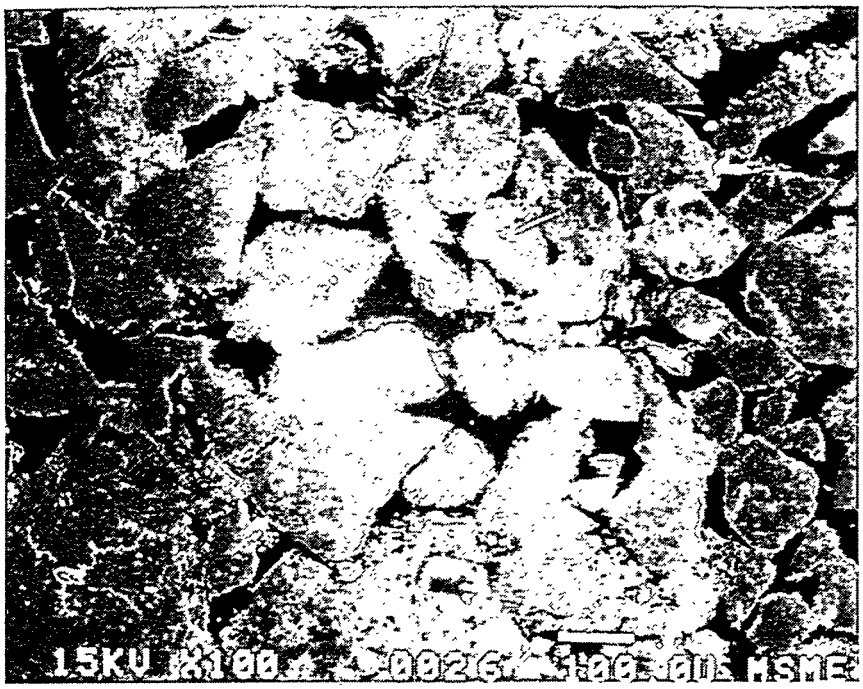

FIG. 3.9a: Typical SEM photomicrograph of Saint-Gilles sandstone. The rock is composed mainly of quartz grains (dark gray). The pore space is impregnated with epoxy (black). Actual width of field is about 1 mm.

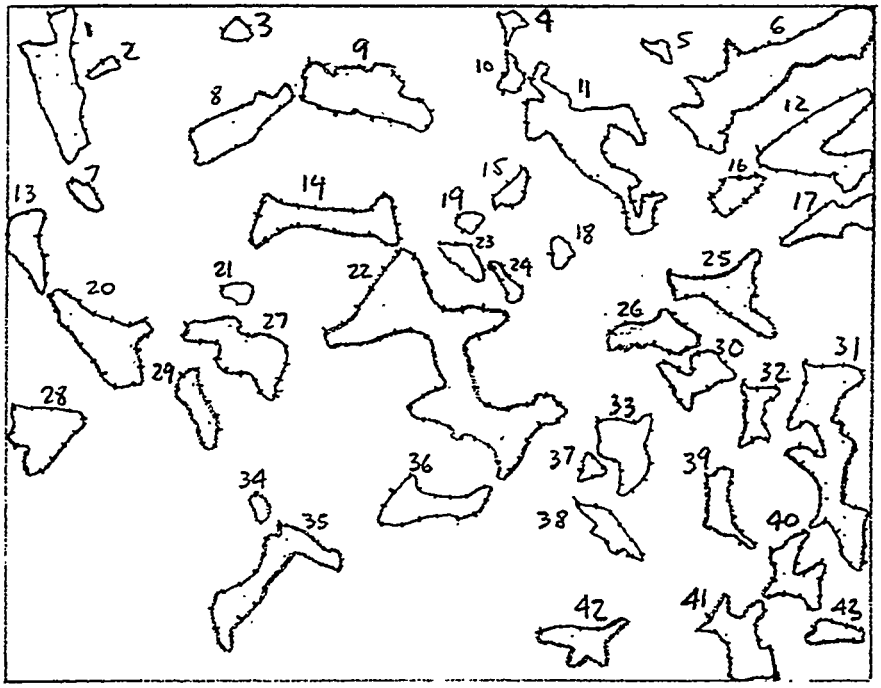

FIG. 3.9b: Pore-space contours obtained from image analysis of the photomicrograph of Saint-Gilles sandstone shown in Fig. 3.9a. The width of field is about 1 mm.

TABLE 3.5: Conductance data - Saint-Gilles sandstone SEM section.

N_i	A_i (units)	P_i (units)	A_i $\times 10^{-10}(m^2)$	P_i $\times 10^{-4}$ (m)	R_{H_i} $\times 10^{-6}$(m)	C_i $\times 10^{-20}$ (m^4)
1	13.5	25	84.38	6.25	13.50	76.89
2	1	4	6.25	1.00	6.25	1.22
3	1.5	5	9.38	1.25	7.50	263.67
4	1	6	6.25	1.50	4.17	54.25
5	1	6	6.25	1.50	4.17	54.25
6	25	38	156.25	9.50	16.45	21134.06
7	1.5	7	9.38	1.75	5.36	134.53
8	9	19	56.25	4.75	11.84	3944.12
9	14	20	87.50	5.00	17.50	13398.44
10	1.5	6.5	9.38	1.63	5.76	156.02
11	19	40.5	118.75	10.13	11.72	8167.34
12	14	24	87.50	6.00	14.58	9304.47
13	5.5	11	34.38	2.75	12.50	2685.55
14	10	21.5	62.50	5.38	11.62	4225.26
15	2	6.5	12.50	1.63	7.67	369.82
16	3	8	18.75	2.00	9.38	823.98
17	5	13.5	31.25	3.38	9.25	1339.59
18	1	4.5	6.25	1.13	5.53	96.45
19	1	4	6.25	1.00	6.25	122.07
20	12.5	17	78.13	4.25	18.38	13199.65
21	1.5	4	9.38	1.00	9.38	411.99
22	39	47	243.75	11.75	20.75	52447.91
23	2.5	8	15.63	2.00	7.82	476.84
24	1.5	7	9.38	1.75	5.36	134.53
25	9	19	56.25	4.75	11.84	3944.12
26	6	12.5	37.50	3.13	11.98	2700.00
27	11	17.5	68.75	4.38	15.70	8488.52
28	9	13.5	56.25	3.38	16.64	7812.50
29	4	12	25.00	3.00	8.33	868.06
30	6	14	37.50	3.50	10.71	2152.42
31	22	36	137.50	9.00	15.28	16046.97
32	4	12.5	25.00	3.13	7.99	800.00
33	7.5	14	46.88	3.50	13.39	4203.95
34	1	4	6.25	1.00	6.25	122.07
35	11.5	22	71.88	5.50	13.07	6137.31
36	7.5	15.5	46.88	3.88	12.08	3429.66
37	1	4	6.25	1.00	6.25	122.07
38	3.5	11	21.88	2.75	7.96	692.07
39	4.5	12	28.13	3.00	9.38	1235.96
40	6	15	37.50	3.75	10.00	1875.00
41	8.5	17	53.13	4.25	12.50	4150.39
42	5.5	14	34.38	3.50	9.82	1657.91
43	2.5	8	15.63	2.00	7.82	476.84

3.1.3 Effect of cross-sectional pore shape on permeability

As part of our analysis of the relationships between pore structure and transport properties, we have studied the effect of pore shape on permeability using the torsion analogy concept borrowed from the theory of elasticity (exact solution) and compared these results to those obtained using the hydraulic radius approximation.

3.1.3.1 *Exact solution*

There are many problems in mathematical physics which lead to the same equation and the same boundary conditions. This is the case for the analogy between the torsion of prismatic bars and the viscous flow through pipes. Thus, the general solution of the torsion problem of prismatic bars of non-circular sections will be used. The stresses are given by the relations (Sokolnikoff, 1956)

$$\tau_{xz} = Gw\frac{\partial \Psi}{\partial y} \; ; \;\; \tau_{yz} = -Gw\frac{\partial \Psi}{\partial x} \, , \tag{13}$$

where $\Psi = \Psi(x, y)$ is the stress function, G the shear modulus of elasticity, and w the angle of torsion per unit length.

If a stress function $\Psi(x, y)$ is assumed to exist such that the equations of static equilibrium are satisfied, then the equation of compatibility in a region Γ in x-y plane that the shear stresses satisfy becomes (Sokolnikoff, 1956):

$$\frac{\partial^2 \Psi}{\partial x^2} + \frac{\partial^2 \Psi}{\partial y^2} = -2 \, . \tag{14}$$

The torsional rigidity is by definition,

$$D = 2G \int_{\Gamma} \Psi dA \, , \tag{15}$$

where G is the shear modulus of elasticity on A, the area of interest.

The equation of conservation of momentum or equation of motion for viscous pipe flow in a region Γ in x-y plane is (Purday, 1949)

$$\nabla^2 u(x,y) = \frac{\partial^2 u}{\partial x^2} + \frac{\partial^2 u}{\partial y^2} = \frac{1}{\mu}\frac{dp}{dz}\,, \tag{16}$$

where z is the coordinate along the axis of the tube, u is the fluid velocity in the z-direction, μ the viscosity of the fluid, and p the fluid pressure.

From the comparison of Eqs. (14) and (16) we can write

$$u = -\frac{1}{2\mu}\frac{dp}{dz}\Psi\,. \tag{17}$$

Then the continuity equation for hydraulic flux can be expressed by

$$q = \int_\Gamma u dA = -\frac{1}{2\mu}\frac{dp}{dz}\int_\Gamma \Psi dA = \frac{-D}{4\mu G}\frac{dp}{dz} = \frac{-kA}{\mu}\frac{dp}{dz}\,. \tag{18}$$

Therefore, if the torsional rigidity D of the section is calculated, the exact permeability k can be calculated.

3.1.3.2 *Hydraulic radius approximation*

According to Hagen-Poiseuille equation, the volumetric flux of fluid through a cylindrical tube of radius a is given exactly by

$$q = \frac{\pi a^4}{8\mu}\nabla p\,. \tag{19}$$

Since the area A of a circle is πa^2 and the perimeter P of a circle is $2\pi a$, then the radius a is $2A/P$. Therefore, the permeability can be expressed in terms of the hydraulic radius as

$$k = \frac{a^2}{8} = \frac{1}{8}\left(\frac{2A}{P}\right)^2 = \frac{1}{2}\left(\frac{A}{P}\right)^2 \equiv \frac{1}{2}R_H^2\,. \tag{20}$$

This equation is exact for circular cross sections. The 'hydraulic radius' method assumes that Eq. (20) can be used for all cross sections.

Now we show examples to test the equivalence of the calculated permeabilities for various pore shapes using the torsion analogy (exact solution) and the hydraulic radius approximation, respectively.

3.1.3.3 *Examples*

1. Circular shape of radius a:

   Since the area A of a circle is πa^2 and the perimeter P of a circle is $2\pi a$, then the radius a is $2A/P$.

   The permeability using the hydraulic approximation is

$$k_{circle}^{H.R.} = \frac{1}{8}\left(\frac{2A}{P}\right)^2 = \frac{a^2}{8}\,. \tag{21}$$

   The torsional rigidity D for a circular shape of radius a is (Sokolnikoff, 1956)

$$D = \frac{\pi G a^4}{2}\,. \tag{22}$$

   Thus

$$q = \frac{-\pi G a^4/2}{4\mu G}\frac{dp}{dz} = \frac{-\pi a^4}{8\mu}\frac{dp}{dz}\,. \tag{23}$$

   According to Darcy's law

$$q = -\frac{kA}{\mu}\frac{dp}{dz} = \frac{-k\pi a^2}{\mu}\frac{dp}{dz}\,, \tag{24}$$

   where k is permeability.

   Thus, the exact permeability is

$$k_{circle}^{EXACT} = \frac{\pi a^4/8}{\pi a^2} = \frac{a^2}{8}\,. \tag{25}$$

   Hence, for a circular shape

$$k_{circle}^{H.R.} \equiv k_{circle}^{EXACT}\,. \tag{26}$$

As expected then for a circular tube, the calculated permeability using the torsion analogy (exact solution) is equivalent to the permeability given by the hydraulic radius approximation.

2. Triangle of side a:

   The area A of an equilateral triangle of side a is $\sqrt{3}a^2/4$, and the perimeter P is equal to $3a$. Thus, $2A/P = \sqrt{3}a/6$.

   The permeability using the hydraulic radius approximation is

$$k_{triangle}^{H.R.} = \frac{1}{8}\left(\frac{2A}{P}\right)^2 = \frac{1}{8}\left(\frac{\sqrt{3}a}{6}\right)^2 = \frac{a^2}{96}\,. \tag{27}$$

   The torsional rigidity is (Berker, 1963)

$$D = \frac{\sqrt{3}Ga^4}{80}\,. \tag{28}$$

   The permeability using the exact solution is

$$k_{triangle}^{EXACT} = \frac{D}{4GA} = \frac{G\sqrt{3}a^4/80}{4G\sqrt{3}a^2/4} = \frac{a^2}{80}\,. \tag{29}$$

   Thus, the error involved in the hydraulic radius approximation is

$$ERROR = \frac{k_{triangle}^{H.R.}}{k_{triangle}^{EXACT}} = \frac{80}{96} \times 100 = -20\%\,. \tag{30}$$

3. Square of side a:

   The area A of a square of side a is a^2, and the perimeter P is equal to $4a$. Thus, $2A/P = a/2$.

   The permeability using the hydraulic radius approximation is

$$k_{square}^{H.R.} = \frac{1}{8}\left(\frac{2A}{P}\right)^2 = \frac{a^2}{32}\,. \tag{31}$$

   The torsional rigidity is (Berker, 1963)

$$D = \frac{2.253Ga^4}{16}\,. \tag{32}$$

The permeability using the exact solution is

$$k_{square}^{EXACT} = \frac{D}{4GA} = \frac{2.253Ga^4/16}{4Ga^2} = \frac{a^2}{28} . \tag{33}$$

Thus, the error involved in the hydraulic radius approximation is

$$ERROR = \frac{k_{square}^{H.R.}}{k_{square}^{EXACT}} = \frac{28}{32} \times 100 = -11\% . \tag{34}$$

4. Slit of length L and width h ($h \ll L$):

   The area A of a slit of length L and width h is Lh, and the perimeter $P \approx 2L$. Thus, $2A/P \approx h$.

   The permeability using the hydraulic radius approximation is

$$k_{slit}^{H.R.} = \frac{1}{8}\left(\frac{2A}{P}\right)^2 = \frac{h^2}{8} . \tag{35}$$

   The torsional rigidity is (Berker, 1963)

$$D = \frac{5.333GLh^3}{16} . \tag{36}$$

   The permeability using the exact solution is

$$k_{slit}^{EXACT} = \frac{D}{4GA} = \frac{5.333GLh^3/16}{4GLh} = \frac{h^2}{12} . \tag{37}$$

   Thus, the error involved in the hydraulic radius approximation is

$$ERROR = \frac{k_{slit}^{H.R.}}{k_{slit}^{EXACT}} = \frac{12}{8} \times 100 = +33\% . \tag{38}$$

5. Ellipse with major axis $2a$ and minor axis $2b$:

   The area A of the ellipse is πab, and the perimeter P is equal to $4aE(i)$ with $i = \sqrt{a^2 - b^2}/a$ (see elliptic integrals, Råde and Westergren, 1992). Thus, $2A/P = \pi b/2E(i)$.

   For an ellipse with $a : b = 4 : 1$, the ratio $2A/P = a/3.325$. Thus, the permeability using the hydraulic radius approximation is

$$k_{ellipse}^{H.R.} = \frac{1}{8}\left(\frac{2A}{P}\right)^2 = \frac{a^2}{88} . \tag{39}$$

The torsional rigidity is (Berker, 1963)

$$D = \frac{G\pi a^4}{68} . \tag{40}$$

The permeability using the exact solution is

$$k_{ellipse}^{EXACT} = \frac{D}{4GA} = \frac{G\pi a^4/68}{4G\pi a^2/4} = \frac{a^2}{68} . \tag{41}$$

Thus, the error involved in the hydraulic radius approximation is

$$ERROR = \frac{k_{ellipse}^{H.R.}}{k_{ellipse}^{EXACT}} = \frac{68}{88} \times 100 = -23\% . \tag{42}$$

For an ellipse with $a : b = 10 : 1$, the ratio $2A/P = a/6.366$. Thus, the permeability using the hydraulic radius approximation is

$$k_{ellipse}^{H.R.} = \frac{1}{8}\left(\frac{2A}{P}\right)^2 = \frac{a^2}{324} . \tag{43}$$

The torsional rigidity is (Berker, 1963)

$$D = \frac{G\pi a^4}{321} . \tag{44}$$

The permeability using the exact solution is

$$k_{ellipse}^{EXACT} = \frac{D}{4GA} = \frac{G\pi a^4/321}{4G\pi a^2/10} = \frac{a^2}{403} . \tag{45}$$

Thus, the error involved in the hydraulic radius approximation is

$$ERROR = \frac{k_{ellipse}^{H.R.}}{k_{ellipse}^{EXACT}} = \frac{403}{321} \times 100 = +26\% . \tag{46}$$

TABLE 3.6: List of comparative values to show equivalence of the calculated permeabilities using the torsion analogy and the hydraulic radius approximation, respectively.

Cross section	k^{EXACT}	$k^{H.R.}$	Error (%)
Circle	$a^2/8$	$a^2/8$	–
Equilateral triangle	$a^2/80$	$a^2/96$	−20
Square	$a^2/28$	$a^2/32$	−11
Slit	$h^2/12$	$h^2/8$	+33
Ellipse $a:b=4:1$	$a^2/68$	$a^2/88$	−23
Ellipse $a:b=10:1$	$a^2/403$	$a^2/324$	+26

A list of comparative values to show equivalence of calculated permeabilities using the torsion analogy and the hydraulic radius approximation, respectively, is presented in Table 3.6. The results of this study show that the error involved in the hydraulic radius approximation lies within ±30%. The approximation does not systematically either underpredict or overpredict the pore conductances, so that the errors will cancel, at least partially, when applied to a network of pores of different cross sections. One may reasonably conclude that the conductivity of a tubular pore is well approximated by the hydraulic radius theory.

Boussinesq expressed the hydraulic flux q in terms of a dimensionless coefficient κ defined by the relationship (Berker, 1963)

$$q = \kappa \cdot \frac{p}{\mu l} \cdot s^2 \,, \tag{47}$$

where s represents the area of the cross section under consideration. The values of the coefficients κ are (Berker, 1963)

for the circle	0.0398
for the square	0.0351
for the equilateral triangle	0.0289

Thus, we can write

$$\kappa_{circle} = 0.0398 > \kappa_{square} = 0.0351 > \kappa_{equilateral\ triangle} = 0.0289 \,. \tag{48}$$

Results of our analysis using the torsion analogy show that for cross sections of equivalent areas after normalizing permeability with respect to the equivalent circular radius a_o,

$$k_{circle} = 0.13a_o^2 > k_{square} = 0.11a_o^2 > k_{equilateral\ triangle} = 0.09a_o^2\ , \tag{49}$$

where k is permeability.

Therefore, the permeability results obtained using the torsion analogy are in close agreement with the Boussinesq solution.

3.1.4 Effect of pore orientation

In the 2-D section under consideration, the pore cross sections are randomly oriented with respect to the directions of the channel axes. The orientation effect has been accounted for by means of the following geometrical and stereological considerations for projected images.

3.1.4.1 *Projected line*

The fundamental relationship for projected lines (Underwood, 1970) relates the mean projected length of a randomly oriented line segment to the true length.

Consider a line segment δl with one end fixed which is free to rotate in any direction described by ϕ and θ. Figure 3.10 shows one octant of the spherical surface of area $S = \pi\delta l^2/2$ generated by rotating the line segment δl.

The average projected length is

$$\overline{\delta l'} = \frac{\int_0^{\pi/2}\int_0^{\pi/2} \delta l'\, dS}{\int_0^{\pi/2}\int_0^{\pi/2} dS} = \frac{\int_0^{\pi/2}\int_0^{\pi/2} \delta l \sin\theta \delta l^2 \sin\theta d\theta d\phi}{\int_0^{\pi/2}\int_0^{\pi/2} \delta l^2 \sin\theta d\theta d\phi}\ . \tag{50}$$

We then have

$$\overline{\delta l'} = \frac{\pi}{4}\delta l\ . \tag{51}$$

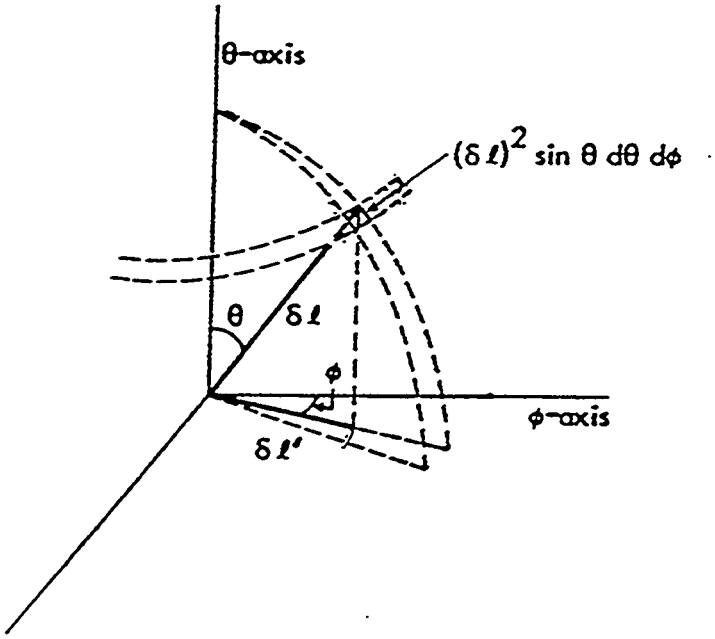

FIG. 3.10: Mean projected length of a randomly oriented linear segment (after Underwood, 1970).

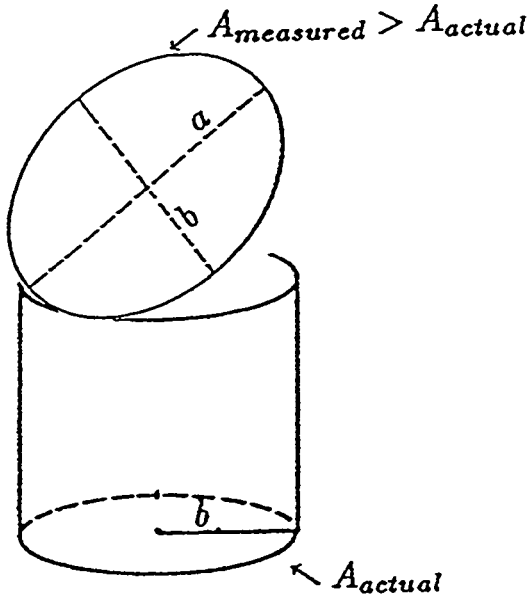

FIG. 3.11: Relationship between area of a circular tube (area actual) and its projection onto a plane (area measured).

3.1.4.2 *Projected area*

Consider a cylindrical tube of circular cross section that has been sliced by a plane oriented at an angle with respect to the channel axis (Figure 3.11). The projected cross section into the 2-D section under consideration is an ellipse with major axis $2a$, minor axis $2b$, and an area measured $A_{measured}$ equal to πab, where $a = b/\cos\theta$. The actual area of the circular section A_{actual} is equal to πb^2.

Thus we can write

$$A_{actual} = \left\langle \frac{1}{\cos\theta} \right\rangle^{-1} A_{measured} \,, \tag{52}$$

where

$$\left\langle \frac{1}{\cos\theta} \right\rangle = \frac{\int_0^{\pi} \int_0^{\theta_{max}} \frac{1}{\cos\theta} a^2 \sin\theta d\theta d\phi}{\int_0^{\pi} \int_0^{\theta_{max}} a^2 \sin\theta d\theta d\phi} \,, \tag{53}$$

with $\theta_{max} = \arctan(L/D)$, where L/D is the maximum ratio of pore length to diameter. Using an average of $L/D = 5$, as estimated from the micrographs, we find that

$$A_{actual} = 0.61 A_{measured} \,. \tag{54}$$

Evaluation of the integral appearing in Eq. (53) shows that the factor $\langle \frac{1}{\cos\theta} \rangle$ is not sensitive to the value chosen for L/D.

3.1.4.3 *Hydraulic radius*

The elliptical cross section in the 2-D section under consideration, with major axis $2a$ and minor axis $2b$, has a measured area $A_{measured}$ equal to πab, and, to within 10%, a measured perimeter $P_{measured} \approx \pi\sqrt{2(a^2+b^2)} = \pi a\sqrt{2(1+\cos^2\theta)}$ (CRC Standard Mathematical Tables, Beyer, W.H., 1988).

The measured hydraulic radius $R_{H_{measured}}$ of each tube is

$$R_{H_{measured}} \equiv \frac{A_{measured}}{P_{measured}} = \frac{\pi ab}{\pi a\sqrt{2(1+\cos^2\theta)}} \,. \tag{55}$$

The actual hydraulic radius $R_{H_{actual}}$ of each tube is

$$R_{H_{actual}} \equiv \frac{A_{actual}}{P_{actual}} = \frac{\pi b^2}{2\pi b} \,. \tag{56}$$

Thus we can write

$$R_{H_{actual}} = \frac{\sqrt{2}}{2} \left\langle \frac{1}{\sqrt{1+\cos^2\theta}} \right\rangle^{-1} R_{H_{measured}} \,, \tag{57}$$

where

$$\left\langle \frac{1}{\sqrt{1+\cos^2\theta}} \right\rangle = \frac{\int_0^{\pi} \int_0^{\theta_{max}} \frac{1}{\sqrt{1+\cos^2\theta}} a^2 \sin\theta d\theta d\phi}{\int_0^{\pi} \int_0^{\theta_{max}} a^2 sin\theta d\theta d\phi} \,. \tag{58}$$

Numerical evaluation of this integral, using $\theta_{max} = \arctan(L/D) = 78.7°$, gives

$$R_{H_{actual}} = 0.85 R_{H_{measured}} \,. \tag{59}$$

3.1.4.4 *Hydraulic conductance*

The elliptical cross section in the 2-D section under consideration, with major axis $2a$ and minor axis $2b$, has a measured area $A_{measured}$ equal to πab, and a measured perimeter $P_{measured} \approx \pi\sqrt{2(a^2+b^2)} = \pi a\sqrt{2(1+\cos^2\theta)}$.

The actual hydraulic conductance $C_{i_{actual}}$ of each tube is (aside from a length factor, which eventually cancels out of the calculations)

$$C_{i_{actual}} = \left(\frac{R_H^2}{2} A\right)_{actual} = \frac{1}{2}\left(\frac{\pi b^2}{2\pi b}\right)^2 \pi b^2 = \frac{\pi b^4}{8} \,. \tag{60}$$

The measured hydraulic conductance $C_{i_{measured}}$ of each tube from the 2-D section under consideration is (aside from a length factor, which eventually cancels out of the calculations)

$$C_{i_{measured}} = \left(\frac{R_H^2}{2}A\right)_{measured} = \frac{1}{2}\left(\frac{\pi ab}{\pi\sqrt{2(a^2+b^2)}}\right)^2 \pi ab = \frac{\pi b^4}{2\cos\theta(1+\cos^2\theta)} \,. \quad (61)$$

Thus we can write

$$(R_H^2 A)_{actual} = \frac{1}{2}\left\langle \frac{1}{\cos\theta(1+\cos^2\theta)} \right\rangle^{-1} (R_H^2 A)_{measured} \,, \quad (62)$$

where

$$\left\langle \frac{1}{\cos\theta(1+\cos^2\theta)} \right\rangle = \frac{\int_0^{\pi}\int_0^{\theta_{max}} \frac{1}{\cos\theta(1+\cos^2\theta)} a^2 \sin\theta d\theta d\phi}{\int_0^{\pi}\int_0^{\theta_{max}} a^2 \sin\theta d\theta d\phi} \,. \quad (63)$$

Numerical evaluation of this integral, using $\theta_{max} = \arctan(L/D) = 78.7°$, gives

$$(R_H^2 A)_{actual} = 0.40(R_H^2 A)_{measured} \,. \quad (64)$$

3.1.4.5 *Tortuosity and projection*

We have derived the tortuosity factor, τ, for randomly oriented cylindrical tubes in three dimensions.

According to the Hagen-Poiseuille equation, the volumetric flux of fluid through a cylindrical tube is given by (Figure 3.12)

$$q = \frac{k}{\mu}\pi b^2 \frac{\triangle p}{\triangle l} = \frac{k}{\mu}\frac{\pi ab}{\cos\theta}\frac{\triangle p}{\triangle y} \,, \quad (65)$$

where θ is the polar angle in spherical polar coordinates.

Since $b = a\cos\theta$ we get

$$\frac{\triangle p}{\triangle l}\pi b^2 = \frac{\triangle p}{\triangle y}\frac{\pi b^2}{\cos^2\theta} \,. \quad (66)$$

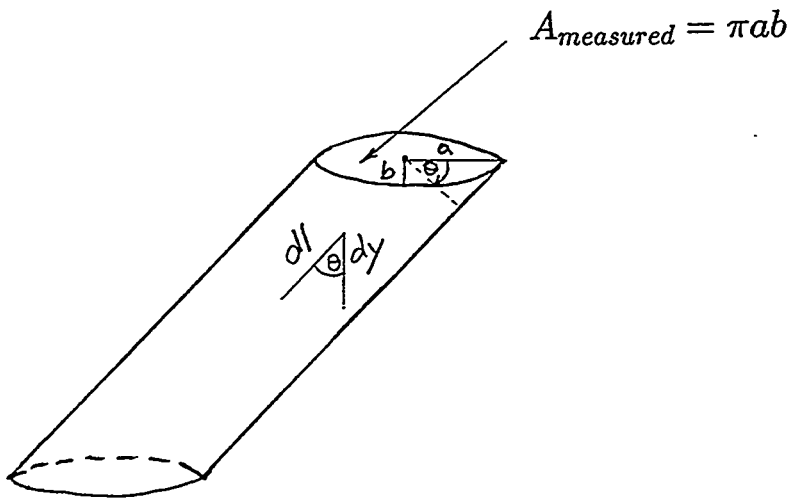

FIG. 3.12: Construction used in calculating the tortuosity factor, τ, for randomly oriented cylindrical tubes in three dimensions.

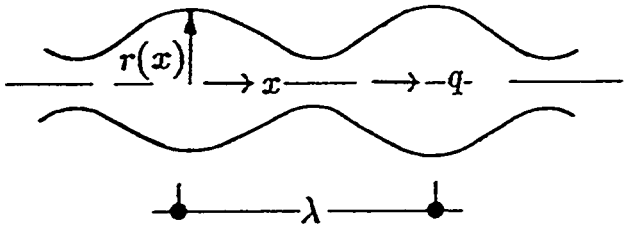

FIG. 3.13: Sinusoidal variation of the radius along the length of a tube used to calculate the constriction hydraulic factor.

We then have

$$\frac{\triangle p}{\triangle y} = \langle \cos^2 \theta \rangle \frac{\triangle p}{\triangle l} , \tag{67}$$

where

$$\langle \cos^2 \theta \rangle = \frac{\int_0^{\pi} \int_0^{\pi/2} \cos^2 \theta a^2 \sin \theta d\theta d\phi}{\int_0^{\pi} \int_0^{\pi/2} a^2 \sin \theta d\theta d\phi} = \frac{\pi/3}{\pi} = \frac{1}{3} . \tag{68}$$

Thus we can write

$$\frac{\triangle p}{\triangle y} = \frac{1}{\langle \cos^2 \theta \rangle^{-1}} \frac{\triangle p}{\triangle l} = \frac{1}{3} \frac{\triangle p}{\triangle l} , \tag{69}$$

with the tortuosity factor defined as follows:

$$\tau \equiv \langle \cos^2 \theta \rangle^{-1} = 3 . \tag{70}$$

3.1.5 Pore body to pore throat ratio dependence

Pore casts of sedimentary rocks, such as that of Berea sandstone and of Saint-Gilles sandstone (Figures 3.3 and 3.4), show that the cross section of a pore typically varies along its length. This factor must be accounted for when estimating the areas and perimeters of the pores, or else the predicted conductances will be overestimated.

We have seen that the Hagen-Poiseuille equation for the volumetric flux of fluid through a cylindrical tube is expressed as

$$q = \frac{\pi r^4}{8\mu} \bigtriangledown p . \tag{71}$$

This form of the Hagen-Poiseuille equation is valid for considering flow of water through a tube of uniform cross-sectional area. To account for the radius variation consider that for a tube of non-uniform cross-sectional area, it is more convenient to use an integral form of the Hagen-Poiseuille equation:

$$q = \frac{\pi}{8\mu} \frac{\triangle p}{\int_{x_1}^{x_2} \frac{dx}{r(x)^4}} , \tag{72}$$

in which the x axis is oriented along the flow line.

Although r may vary with x, the volumetric flowrate q must be constant across all cross sections. If Eq. (72) is written in the standard form $q = C_H \triangle p$, we find that

$$C_H = \frac{\pi}{8\mu l} \langle r^{-4} \rangle^{-1} , \tag{73}$$

where the average is taken over the length of the tube.

If we estimate from the micrograph the radius of such a tube, we will be estimating the mean value of the radius, $\langle r \rangle$, and thus will overestimate the conductance by an amount

$$\frac{C_{H_{actual}}}{C_{H_{measured}}} = \frac{\langle r^{-4} \rangle^{-1}}{\langle r \rangle^4} \equiv f , \tag{74}$$

where f is the *hydraulic constriction factor.*

The magnitude of this contriction factor will depend on the extent to which the pore radius varies. If the radius is in fact constant, then $\langle r^{-4} \rangle = \langle r \rangle^{-4}$, and $f = 1$. In order to relate f to a parameter that may be relatively simple to estimate, consider the case where the radius varies in a sinusoidal manner along the length of the tube (See Figure 3.13), according to the expression

$$r(z) = \langle r \rangle [1 + \xi \sin(2\pi x/\lambda)] , \tag{75}$$

where λ is the wavelength of the radius variations. This type of variation is supported by some pore casts, such as that of Berea sandstone shown in Figure 3.3.

For convenience, we can assume that an integral number of segments of length λ will fit into the total length l. The hydraulic constriction factor can then be expressed as

$$\frac{1}{f} = \frac{\langle r^{-4} \rangle}{\langle r \rangle^{-4}} = \frac{1}{\lambda} \int_0^{\lambda} [1 + \xi \sin(2\pi x \lambda)]^{-4} dx \, . \tag{76}$$

Using the change of variable $\varpi = 2\pi x \lambda$, the integral in Eq. (76) takes the form

$$\frac{1}{f} = \frac{1}{2\pi} \int_0^{2\pi} (1 + \xi \sin \varpi)^{-4} d\varpi \, . \tag{77}$$

With the aid of integral tables, the constriction factor f can be expressed as

$$f = \frac{256 \varrho^{7/2}}{(1+\varrho)^4 (5\varrho^3 + 3\varrho^2 + 3\varrho + 5)} \, , \tag{78}$$

where $\varrho = (1 - \xi)/(1 + \xi) = r_{min}/r_{max}$. The factor f is plotted in Figure 3.14, as a function of the parameter r_{min}/r_{max}. This factor may be as small as 0.26 for a quite reasonable value of $r_{min}/r_{max} = 0.33$ estimated from a pore cast of Saint-Gilles sandstone (See Figure 3.4). We have estimated a throat-to-pore radius ratio of 0.50 from a pore cast of Berea sandstone, and have tentatively used this value for a consolidated rock. The throat-to-pore radius aspect ratio of 0.50 for Berea sandstone is further verified by analysis on the relationship of capillary pressure of Berea sandstone to microgeometry in Chapter 5.

Although some sandstones also exhibit roughness at scales much smaller than the average pore diameter, it is known that such roughness has little effect on the hydraulic conductance (Berryman and Blair, 1987) and can therefore be ignored.

3.1.6 Permeability Calculation

Now we show how the continuum value of the hydraulic conductance is calculated. Recall that the hydraulic conductance per unit length of each tube is given by Eq. (12) as

$$C_i = \frac{1}{2} R_H^2 A \, .$$

According to the Hagen-Poiseuille equation, the volumetric flux of fluid through one tube is given by

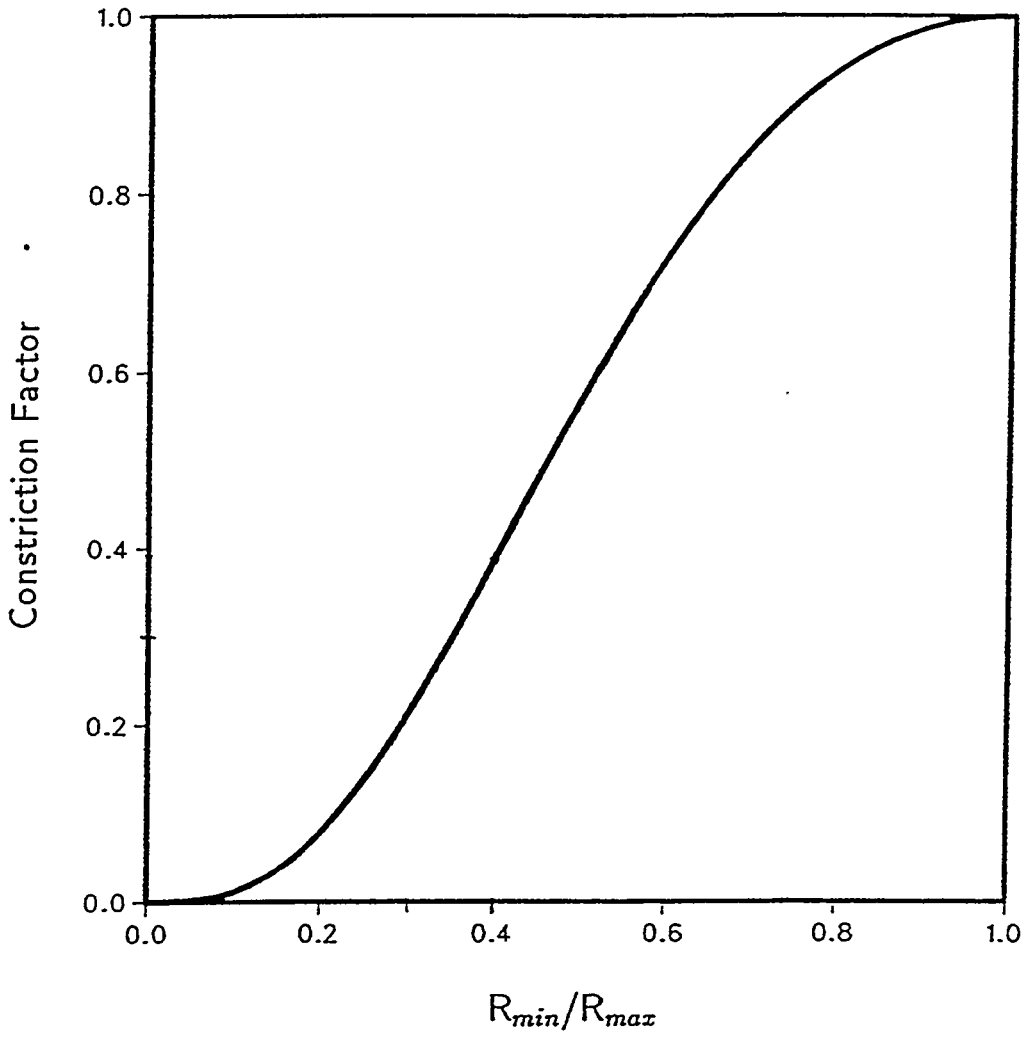

FIG. 3.14: Constriction factor for hydraulic flux as function of the ratio of the minimum pore radius to the maximum pore radius of an individual pore. The calculated conductances of the pores must be multiplied by this factor, which account for the converging-diverging nature of the pore tubes.

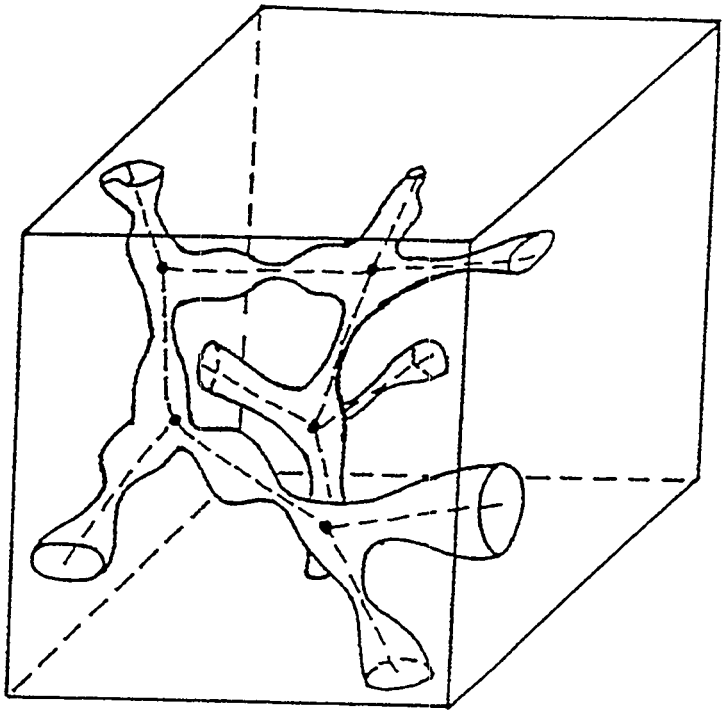

FIG. 3.15: Microscopically inhomogeneous pore system and its skeleton (after Doyen, 1988).

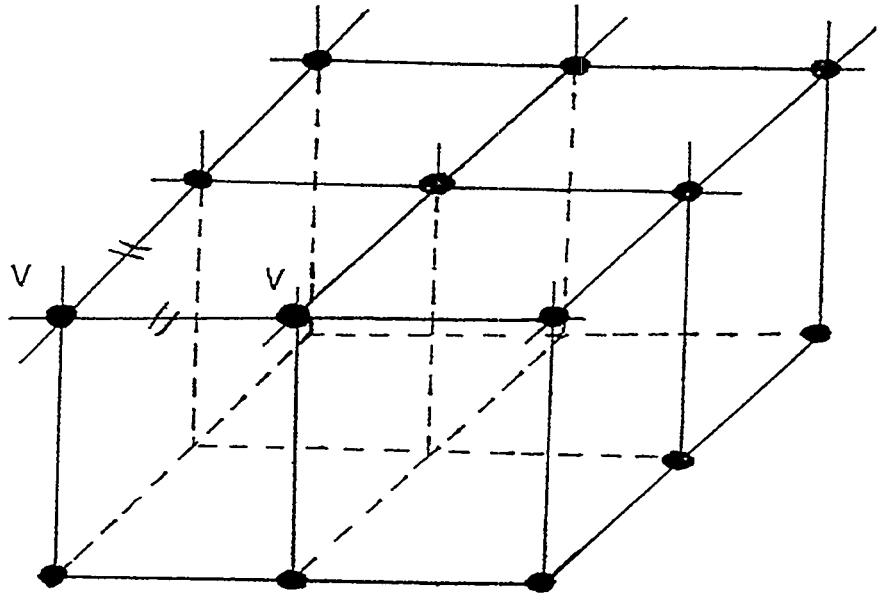

FIG. 3.16: Cubic lattice representation of the pore structure employed to calculate the permeability of sedimentary rocks with the effective medium theory.

$$q_i = \frac{C_i}{\mu} A \bigtriangledown p = \frac{R_H^2 A}{2\mu} \bigtriangledown p \,. \tag{79}$$

Study of stereo SEM photomicrographs of Berea sandstone has indicated the presence of a statistically isotropic three-dimensional pore structure represented by Figure 3.15. These observations have led to the idealization that the pores of varying size are arranged on a cubic lattice (Figure 3.16), so that the coordination number, which is the number of pores that meet at each node, is 6.

Finally, the individual conductors are imagined to be placed along the bonds of a cubic lattice in the effective medium. Recall that for a general discrete distribution of conductances, the effective medium expression (Eq. 6) takes the form

$$\sum_{i=1}^{N} \frac{C_{eff} - C_i}{[(z/2) - 1]C_{eff} + C_i} = 0 \,.$$

By solving the above equation numerically for a cubic lattice (z = 6), we have then calculated the value of the effective conductance given the individual pore conductances obtained from the SEM micrographs (See Code Listing 3.1).

In the cubic lattice, the total volumetric flux in the vertical direction is

$$q = \frac{1}{\tau} \sum_i q_{eff} = \frac{N C_{eff}}{\tau \mu} \bigtriangledown p \,, \tag{80}$$

where q_{eff} is the volumetric flux of fluid through an effective conductor and τ is the tortuosity of a cubic lattice, which is exactly equal to 3 (since one-third of the pore tubes are aligned in each of the three lattice directions).

According to the Darcy equation, the total volumetric flux through the porous medium is given by

$$q = \frac{k}{\mu} \bigtriangledown p A_{total} \,, \tag{81}$$

where k is the permeability and A_{total} is the total area of the porous medium under consideration.

Equating Eq. (80) to Eq. (81) gives the continuum value of the hydraulic conductance that is related to the effective conductance of the individual tubes:

$$k = \frac{NC_{eff}}{\tau A_{total}} . \tag{82}$$

The tortuosity for randomly oriented cylindrical tubes, $\tau \equiv \langle \cos^2 \theta \rangle^{-1} = 3$ has been derived independently (See Section 3.1.4).

3.1.7 Results and discussion

In this investigation, a network model has been developed for calculating permeability from microgeometry; this analytical model is simple, reliable, and permits accurate prediction of the laboratory measured permeability of sedimentary rocks. Calculated permeabilities for different rocks and for different coordination numbers are presented in Tables 3.7 to 3.11. A comparison between laboratory measured and predicted permeabilities with the cubic lattice-network model is given in Table 3.12. Good agreement was found between measured and predicted permeabilities for a variety of sandstones when using the cubic lattice model, with essentially no arbitrary adjustable parameters. The major conclusions that can be drawn from this study are as follows:

1. The pore structure is the most important variable influencing the permeability of sedimentary rocks.

2. The effects of the pore structure are interrelated in a complex manner with the porosity, specific surface area, and pore shape factors in the permeability analytical expression given by Eq. (82). As with the standard Kozeny-Carman model, the predicted permeability is proportional to the number of pores.

3. All the parameters in our model have an unambiguous physical meaning and are readily measured from SEM photomicrographs of rock thin sections.

TABLE 3.7: Calculated permeability data - Berea sandstone SEM section B.

z	C_{eff} (m^4)	F_s	r_{min}/r_{max}	F_c	N	A_{total} (m^2)	τ	k (m^2)	k (D)
2	4.54×10^{-20}	0.40	0.50	0.55	35	9.63×10^{-7}	3*	1.21×10^{-13}	0.12
6	18.2×10^{-20}	0.40	0.50	0.55	35	9.63×10^{-7}	3	4.84×10^{-13}	0.49
∞	56.0×10^{-20}	0.40	0.50	0.55	35	9.63×10^{-7}	3*	14.9×10^{-13}	1.51

*Assumed.

TABLE 3.8: Calculated permeability data - Berea sandstone SEM section T.

z	C_{eff} (m^4)	F_s	r_{min}/r_{max}	F_c	N	A_{total} (m^2)	τ	k (m^2)	k (D)
2	7.49×10^{-20}	0.40	0.50	0.55	35	9.84×10^{-7}	3*	1.89×10^{-13}	0.19
6	24.2×10^{-20}	0.40	0.50	0.55	35	9.84×10^{-7}	3	6.12×10^{-13}	0.62
∞	59.9×10^{-20}	0.40	0.50	0.55	35	9.84×10^{-7}	3*	15.2×10^{-13}	1.53

*Assumed.

TABLE 3.9: Calculated permeability data - Massilon sandstone SEM section.

z	C_{eff} (m^4)	F_s	r_{min}/r_{max}	F_c	N	A_{total} (m^2)	τ	k (m^2)	k (D)
2	11.7×10^{-19}	0.40	0.50	0.55	48	8.74×10^{-6}	3*	0.47×10^{-12}	0.47
6	90.7×10^{-19}	0.40	0.50	0.55	48	8.74×10^{-6}	3	3.65×10^{-12}	3.65
∞	525×10^{-19}	0.40	0.50	0.55	48	8.74×10^{-6}	3*	21.1×10^{-12}	21.1

*Assumed.

TABLE 3.10: Calculated permeability data - Boise sandstone SEM section.

z	C_{eff} (m^4)	F_s	r_{min}/r_{max}	F_c	N	A_{total} (m^2)	τ	k (m^2)	k (D)
2	8.96×10^{-20}	0.40	0.50	0.55	47	9.84×10^{-7}	3*	3.14×10^{-13}	0.32
6	45.0×10^{-20}	0.40	0.50	0.55	47	9.84×10^{-7}	3	15.8×10^{-13}	1.59
∞	80.1×10^{-20}	0.40	0.50	0.55	47	9.84×10^{-7}	3*	28.1×10^{-13}	2.83

*Assumed.

TABLE 3.11: Calculated permeability data - Saint-Gilles sandstone SEM section.

z	C_{eff} (m^4)	F_s	r_{min}/r_{max}	F_c	N	A_{total} (m^2)	τ	k (m^2)	k (D)
2	3.37×10^{-20}	0.40	0.33	0.27	43	9.84×10^{-7}	3*	1.59×10^{-13}	0.16
6	21.2×10^{-20}	0.40	0.33	0.27	43	9.84×10^{-7}	3	3.34×10^{-13}	0.34
∞	48.3×10^{-20}	0.40	0.33	0.27	43	9.84×10^{-7}	3*	7.59×10^{-13}	0.77

*Assumed.

4. When applying the method and evaluating our results one has to keep in mind that the effective medium theory is expected to work best when spatial fluctuations of hydraulic (or current) flux are small in a relative scale. In Berea sandstone for instance, our laboratory imbibition experiments in combination with SEM analysis of the pore space indicate that the distribution of pores and throats controlling permeability is narrow. Consequently, the effective medium theory is expected to and does give very good results in Berea sandstone.

5. The results given in Tables 3.7 to 3.11 emphasize the importance of pore connectivity in understanding the relationship of permeability to rock microstructure. For example, if a Kozeny-type parallel tube model ($z = \infty$) or a serial model ($z = 2$) is applied instead, permeability is overpredicted or underpredicted, respectively.

6. The investigation shows that the effective medium approximation with a parallel-tube or Kozeny-Carman arrangement with a coordination number $z = \infty$, overpredicts the measured permeability of Berea sandstone by a factor of three, and that of Massilon sandstone by a factor of six, respectively.

7. Thus, it is found that the permeability predicted with the effective medium approximation assuming a cubic lattice arrangement of the pores is consistent with the Kozeny-Carman formulas for a 'principal' pore network approaching microscopic homogeneity such as Berea sandstone's (Section 3.3.4).

8. The analysis on the effects of pore constrictivity show that permeability is controlled by connected intergranular pore throats (pore constrictions in between the grains).

9. It is found that intergranular pore throats are smaller than pore bodies, with an aspect ratio $r_{min}/r_{max} = 0.50$ for the consolidated sandstones under study.

10. For a lightly consolidated rock such as Saint-Gilles sandstone, an aspect ratio of $r_{min}/r_{max} = 0.33$ is detected. This is a direct result of the lower degree of consolidation and the more angular particle shape.

TABLE 3.12: Measured vs. predicted intrinsic permeabilities of four sedimentary rocks.

Rock	$k_{measured}$		$k_{predicted}$ ($z^a = 6$)	
	(m^2)	(d)	(m^2)	(d)
Berea sandstone	4.80×10^{-13}	0.48[b]	5.55×10^{-13}	0.56
Boise sandstone	13.0×10^{-13}	1.30[b]	15.8×10^{-13}	1.59
Massilon sandstone	25.0×10^{-13}	2.50[c]	36.5×10^{-13}	3.65
Saint-Gilles sandstone	1.70×10^{-13}	0.17[d]	3.34×10^{-13}	0.34

[a]Coordination number.

[b]Distilled water used as permeant.

[c]Data from Koplik et al., 1984.

[d]Data from Leblanc, 1988.

11. The effect of pore shape on permeability was studied by comparing the hydraulic radius approximation predictions with the exact permeabilities of various polygonal-shaped pores, and the error involved was calculated. The results of this study show that the error involved in the hydraulic radius approximation lies well within $\pm 30\%$ (See Table 3.6). The approximation does not systematically either underpredict or overpredict the pore conductances, so that the errors will partially cancel when applied to a network of pores of different cross sections.

12. For equivalent pore areas, Eq. (49) shows that permeability of polygonal pore shapes is not very sensitive to decreasing pore perimeter. This result is a direct consequence of the fact that the fluid velocity vanishes at the pore-grain interface. Therefore, small scale roughness is irrelevant to permeability.

3.2 Statistical approach using the perimeter-area power-law relationship of pores

Since the intrinsic permeability is a measure of the viscous resistance to fluid flow through the rock pores and is controlled by the geometry and topology of the pore space, it is expected to correlate with the amount of surface area of the pore system. In this Section, a brief discussion is given of how the perimeter-area power-law relationship of pores, along with a pore-size distribution, can be used to estimate the permeability. Consider Figure 3.17. If the outer circle has radius R_o and the inner circle (dashed line) has radius R_i, then the permeability k of a single such rough-walled cylindrical pore must satisfy (Berryman and Blair, 1984)

$$k_i \leq k \leq k_o \,, \tag{83}$$

where $k_o = R_o^4/8$, and $k_i = R_i^4/8$. If $R_o = R_i + \delta R$, then for small δR we have

$$\frac{R_i^2}{8} \leq k \leq \frac{R_i^2}{8}\left(1 + 4\frac{\delta R}{R_i}\right) \,. \tag{84}$$

In terms of hydraulic radius this can be written as

$$\frac{1}{2}\left(\frac{A_i}{P_i}\right)^2 \leq k \leq \frac{1}{2}\left(\frac{A_i}{P_i}\right)^2\left(1 + 4\frac{\delta R}{R_i}\right) \,, \tag{85}$$

where A_i and P_i are the inner tube area and perimeter, respectively.

If the surface is very rough (e.g., fractal), the pore perimeter may become so large that Eq. (85) is not satisfied. Nevertheless, it follows from Eqs. (84) and (85) that an effective hydraulic radius may be used such that

$$\left(\frac{A_i}{P_i}\right) \leq \overline{\left(\frac{A}{P}\right)} \leq \left(\frac{A_o}{P_o}\right) \,. \tag{86}$$

The parameter $\overline{(\frac{A}{P})}$ has the significance of being the hydraulic radius of a smoothed representation of the true void/solid interface. For a single straight tube (Eq. 84), if we make an error of 1% in estimating the tube radius, the error in the estimate of k

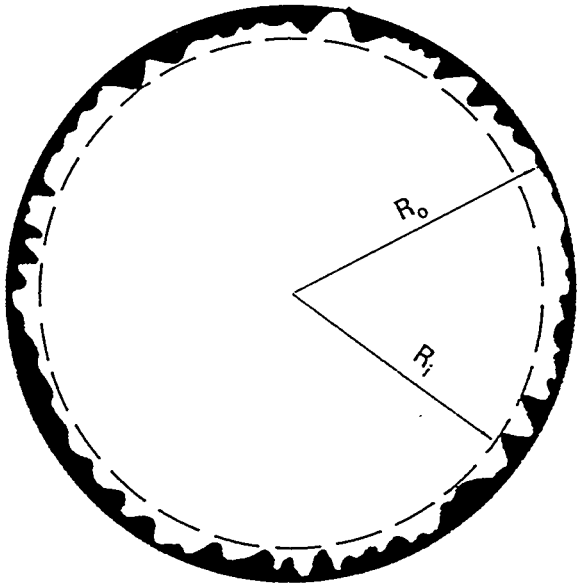

FIG. 3.17: Schematic drawing of a rough-walled tube (of radius R_o). Surface roughness does not have a strong effect on the overall fluid permeability of a tube, because a slightly smaller tube (of radius R_i) is known to have a comparable permeability (after Berryman and Blair, 1987).

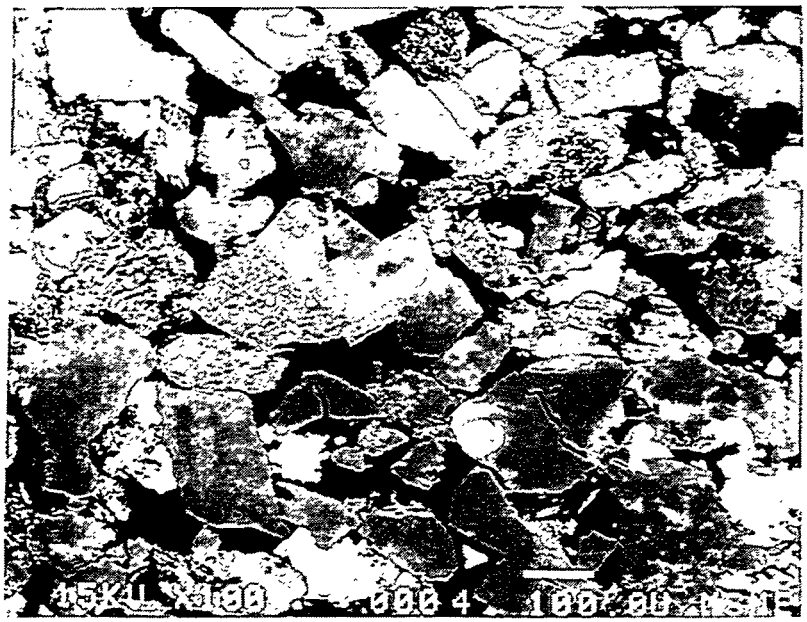

FIG. 3.18: Typical serial section of Saint-Gilles sandstone at 100x magnification. The mineral grains of different shades are quartz, carbonate, feldspar, and muscovite, whereas the darkest regions represent pore space.

TABLE 3.13. Perimeter-area power-law relationship γ parameter and correlation coefficient r measured from perimeter-area data of five sedimentary rocks.

Rock	$\phi^a_{measured}$ (%)	γ	r
Berea sandstone	22	1.49	0.99
Boise sandstone	26	1.43	0.98
Massilon sandstone	22[b]	1.43	0.98
Saint-Gilles sandstone	21	1.49	0.98
Indiana limestone	14	1.67	0.99

[a]Porosity.

[b]Data from Koplik et al., 1984.

is 4%, at worst. Indeed, since the fluid velocity vanishes at the pore-grain interface, the permeability k should not be sensitive to surface roughness.

3.2.1 Perimeter-area power-law relationship of pores

Perimeter-area relationships of a smooth representation of pores are estimated from scanning electron micrographs of thin sections of typical reservoir-type sedimentary rocks (See Figure 3.18). The basic method involves counting size and perimeter grid (or pixel) units for every feature in a standard scanning electron micrograph of some fixed magnification. The analysis was carried out using both a manual and an automated image analysis procedure to verify the accuracy of the manual technique (See Section 3.1.2 for details). The digitized thin sections (Figures 3.19a and 3.20a) then show pore space in white, and mineral grains in black. This method was used to estimate the area-perimeter statistics for a group of pores in a thin section.

It is found that the perimeter-area relationship of such a representation of the true void/solid interface satisfies the perimeter-area power-law relationship

$$A = mP^{\gamma}\,, \tag{87}$$

where $\log m$ is the intercept on the $\log A$ axis, and γ the slope of the $\log A$-$\log P$ plot (Figures 3.19b and 3.20b). The constants m and γ appearing in Eq. (87) are found by performing a linear regression on the log perimeter-log area data. From this analysis we find slopes ranging from 1.43 to 1.49 for the four sandstones examined and a slope of 1.67 for an Indiana limestone (Table 3.13).

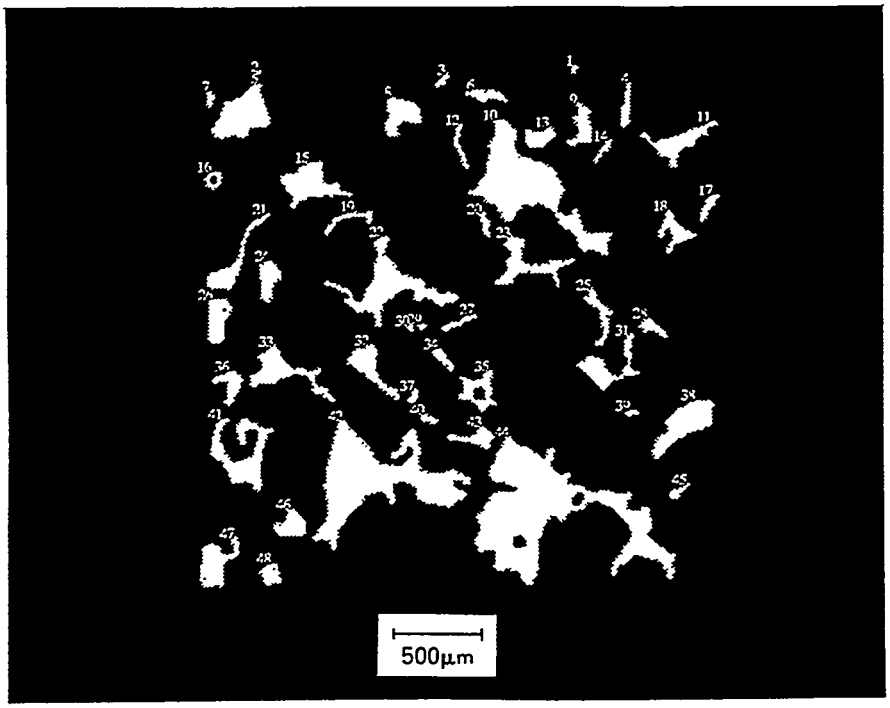

FIG. 3.19a: Pore-space contours obtained from serial section of Massilon sandstone (after Koplik et al., 1984).

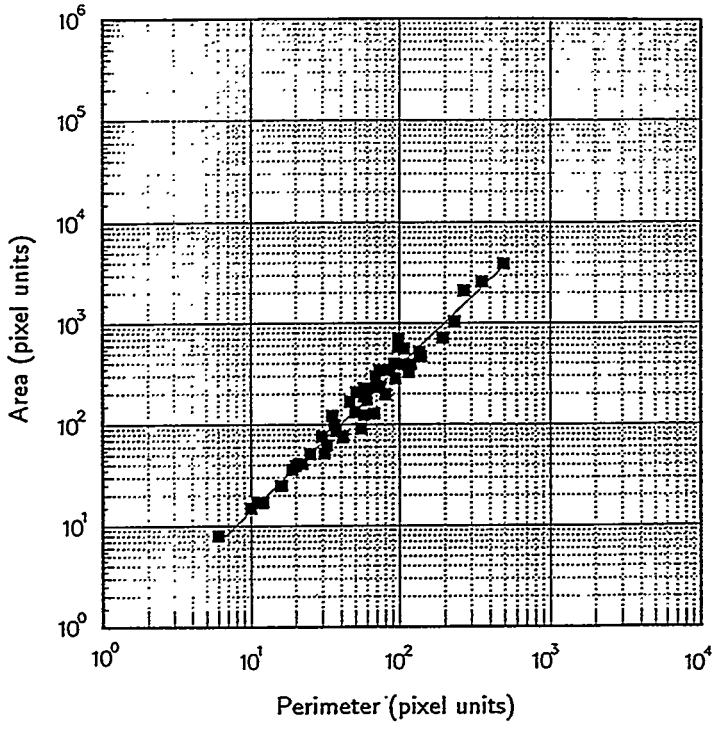

FIG. 3.19b: Perimeter-area power-law relationship for Massilon sandstone obtained from pore-space contours shown in Fig. 3.19a.

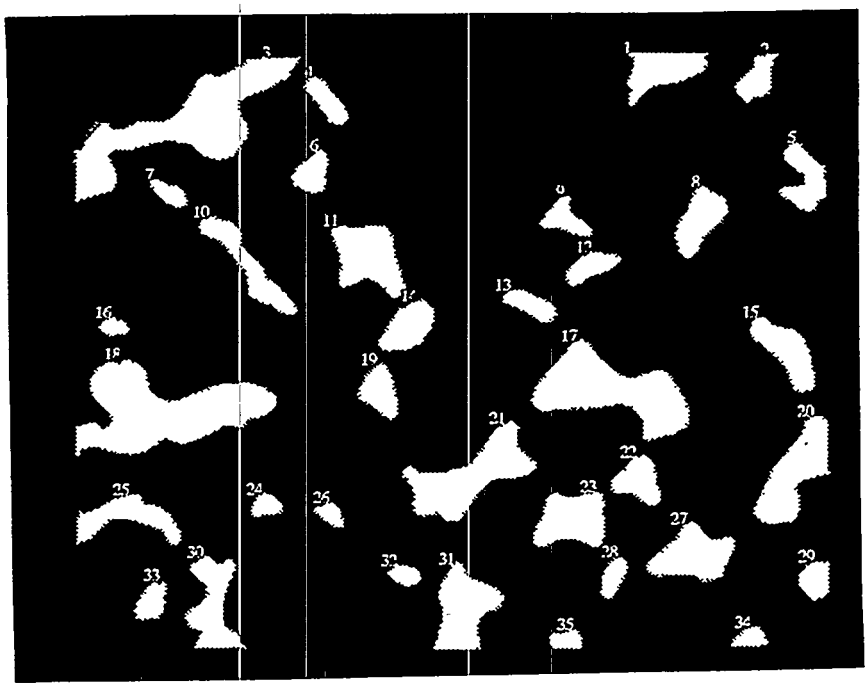

FIG. 3.20a: Pore-space contours obtained from image analysis of the photomicrograph of Berea sandstone (Section B) shown in Fig. 3.5a. The width of field is about 1 mm.

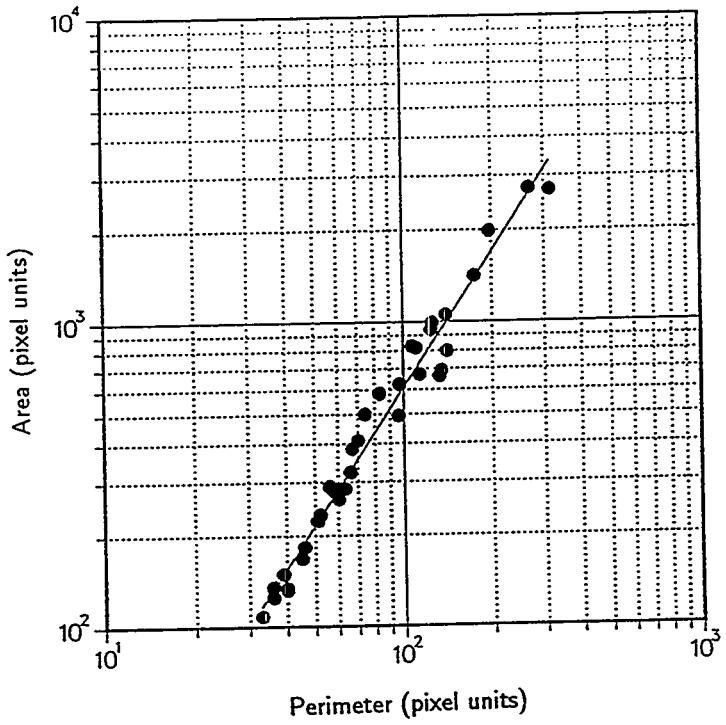

FIG. 3.20b: Perimeter-area power-law relationship of pores for Berea sandstone obtained from pore-space contours shown in Fig. 3.20a.

3.2.2 Permeability implications

We now show how the area-perimeter power-law relationship of a smoothed representation of the pore space of a rock can be used, in conjunction with a pore-size distribution and a classical model for permeability, to yield reasonable estimates of permeability. The Kozeny-Carman model for transport through a porous medium is based on the idealization of the pore space as consisting of a bundle of parallel tubes, the total conductance of which is merely the sum of the individual conductances. It is traditional to then divide this result by a tortuosity factor, $\tau = 3$, to account for the fact that, in a hydraulically isotropic rock, we would expect only one-third of the total number of tubes to be oriented in each of the three orthogonal directions (See Section 3.1.4.5 for specifics). If $n(A)$ is the number distribution function for pores of cross-sectional area A in an area of rock having total cross section of A_{total} and $C(A)$ is the conductance of each pore of area A, then the total conductance can be expressed as

$$C_{total} = \int_0^\infty n(A)C(A)dA\,. \tag{88}$$

In practice, of course, the distribution function $n(A)$ will vanish for all A greater than some A_{max}, although it is often convenient to represent $n(A)$ by a function that drops off, say, exponentially as $A \to \infty$.

If the pore tubes were all of circular cross section, their individual conductances would be given by the exact Hagen-Poiseuille law. As explained in Section 3.1.3, the Hagen-Poiseuille solution can be modified to account for irregular cross sections by using the 'hydraulic radius' approximation, which predicts a conductance of $A^3/2P^2$ for a tube of cross-sectional area A and perimeter P. Invoking the perimeter-area power-law relationship $P = m^{-1/\gamma}A^{1/\gamma}$, the hydraulic conductance can be expressed as $C(A) = A^{3-2/\gamma}/2m^{-2/\gamma}$. Combining this with the general expression (88) for the total conductance yields

$$C_{total} = \frac{1}{\tau}\int_0^\infty \frac{n(A)A^{3-2/\gamma}}{2m^{-2/\gamma}}dA\,. \tag{89}$$

We now define a normalized distribution function $\beta(A) = n(A)A/\phi A_{total}$, where

the total porosity is defined as A_{pores}/A_{total}. This distribution function has the property that $\int \beta(A)dA = 1$. The total conductance can then be expressed as

$$C_{total} = \frac{\phi A_{total}}{2m^{-2/\gamma_T}} \int_0^\infty A^{2(1-1/\gamma)} \beta(A) dA \, . \tag{90}$$

We have found that the area frequency distribution of the pores (Figures 3.21 and 3.22) can be well approximated by a lognormal distribution:

$$\hat{\beta}(u) = (2\pi\sigma_u^2)^{-1/2} \exp[-(u-u_o)^2/2\sigma_u^2] \, , \tag{91}$$

where $u = \log A$, $u_o = \log A_o$, where A_o is the most probable area, and σ_u is the variance of $\log A$. The corresponding mean area A_m is larger than the most probable area and is given by

$$A_m = A_o \exp[(\sigma_u \ln 10)^2/2] \, . \tag{92}$$

The permeability coefficient k can then be estimated as

$$\begin{aligned} k &= \frac{C_{total}}{A_{total}} = \frac{\phi}{2m^{-2/\gamma_T}} \int_0^\infty A^{2(1-1/\gamma)} \beta(A) dA \, , \\ &= \frac{\phi}{2m^{-2/\gamma_T}} A_m^{4(1-1/\gamma)^2} A_o^{2(1-1/\gamma)(2/\gamma-1)} \, . \end{aligned} \tag{93}$$

In terms of the variance of $\log A$, the permeability can be expressed as

$$k = \frac{\phi}{2m^{-2/\gamma_T}} A_m^{2(1-1/\gamma)} \exp^{-2(1-1/\gamma)(2/\gamma-1)[(\sigma_u \ln 10)^2/2]} \, . \tag{94}$$

As with the standard Kozeny-Carman model, if the pore sizes are held constant, the predicted permeability scales with the porosity, which is to say it is proportional to the number of pores. It is worth noting that if the perimeter-area relationship of the pores follows the law derived by Mandelbrot (1982) for islands whose boundaries are fractal, $P = \epsilon^D A^{D/2}$, where ϵ is some constant that depends on the length of the measuring grid size and D is the fractal dimension of the pore perimeter, then the

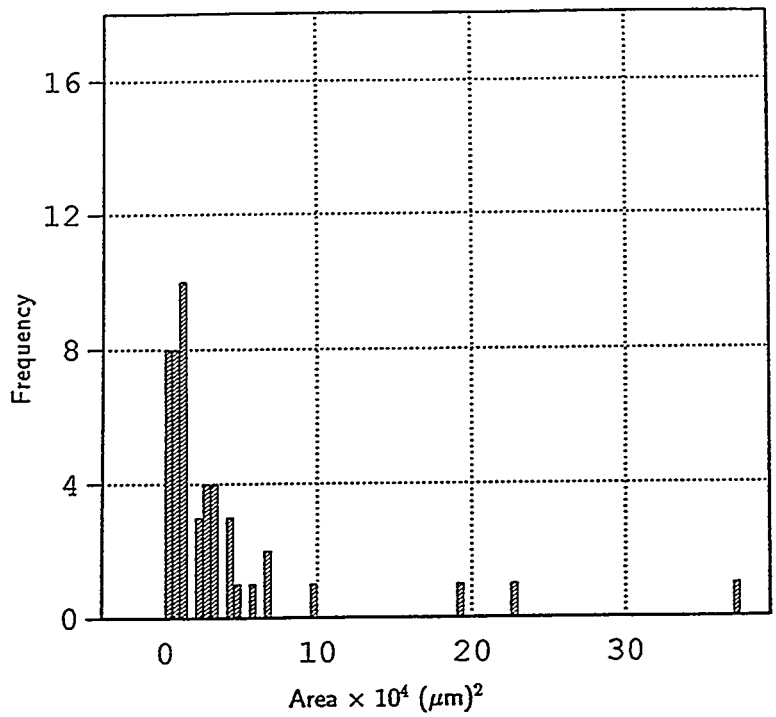

FIG. 3.21: Pore-size distribution of Massilon sandstone obtained from pore-space contours shown in Fig. 3.19a.

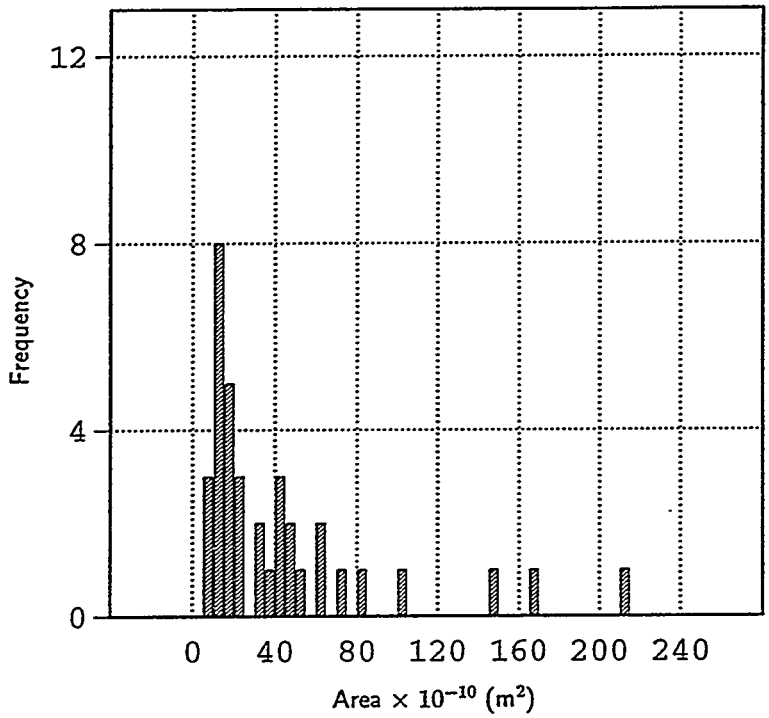

FIG. 3.22: Pore-size distribution of Berea sandstone obtained from pore-space contours shown in Fig. 3.20a.

parameter ϵ would quantify the perimeter of the pore cross sections when the pores are projected back into three dimensions. The parameter ϵ would in some sense represent the pore actual surface area, k being a decreasing function of ϵ. Therefore, if the rock pore boundaries are very rough (e.g., fractal), not only would the physical bounds for permeability be violated (Eqs. 84 and 85), but also the predicted permeabilities given by Eq. (94) would be artificially lowered by several orders of magnitude.

3.2.3 Effects of pore orientation and constrictivity

In the two-dimensional sections under consideration, the pore cross sections are randomly oriented with respect to the channel axes. The orientation effect has been taken into account by means of geometrical and stereological considerations, which indicate a stereological factor of 0.40 (See Section 3.1.4). In addition, constrictions within the individual branch channels, i.e., pore throats and bodies, have been taken into account using an analysis based on a sinusoidal variation of cross section which gives a hydraulic constriction factor of 0.55 (See Section 3.1.5).

3.2.4 Results and discussion

In this investigation, we have constructed a model that allows reasonable predictions of the permeability of sedimentary rocks, based on the perimeter-area power-law relationship of pores and the pore-size distribution. Since the permeability of rocks can range over many orders of magnitude, this prediction is not trivial. Calculated permeabilities for two different rocks are presented in Table 3.14. Image analysis of the pore system of Massilon sandstone yields values $A_m = 13.5 \times 10^4$ μm^2, $\sigma_u = 0.43$, $\gamma = 1.43$, and $m = 1.17$ μm$^{2-\gamma}$. Similarly, for Berea sandstone, $A_m = 77.9 \times 10^2$ μm^2, $\sigma_u = 0.42$, $\gamma = 1.49$, and $m = 0.66$ μm$^{2-\gamma}$. Equation (94) then predicts a permeability of 10.9 D for Massilon sandstone, and of 1.5 D for Berea sandstone, respectively (after applying the hydraulic stereological and constriction corrections) (See Table 3.14). A comparison between these results, the laboratory-measured and the predicted permeabilities with the cubic lattice-network model, is given in Table 3.15. As would be expected for an essentially parallel arrangement of conductors, as is assumed in the model, the predicted values are higher but of the same order of magnitude as the experimentally measured values of 2.5 D for Massilon sandstone (Koplik, 1984), and

TABLE 3.14: Calculated permeability data - Massilon and Berea sandstones SEM photomicrographs.

Rock	A_m (μm^2)	σ_u	γ	m (μm$^{2-\gamma}$)	F_s	F_c	τ	k (μm^2)	k (D)
Massilon	13.5×10^4	0.43	1.43	1.17	0.40	0.55	3*	10.8	10.9
Berea	77.9×10^2	0.42	1.49	0.66	0.40	0.55	3*	1.50	1.52

*Assumed.

TABLE 3.15: Measured vs. predicted intrinsic permeabilities - Massilon and Berea sandstones.

	$k_{measured}$		$k_{predicted}$		$k_{predicted}$ ($z^a = 6$)	
Rock	(m^2)	(D)	(m^2)	(D)	(m^2)	(D)
Massilon	25.0×10^{-13}	2.50[b]	108×10^{-13}	10.9	36.5×10^{-13}	3.65
Berea	4.80×10^{-13}	0.48[c]	15.0×10^{-13}	1.52	5.55×10^{-13}	0.56

[a]Coordination number.

[b]Data from Koplik et al., 1984.

[c]Distilled water used as permeant.

of 0.48 D for Berea sandstone (using distilled water as permeant) (See Table 3.15). The major conclusions that can be extracted from this study are as follows:

1. The pore structure is the most important variable influencing the permeability of sedimentary rocks.

2. Equation (94) shows that k is an increasing function of both the mean pore size and the variance of the pore size, as would be expected for an essentially parallel arrangement of conductors.

3. All the parameters in our model have an unambiguous physical meaning and are readily measured from SEM photomicrographs of rock thin sections.

4. As with the standard Kozeny-Carman model, if the pore sizes are held constant, the predicted permeability scales with the porosity, which is to say it is proportional to the number of pores.

5. Since the parameter m in Eq. (94) quantifies the perimeter of the pore cross sections, when the pores are projected back into three dimensions, m will represent the pore surface area; hence k is a decreasing function of m.

6. Our expression for k includes some length scale raised to the $2 - 2/\gamma$ power. It has a resemblance to that derived by Hansen and Skjeltorp (1988). Our result is more explicit in that our length scale is clearly identified in terms of the pore size distributions.

7. The analysis on the effects of pore constrictivity show that permeability is controlled by connected intergranular pore throats (pore constrictions in between the grains). It is found that intergranular pore throats are smaller than pore bodies, with an aspect ratio $r_{min}/r_{max} = 0.50$ for the consolidated sandstones under study.

8. Results in Table 3.15 show that the parallel-tubes statistical model overpredicts the measured permeability of Berea sandstone by a factor of three, and that of Massilon sandstone by a factor of four.

9. The parallel-tubes statistical model is consistent with the effective medium approximation and Kozeny-Carman formulas for a 'principal' pore network approaching microscopic homogeneity such as Berea sandstone's (Chapter 3.3).

10. Of course, more accurate estimates of the permeability require more sophisticated models than the parallel-tubes model, which will somehow account for factors such as the interconnectedness of the pore-tube network (See Section 3.1 and Table 3.15); the above examples were intended to be plausible demonstrations of how direct pore microgeometry measurements such as the area-perimeter power-law information, along with a pore-size distribution, can be used for making quantitative predictions of the permeability.

3.3 Note on the validity of the Kozeny-Carman formulas for consolidated porous media

The simplest and oldest capillaric model is one representing the porous medium by a bundle of parallel capillaries of uniform radius. In deriving this Kozeny-Carman model, the multiple connectivity of the pore space is completely neglected. Applying the well-known law of Hagen-Poiseuille for N circular tubes of radius r, and relating the result to the macroscopic Darcy's law, it follows that the permeability k of the bundle of capillaries is given by (Scheidegger, 1974)

$$k = \frac{N\pi\bar{r}^4}{8} = \frac{\phi\bar{r}^2}{8}\,, \tag{95}$$

where $\bar{r}$ represents an 'average' pore radius, and 'porosity' $\phi = N\pi\bar{r}^2$. This model gives permeability in one direction only. All capillaries being parallel, there can be no flow orthogonal to the capillaries. A simple modification to Eq. (95) consists of putting one-third of the capillaries in each of the three spatial dimensions. To account for this, the tortuosity factor, $\tau = 3$, is introduced, and Eq. (95) takes the form

$$k = \frac{N\pi\bar{r}^4}{8\tau} = \frac{\phi\bar{r}^2}{8\tau}\,. \tag{96}$$

The above expression for permeability can be compared with Eq. (82) which determines observed permeability of sedimentary rocks from microgeometry with reasonable accuracy (section 3.1), based on the assumption of a regular cubic lattice, consisting of pores of different shapes and varying cross sections:

$$k = \frac{NC_{eff}}{\tau A_{total}}\,.$$

If there are no marked spatial variations of the channel dimensions, the rock is microscopically homogeneous with individual conductances $C_1 = C_2 = ... = C_i = C_{eff} = C$, and the effective conductance becomes independent of the average lattice coordination number z. Therefore, under conditions of microscopic homogeneity we can write

$$k = \frac{NC_{eff}}{\tau A_{total}} = \frac{N\frac{1}{2}R_H^2 A}{\tau A_{total}} = \frac{\phi r^2}{8\tau}\,, \tag{97}$$

and Eq. (82) and Eq. (96) become equivalent. Indeed, the hypothesis of microscopic homogeneity of the pore space is implicit in the derivation of the Kozeny-Carman equations. This would be the case of a rock pore space characterized by a very narrow distribution of channel dimensions, e.g., a single-spike pore-size distribution or a distribution characterized by a single size. However, the pore space of a rock is generally characterized by a wide distribution of channel dimensions, and so the permeabilities predicted by the Kozeny-Carman equations deviate from the measured values. In this case, it will be shown that the Kozeny-Carman formulas based on a parallel arrangement of the pores give an upper bound on the rock permeability.

In section 3.1, a regular cubic lattice, consisting of pores of varying cross sections and different shapes, was introduced as a pore structure model. Permeabilities of sandstones obtained with this model are in good agreement with experimental data. This outcome confirms previous research by Chatzis and Dullien (1985), who found that the simple cubic (or tetrahedral) network of angular pores yields good agreement with the observed data when modeling the mercury porosimetry curve for a variety of sandstones. These results are not surprising when one notes that the above properties are strong functions of the pore structure of the sample, which is multiply connected (Figures 3.3 and 3.4). On the other hand, consider Berryman and Blair's (1986) estimates of Berea sandstone permeability using digitized SEM images of rock sections. Parameters such as porosity, specific surface area, and formation factor were employed to successfully predict permeability from Kozeny-Carman relations, and so there seems to be a discrepancy. Hence, there is a need to assess the region of validity of the Kozeny-Carman formulas to predict permeability of consolidated porous media from microgeometry, as it relates to the microscopic spatial variation of channel dimensions. It is also important to evaluate the extent to which the parallel pore structure model moves away from the regular cubic model as the pore space becomes more and more inhomogeneous at the pore scale. We undertook this research with five main objectives in mind: (1) to re-examine the effective medium theory to treat conductor networks based on the distribution of individual conductances, (2) to study the region of validity of the effective medium theory by comparing its results with con-

ductances evaluated numerically using large 3-D simple cubic networks in which the values of the conductances are chosen by a Monte Carlo procedure from one of several distributions (Kirkpatrick, 1971), (3) to compare results with the critical-path analysis (Ambegaokar et al., 1971) which focuses on the details of the critical paths along which much of the flow must occur (the total conductance obtained by this method gives an upper bound for conductivity valid for the case of a very broad distribution of channel dimensions, e.g., a microscopically heterogeneous porous medium), (4) to study the validity of the Kozeny-Carman formulas for consolidated porous media as they relate to the microscopic spatial variations of channel dimensions using the effective medium theory, network theory, and the critical path analysis, and ultimately (5) to compare the analytical results thus obtained with experimental results for a variety of consolidated porous materials.

3.3.1 Region of validity of the effective medium theory

Recall section 3.1.1 where it was shown that the average effect of a random distribution of conductances in the effective medium can be expressed by giving all conductances a single value C_{eff}, and choosing C_{eff} such that the effects of changing any conductance back to its true value will, on the average, cancel. Changing the value of a conductance located along the electric field from C_{eff} to C_o causes an additional voltage V_o to be induced across C_o given by Eq. (5),

$$V_o = \frac{V_{eff}(C_{eff} - C_o)}{C_o + (\frac{z}{2} - 1)C_{eff}} ,$$

where V_o is the voltage drop between adjacent rows far from C_o, and z, the number of bonds at each node of the network, is 6 for the simple cubic lattice employed in our model. If the conductances are distributed according to some distribution function $f(C)$, the self-consistency condition for C_{eff} is

$$0 = \langle V_o \rangle = C_{eff} \int f(C) \left[\frac{C_{eff} - C}{C + (\frac{z}{2} - 1)C_{eff}} \right] dC . \qquad (98)$$

Assume a binary distribution of conductances C_{ij}, in which two values C_1 and C_2 occur with probabilities f and $1 - f$, respectively. Applying Eq. (98), we can write

$$f\frac{C_{eff}-C_1}{C_1+(\frac{z}{2}-1)C_{eff}}+(1-f)\frac{C_{eff}-C_2}{C_2+(\frac{z}{2}-1)C_{eff}}=0\,. \tag{99}$$

The following quadratic equation on C_{eff} is thus obtained:

$$\left(\frac{z}{2}-1\right)C_{eff}^2+C_{eff}\left(C_2\left[\frac{z}{2}(f-1)+1\right]+C_1\left[1-\frac{z}{2}f\right]\right)-C_1C_2=0\,. \tag{100}$$

Solving, we get

$$\begin{aligned} C_{eff} &= \frac{-C_2\left[\frac{z}{2}(f-1)+1\right]-C_1\left[1-\frac{z}{2}f\right]}{z-2} \\ &\pm \frac{\sqrt{\left(C_2\left[\frac{z}{2}(f-1)+1\right]+C_1\left[1-\frac{z}{2}f\right]\right)^2-4\left(\frac{z}{2}-1\right)C_1C_2}}{z-2}\,. \end{aligned} \tag{101}$$

Now let $C_2\rightarrow 0$, in which case C_{eff} becomes

$$C_{eff}=\frac{-C_1\left[1-\frac{z}{2}f\right]\pm C_1\left[1-\frac{z}{2}f\right]}{z-2}\,, \tag{102}$$

with solutions

$$C_{eff_1}=0\,, \tag{103}$$

and

$$C_{eff_2}=\frac{-2C_1\left[1-\frac{z}{2}f\right]}{z-2}\,. \tag{104}$$

For a simple cubic lattice, $z=6$, and the non-zero root for C_{eff} becomes

$$C_{eff}=\frac{C_1}{2}[3f-1]\,. \tag{105}$$

Thus

$$\frac{C_{eff}}{C_1} = \frac{3}{2}f - \frac{1}{2}\,. \tag{106}$$

This result is plotted in Fig. 3.23. Therefore, for $C_2 \ll C_1$, Eq. (106) predicts a linear decrease in C_{eff} with decreasing f, with $C_{eff} \to 0$ when $f \to 1/3$.

3.3.2 Numerical evaluation of the conductances of large regular 3-D networks

To study the region of validity of the effective medium theory, Kirkpatrick (1971) evaluated numerically the conductances of large regular 3-D networks, in which the simple cubic values of the conductances (the bonds of the arrays) are chosen by a Monte Carlo procedure from a distribution. The voltages V_i at the nodes of each network, and from the total current flow for a fixed external applied voltage, were calculated by a relaxation procedure based upon the Kirchhoff current law, allowing C_{eff} to be determined. If C_{ij} is the conductance of the link between adjacent nodes i and j, the condition that all currents into node i cancel is given by Eq. (1)

$$\sum_j C_{ij}(V_i - V_j) = 0\,.$$

Resistor networks give a discrete model of a continuous medium in which conductance varies with position. Kirkpatrick (1971) studied the behavior of a simple cubic network of conductances with binary disorder. The values of the conductances are 1 with probability f, and $C_2 \ll 1$ with probability $(1-f)$, assigned at random. Calculations for networks with 15^3 nodes (data points) and predictions of the effective medium theory are given for three values of C_2 in Fig. (3.23). For $C_2 \ll C_1$ the data shows a linear dependence except in the critical regions where $C_{eff}/C_1 \ll 0.1$ for the binary distribution. Hence, the effective medium theory is expected to work best when the spatial fluctuations in the current (or the channel dimensions) are relatively small. This limit leads to $C_{eff}/C_1 \to 1.0$. The opposite limit occurs when most of the current is channeled along the paths of least resistance or critical paths along which much of the current will flow. This limit leads to $C_{eff}/C_1 \to C_c$, where C_c is the critical conductance (section 3.3.3). Indeed, the effective medium theory works as long as we are not too close to f_c, the percolation limit.

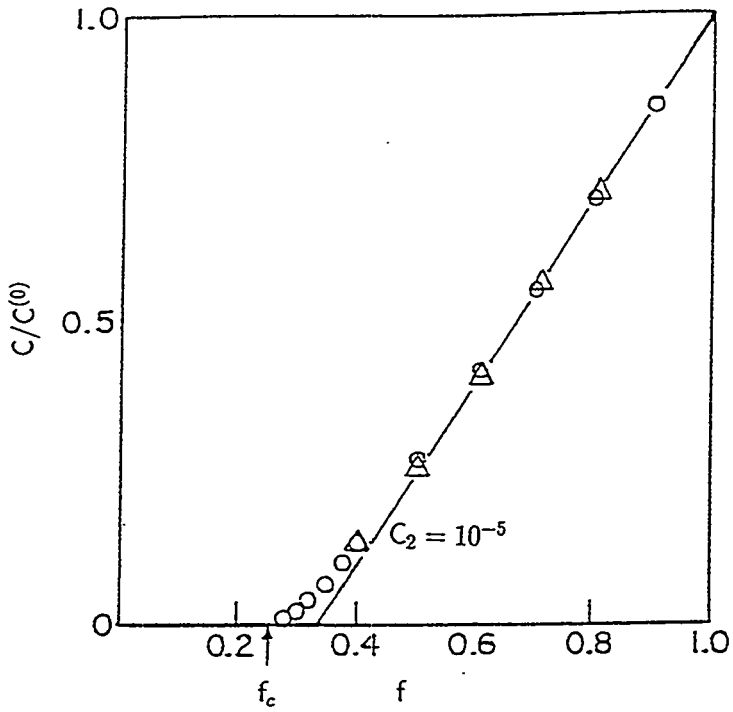

FIG. 3.23: Total conductance of a simple cubic network of conductances C_{ij} with binary disorder. Values of the conductances are 1 (with probability f) and $C_2 < 1$ (probability $1 - f$), assigned at random. Calculations for networks with 15^3 nodes (data points) and predictions of the effective medium theory (solid line) are displayed. f_c indicates the critical concentration for bond percolation on this lattice (after Kirkpatrick, 1971).

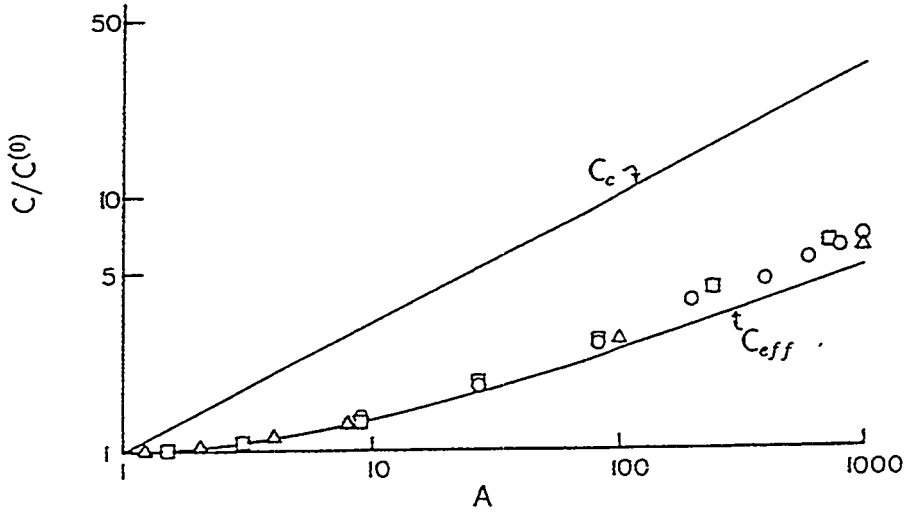

FIG. 3.24: Symbols show total conductance of a simple cubic network of 15^3 nodes, with values of the conductances chosen at random from the distribution $f(C) = (2C \log A)^{-1}$ with conductances C_{ij}'s range from A^{-1} to A. The critical path C_c and the effective conductance C_{eff} have also been plotted (after Kirkpatrick, 1971).

Kirkpatrick (1971) also calculated conductances of 3-D cubic networks of 15^3 nodes, with values of the conductances chosen at random, distributed uniformily with a distribution $f(C) = (2C \ln A)^{-1}$ and the conductances range from A^{-1} to A, and compared this result with the effective medium theory (Fig. 3.24).

3.3.3 Region of validity of the critical path analysis

Ambegaokar et al. (1971) have suggested that most of the current is channeled through the paths of least resistance at low temperatures, in inelastic hopping conduction among localized states. The localized states may be viewed as the nodes i of a random network of conductances C_{ij} with the conductance connecting any two states depending exponentially on the distance between them as well as on their energies. Ambegaokar et al. (1971) suggested that at low temperatures the conductances of such networks, and its temperature dependence, can be estimated by looking at the critical paths, and characterizing them by a critical conductance C_c. The critical conductance can be defined by a simple construction as follows. The resistance network can be considered as composed of three parts (Ambegaokar et al., 1971):

1. A set of isolated 'zones' of high conductance, each region consisting of a group of sites linked together by conductances $C_{ij} \gg C_c$.
2. A relatively small number of conductors with C_{ij} of order C_c, which connect together a subset of the high conductance clusters to form an infinite network that spans the sytem. Conductors in categories (1) and (2) are said to form the 'critical subnetwork'.
3. The remaining conductors with $C_{ij} \ll C_c$.

It is worth noting that in the critical path analysis, the conductances of order C_c determine the conductance of the network. The conductances in category (1) could all be set equal to infinity without greatly affecting the total conductance because the current has to pass through conductances of order C_c to get from one end of the system to the other. The conductances with $C_{ij} \ll C_c$ make a negligible contribution to total conductance because they are effectively shorted out by the critical subnetwork of conductors with $C_{ij} \gg C_c$. Thus the conductances are all removed from the network

and then replaced one by one, the largest first. The values of C_{ij} at which extended paths open up is C_c.

Ambegaokar et al. (1971) argue that for a very broad distribution of conductances, as is the case for low temperatures, the conductance may be expressed as

$$C \approx L^{-1} C_c \,, \tag{107}$$

where L^{-1} is less sensitive to the characteristics of the distribution of conductances than is C_c itself. Hence the temperature dependence of C is taken to be of that of C_c alone, the factor L^{-1} adding corrections of order of $\ln C_c$ or less. This analysis yields a very simple and elegant derivation of the $T^{-1/4}$ Mott law for conduction at low temperatures.

The percolation threshold, $f_c = 0.25$, of the numerical bond problem in the 3-D lattice is shown in Fig. 3.23. This value has also been reported elsewhere (Efros, 1986). If f denotes the ratio of conducting bonds to the total number of bonds, the conductance vanishing at a certain value of f is the threshold (critical) value or percolation threshold. Since $f_c = 0.25$, if the conductances are distributed uniformily over the interval (A^{-1} to A) with the weight factor $f(C) = (2C \ln A)^{-1}$, then the critical conductance C_c is easily obtained as follows:

$$f_c = \frac{\int_{C_c}^{A} f(C) d(C)}{\int_{A^{-1}}^{A} f(C) dC} = \frac{\frac{1}{2 \ln A} \int_{C_c}^{A} \frac{dC}{C}}{1} = 0.25 \;\; \Rightarrow \;\; \ln \frac{A}{C_c} = \ln A^{1/2} \,, \tag{108}$$

and

$$C_c = A^{1/2} \,. \tag{109}$$

The critical conductance for such a distribution is plotted in Fig. 3.24. For the distribution used in the calculation and for the conductances increasing up to $A \approx 1000$, this plot shows that: (1) The effective medium theory and C_{eff} for the simple cubic case only slightly underestimates the observed conductances, and (2) the conduction process is not dominated by the paths of least resistance, and the critical path analysis is immaterial.

3.3.4 Region of validity of the Kozeny-Carman formulas for consolidated porous media and the microscopic spatial variations of channel dimensions

In order to establish the validity of the Kozeny-Carman formulas for consolidated porous media, we will use the effective medium theory and assume that the conductances are distributed according to $f(C) = (2C \ln A)^{-1}$ for $A^{-1} \leq C \leq A$. The parallel ($z = \infty$) and the series ($z = 2$) arrangements will be compared to the simple cubic arrangement of the conductors ($z = 6$). In particular, the parallel arrangement (on which Kozeny-Carman formulas are based) will be compared to the simple cubic arrangement of conductors, since it was the latter that was tested with reasonable accuracy against experimental data to calculate permeability of consolidated porous media from microgeometry (Section 3.1). Also, Chatzis and Dullien (1985) have found that the simple cubic network yields results in very good agreement with the experimental data when modeling the mercury porosimetry curve for a variety of sandstones. For comparison purposes, in addition to the effective medium theory results, we plot the observed conductances obtained for a simple cubic arrangement of conductors by Kirkpatrick (1971), and the critical path analysis results in Fig. 3.25.

3.3.4.1 Parallel arrangement of the conductors

For any z we can rewrite Eq. (98) as follows

$$I = \int_{A^{-1}}^{A} \frac{dC}{2C \ln A} \left[\frac{C_{eff} - C}{\frac{C}{z} + \left(\frac{1}{2} - \frac{1}{z}\right) C_{eff}} \right] = 0 \,. \tag{110}$$

For a parallel arrangement of the conductors, $z \rightarrow \infty$, and we can write

$$I = \int_{A^{-1}}^{A} \frac{dC}{C} - \frac{1}{C_{eff}} \int_{A_{-1}}^{A} dC = 0 \,. \tag{111}$$

The two integrals can be evaluated to yield

$$\int_{A^{-1}}^{A} \frac{dC}{C} = 2 \ln A \,, \tag{112}$$

and

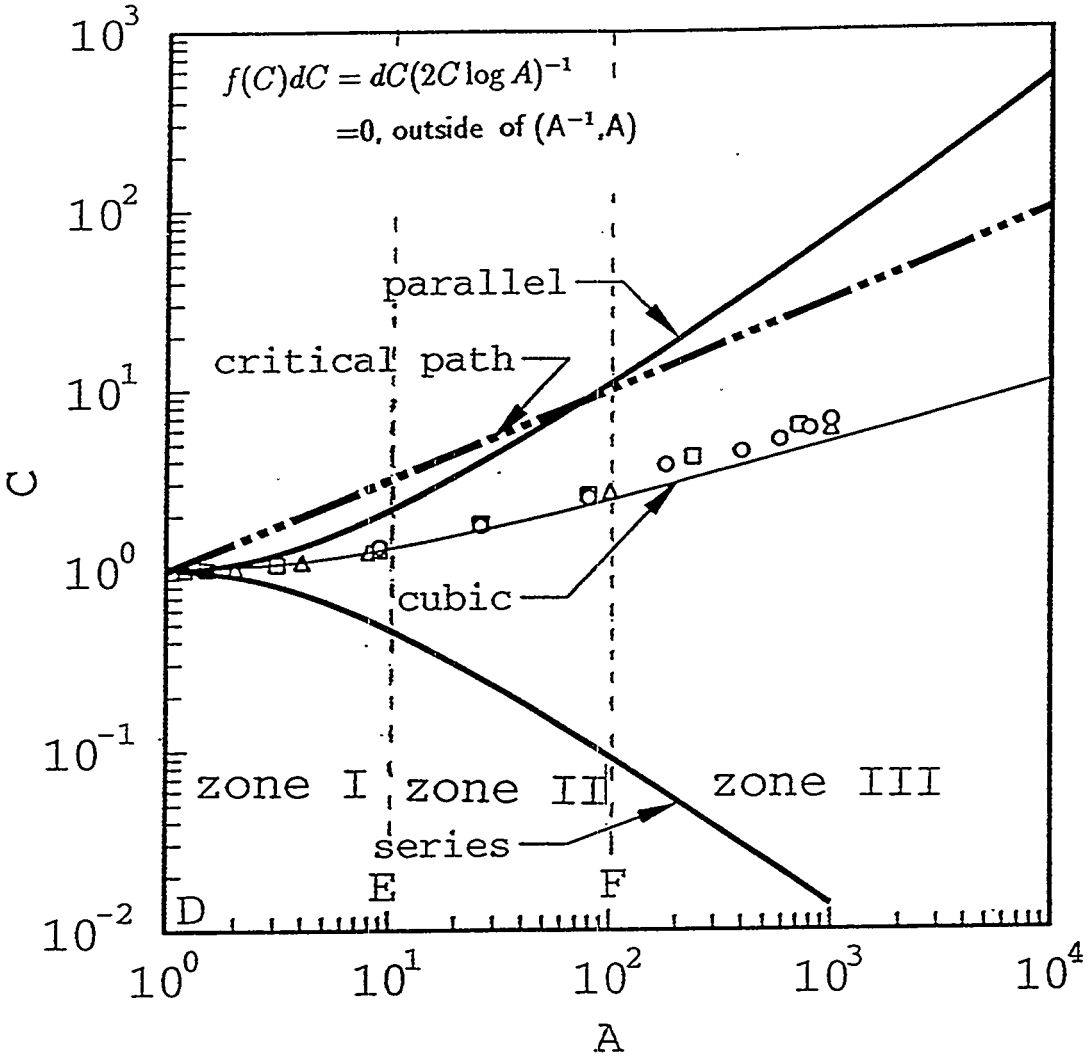

FIG. 3.25: Conductance envelope. The plot shows effective conductances of a parallel, simple cubic, and series networks of conductors, with values of the conductances chosen at random from the distribution $f(C)$ indicated. The critical path conductance and the total conductance of a simple cubic network from previous figure (data points) have also been plotted. Zones I, II, and III correspond to zones within which the Kozeny-Carman formulas are valid, approximately valid, and not valid, respectively.

$$\int_{A^{-1}}^{A} dC = \frac{A^2 - 1}{A} . \tag{113}$$

Thus, for a parallel arrangement of the conductores, C_{eff} is determined by

$$2C_{eff} \ln A = \frac{A^2 - 1}{A} . \tag{114}$$

Results are plotted in Fig. 3.25. Clearly, when $A^{-1} = A = 1$, C_{eff} becomes independent of coordination number z.

3.3.4.2 Series arrangement of the conductors

For a series arrangement of the conductors, $z = 2$, Eq. (98) gives

$$I = \int_{A^{-1}}^{A} \frac{dC}{2C \ln A} \left[\frac{C_{eff} - C}{C + \left(\frac{2}{2} - 1\right) C_{eff}} \right] = 0 . \tag{115}$$

Thus

$$I = C_{eff} \int_{A^{-1}}^{A} \frac{dC}{C^2} - \int_{A^{-1}}^{A} \frac{dC}{C} = 0 . \tag{116}$$

Solving the two integrals yields

$$\int_{A^{-1}}^{A} \frac{dC}{C^2} = \frac{A^2 - 1}{A} , \tag{117}$$

and

$$\int_{A^{-1}}^{A} \frac{dC}{C} = 2 \ln A . \tag{118}$$

Thus, for a series arrangement of the conductors, C_{eff} is determined by

$$C_{eff} \left[\frac{A^2 - 1}{A} \right] = 2 \ln A . \tag{119}$$

Results are plotted in Fig. 3.25. Clearly, as $A^{-1} = A \to 1$, C_{eff} approaches independency of coordination number z.

3.3.4.3 Simple cubic arrangement of the conductors

For a simple cubic lattice, $z = 6$, Eq. (110) gives

$$I = \int_{A^{-1}}^{A} \frac{dC}{2C \ln A} \left[\frac{C_{eff} - C}{C + \left(\frac{6}{2} - 1\right) C_{eff}} \right] = 0 \,. \tag{120}$$

Thus

$$I = \int_{A^{-1}}^{A} \frac{C_{eff} dC}{C(C + 2C_{eff})} - \int_{A^{-1}}^{A} \frac{dC}{C + 2C_{eff}} = 0 \,. \tag{121}$$

Solving the partial integrals

$$\int_{A^{-1}}^{A} \frac{C_{eff} dC}{C(C + 2C_{eff})} = -\frac{1}{2} \left[\ln \frac{2C_{eff} + A}{2C_{eff} + A^{-1}} - 2 \ln A \right] \,, \tag{122}$$

and

$$\int_{A^{-1}}^{A} \frac{dC}{C + 2C_{eff}} = \ln \frac{A + 2C_{eff}}{A^{-1} + 2C_{eff}} \,. \tag{123}$$

Thus C_{eff} for a simple cubic lattice is determined by

$$3 \ln \frac{2C_{eff} + A}{2C_{eff} + A^{-1}} = 2 \ln A \,. \tag{124}$$

Results are plotted in Fig. 3.25. Comparing the three plots (parallel, series, and cubic), as $A^{-1} = A \to 1$, C_{eff} approaches 1, irregardless of coordination number.

The solution to Eq. (123) for $A \to \infty$ is readily obtained:

$$3 \ln \frac{2C_{eff} + A}{2C_{eff}} = 3 \ln A - 3 \ln 2C_{eff} = 2 \ln A \,, \tag{125}$$

and

$$C_{eff} \approx \frac{1}{2} A^{1/3} \,. \tag{126}$$

For very large A, the data falls approximately on a straight line of slope $\sim 1/3$.

3.3.4.4 Results and discussion

Figure 3.25 shows a log-log plot of C_{eff} for the parallel, series, and the cubic arrangements, respectively. For comparison purposes, in addition to the effective medium theory results, we have plotted the critical path analysis results and the results obtained by Kirkpatrick (1971) for a simple cubic arrangement of conductors. In particular, the parallel arrangement will be compared to the simple cubic arrangement of conductors, since the latter was tested with reasonable accuracy against experimental data to calculate permeability of consolidated porous media from microgeometry (section 3.1). This result simply confirmed previous findings by Chatzis and Dullien (1985) when modeling the mercury porosimetry curve for sandstones. For the distribution used in the calculation and for the range of conductances increasing up to $A \approx 1000$, this plot shows that: (1) C_{eff} for the simple cubic case only slightly underestimates the observed conductances, (2) C_{eff} for the series case provides a lower bound for the observed conductances, (3) C_c is the uppermost bound for the observed conductances up to $A \approx 70$, whereas C_{eff} for the parallel case is the upper most bound thereafter, and (4) the conduction process is not dominated by the paths of least resistance, making the critical path analysis irrelevant.

To explore the region of validity of the Kozeny-Carman formulas, we have utilized the conductance envelope for the given distribution of conductances (Fig. 3.25), and divided it into three zones: zone I ($1 < A < 10$), a zone within which the Kozeny-Carman formulas are valid; zone II ($10 \leq A \leq 100$), a zone within which the Kozeny-Carman formulas are approximately valid within limits; and zone III ($A > 100$), a zone within which the Kozeny-Carman formulas are not valid. Zone I, in which conductance span A varies between limits 1 (point D) and 10 (point E), is characterized by conductances C_{eff} for the parallel case being less than two times higher than the cubic case over much of the conductance span. In this zone, the Kozeny-Carman relations are valid within experimental error. Consider, for exam-

ple, that in the analytical expression for permeability given by Eq. (82), the error incurred in the hydraulic radius approximation lies within ±30%. Notice that point D corresponding to the limit $A = 1 = A^{-1}$ is associated with the point at which $C_{eff} = 1$. Therefore, at point D, the porous medium is microscopically homogeneous, and the Kozeny-Carman formulas are strictly valid. In zone I, the spatial fluctuations in channel dimensions are small and the Kozeny-Carman formulas are very accurate. Notice also, that in this zone the critical path conductance C_c provides an upper most bound, and C_{eff} for the series case ($z = 2$) provides a lower bound conductance. Zone II, in which conductance span A varies between limits 10 (point E) and 100 (point F), is characterized by conductances C_{eff} for the parallel case being less than an order of magnitude higher than the simple cubic case. Since the permeability of rocks can range over many orders of magnitude, from about 10^{-11} m^2 down to about 10^{-20} m^2, an estimation of permeability within less than an order of magnitude of the observed value may be sufficient for many practical applications. However, in this zone the pore system is, strictly speaking, microscopically inhomogeneous. Zone II is a transition zone regarding the upper bound conductance because when $A \approx 80$, C_{eff} for the parallel case becomes the upper bound conductance. C_{eff} for the series case provides of a lower bound conductance during the whole span. Zone III, in which conductance span A varies between limits 100 (point F) and higher is characterized by conductances C_{eff} for the parallel case being more than order of magnitude higher than the simple cubic case. At this stage, the pore system is considered highly inhomogeneous. Notice that C_{eff} for the parallel case is here the uppermost bound. The critical path conductance, C_c, is accurate only to within an order of magnitude.

3.4 Comparison of analytical and experimental results

The analytical results for permeability calculated in the manner described above will now be (1) compared against analytical and experimental results for sandstones obtained by Chatzis and Dullien (1985), (2) compared with analytical and experimental results for sandstones obtained previously (sections 3.1 and 3.2), and (3) analyzed in light of the mercury porosimetry experimental data for a variety of sandstones obtained by Batra (1973).

As shown in section 3.1, our permeability model was able to predict the property

for a variety of sandstones while using, in every case, the same cubic lattice as the pore-structure. Chatzis and Dullien (1985) also introduced a regular cubic lattice, consisting of capillary tubes of uniform, but angular cross section, at the intersections of which are angular bulges. Drainage-type penetration numerical experiments were performed in a number of regular networks representing the pore space, using a modified site-percolation approach. All of their networks are composed of two topological entities: capillaries and nodes. The correlation between the probability of a capillary being open and that of a node being open is considered in the calculation. From these results the porosimetry curve of mercury in sandstones, the relative permeability curve of mercury in sandstones, and the relative permeability curve of oil in a sandpack were calculated. The physical basis of the calculations is a one-to-one correspondence between the probability of a capillary being open, and the cumulative distribution function of capillary diameters. Capillaries and bulges are characterized by size distribution functions, and the bulges of different sizes are distributed randomly over the nodal points (sites) of the network. The choice of the size of a capillary is limited by the condition that it may not exceed the size of either of the two bulges located at the two ends of the capillary. In the calculations, realistic capillary and node diameter distribution functions, pore shapes and relationships between the volume and the diameter of a pore were assumed. In their model, however, the aspect of the pore structure called 'geometry', such as the dimensions and the orientation of the pores, are not modeled. The cubic (or tetrahedral) network was found to give results in good agreement with the experimental data (Fig. 3.26).

The angular bonds (pore throats) correspond to pores of diameter D_b. Consistency with the customary definition of pore size used in mercury porosimetry, with the aid of the well-known relationship of Laplace, enables Chatzis and Dullien (1985) to define the capillary diameters as follows

$$D_{b_k} = 2R_{b_k} \cos\theta \,, \tag{127}$$

where R_{b_k} is the radius of curvature of the meniscus of the nonwetting phase at the prevailing capillary pressure, θ is the contact angle, and D_{b_k} is the diameter of capillary k.

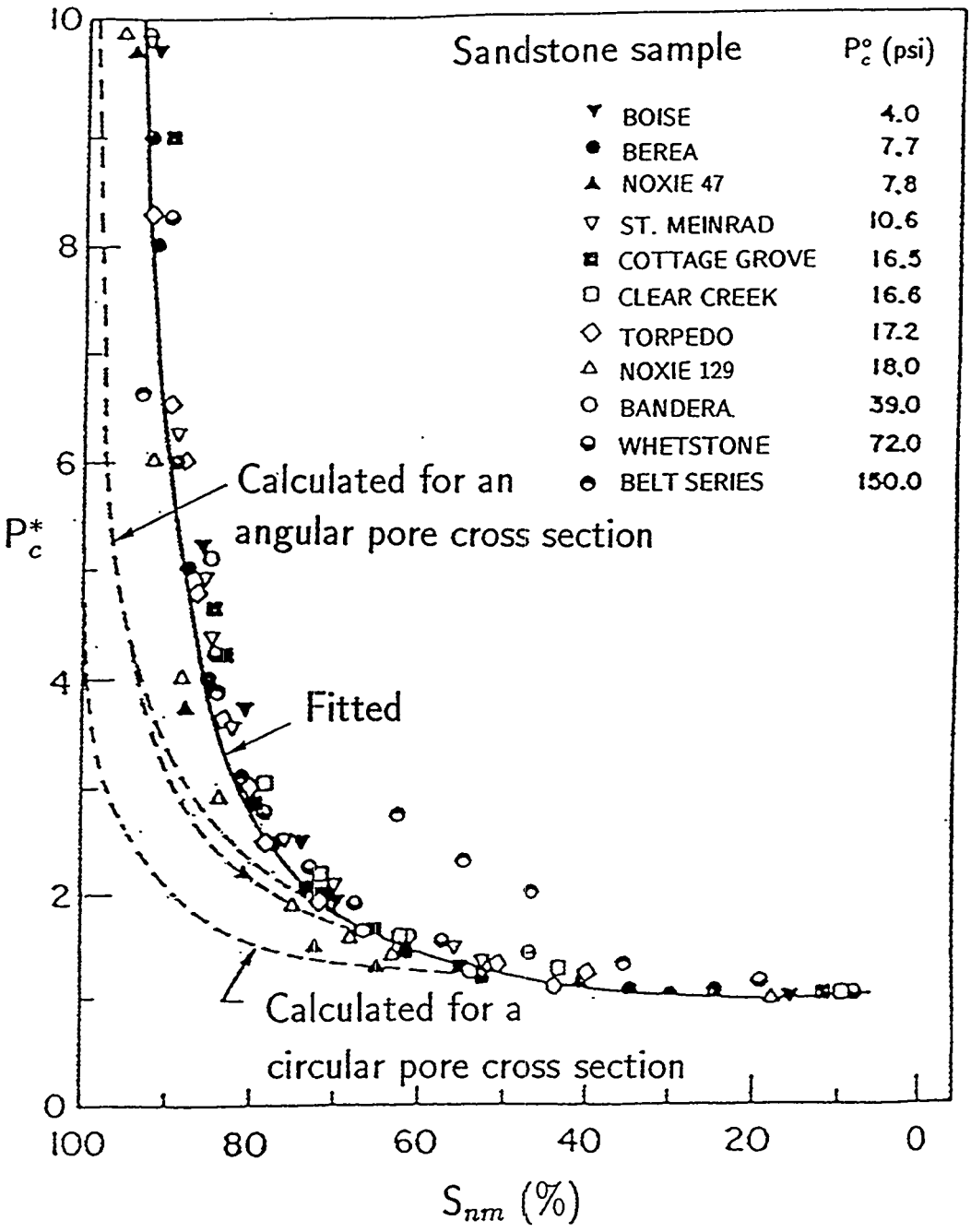

FIG. 3.26: Dimensionless experimental mercury-porosimetry data and analytical curve of sandstone samples. A regular cubic lattice consisting of capillary tubes of angular cross section, at the intersection of which there are angular bulges, is introduced as a pore structure model. The experimental data for all of the sandstone samples (except Belt Series) are well fitted by a single curve (solid line). The capillary pressure is normalized to the breakthrough capillary pressure P_c^o (after Chatzis and Dullien, 1985).

TABLE 3.16: Calculation of the mercury porosimetry curve of the Berea (BE-1) sandstone sample (after Chatzis and Dullien, 1985).

P^*_{ck}	D_{b_k}	$D^2_{b_k} f_b$	D_{s_k}	$D^2_{s_k} f_s$	S^*_{nmk}	S^o_{nmk}
1.00	29.5	102.3	44.5	848.0	0.113	0.170
1.02	28.8	104.9	44.0	843.8	0.164	0.252
1.09	27.0	109.5	42.5	826.3	0.286	0.415
1.15	25.5	110.6	41.0	802.1	0.365	0.519
1.23	24.0	109.4	39.5	771.8	0.443	0.599
1.32	22.4	105.6	38.0	735.9	0.496	0.667
1.43	20.7	99.1	37.0	709.2	0.552	0.724
1.54	19.2	91.4	35.5	665.3	0.605	0.776
1.68	17.6	81.6	34.0	617.0	0.659	0.824
1.84	16.0	70.6	33.0	582.6	0.708	0.862
2.06	14.3	58.1	31.5	527.6	0.764	0.902
2.36	12.5	44.7	30.0	468.3	0.818	0.937
2.78	10.6	31.1	28.5	403.1	0.869	0.965
3.47	8.5	17.8	27.0	327.5	0.918	0.987
5.90	5.0	0	25.0	0	0.972	1.000

Analogously, for angular nodes (pore bodies) of diameter D_{s_k}:

$$D_{s_k} = 2R_{s_k} \cos\theta \,, \tag{128}$$

where R_{s_k} is the radius of curvature of the meniscus of the nonwetting phase at the prevailing capillary pressure, θ is the contact angle, and D_{s_k} is the diameter of pore body k.

Table 3.16 (Chatzis and Dullien, 1985) gives the calculated values of the mercury porosimetry curve of the Berea (BE-1) sandstone sample using a cubic lattice of noncircular (and circular) pores. Berea (BE-1) sandstone has almost the same macroscopic transport properties as the Berea sandstone used in our experiments (i.e., porosity of 22%, permeability to N_2 of 400 mD, and a formation factor of 15.5). The capillary pressure P^*_{ck} is given relative to the breakthrough pressure P^o_c. The diameters of the pores D_{b_k}, and D_{s_k} were calculated for the prevailing capillary pressure and its corresponding saturation. The density functions $f_b(D_b)$ and $f_s(D_s)$ were assumed to be given by the beta function. The saturations $S^*_{nm_k}$ and $S^o_{nm_k}$ are the saturations of the angular and circular pore networks, respectively.

To compare our analytical calculations for permeability obtained above with the results obtained by Chatzis and Dullien (1985) for Berea (BE-1), we need first to relate the diameter D_k of each angular pore to its individual hydraulic conductance C_k (Equation 12). Schultze (1925a,b) has shown that the capillary pressures for noncircular capillaries under the assumption of zero contact angle are given by

$$P_c = \frac{\epsilon}{R_H}\,; \quad \frac{1}{R_H} = \frac{1}{r_1} + \frac{1}{r_2}\,, \tag{129}$$

where ϵ is the surface tension, r_1 and r_2 the principal radius of curvature, and R_H the hydraulic radius as defined previously. For an equilateral triangle of side a, the equivalence of the reciprocal of the hydraulic radius and the reciprocal mean radius of curvature is (Carman, 1941)

$$\frac{1}{R_H} = \frac{1}{r_1} + \frac{1}{r_2} = \frac{2}{R_k} = \frac{4}{D_k}\,. \tag{130}$$

Thus, at zero contact angle, D_k and R_H are related. The area A and the perimeter P of the equilateral triangular pore are $\sqrt{3}a^2/4$ and $3a$, respectively. The hydraulic radius is $R_H = A/P = \sqrt{3}a/12$, and the pore diameter is $D_k = \sqrt{3}a/3$. Therefore, the angular pore area in terms of the diameter D_k is $A = 3\sqrt{3}D_k^2/4$.

Recall Eq. (12) used earlier for calculating the individual pore conductances

$$C_k = \frac{1}{2} R_H^2 A\,.$$

In terms of pore diameter D_k, and under the assumption of zero contact angle, the pore conductance becomes

$$C_k = \frac{3\sqrt{3}}{128} D_k^4\,. \tag{131}$$

Table 3.16 (Chatzis and Dullien, 1985), gives the calculated pore diameters D_k for Berea sandstone (BE-1) for the full range of capillary pressures and saturation. At this stage, we need to calculate the pore conductances of the 'primary' pore network which is the one accountable for hydraulic transport. Our experimental results have consistently shown that the hydraulically active or 'primary' pore network in sandstones

consists of intergranular pores (bodies and throats), situated in between the grains (Chapters 4, 5, and 6). The hydraulically active or 'primary' network of intergranular pores in Berea sandstone comprises about 80% of the total rock porosity. About 20% of the total rock porosity consists of grain-contact pores; both inside the cementing material, and a few between grains when the pore has been narrowed down by deposits to a very narrow gap. Since the contribution of the grain-contact or 'secondary' network to hydraulic transport is small, it can therefore be considered hydraulically inactive (see Chapter 6). The pore (pore throat) diameters of the 'principal' network of Berea sandstone range from the critical diameter $D_c = 29.5$ μm corresponding to the breakthrough pressure P_c° (and corresponding saturation $S^*_{nm_k} = 0.113$) to the value $D_{b_k} = 12.5$ μm (and corresponding saturation $S^*_{nm_k} = 0.80$). The breakthrough diameter $D_c = 29.5$ μm is the largest diameter of the first connected cluster that spans the whole sample. On the other hand, the pore diameter $D_{b_k} = 12.5$ μm is the minimun diameter of the 'principal' network, consisting of intergranular pores, i.e., in between grains. From the 'principal' network of Berea sandstone (BE-1), the maximum and minimum pore diameters are thus obtained, and the ratio of critical to minimum pore conductances calculated with the aid of Eq. (129) is

$$\frac{C_c}{C_{min}} = \frac{D_c^4}{D_{min}^4} = \frac{29.5^4}{12.5^4} \approx 31 \,. \tag{132}$$

Using the C_c/C_{min} ratio for Berea sandstone, it is then possible to go to the general conductance plot (Fig. 3.25) and obtain the ratio of effective conductance for the parallel case ($z = \infty$) to the effective conductance for the cubic case ($z = 6$)

$$\frac{C_{eff_{parallel}}}{C_{eff_{cubic}}} \approx 3 \,. \tag{133}$$

The above result is consistent with previous calculations on permeability of Berea sandstone presented in sections 3.1 and 3.2. For example, conductance calculations for Berea sandstone section B presented in section 3.1 (Table 3.17), using the effective medium theory in conjunction with the 'principal' pore network, gave effective conductances for the parallel case ($z = \infty$) and for the cubic case ($z = 6$) such that their ratio is given by

TABLE 3.17: Calculated effective conductance data of various sandstones obtained from SEM 2-D sections (Chapter 3.1).

Rock	$C_{eff}\ (z^* = \infty)\ (\mathrm{m}^4)$	$C_{eff}\ (z^* = 6)\ (\mathrm{m}^4)$	$\frac{C_{eff}\ (z^*=\infty)}{C_{eff}\ (z^*=6)}$
Berea sandstone B	56.0×10^{-20}	18.2×10^{-20}	3.1
Berea sandstone T	59.9×10^{-20}	24.2×10^{-20}	2.5
Boise sandstone	80.1×10^{-20}	45.0×10^{-20}	1.8
Massilon sandstone	525×10^{-19}	90.7×10^{-19}	5.8
Saint-Gilles sandstone	48.3×10^{-20}	21.2×10^{-20}	2.3

*Coordinatiom number.

TABLE 3.18: Calculated permeability data of two sandstones from rock micro-geometry assuming a parallel pore model (Chapter 3.2).

Rock	$k\ (z^* = \infty)\ (\mathrm{m}^2)$	$k_{measured}\ (\mathrm{m}^2)$	$\frac{k\ (z^*=\infty)}{k_{measured}}$
Berea sandstone B	15.0×10^{-13}	4.8×10^{-13a}	3.1
Massilon sandstone	10.8×10^{-12}	2.5×10^{-12b}	4.3

[a]Distilled water used as permeant.

[b]Data from Koplik et al., 1984.

$$\frac{C_{eff_{parallel}}}{C_{eff_{cubic}}} = \frac{56.0 \times 10^{-20}\ m^4}{18.2 \times 10^{-20}\ m^4} \approx 3\ . \tag{134}$$

Analogously, for Berea sandstone section T shown in section 3.1 (Table 3.17), the effective medium theory in conjunction with the 'principal' network gave effective conductances such that their ratio is

$$\frac{C_{eff_{parallel}}}{C_{eff_{cubic}}} = \frac{59.9 \times 10^{-20}\ m^4}{24.2 \times 10^{-20}\ m^4} \approx 3\ . \tag{135}$$

Similarly, in section 3.2 (Table 3.18), it was shown that a model based on the 'principal' pore network, a parallel arrangement, and a pore size distribution, gave the permeability for Berea sandstone section B such that its ratio to the observed value is

$$\frac{k_{parallel}}{k_{measured}} = \frac{15.0 \times 10^{-13}\ m^2}{4.8 \times 10^{-13}\ m^2} \approx 3\ . \tag{136}$$

It is then concluded that Berea sandstone hydraulically active conductances fall

into zone II of Fig. 3.25, and that the Kozeny-Carman relations are valid within a factor of three of the measured permeability values. But, how general is this result for most sandstones, especially considering that the range of pore diameters may vary widely from one rock to another? This issue becomes quite clear when one examines the normalized experimental capillary pressure curves shown in Fig. 3.26 for a variety of sandstones. They almost without exception can be represented by a single function (solid line). This is a direct consequence of the 'similarity' in the geometrical sense of the pore structure and of the 'principal' pore network of ten of the eleven sandstone samples under study. The absolute magnitudes of the pore sizes alone do not determine the results of these calculations. It is the pore diameters and pore conductances of the hydraulically active pore network, relative to the breakthrough pore diameter and corresponding conductance, rather than the absolute magnitudes of the pore diameters and corresponding conductances of the complete network, that determine the permeability and capillary pressure results. The successful prediction of permeability from microgeometry (section 3.1), and of the mercury porosimetry curve by Chatzis and Dullien (1985) of several sandstone samples, using the same cubic lattice network model as pore structure, which may appear surprising at first considering that the range of pore diameters sizes vary widely from one rock to another, becomes apparent.

Finally, it is established that the permeabilities of most sandstones fall in zone II of the conductance envelope (Fig. 3.25), and that the permeabilities predicted by the Kozeny-Carman formulas are valid within more or less a factor of three of the observed values. Consequently, even though the complete pore space system of most sandstones is strictly speaking inhomogeneous, the hydraulically active or 'principal' network approaches homogeneity. As the rock 'principal' pore network becomes more and more inhomogeneous, the conductance plot shows that the Kozeny-Carman formulas become less and less applicable. For a very inhomogeneous 'principal' network, Fig. 3.25 shows that the critical path analysis can be applied within limits.

CODE LISTING 3.1: FORTRAN source code for calculating the effective conductance given the individual conductances using the effective medium theory.

```
c**********************************************************************
c
c      Program Per: This program calculates the effective conductance in a
c                   porous medium using the effective medium approximation
c
c      created:   7/4/90   E. Schlueter
c
c      modified:  xx/xx/xx
c
c**********************************************************************
c
c     DECLARATIONS
c
      dimension hydr(5000), area(5000), peri(5000), c(5000), n(5000)
c
c**********************************************************************
c
c     INPUT DATA AND INITIALIZE
c
         open (unit=1, file='per_in.dat', status='old')
         open (unit=2, file='per_out.dat', status='old')
c
1     format(' input coon,imax')
ccc      write(5,1)
ccc      read (5,*) coon,imax
      read (1,*) coon,shfa,imax
      fact=(coon/2.)-1.
c
      do 5 i=1,imax
2        format(' input c(',i2,')')
ccc         write(5,2)i
ccc         read (5,*) c(i)
         read (1,*) j, n(i), c(i) ! j,area(i),peri(i)
c
c**********************************************************************
c
c     CALCULATIONS
c
c**********************************************************************
c
c     CALCULATION OF CONDUCTANCES
c
ccc      hydr(i)=area(i)/peri(i)
ccc      c(i)=hydr(i)*hydr(i)/shfa
5     continue
c
c**********************************************************************
c
c     CALCULATION OF MAXIMA AND MINIMA CONDUCTANCES
c
      cmax=0
      cmin=1.e6
c
      do 10 i=1,imax
         cmax=amax1(cmax,c(i))
         cmin=amin1(cmin,c(i))
10    continue
c
c**********************************************************************
c
      del_ceff=cmax-cmin
      jmax=11
      fuad=0
      ceff=cmin
```

```
      do 20 k=1,4
         del_ceff=del_ceff/10.
         do 30 j=1,jmax
c
c*************************************************************************
c
c     BISECTION LOOP
c
            ceff_old=ceff
            ceff=ceff+del_ceff
            fuad=sum(ceff,c,fact,imax,n)
c
            if(fuad .gt. 0.) then
               ceff=ceff_old
               go to 20
            endif
c
30       continue
20    continue
c
c*************************************************************************
c
c     FORMAT STATEMENTS
c
101      format('EFFECTIVE INTRINSIC PERMEABILITY CALCS.'//,
     &      'coon = ', e9.3, '   shfa = ', f9.3, '   ceff = ', f10.3,
     &      '[m*m]', /)
c102      format(xxx,...
c
c*************************************************************************
c
c     WRITE OUTPUT DATA
c
      write(5,6) ceff
6     format(' ceff = ',f10.3)
      write(2,101) coon,shfa,ceff
c
      close (unit=1, status='keep')
      close (unit=2, status='keep')
      end
c
c*************************************************************************
c
c     CALCULATION OF EFFECTIVE CONDUCTANCES
c
      function sum(ceff,c,fact,imax,n)
      dimension c(5000), n(5000)
      sum=0
c
      do 50 i=1,imax
         do 45 k=1,n(i)
         func=(ceff-c(i))/(fact*ceff+c(i))
         sum=sum+func
45       continue
50    continue
c
      return
      end
c
c*************************************************************************
```

4 PREDICTING ELECTRICAL CONDUCTIVITY OF SEDIMENTARY ROCKS FROM MICROSTRUCTURE

4.1 Analytical approach using individual conductances

In the study summarized here, the electrical conductivity of sedimentary rocks is predicted from the microscopic geometry and connectivity of the pore space. We have preserved the same intergranular pore model structure used to predict hydraulic permeability (Chapter 3). The cross-sectional areas of the individual pores are estimated from 2-D scanning electron micrographs of rock cross sections (Figures 3.5 to 3.9). The electrical conductivity of the individual pores is determined from the geometrical parameters, using Ohm's law. In the section under consideration, the pore cross sections are assumed to be randomly oriented with respect to the directions of the channel axes. The orientation effect has been corrected by means of geometrical and stereological considerations. Account is also taken for possible variation of the cross-sectional area along the length of each tube, e.g., pore necks and bulges. The effective-medium theory of solid-state physics is then used to replace each individual conductance with an effective average conductance of each pore. Finally, the pores are assumed to be arranged on a cubic lattice, which allows the calculation of overall macroscopic values for the electrical conductivity. Preliminary results, using Berea, Boise, Massilon, and Saint-Gilles sandstones, show fair to good agreement between the predicted and measured electrical conductivities, with essentially no arbitrary parameters in the model. In particular, good agreement was found in the case of a poorly cemented rock such as Saint-Gilles sandstone, whereas the agreement was not very good for two well-cemented rocks, Boise and Berea. The possible reason(s) for this effect are under investigation.

4.1.1 Effect of cross-sectional shape

The electric conductance per unit length of each cylindrical tube of area A is

$$C_{e_i} = \frac{A}{\rho_w}, \tag{137}$$

where ρ_w is the resistivity of the fluid; this expression is exact regardless of the pore shape.

4.1.2 Effect of pore orientation

In the two-dimensional sections under consideration, however, the pore cross- sections are randomly oriented with respect to the directions of the channel axes. The orientation effect has been corrected by means of geometrical and stereological considerations (Chapter 3.1.4.2):

$$A_{actual} = \left\langle \frac{1}{\cos\theta} \right\rangle^{-1} A_{measured} = 0.61 A_{measured} ,$$

where the brackets denote a spherical average for pores of random orientation.

4.1.3 Effect of pore constrictivity

Constrictions within the individual branch channels, i.e., pore necks and bulges, have been taken into account using an analysis based on a sinusoidal variation of cross section. In the electric conductance analysis, for example, the factor accounts for the ratio of $\langle R^{-2} \rangle^{-1}$, which governs the conductance of a tube of varying radius, to $\langle R \rangle^2$, which is the value estimated from the micrographs (Chapter 3.1.5). We have estimated a throat-to-pore radius ratio of 0.5 from a pore cast of Berea sandstone, and tentatively use this value for each rock. This ratio then indicates an electric constriction factor of 0.86 (Figure 4.1).

4.1.4 Effective medium theory

Study of scanning electron micrographs of Berea sandstone has indicated the presence of a statistically isotropic 3-D pore structure. These observations have led to the assumption that the pores of varying size are arranged on a cubic lattice, so that the coordination number of the network is 6. The effective-medium theory from solid-state physics (Kirkpatrick, 1973) is then used to replace each individual conductance with an effective average conductance, as follows.

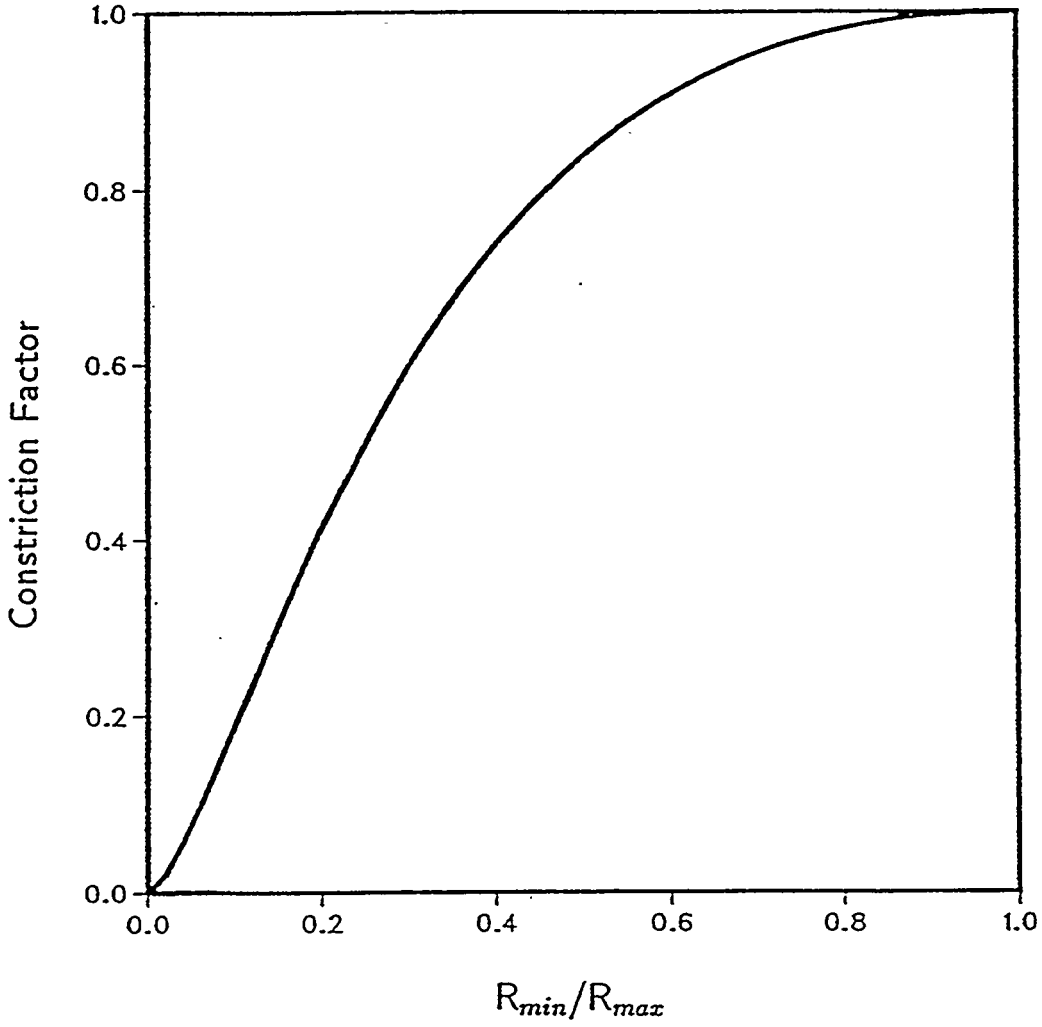

FIG. 4.1: Constriction factor for electric flux as function of the ratio of the minimum pore radius to the maximum pore radius of an individual pore. The calculated conductances of the pores must be multiplied by this factor, which account for the converging-diverging nature of the pore tubes.

For a general discrete distribution of conductances, the resulting equation defining the effective conductance is given by Eq. (6)

$$\sum_{i=1}^{N} \frac{C_{eff} - C_i}{[(z/2) - 1]C_{eff} + C_i} = 0 \,,$$

where the sum is over all N conductive elements and z is the average coordination number of the lattice. For a coordination number of $z = 6$, the above equation has been solved numerically to allow for the calculation of the effective-medium conductance, given the individual conductances (Code Listing 3.1).

The electrical conductivity is often quantified by the 'formation factor', which is the ratio of the resistance of the electrolyte-saturated rock sample to the resistance of an equal volume of electrolyte solution. The electric conductance per unit length of an equal volume of electrolyte solution is

$$C_w = \frac{A_{total}}{\rho_w} \,, \tag{138}$$

where A_{total} is the total area of the rock sample.

The electric conductance per unit length of the electrolyte-saturated rock sample is (a unit cubic cell is used to relate the effective electric tube conductance to the continuum)

$$C_e = \frac{N A_{eff}}{\tau} \frac{1}{\rho_w} \,, \tag{139}$$

where A_{eff} is the effective pore area of the individual tubes, N is the number of pore tubes in the scanning electron photomicrograph, and τ is the tortuosity of a cubic lattice, which is 3.

Thus, the formation factor is given by

$$F = \frac{C_w}{C_e} = \frac{\tau A_{total}}{N A_{eff}} \,. \tag{140}$$

TABLE 4.1: Measured vs. predicted formation factors of four sedimentary rocks.

Rock	$F_{measured}$	$F_{predicted}$ $(z^a = 6)$
Berea sandstone	15.9[b]	44.1
Boise sandstone	11.0[b]	27.2
Massilon sandstone	11.8[c]	52.2
Saint-Gilles sandstone	13.5[b]	13.1

[a] Coordination number.

[b] Zinc nitrate solution used as electrolyte.

[c] Data from Koplik et al., 1984.

4.1.5 Results and discussion

Preliminary results are presented in Table 4.1. Fair to good agreement was found between measured and predicted electrical conductivities for a variety of sandstones when using the cubic lattice model with essentially no arbitrary adjustable parameters. In particular, good agreement was found in case of a poorly cemented rock such as Saint-Gilles sandstone, whereas the agreement was not very good for two well-cemented rocks, Berea and Boise. The possible reasons(s) for this effect are being investigated experimentally (See Chapter 4.2). Caruso et al. (1985) have shown that the total porosity of a cemented rock such as Berea sandstone consists of 72% intergranular porosity (Figures 3.5b and 3.6b), 13% connective porosity (grain contacts), and 15% microporosity. Even though most of the rock's porosity is intergranular, there are significant amounts of the other types. Since electrical conductivity is proportional to the sum of the areas of the tubes, whereas permeability is proportional to the sum of squares of areas, tubes of relatively smaller diameter, if numerous, can have a significant effect on conductivity, yet a negligible effect on permeability. In addition, the presence of connected thin sheets and small throats associated with micropores provide additional paths for the current to flow, the net effect being an increase in effective coordination number of the lattice for electrical conductivity. In this study, we have preserved the intergranular pore model structure used to predict intrinsic permeability from microgeometry. However, it is likely that in some cases this basic pore model structure needs to be modified to incorporate relevant rock geometrical and topological characteristics important for electrical conductivity.

4.2 Experimental approach using microscopic distribution of solid hydrocarbon (paraffin wax) in the pore space

In our experimental electrical conductivity studies, we have employed a wetting fluid that can be frozen in place: (1) to allow measurement of effective properties with an electrolyte solution in the rock pore spaces not occupied by a wetting fluid, (2) to allow direct observation and analysis of the wetting-fluid distribution at each fluid-saturation regime, and (3) to understand how the wetting-fluid invasion process is controlled by rock pore structure and topology with the aid of a complete pore cast. In addition, disseminated clay, often in the form of aggregates, may line the rock pores or be distributed between the grains of the matrix. The clay minerals act as a separate conducting path additional to that contributed by the saline solution in the rock pores. The conductivity of the rock containing disseminated clay therefore has two components: one is the conductivity of the fluid-filled pores of the rock; the other one is the conductivity of the disseminated clays which are the solid phases that primarily exhibit surface reactivity in rocks and soils (Sposito, 1984). This is a direct consequence of the fact that clay particles have large surface areas. In order to measure surface conductance, the geometry of the system must be known. In the case of rocks, the exact pore geometry that affects the total conductance is unknown. Furthermore, it can change due to dispersion and flocculation of the clay minerals in the pores. Thus it is forseen that the presence of clay may greatly complicate the quantitative evaluation and interpretation of experimental data. In our experimental studies, we have isolated the effect of clay minerals on formation factor and assessed the surface conductance contribution due to the presence of clays.

The conductivity of a rock (consisting of electrically nonconductive particles) saturated with a conducting electrolyte has been shown by Archie (1942) to depend upon the conductivity of the electrolyte and a geometrical (e.g., formation) factor. In such a system, the electrical conductance of the saturated rock is proportional to the conductance of the electrolyte solution; the constant of proportionality (always > 1) is a geometrical factor called the formation factor. The formation factor of a fully saturated rock is defined as the ratio of the resistance of the brine-saturated rock to the resistance of an equal volume of brine

$$F = \frac{\rho(electrolyte - saturated\ \ sample)}{\rho(electrolyte\ \ solution)} ,$$

where F is the formation factor, and ρ the resistivity.

The assumptions implicit in the formation factor concept are: (1) The conduction process is electrolytic and it occurs only through the network of saline solution filling the pores, (2) the properties of the saline solution filling the pores are uniform, and (3) there are no surface conductivity effects. In such a system, the plot of the electrical conductance of the saturating solution versus the electrical conductance of the rock saturated with the solution is a straight line passing through the origin.

When more than one fluid is present, e.g., oil/water, the empirically determined Archie saturation is often found to vary according to

$$F = \phi^{-m} S_w^{-n} , \tag{141}$$

where F is the effective formation factor, ϕ is the porosity, S_w the electrolyte saturation, and m and n are dimensionless empirically determined constants. The value of m varies with the extent to which a rock is cemented, from about 1.3 for unconsolidated sands to 2.3 for consolidated sandstones (Wyllie, 1963). The value of n depends to a large extent on the wettability of a reservoir rock (Anderson, 1986). In rocks that are wholly oil-wet, i.e., rocks in which water is the nonwetting phase, $3.0 < n < 4.0$, whereas if the rock surface is entirely water-wet, $1.8 < n < 2.0$ (Anderson, 1986). The Archie saturation equation assumes that the saturation/resistivity relation is unique (i.e., only one resistivity is measured at a given saturation), n is constant for a given porous medium, and all the saline solution contributes to the flow of electric current. To verify these assumptions, we have analyzed the experimental electrical conductivity data in light of the role of the pore structure and topology in the wetting-fluid invasion process with the aid of fluid distributions at each saturation regime, a complete pore cast, and its associated rock section.

Laboratory electrical conductivity data for fully and partially-saturated samples of Berea sandstone with a wetting fluid is presented. In our study, we employ a

wetting fluid (paraffin wax) that can be frozen in place at controlled saturations to allow us to examine the occupied pore space after the experiment. The effective formation factors for an electrolyte in the pore spaces not occupied by the paraffin are measured at various saturations after solidifying the paraffin in place. The effect of clay and other surface reactive minerals on Berea sandstone formation factor is first isolated, and their surface conductance contribution to overall conductivity assessed. The electrical conductivity experimental data is analyzed in light of the role of the pore structure on the wetting fluid invasion process with the aid of direct observation of fluid distributions at each saturation regime, a complete pore cast, and its corresponding rock section. Finally, the effect of partial hydrocarbon saturation on overall Berea sandstone conductivity, and on the Archie saturation exponent n, is studied.

4.2.1 Apparatus and procedure

The apparatus that was used in this study was designed to measure simultaneously both hydraulic and electrical conductivity (Figure 4.2). The rock core (5 cm in diameter and 5 cm in length) is encased in its rubber jacket and placed in the test cell. The test cell base is connected directly to the bottom of the sample, and a centrally located orifice is attached to allow fluids to flow through the mounted core. The electrodes are connected to the top and bottom of the core sample so that any current flow between them will necessarily pass through the core. A confining pressure of 50 psi (3.4 atm) is applied using nitrogen gas. Fluid flow through the core is controlled by a syringe pump providing a constant flow rate of 200 ml/hr. The basic procedure used for measuring the formation factor in a 100% electrolyte-saturated sample is first to vacuum saturate each core completely with distilled water. An aqueous zinc nitrate solution of known resistivity is then pumped through the core, and flow is continued for a sufficient time to establish constant pressure and resistance readings. It was found that about four pore volumes of electrolyte is required to achieve steady state. In our experiments, we used samples of Berea sandstone, which is a homogeneous sedimentary rock used as a reference rock in the petroleum industry. The intrinsic permeability and porosity of a Berea sandstone core are about 600 mD (600×10^{-15} m^2) and 22%, respectively. It is estimated to be of Mississippian age and is found in Berea, Ohio.

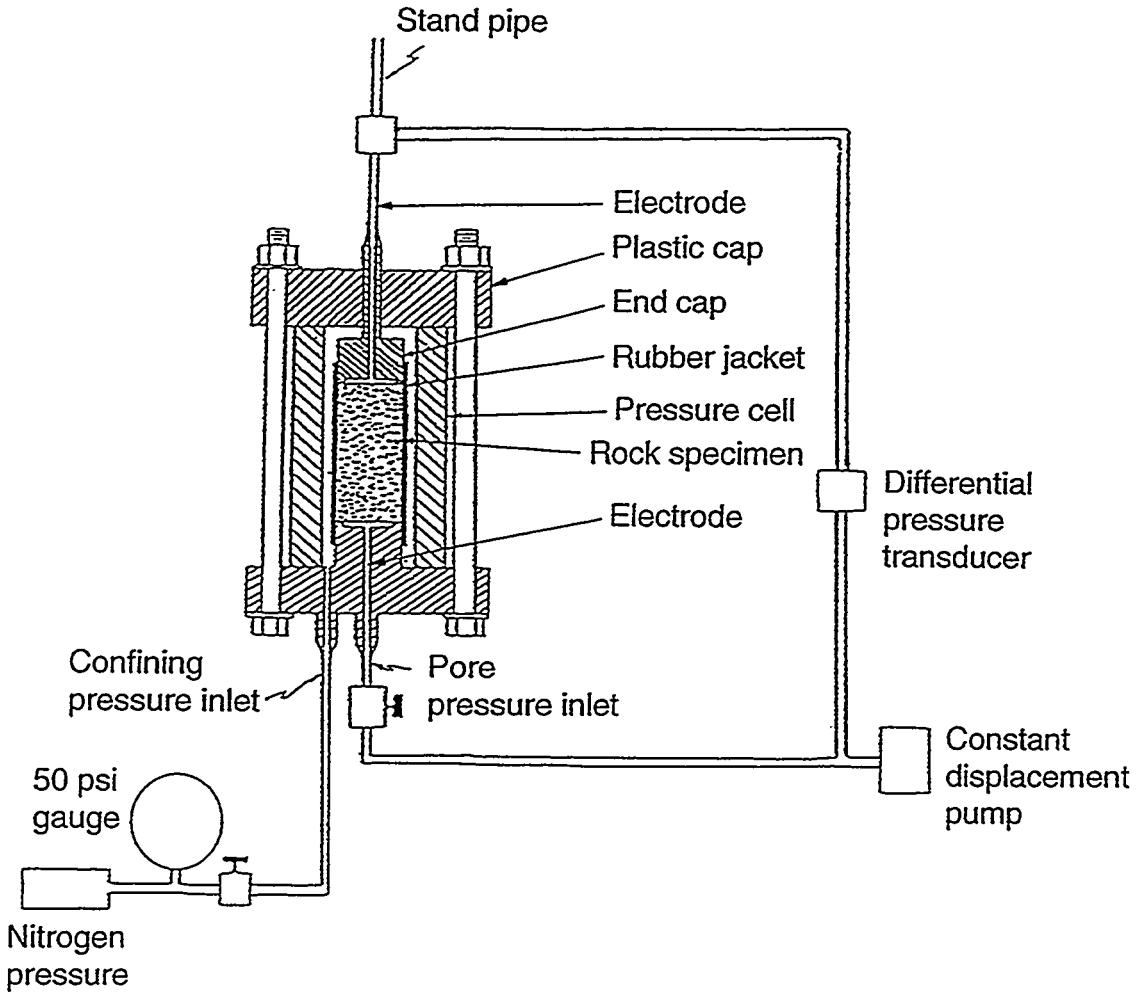

FIG. 4.2: Schematic representation of the laboratory apparatus designed to simultaneously measure both electrical and hydraulic conductivity.

TABLE 4.2: Formation factor data for Berea sandstone with a 0.5 M zinc nitrate solution used as electrolyte.

Berea Sandstone	$\phi^a_{measured}$ (%)	$F^b_{measured}$
KS4	21.9	15.0
KS6	22.6	14.3
KS7	22.0	17.7
KS9	22.2	15.9

[a]Porosity.

[b]Formation factor.

4.2.2 Effect of hydrocarbon saturation

The conductivity of the pore system can be varied either by altering the salinity of the water in the pores or by changing the quantity of water of a particular salinity by introducing another solid/fluid phase into the pore space. To determine the effect of partial fluid saturation on formation factor, we utilized Berea sandstone samples that had been permeated with a sequence of triple-distilled water (to measure the hydraulic conductivity), followed by a 0.5-M zinc nitrate solution and again flushed with distilled water. This procedure was applied to every sample to find the formation factor before the paraffin application (Table 4.2). The samples were then oven dried. After measuring the formation factor, the samples were partially filled with paraffin wax at controlled saturations of 20%, 30%, 40%, 50%, 60%, and 70%. The hydrocarbon paraffin is a wetting phase with a density of 0.76 g/cm^3, and a melting point of 56°C. It is applied at temperatures higher than its melting point in the core axial direction, until uniform saturation is achieved throughout the sample (Figure 4.3). The paraffin is then solidified in place at ambient temperature. After the hydrocarbon paraffin application, the rock grain surfaces became hydrophobic. To measure the effective formation factor, the rock samples that were partially saturated with paraffin were permeated with a 0.5-M zinc nitrate solution at pH $\sim$ 4. The effective formation factor vs. paraffin saturation is presented in Figure 4.4 (case A). Experiments in which the formation factor had not been measured prior to paraffin impregnation were repeated on a new and clean set of samples. The result is shown in Figure 4.4 (case B). In summary, good agreement within experimental error was found between the two sets of experiments A and B.

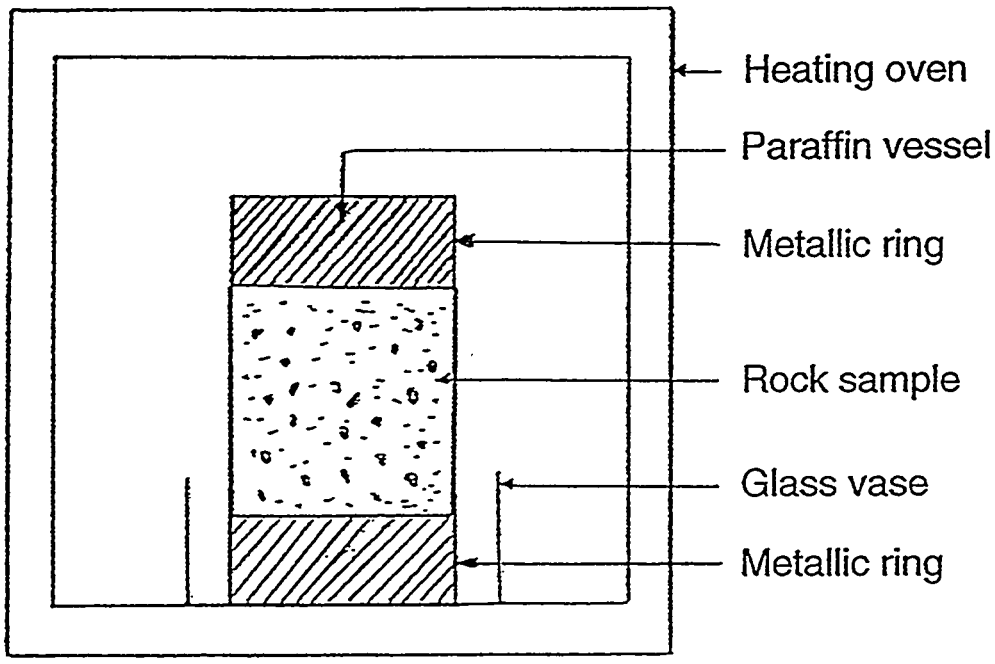

FIG. 4.3: Experimental setup for one-dimensional paraffin impregnation.

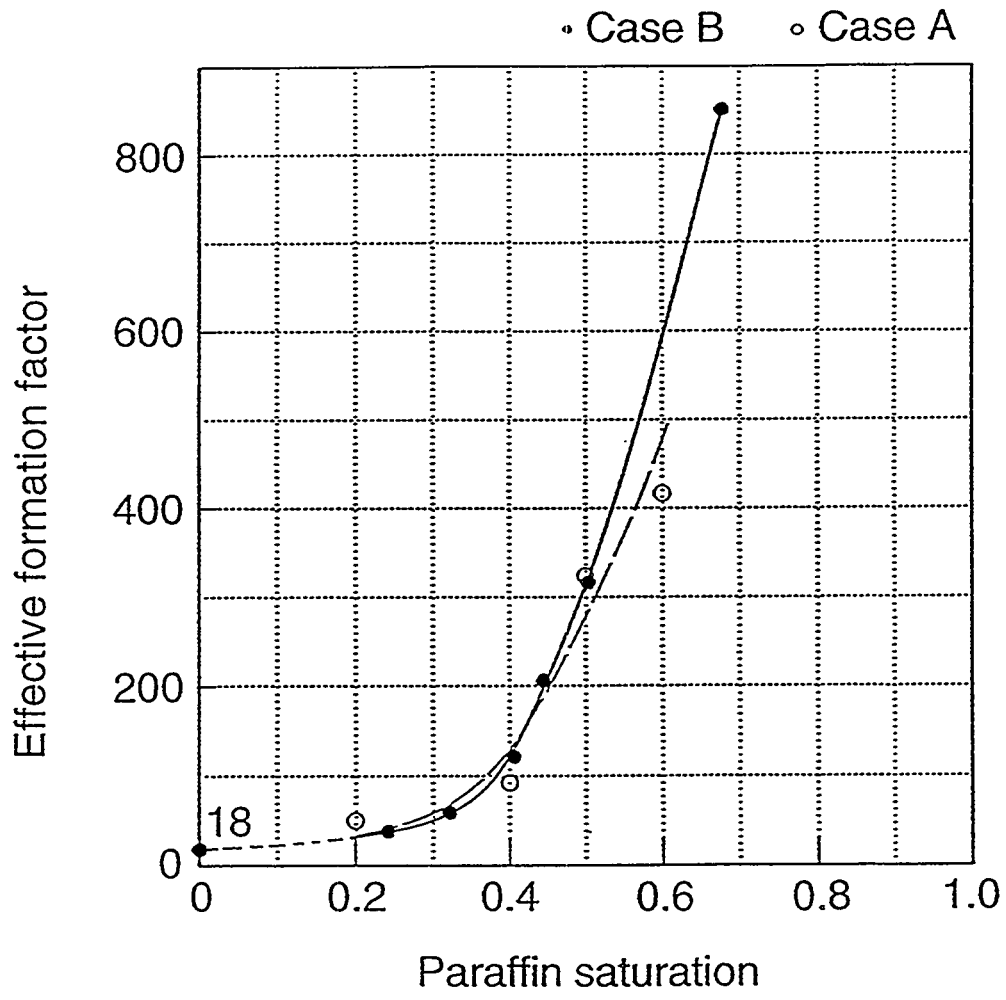

FIG. 4.4: Effective formation factor vs. paraffin saturation for Berea sandstone. The pore space was partially saturated with hydrocarbon paraffin. The remaining portion of the pore space was filled with a 0.5-M zinc nitrate solution. Cases A and B correspond to experimental data on samples subjected or not subjected to a formation-factor measurement before paraffin application, respectively.

4.2.3 Effect of clay

X-ray diffraction studies by Khilar and Fogler (1984), in conjunction with scanning electron microscopy (Figure 4.5) and energy-dispersive x-ray analysis (Figure 4.6), indicate that Berea sandstone contains $\sim$ 8% by weight of dispersable and swelling clays (mainly kaolinite with some illite and smectite), 80% quartz, and 12% feldspar. To reduce the tendency for the clays to disperse, zinc, a bivalent cation, was used. For solutions with cations of valence > 1, at pH $= 7$, no critical salt concentration has been found below which clay is released from Berea sandstone pore walls (Khilar and Fogler, 1984). It is important to recognize that the clay minerals present in the rock have been immobilized by coating the pores with hydrocarbon paraffin. Therefore, the formation factor extrapolated to an electrolyte saturation of unity (i.e., no hydrocarbon paraffin) corresponds to the formation factor of the clean rock without clays and without any surface conduction effects caused by the presence of surface reactive minerals. Formation factor at a paraffin saturation of zero, $F = 18$ (Figure 4.4), has been extrapolated from a plot of the multiplicative inverse of the residual formation factor vs. paraffin saturation. This hypothesis was verified by partially removing clays in a Berea sandstone core by acid treatment with a mixture of 6% hydrochloric and 1.5% hydrofluoric acids (R. Suarez-Rivera, personal communication, 1991). After the core was treated and clays flushed out, the formation factor was found to be 16.4, larger than the average formation factor of 15.7, measured for samples containing clay (Table 4.2).

4.2.4 Effect of surface conductance

To investigate the magnitude of surface conductance contribution due to clays and other surface reactive minerals on formation factor, we investigated the influence of solution concentration on rock electrical conductivity. For that purpose, resistivity experiments were performed on two Berea sandstone cores. The first core was permeated with solutions of zinc nitrate at increasing concentrations of 0.05 M, 0.1 M, and 0.5 M while measurements of resistivity were taken. After equilibrium had been reached with one solution, another zinc nitrate solution of lower resistivity was flowed through the core, and a constant resistance reading was again obtained. To obtain

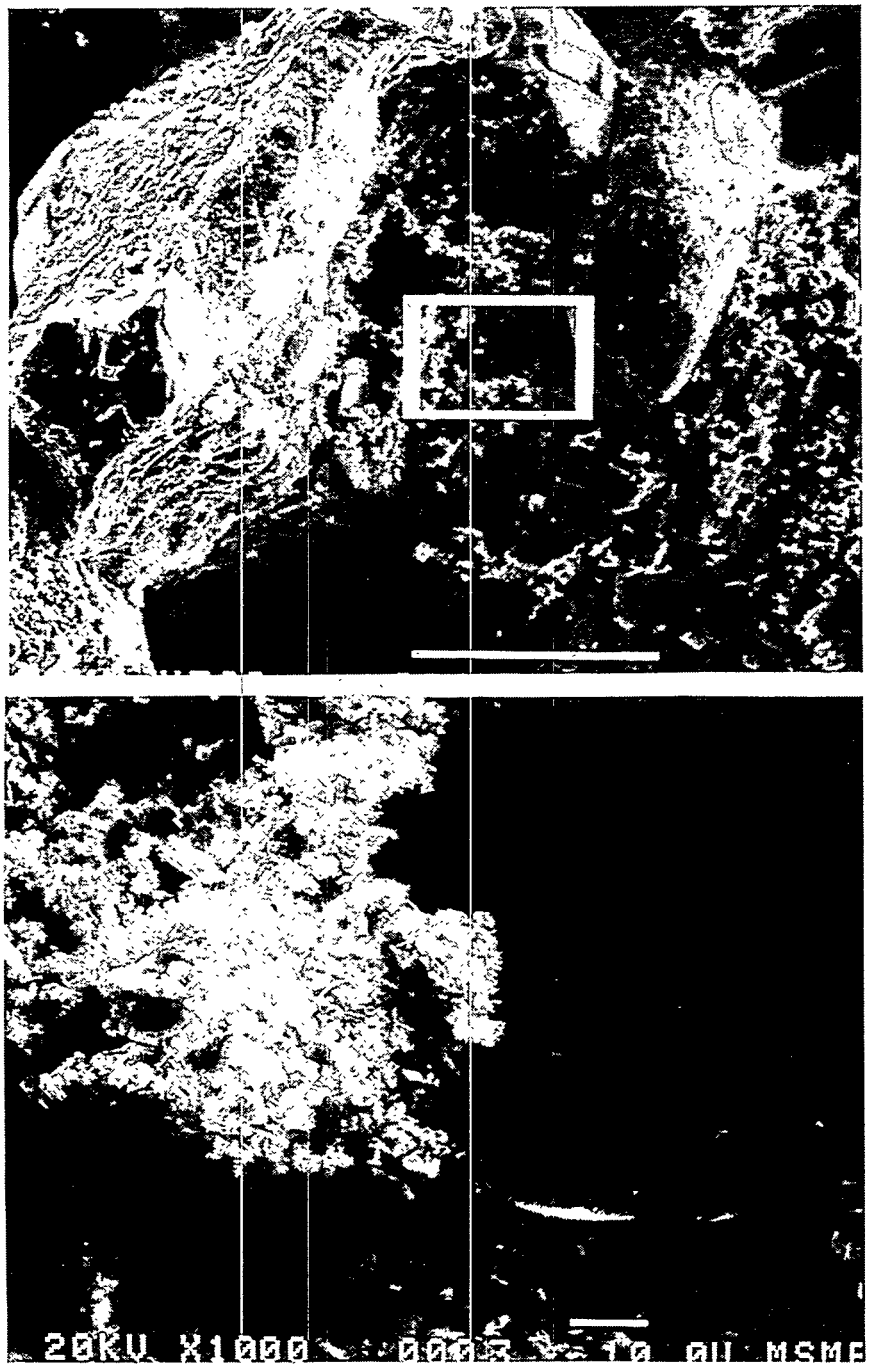

FIG. 4.5: SEM photomicrographs of a Berea sandstone specimen showing the presence of fine-grained clay minerals (mainly kaolinite) partly filling pores between quartz grains.

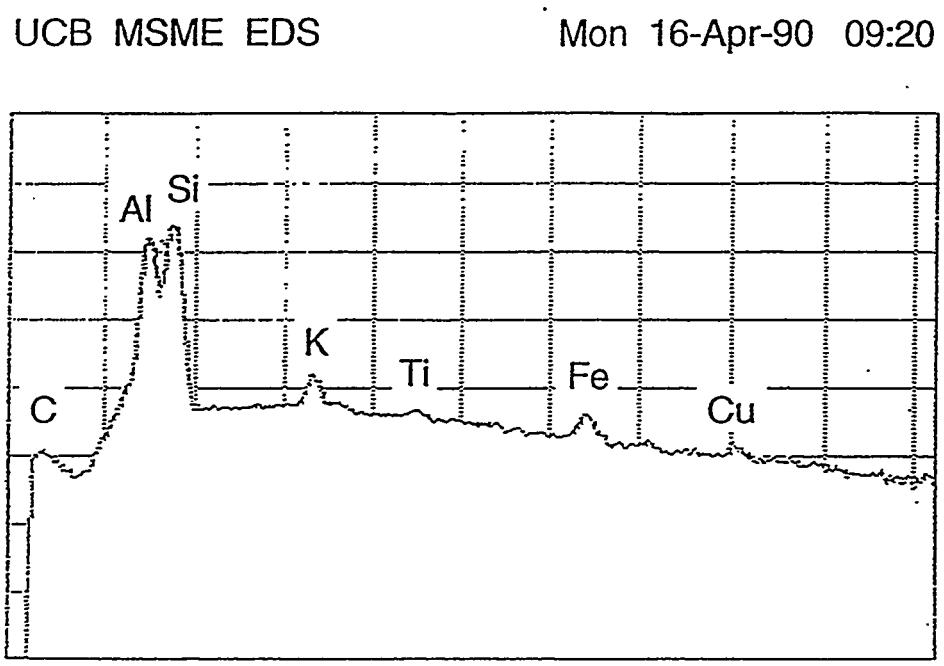

FIG. 4.6: X-ray spectrum of clay minerals coating Berea sandstone sample pores shown in figure 6.4. EDX analysis yielding nearly equal peak heights of Si and Al confirms the identification as kaolinite.

TABLE 4.3: Resistivity data for Berea sandstone with zinc nitrate solution saturating the sample.

M[a]	pH (effluent)	ρ_w^b (ohm-m)	ρ_r^c (ohm-m)
0.5	—	0.19	3.35
0.1	—	0.68	10.4
0.05	—	1.24	20.1
0.01	4.0	5.08	73.9
0.005	4.5	9.01	101

[a]Solution molarity.

[b]Solution resistivity.

[c]Rock resistivity.

a more complete set of electrical conductivities measurements at low electrolyte concentrations, the procedure was repeated on a new core with solutions that included salinities 0.005 M and 0.01 M zinc nitrate (pH of the effluent was found to vary from about 4.5 to about 4.0, respectively). The data thus obtained enabled the formation factor of the rock to be computed and also confirmed the ability of an invading fluid to displace interstitial water from a rock core. The results are given in Table 4.3. The conductivity of the fluid (κ_w) vs. the conductivity of the fully saturated rock (κ_r) data are plotted in Figure 4.7. As observed, minor deviations from the Archie formation factor concept are present at low electrolyte concentration. There is a rapid initial increase in rock conductivity as the solution concentration increased up to about 0.005 M. When the solution in equilibrium was more concentrated than 0.005 M, there was a decrease in rock conductivity with an increase in solution conductivity until a solution concentration of about 0.05 M. Thereafter, the formation factor is constant at least over the range of concentrations studied.

The shape of the (κ_w-κ_r) curve at low electrolyte concentrations may be interpreted in light of the mechanisms and factors controlling clay-fluid interactions as they relate to clay-water electrolytic conduction. Berea sandstone contains mainly kaolinite clay. At $4.0 < \text{pH} < 4.5$, and electrolyte concentrations lower than 0.01 M, experiments in kaolinite clay by Williams and Williams (1978) using sodium cloride as electrolyte (Figure 4.8), show that an increase in solution concentration produces a decrease in ion mobility, and thus a reduction in electrical conductivity. In addition, for clay-water systems, an increase in salt concentration is expected to compress the diffuse double layer, to decrease the electrical interaction between the cations and the clay

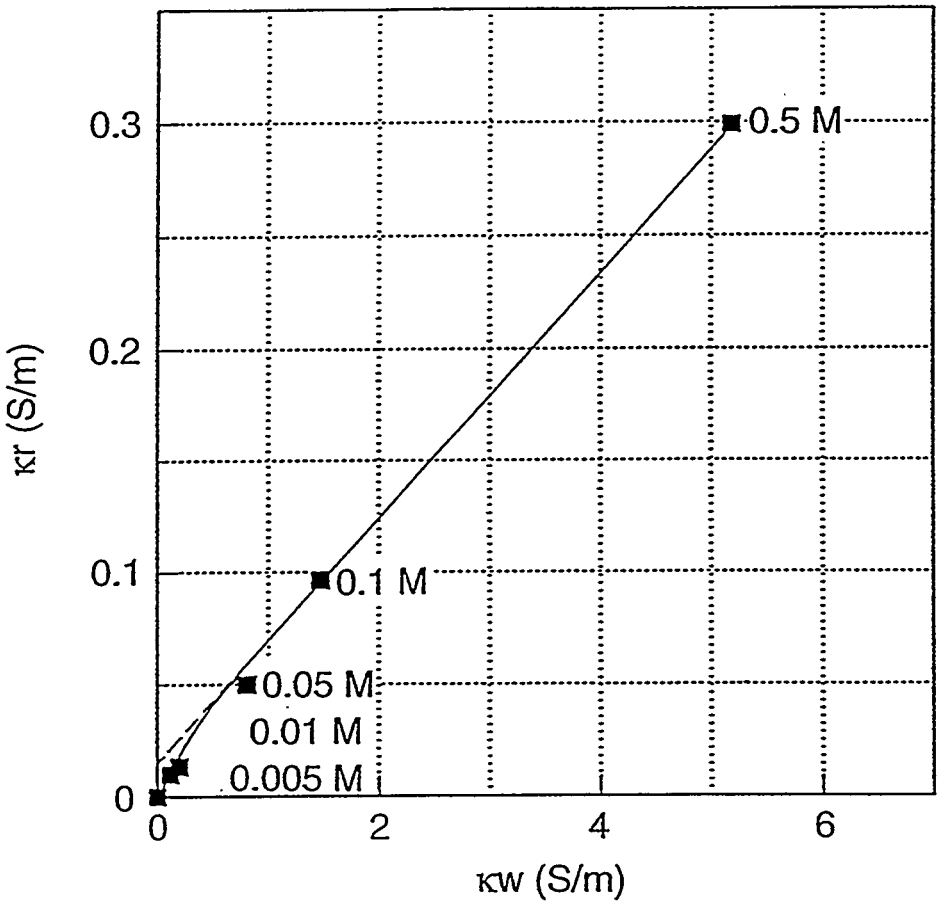

FIG. 4.7: Conductivity data of Berea sandstone at different electrolyte concentrations. Zinc nitrate electrolyte solutions with concentrations 0.005-0.5 M were used.

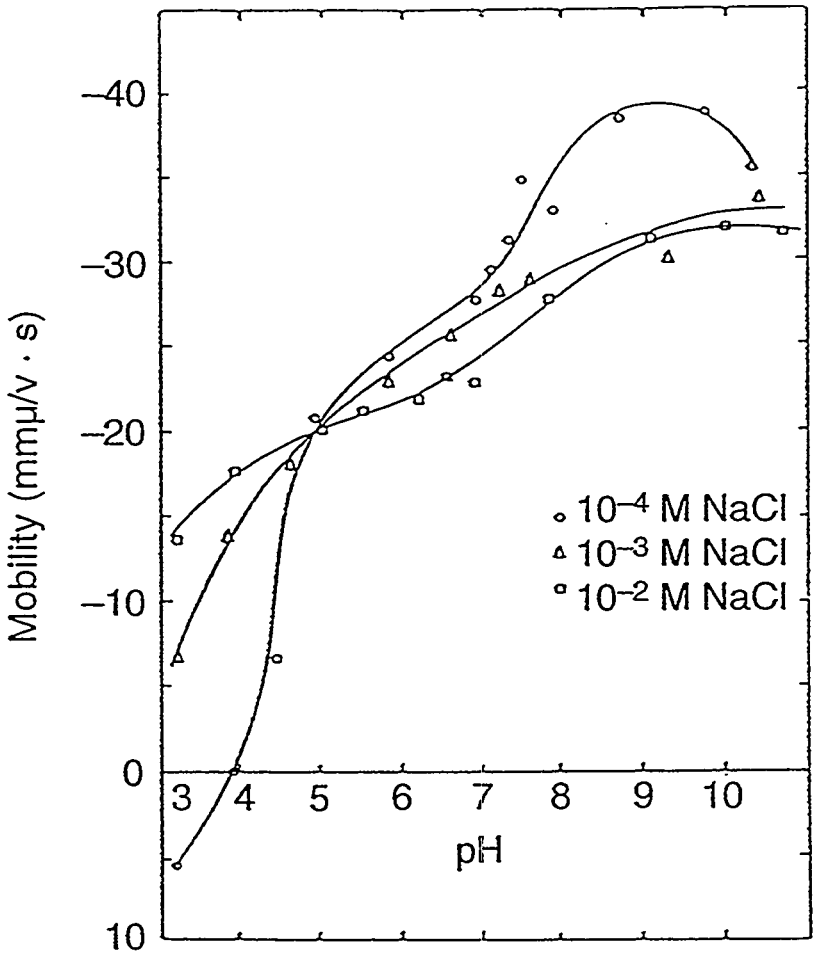

FIG. 4.8: Mobility for kaolinite as a function of salt concentration and pH (after Williams and Williams, 1978).

surface, and to reduce the electrical conductivity. At higher electrolyte concentrations the double layer compresses further, there is a more energetic conductive path through the solution, and the (κ_w-κ_r) plot becomes linear.

The trend of change in rock electrical conductivity at low electrolyte concentrations does reflect the contribution to surface conduction of clays and other surface reactive minerals. However, our experimental results show that for Berea sandstone, the surface conduction component due to clay minerals (mainly kaolinite) represents a minor contribution to overall electrical conductivity, and therefore can be ignored for most applications.

4.2.5 Effect of pore structure and topology

To understand how pore structure and topology control the transport property under consideration, the electrical conductivity data (Figure 4.4) have been studied in light of the wetting-fluid distributions at each saturation regime (Figures 4.9 to 4.11) with the aid of a complete rock pore cast (Figure 4.12) and its associated rock section (Figure 4.13). The rock pore cast was obtained from a rock specimen that had been fully impregnated with Wood's metal alloy and the quartz grains removed by hydrofluoric acid. The rock pore cast and its associated rock section clearly reveal that the pore space is composed of grain-contact porosity (e.g., thin sheets and micropores) and intergranular porosity. Figure 4.9 shows a scanning electron microscope (SEM) photomicrograph collage of a Berea sandstone specimen that has been partially saturated with approximately 20-30% paraffin. The gray phase corresponds to quartz grains, the white phase corresponds to pores that have been impregnated with paraffin, and the black phase corresponds to the remaining pore space, which was filled with blue epoxy for imaging purposes. Paraffin has invaded mainly grain-contact pore space (i.e., thin sheets and micropores) and intergranular pore space connected by smaller throats but has only coated the available intergranular channels connected by larger throats. A substantial effect on effective formation factor is observed. Therefore, the fraction of the pore structure connected by smaller constrictions (e.g., grain-contact pore space) provides important alternative routes to intergranular conduits connected by larger throats for the ions to travel.

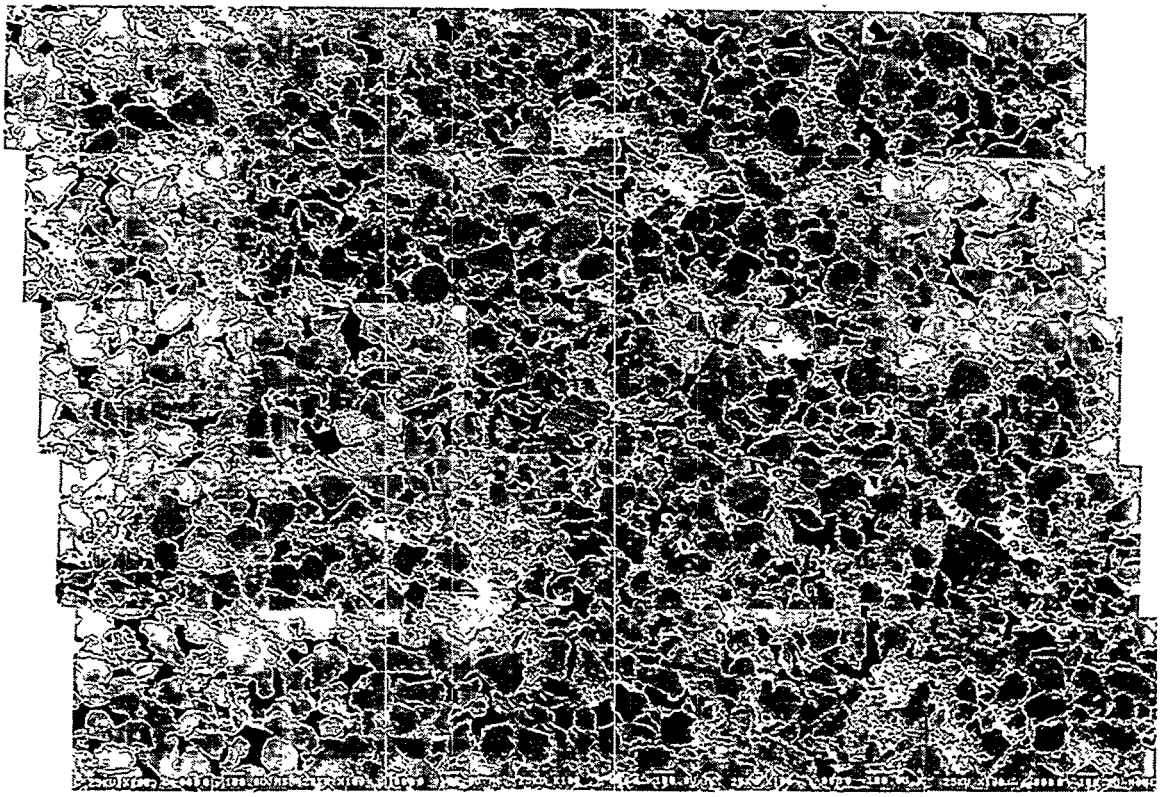

FIG. 4.9: SEM photomicrograph collage of a Berea sandstone specimen impregnated with approximately 20-30% paraffin. The actual width of field is about 6 mm. The gray phase is quartz grains, the white phase is pores saturated with paraffin, and the black phase is remaining pores filled with blue epoxy for imaging purposes.

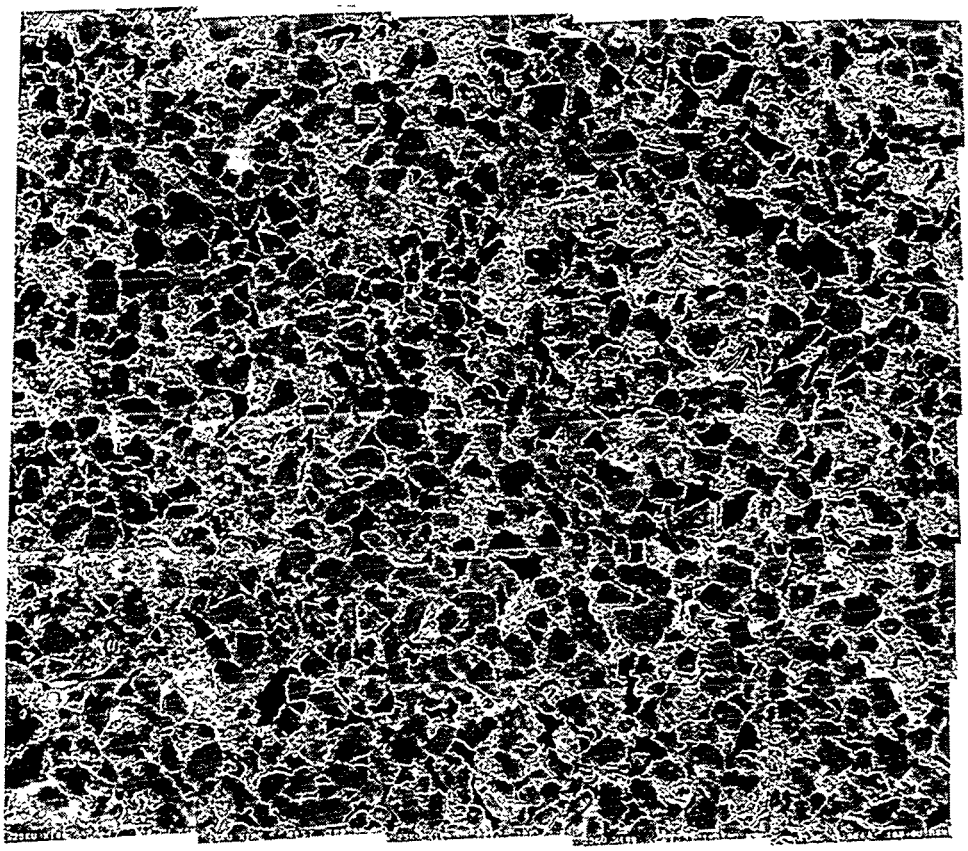

FIG. 4.10: SEM photomicrograph collage of a Berea sandstone specimen impregnated with approximately 40-50% paraffin. The actual width of field is about 6 mm. The gray phase is quartz grains, the white phase is pores saturated with paraffin, and the black phase is remaining pores filled with blue epoxy for imaging purposes.

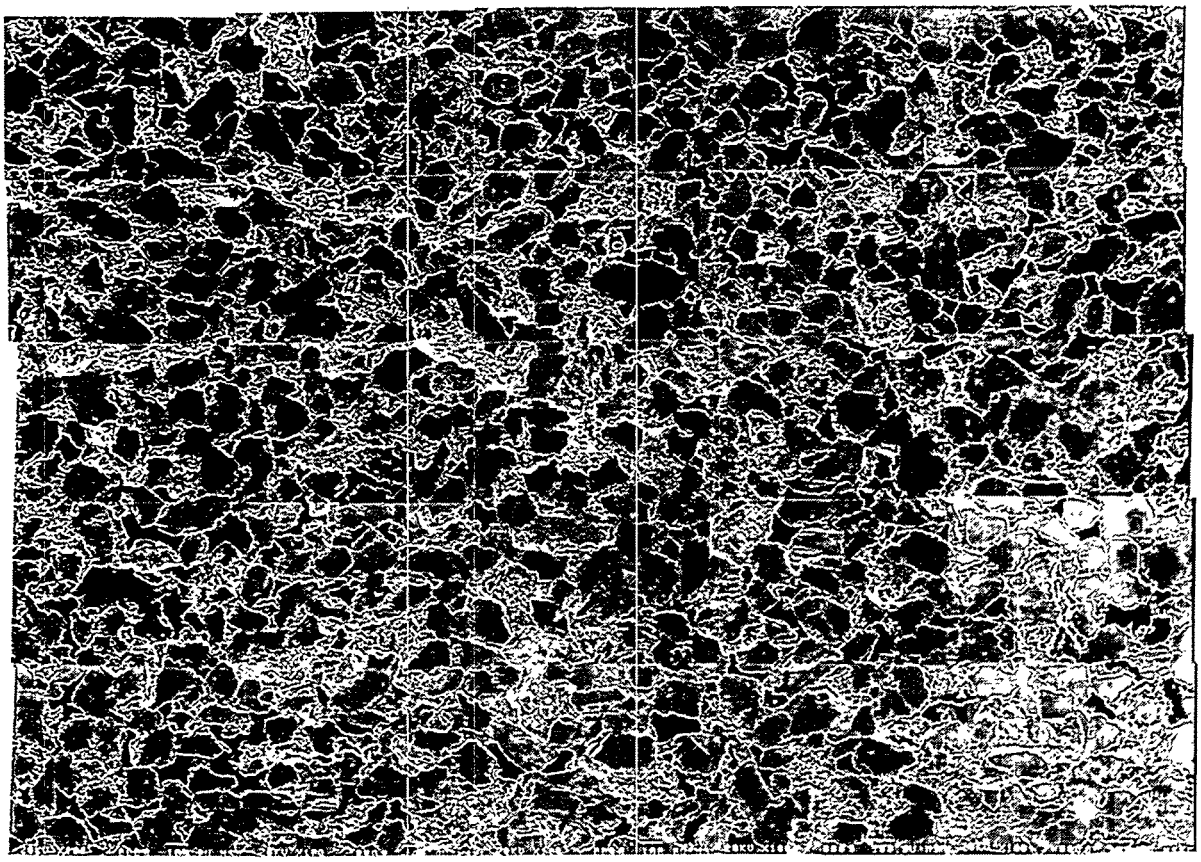

FIG. 4.11: SEM photomicrograph collage of a Berea sandstone specimen impregnated with approximately 60-70% paraffin. Actual width of field is about 6 mm. The gray phase is quartz grains, the white phase is pores saturated with paraffin, and the black phase is remaining pores filled with blue epoxy for imaging purposes.

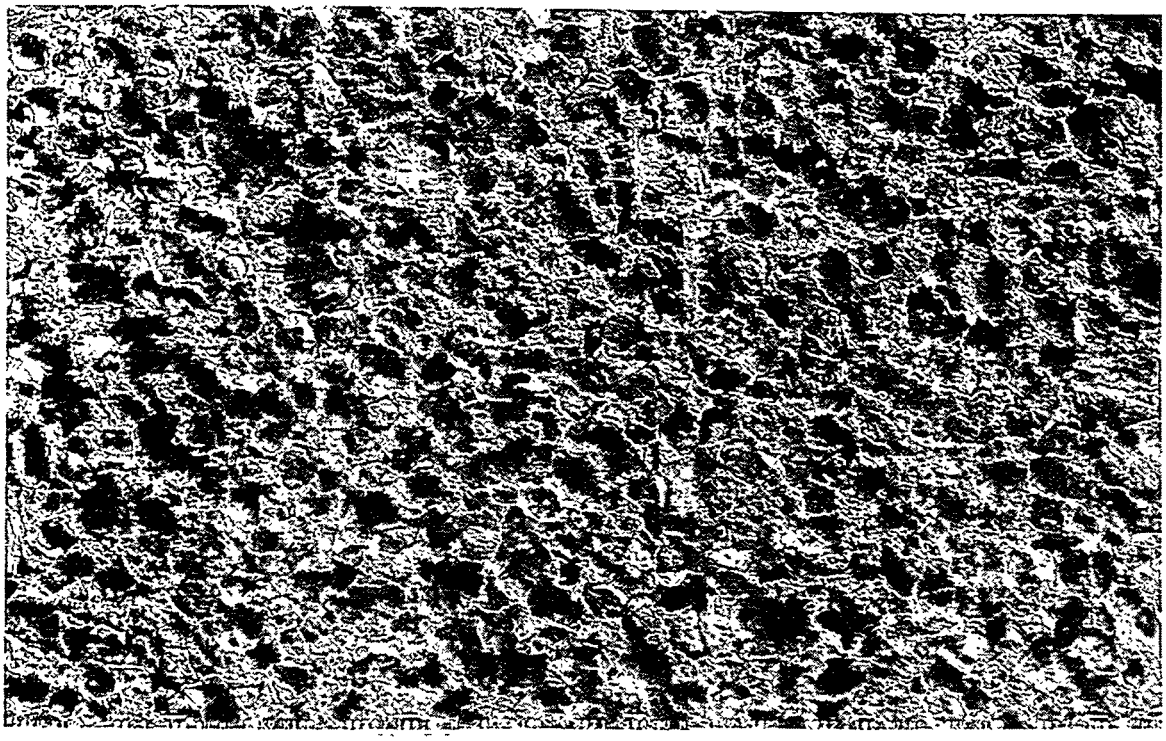

FIG. 4.12: SEM photomicrograph collage of a Berea sandstone pore cast. Actual width of field is about 6 mm. The rock pore space was completely filled with Wood's metal alloy and the quartz grains removed by hydrofluoric acid to allow direct observation of the pore structure.

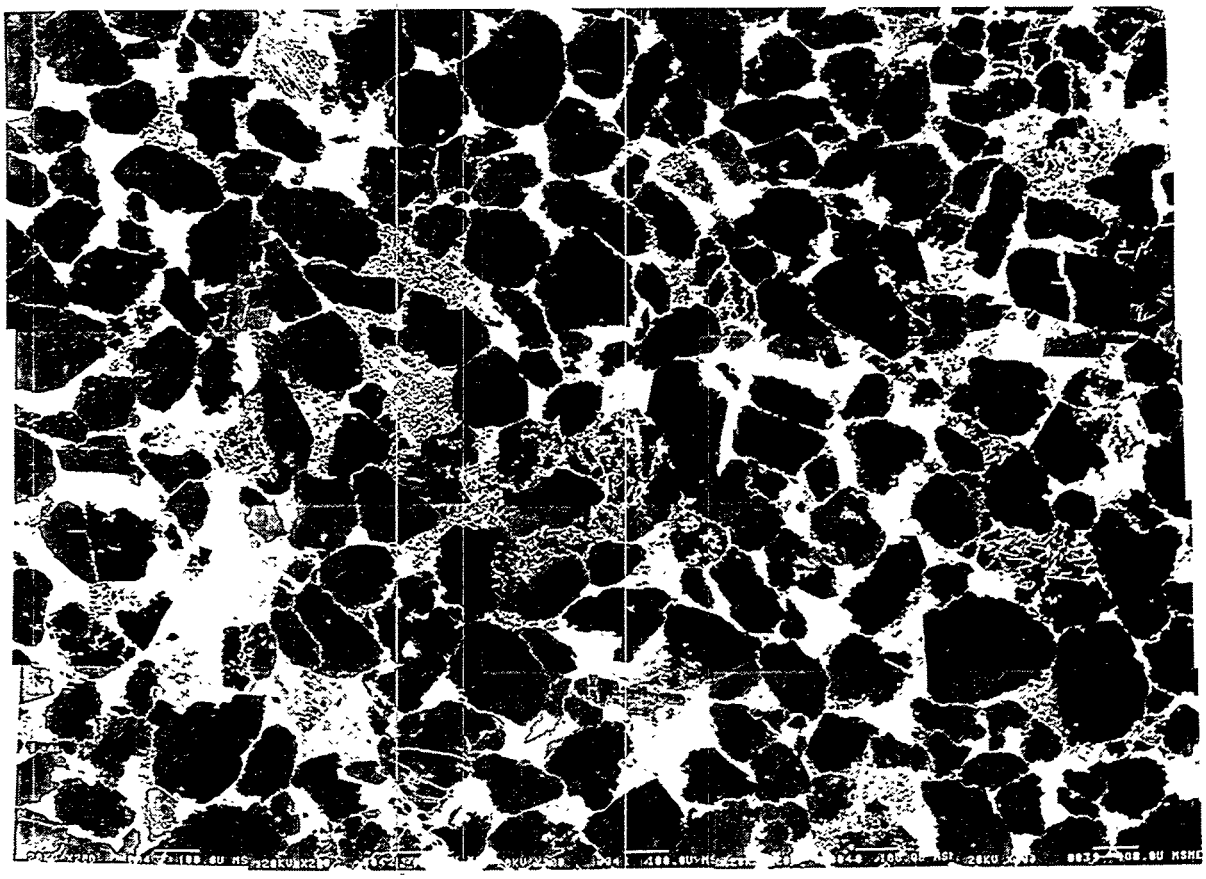

FIG. 4.13: SEM photomicrograph collage of a Berea sandstone sample fully impregnated with Wood's metal alloy. Actual width of field is about 3 mm. The gray phase is quartz grains, and the white phase is pores saturated with the alloy. The section reveals that the pore space is composed of grain-contact porosity (i.e., thin sheets and micropores) and intergranular porosity.

Figure 4.10 shows an SEM photomicrograph collage of a rock specimen partially saturated with approximately 40-50% paraffin. At this stage, we are filling intergranular conduits connected by the larger throats, and a portion of the electrolyte has apparently lost continuity as the paraffin saturation is increased over $\sim$ 30%, so that the resistivity increases at a faster rate. A still larger effect on effective formation factor is observed. Figure 4.11 shows an SEM photomicrograph collage of a rock specimen partially saturated with approximately 60-70% paraffin. We have filled almost all intergranular conduits connected by larger throats. A few intergranular pores not well connected still remain unfilled. When paraffin saturation is $\sim$ 70%, the whole pore structure behaves as though it was disconnected.

4.2.6 The saturation exponent in Archie's law

Electrical conductivity data presented in Figure 4.4 (case B) have been replotted on a logarithmic scale for the effective formation factor vs. electrolyte saturation (Figure 4.14). To understand their physical significance, we have divided the plot into three zones: zone I, a linear zone of electrolyte saturations between about 0.7 (S_{crit}) and 1, with an Archie exponent of n $\sim$ 3; zone II, a linear zone between electrolyte saturations of about 0.5 and 0.7, with an Archie exponent of n $\sim$ 5; and zone III, a zone of electrolyte saturations less than 0.5. Zone I, with an Archie saturation exponent of $\sim$ 3, reflects the fact that grain-contact pore space (i.e., thin sheets and micropores) and intergranular pore space connected by the smaller throats provide important alternate paths to intergranular conduits connected by larger throats for the ions to travel. Zone II, with an Archie saturation exponent of $\sim$ 5, reflects the fact that as the electrolyte saturation is lowered below S_{crit}, part of the rock structure composed of pores connected by the smaller throats becomes inactive. In addition, intergranular conduits connected by larger throats start being filled and partially filled with paraffin wax. Thus part of the electrolyte available for the transport of ions loses continuity and the resistivity is increased at a faster rate.

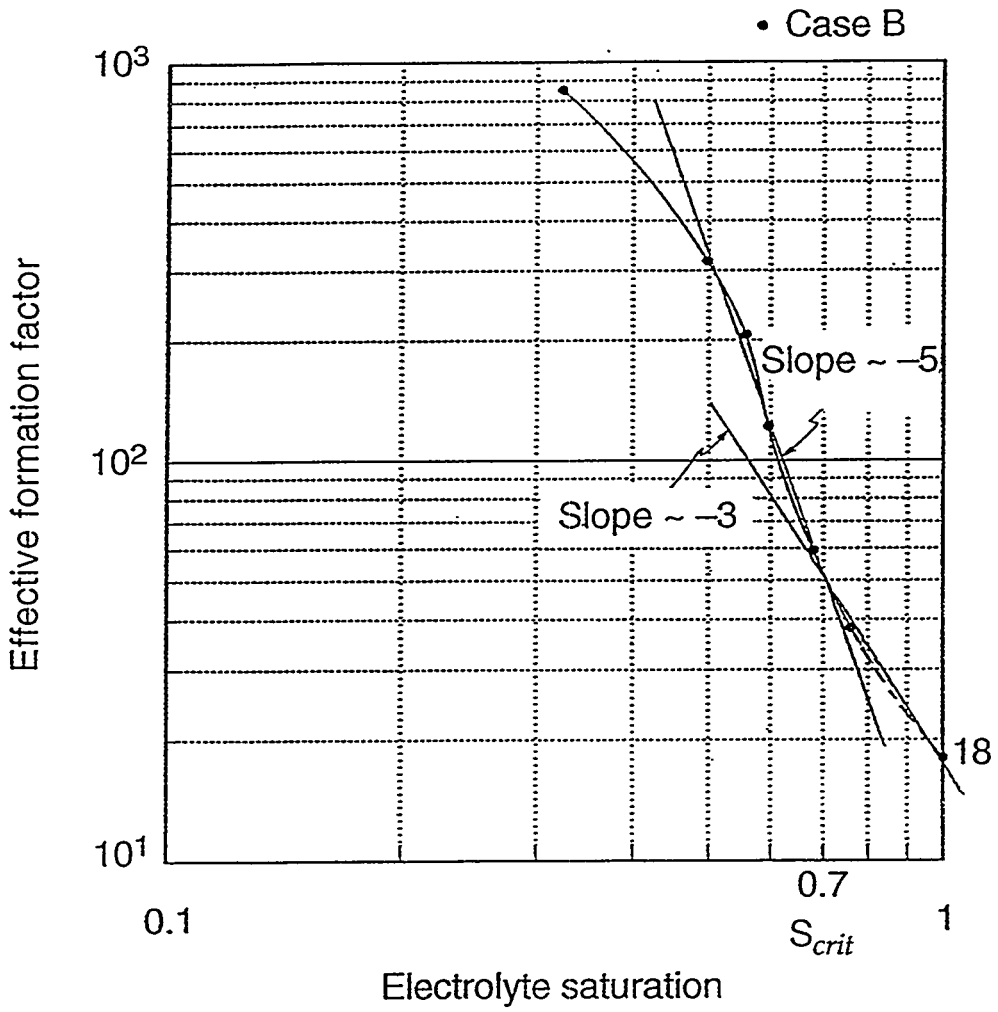

FIG. 4.14: Effective formation factor vs. electrolyte saturation for Berea sandstone (case B). The pore space was partially saturated with hydrocarbon paraffin, with the remainder of the pore space filled with a 0.5-M zinc nitrate solution.

4.2.7 Results and discussion

Formation factor of a partially saturated rock with a wetting phase is controlled by the rock structure and topology as well as the physics and chemistry of mineral-fluid interactions. To understand the relationships, we have measured the effective formation factor with an electrolyte in the pore spaces not occupied by a wetting fluid (paraffin wax) after solidifying the fluid in place. It is important to recognize that when the rock is partially saturated with the hydrocarbon paraffin, the clay minerals present in the rock pore space are immobilized. Thus formation factor extrapolated to an electrolyte saturation of unity (and paraffin saturation of zero), $F = 18$, corresponds to the formation factor of the 'clean' rock (e.g., without clay). Even though the change in the trend of rock electrical conductivity at low electrolyte concentrations does represent the contribution of surface conduction due to clays, this contribution is negligible.

Effective formation factor data have been studied in light of the wetting-phase distribution observed at different saturations with the aid of a complete pore cast and its associated rock section. Our analysis shows that (1) $\sim$ 30% of the pore space consists of grain-contact pores (i.e., thin sheets and micropores) and intergranular pores connected by smaller throats, (2) $\sim$ 40% of the pore space comprises intergranular conduits composed of pores connected by larger throats, and (3) $\sim$ 30% of the intergranular pore space remains disconnected. The grain-contact pore space of large surface areas (thin sheets), micropores, and intergranular pores connected by smaller throats provide important alternate paths to the intergranular conduits connected by larger throats for the ions to travel. Therefore, for a consolidated rock such as Berea sandstone, we find no unique relationship between effective formation factor and electrolyte saturation, nor do we find a unique definition of the Archie saturation exponent, n, for the full range of saturation (Figures 4.4 and 4.14). Finally, the Archie saturation exponent n is found to vary from approximately 3 when connected grain-contact pore space (i.e., thin sheets and micropores) and intergranular pores connected by smaller throats are filled with hydrocarbon paraffin to approximately 5 when intergranular conduits connected by the larger throats are filled with hydrocarbon paraffin, with a critical electrolyte saturation (S_{crit}) of 0.7.

4.3 Comparison of analytical and experimental results

We have employed a simple cubic lattice-network model of electrical conductivity utilizing a smooth representation of the intergranular pore space (e.g., in between the grains). With this model we have found that the same pore system is responsible for both electrical and hydraulic properties of a lightly consolidated rock such as Saint-Gilles sandstone. Moreover, for a heavily consolidated rock such as Berea sandstone, we found that the pore space responsible for hydraulic properties is not responsible alone for electrical properties. The results from the cubic lattice-effective medium model suggest that it is mainly the electrolyte presence at the contacts that is important, and that the uniform coverage with electrolyte elsewhere on the grain surfaces has no part in determining electrical properties.

The importance of grain contacts on electrical properties led us to investigate the role of grain contacts in the electrical resistivity of a consolidated rock such as Berea sandstone. Experimentally it was found that an addition of 20% of an insulating wetting fluid (paraffin wax) to these contacts causes a dramatic increase in resistance, suggesting that grain contacts are a dominant factor in the electrical behavior of consolidated sandstones. It was also found a distinct change in the resistivity variation at the transition from surface to bulk electrolyte behavior in Berea sandstone. (Fig. 4.14), implying that the grain-contact conductivity component can be added to the intergranular one.

The fact that the electrical properties change substantially with the addition of only 20% of an insulating wetting fluid suggests that the electrolyte at the grain contacts may also play an important role in electrical properties, i.e., act as bottlenecks, in the electrical conduction process of consolidated rocks. In order to accurately predict electrical conductivity or formation factor of sedimentary rocks from microgeometry one must rigorously superimpose the resistivity of the electrolyte at the grain contacts to the resistivity of the electrolyte in the intergranular pore space.

5 PREDICTING THE CAPILLARY PRESSURE OF BEREA SANDSTONE FROM MICROSTRUCTURE

In this study, an attempt has been made to understand, through analysis and experiment, how the capillary pressure saturation relationship is controlled by the rock pore structure and the distribution of wetting and nonwetting phases in the pore space. For this purpose, we have made analytical calculations of capillary pressure on the basis of pore microgeometry. As a zero-order approximation, we have idealized the porous medium as consisting of an assembly of parallel capillaries of arbitrary cross sections. Recall, for example, that the 'principal' pore network of Berea sandstone approaches microscopic homogeneity, and that in this case the parallel-tube model is approximately valid for the prediction of permeability (Chapter 3.3). The mathematical expression for capillary pressure as a function of saturation depends on the distribution of pore hydraulic radii and the area-perimeter power-law relationship of pores (Chapter 3). Two-dimensional scanning electron microscope photomicrographs of rock cross sections have been employed to measure directly the areas, perimeters, and hydraulic radii of the individual pores. These quantities have been measured directly from two-dimensional SEM photomicrographs of rock sections. Account is taken of the fact that the cross sections are randomly oriented with respect to the channel axes. The predictions of our model are compared with laboratory capillary pressure curves obtained with a technique using Wood's metal alloy as the nonwetting phase instead of conventional mercury porosimetry. This technique allows for direct examination and analysis of the fluid distributions in the rock pore space.

5.1 Description of analytical model

In two-phase conditions, the capillary pressure between wetting and nonwetting phases in a circular tube of radius r is given by Laplace's equation (Scheidegger, 1974)

$$P_c = \frac{2\varsigma \cos\alpha}{r}, \tag{142}$$

where ς is the surface tension between wetting and nonwetting phases and α the contact angle between the wetting phase meniscus and the tube wall.

TABLE 5.1: List of comparative values to show equivalence of the reciprocal hydraulic radius ($1/R_H$) and the reciprocal mean radius of curvature [$(1/r_1)+(1/r_2)$] in a capillary (r_i is the radius of the inscribed circle) (after Carman, 1941).

Cross-section		$(1/r_1)+(1/r_2)$	$1/R_H$
Circle		$2/r$	$2/r$
Parallel plates		$1/b$	$1/b$
Rectangle		$1/a+1/b$	$1/a+1/b$
Equilateral triangle		$2/r_i$	$2/r_i$
Square		$2/r_i$	$2/r_i$
Ellipse	$a:b=2:1$	$1.50/b$	$1.54/b$
	$a:b=5:1$	$1.20/b$	$1.34/b$
	$a:b=10:1$	$1.10/b$	$1.30/b$

If the capillaries are not circular, the equation for the capillary pressure has to be generalized by replacing $2/r$ by $(1/r_1)+(1/r_2)$ (Scheidegger, 1974):

$$P_c = \varsigma\left(\frac{1}{r_1}+\frac{1}{r_2}\right), \tag{143}$$

where r_1 and r_2 are the principal radii of curvature of the meniscus.

If the pore openings are not of a simple geometric form, Eq. (143) is still a valid expression for the capillary pressure. To obtain a theoretical relationship between the saturation and capillary pressure for a porous medium, an analytical expression for the average interfacial curvature as a function of saturation has to be found. This is a very difficult task.

5.1.1 Effect of cross-sectional pore shape

Schultze (1925 a,b) has shown experimentally that the capillary pressures for such capillaries under the assumption of zero contact angle are given approximately by the equation

$$P_c = \frac{\varsigma}{R_H}, \tag{144}$$

where R_H is the ratio of area to perimeter of the capillary. A list of comparative values for testing Eq. (144) is given in Table 5.1 (Carman, 1941). Since Eq. (144)

gives a reasonably accurate prediction of capillary pressure in non-circular capillaries, it can be assumed to be applicable to the capillary channels in a porous medium (Scheidegger, 1974).

5.1.2 Capillary pressure analysis

In our model, it is assumed that there is no accessibility problem; i.e., regardless of the spatial arrangement of pores, the pores are occupied by the nonwetting phase in the order of largest pores first. Similarly, for the wetting phase, the pores are occupied by the wetting phase in the order of smallest pores first. Therefore, given a hydraulic radius distribution of intergranular pore space $\beta(R_H)$, and assuming that the pores are filled by the wetting phase in ascending order up to a cut-off radius $R_H^{'}$, we may write the saturation of the wetting phase $S_w(R_H^{'})$ as (Appendix B)

$$S_w(R_H^{'}) = \frac{\int_0^{R_H^{'}} A(R_H)\beta(R_H)dR_H}{\int_0^{\infty} A(R_H)\beta(R_H)dR_H} , \tag{145}$$

where the pore hydraulic radius is defined as the ratio of the pore area A to the pore perimeter P.

Measurements of hydraulic radius of intergranular pore space obtained from 2-D SEM photomicrographs of Berea sandstone rock sections have been found to follow a skewed distribution that is well approximated by a log-normal distribution. The log-normal distribution is given by the following expression (hydraulic radius $R_H \geq 0$) (Appendix B):

$$\beta(R_H) = \frac{1}{\sqrt{2\pi}\sigma \ln 10} \frac{1}{R_H} \exp\left(\frac{-[\log R_H - \log R_{H_o}]^2}{2\sigma^2}\right) , \tag{146}$$

where R_{H_o} is the most probable hydraulic radius, and σ the variance of $\log R_H$. The corresponding mean hydraulic radius R_{H_m} is larger than the most probable hydraulic radius; it is

$$R_{H_m} = R_{H_o} \exp\left(\frac{[\sigma \ln 10]^2}{2}\right) . \tag{147}$$

Invoking the perimeter-area power-law relationship (Eq. 87) gives

$$A = mP^{\gamma} ,$$

where $\log m$ is the intercept on the $\log A$ axis, and γ the non-integer slope of the $\log A$-$\log P$ plot. The area can be expressed in terms of the hydraulic radius as follows:

$$A(R_H) = m^{\frac{1}{1-\gamma}} R_H^{\frac{\gamma}{\gamma-1}} . \tag{148}$$

Expressed in terms of the cutoff hydraulic radius, Eq. (145) becomes

$$S_w(R_H^{'}) = \frac{\int_0^{R_H^{'}} R_H^{\frac{\gamma}{\gamma-1}} \beta(R_H) dR_H}{\int_0^{\infty} R_H^{\frac{\gamma}{\gamma-1}} \beta(R_H) dR_H} . \tag{149}$$

Integrating Eq. (149) yields

$$S_w(R_H^{'}) = \frac{1}{2}\left(1 + erf\left[\frac{(\log R_H^{'} - \delta)}{\sqrt{2\sigma^2}}\right]\right) , \tag{150}$$

where the cut-off hydraulic radius is given by

$$R_H^{'} = 10^{\delta - \sqrt{2\sigma^2} erfi(1-2S_w)} , \tag{151}$$

where $\delta = \sigma^2 \ln 10(\frac{\gamma}{\gamma-1}) + \log R_{H_o}$, σ is the variance of $\log R_H$, and erf and $erfi$ are the error and the inverse error function, respectively. The capillary pressure is then given by

$$P_c = \frac{\varsigma}{R_H^{'}} = \varsigma 10^{\sqrt{2\sigma^2} erfi(1-2S_w(R_H^{'})) - \delta} . \tag{152}$$

Capillary pressure is specific to the nature of the two fluids involved. If no specification is made, it is understood that the displaced fluid is vacuum. If the displaced fluid is a vacuum, and the external pressure P_c is applied in a nonwetting fluid, then all capillaries with with a radius larger than $R_H^{'}$ will be totally filled.

5.1.3 Effect of pore orientation

In the two-dimensional sections under consideration, however, the measured areas and perimeters will not be identical to the actual areas and perimeters of the pore cross sections cut perpendicular to the channel axes. The orientation effect has been corrected by means of the following geometrical and stereological considerations, which are exact for the case of circular cross sections (Chapter 3.1.4).

For the hydraulic radius,

$$(R_H)_{actual} = \frac{\sqrt{2}}{2}\left\langle \frac{1}{\sqrt{1+\cos^2\theta}} \right\rangle^{-1} (R_H)_{measured} = 0.85(R_H)_{measured}\,, \qquad (153)$$

where the brackets denote a spherical average for pores of random orientation.

5.2 Experimental imbibition with Wood's metal

In this experimental investigation, we have sought to examine the relationship between the microscopic pore occupancy by the nonwetting fluid and its effect on capillary pressure. We have used three-dimensional imbibition of a nonwetting Wood's metal alloy instead of the conventional mercury porosimetry. This technique offers the advantage of allowing analysis of the occupied pore space after the experiment. Wood's metal is an alloy of approximately 43% Bi, 38% Pb, 11% Sn, and 9% Cd, with a specific gravity of 9.6, a viscosity of about 1.3 $\times 10^{-3}$ Pa·s at 75°C, and a surface tension of about 400 mN/m (Yadav et al., 1987). The setup for the three-dimensional imbibition experiments is shown in Figure 5.1. It consists of a metallic container of Wood's metal placed in a metal vacuum chamber provided with a lucite window and surrounded by a heating element to keep the metal molten. The melting point varies from about 50°C to 70°C, depending on its composition. A micrometer is attached to the metallic container to determine the pressure at which the Wood's metal first enters the specimen. The 50 mm-long and 50 mm-diameter sandstone sample is first oven-dried, and then immersed in the molten Wood's metal in the metallic container and placed in the metal vacuum chamber. Then the sample is de-aired by applying a full vacuum for about 60 minutes, until no air bubbles are observed through the lucite

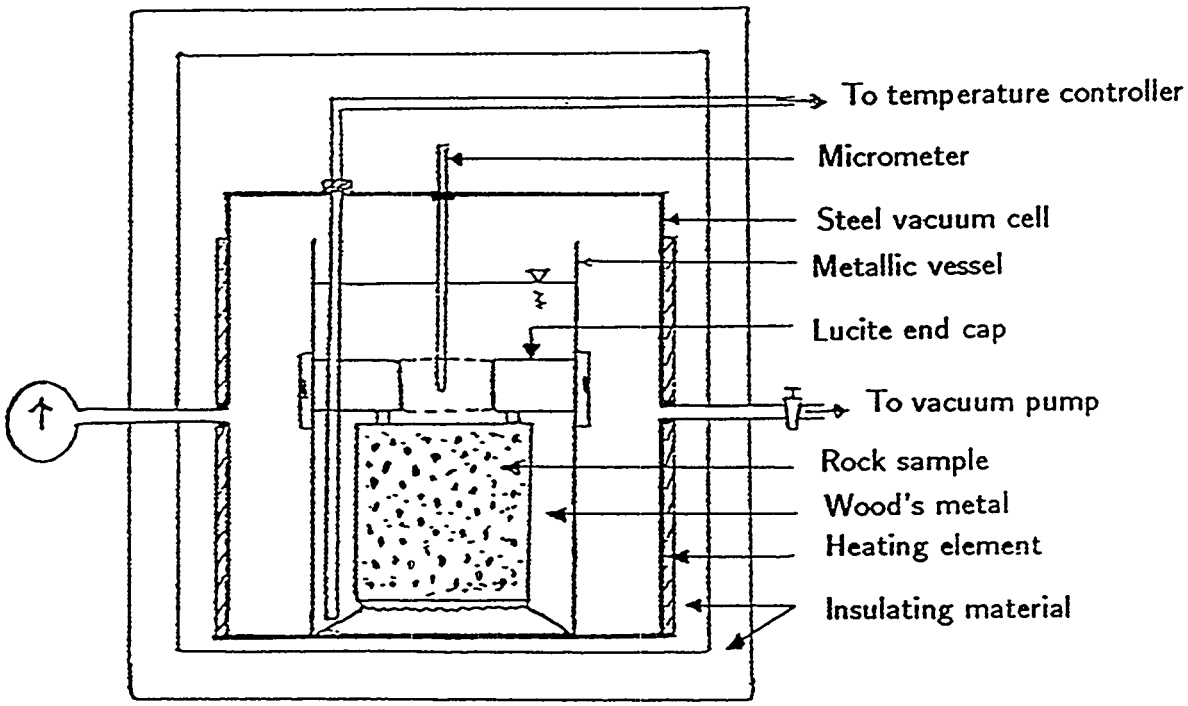

FIG. 5.1: Experimental setup for three-dimensional Wood's metal imbibition.

window. A sub-atmospheric pressure is applied by drawing a partial vacuum, which is maintained at the desired value by a regulating valve until capillary equilibrium is achieved. Each sample was allowed to imbibe for approximately 90 minutes at a fixed pressure, and until no movement of Wood's metal was noticed through the lucite window. At a pressure of about 5-6 psia, the micrometer signaled the first indication of Wood's metal entering the pore space (probably an edge effect on the sample sides). The capillary pressure experiment was repeated on several samples by applying pressure in the range of approximately 6 to 14 psia. The imbibed samples were cut into four axial quarters, each of which had a different saturation. To minimize the effect of gravity, we took the top quarter of each imbibed specimen at a particular equilibrium pressure and measured its saturation.

Figure 5.2 shows the experimental capillary pressure curve obtained when partially saturating the rock with the nonwetting fluid. Fluid saturation increases rather sharply with a corresponding small increase in capillary pressure in the saturation range from about 10 to 50%. Our result is consistent with typical capillary pressure curves based on conventional mercury porosimetry saturation for Berea (BE-1) sandstone (Figure 5.3). Berea (BE-1) sandstone has almost the same macroscopic properties as the Berea sandstone we used in our experiments (e.g., porosity of 22%, permeability to N_2 of 400 mD, and a formation factor of 15.5).

5.2.1 Examination of Wood's metal distribution in the pore space

To understand how pore structure and topology control the physical property under consideration, we have studied the capillary pressure data in light of the nonwetting fluid distributions observed at each equilibrium pressure. For this purpose, optical and scanning electron microscopic examinations of the tops of samples (after cutting off 3 mm) have provided valuable insights into the pore-level complexity of the natural porous media. Figure 5.4 shows an optical photograph of the fluid distributions obtained in top axial quarters (top and bottom) in the pressure range 6.8 to 7.7 psia. It is observed that the nonwetting fluid flow network is composed of a set of imbibing clusters correlated in space. At every pressure step, the nonwetting fluid resides in the pores accessible through throats with a radius larger than that corresponding to the current equilibrium capillary pressure. As the pressure

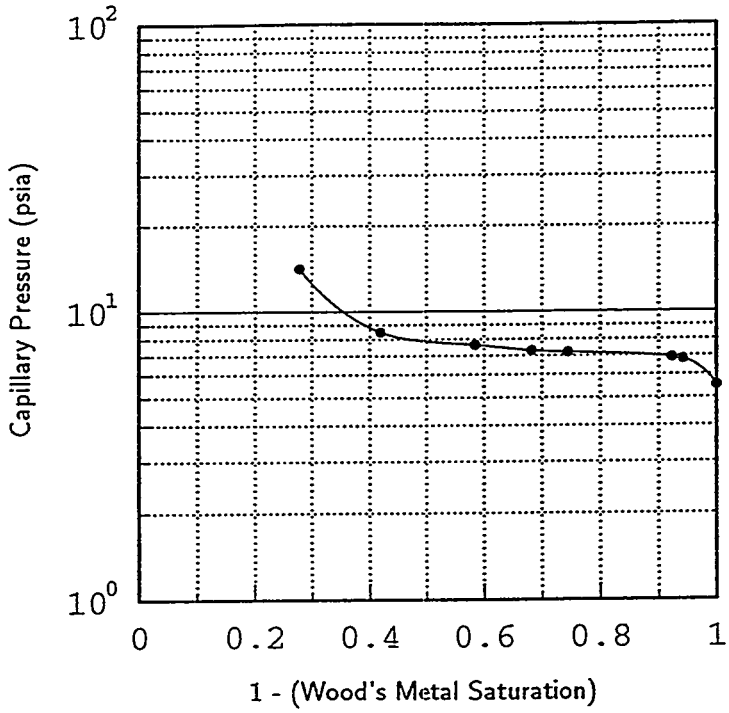

FIG. 5.2: Experimental capillary pressure function of Berea sandstone. The rock has been impregnated with a nonwetting fluid (Wood's metal) at different equilibrium pressures and solidified in place. The procedure allows for direct observation and analysis of the fluid distribution at a fixed pore pressure and saturation level.

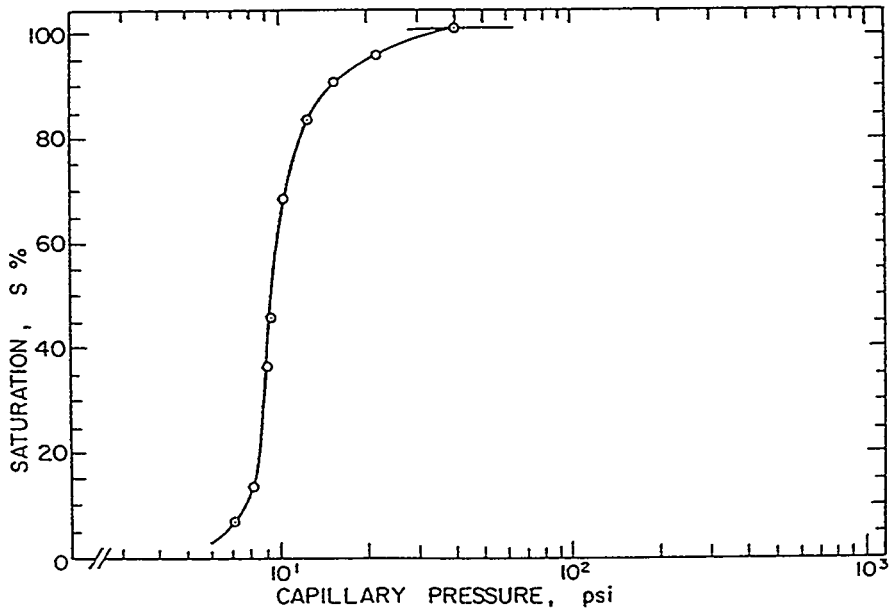

FIG. 5.3: Experimental mercury porosimetry saturation curve of Berea sandstone (after Chatzis and Dullien, 1977).

increases, the nonwetting phase saturation increases and the nonwetting fluid invades successively smaller pores and becomes connected to regions which were separated from this phase by small throats. Optical photograghs of enlarged fluid distributions in top axial quarters obtained by partially saturating the rock with Wood's metal at equilibrium pressures of 6.8, 6.9, and 7.2 psia are presented in Figures 5.5, 5.6, and 5.7, respectively. At 6.8 psia (Figure 5.5), the fluid has preferentially penetrated the sample sides. The saturation is greatest near the perimeter of the sample and least at the center. This observation suggests that pores near the cylindrical surface of the sample are better connected than those towards the center. This interconnection could arise from exposure of pores where they intersect the surface, or from damage adjacent to this surface. At 6.9 psia (Figure 5.6), a saturation gradation is observed in the direction of flow at this pressure (preferentially horizontal). The longer flow paths are connected by smaller constrictions, so fewer flow channels lead to the sample center starting from all available channels at the sample surface. At pressures of 7.2 psia (Figure 5.7) and greater, the nonwetting fluid invades more and more smaller pores, becoming connected to regions that were separated to this phase by smaller pores, and the clusters of nonwetting phase become larger and larger. Figure 5.8 shows an SEM photomicrograph collage of a 1 in $\times$ 1 in rock specimen saturated with approximately 50% of Wood's metal at 8.5 psia equilibrium pressure. An SEM photomicrograph collage of an enlarged partial section from the last figure and its associated pore contours areas (Figure 5.9), show that there are many large (intergranular) pore segments connected by small throats that do not contribute to the flow of the nonwetting phase in the rock. In addition, the grain-contact pore space (i.e., thin sheets and micropores) does not contribute, either. Furthermore, simple statistical analysis of pore contour areas obtained from Figure 5.9 has shown that relatively few conduits connected by large intergranular throats carry up to about 50% of the nonwetting fluid in the porous media under consideration, producing a clustered structure.

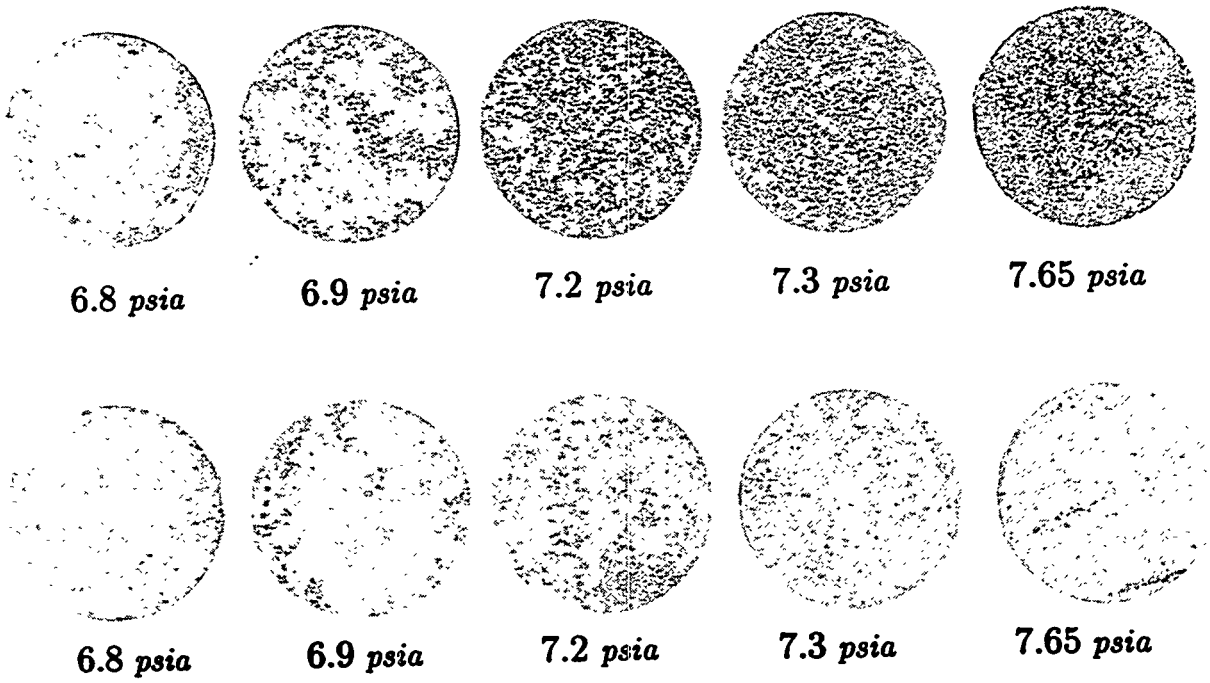

FIG. 5.4: Top and bottom axial quarter sections of Berea sandstone core partially saturated with a nonwetting fluid (Wood's metal) at different equilibrium pressures and solidified in place. The procedure allows for direct observation and analysis of the fluid distribution at a fixed pore pressure and saturation level. The sections reveal that the fluid distributions are composed of a set of imbibing clusters correlated in space.

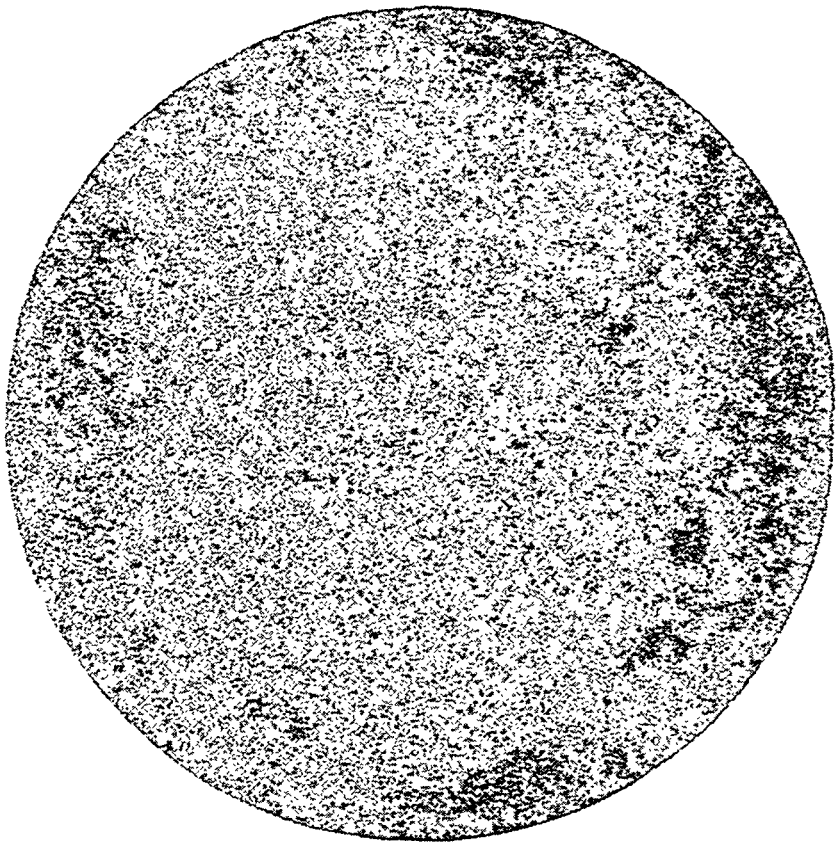

FIG. 5.5: Top section of a Berea sandstone core partially saturated with a nonwetting fluid (Wood's metal) at an equilibrium pressure of 6.8 psia and solidified in place. The procedure allows for direct observation and analysis of the fluid distribution at this pressure and correspondent saturation level.

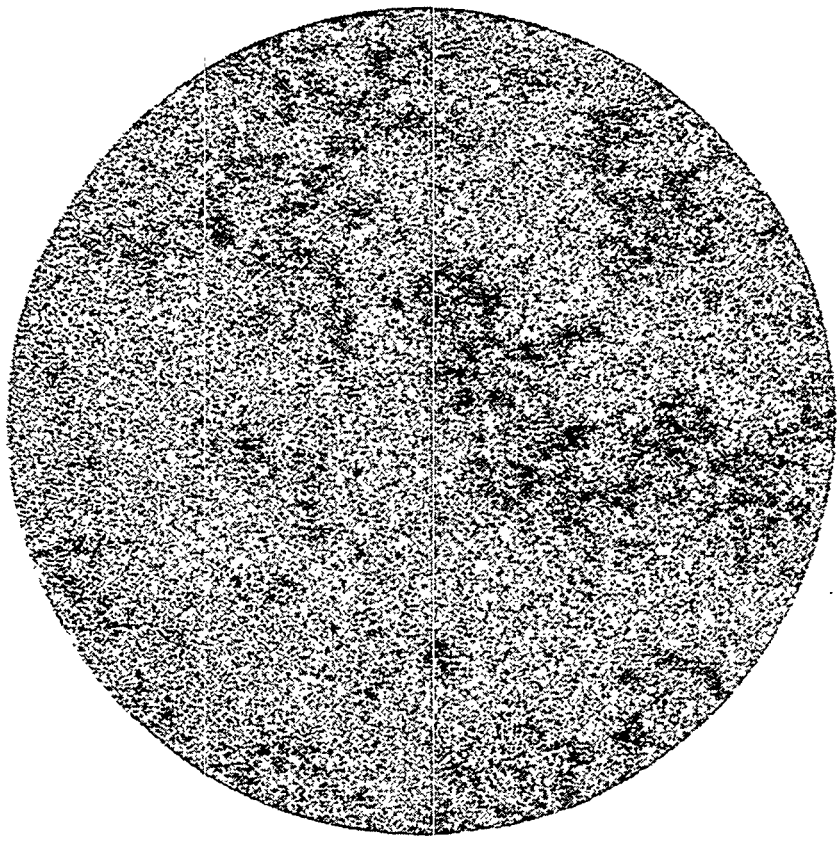

FIG. 5.6: Top section of Berea sandstone core partially saturated with a nonwetting fluid (Wood's metal) at an equilibrium pressure of 6.9 psia and solidified in place. The procedure allows for direct observation and analysis of the fluid distribution at this pressure and correspondent saturation level.

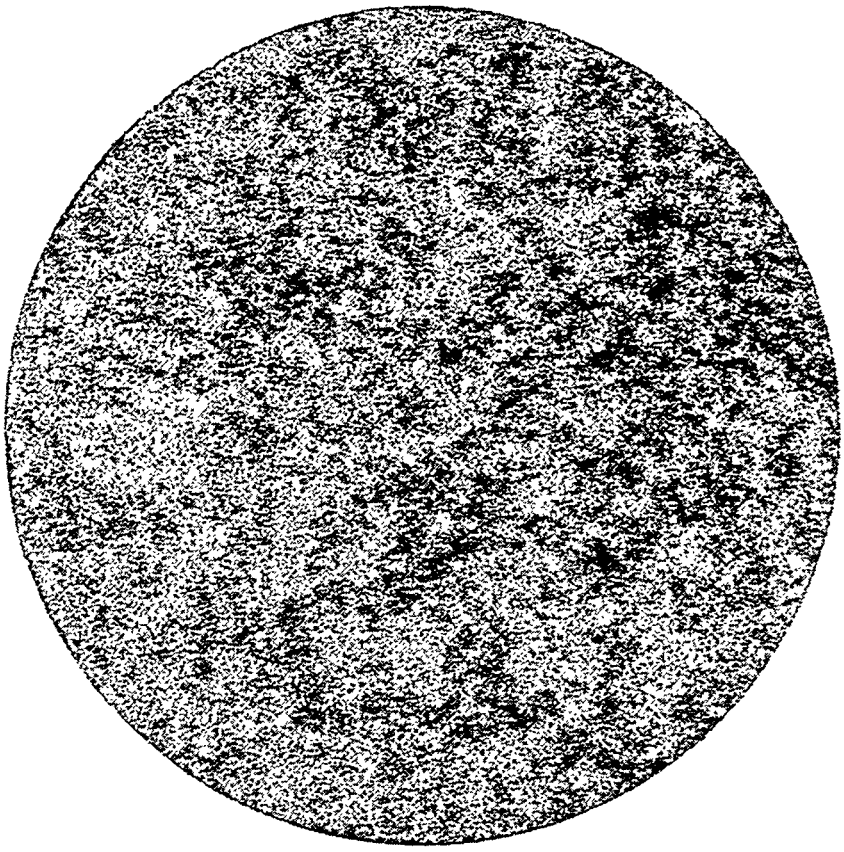

FIG. 5.7: Top section of Berea sandstone core partially saturated with a nonwetting fluid (Wood's metal) at an equilibrium pressure of 7.2 psia and solidified in place. The procedure allows for direct observation and analysis of the fluid distribution at this pressure and correspondent saturation level.

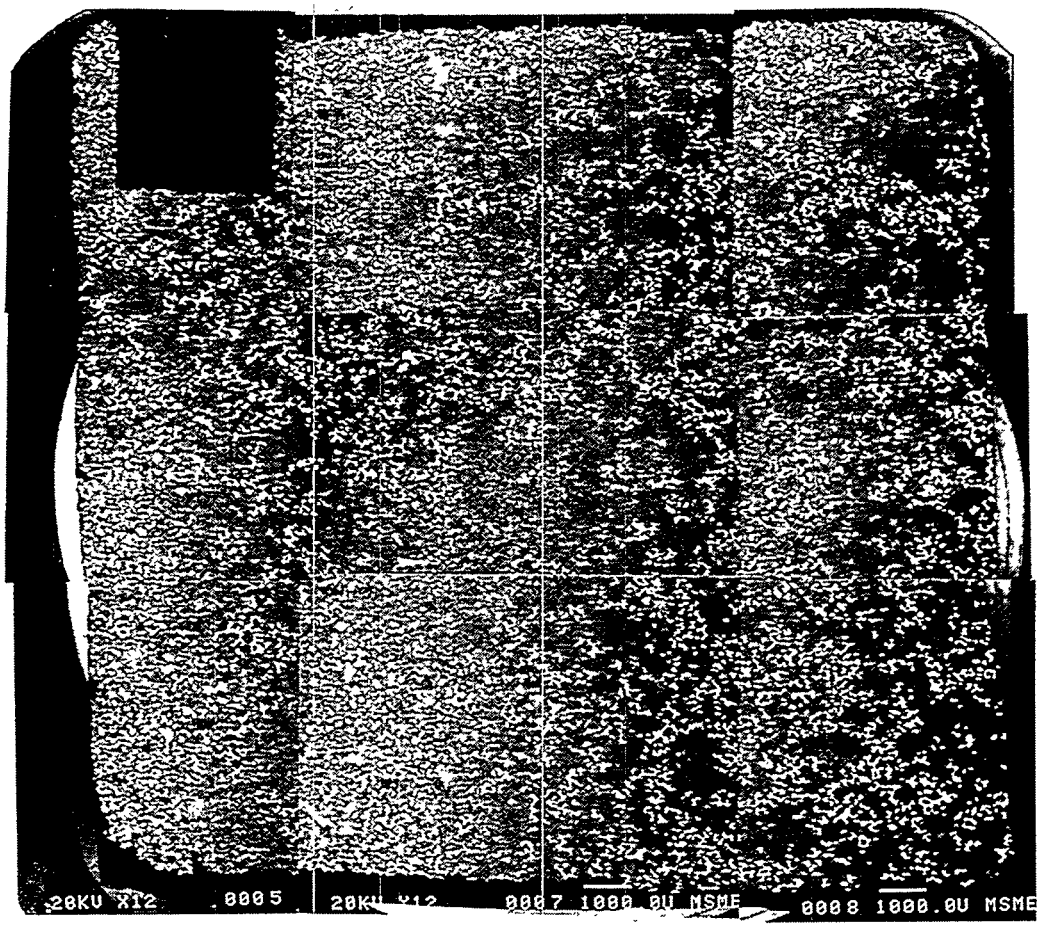

FIG. 5.8: SEM photomicrograph collage of a 1 in $\times$ 1 in Berea sandstone specimen partially saturated with approximately 50% Wood's metal at 8.5 psia equilibrium pressure. The rock is composed mainly of quartz grains (gray phase) and pore space that has been impregnated with Wood's metal (white phase) and epoxy (black phase) for imaging purposes.

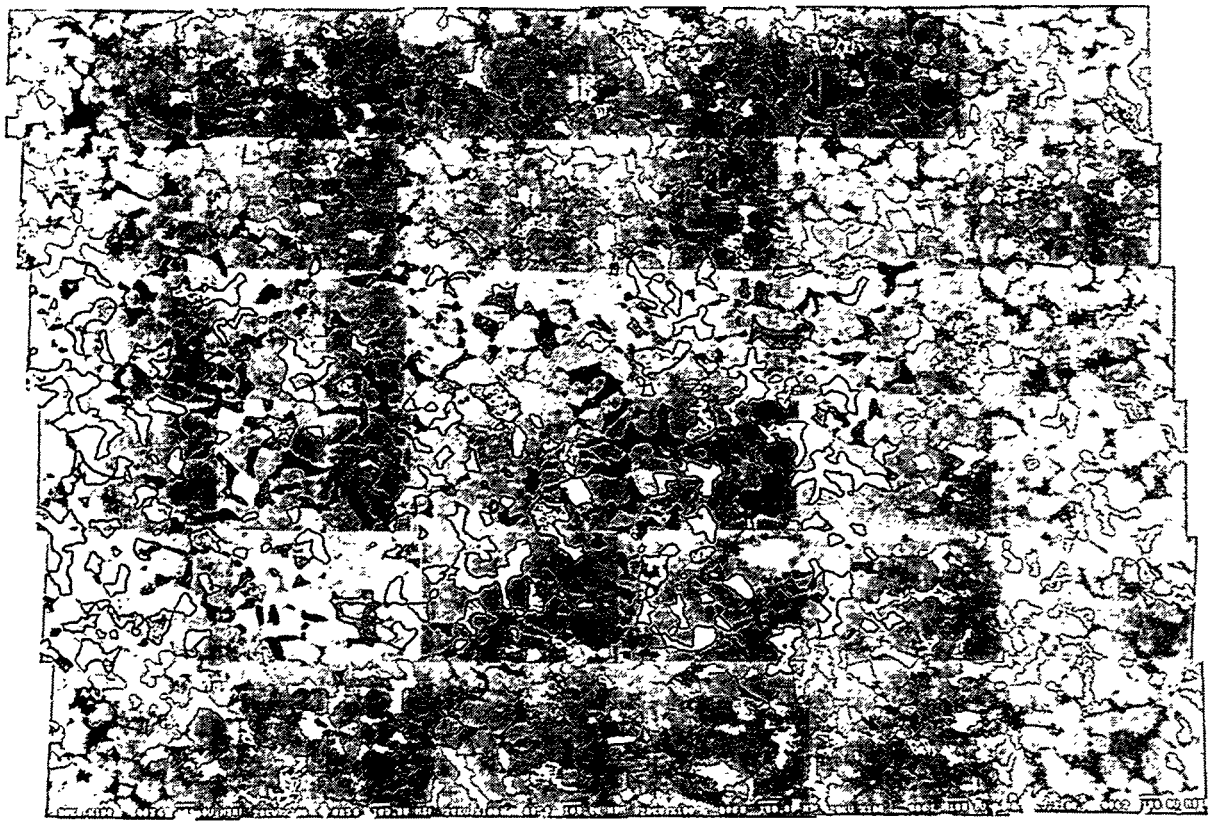

FIG. 5.9: SEM photomicrograph collage of an enlarged partial section obtained from a Berea sandstone sample partially saturated with approximately 50% Wood's metal (white phase) at 8.5 psia pressure shown in Fig. 5.8. Actual width of field is about 6 mm.

5.3 Comparison of analytical and experimental results

In this section, we calculate the predicted capillary pressure function for Berea sandstone for comparison with our experimental data. A typical scanning electron microscope photomicrograph of Berea sandstone is presented in Figure 3.5a. Computerized analysis of Berea sandstone image shows contours of intergranular pore space (Figure 3.10a) from which the perimeter-area power-law relationship of pores (Figure 3.20b) and the distribution of pore hydraulic radii have been obtained (Figure 5.10b). It is worth noting that the contours of intergranular pore space shown in Figure 3.5b are the same contours from which the transport properties (hydraulic and electric) have been previously calculated (Chapters 3 and 4). The analytical capillary pressure function for Berea sandstone has been computed using $\varsigma = 0.40$ N/m (surface tension), $\gamma = 1.49$ (perimeter-area power-law noninteger slope), $R_{H_m} = 12.8$ μm (mean hydraulic radius), $\sigma = 0.41$ (standard deviation), and $(R_H)_{actual}/(R_H)_{measured}$ $= 0.85$ (stereological correction). Preliminary results are presented in Figure 5.11. As expected, the predicted capillary pressure function from such a hydraulic radius distribution does not fit the experimental capillary pressure. The photomicrographic pore-size distribution gives a good measure of the larger pore bodies, but the smaller pore throats usually remain undetected. In addition, it is generally understood that mercury (or Wood's metal) intrusion pore-size distribution does not reveal the presence of larger pore bodies and assigns their volume to pore throats. To fit the analytical to the experimental function at approximately 50% fluid saturation, a distribution represented by $R_{H_m} = 6.6$ μm and $\sigma = 0.14$ is needed. The mean hydraulic radius, $R_{H_m} = 6.6$ μm, corresponds to the mean hydraulic radius of the intergranular throats of the medium, possibly the same throats that largely control hydraulic conductivity (Chapter 3). Thus, our preliminary analyses show that the experimental capillary vs. saturation function (in the saturation range up to about 50%) is controlled primarily by large intergranular pore throats of narrow size distribution, represented by a mean hydraulic radius of about 6.6 μm and a standard deviation of 0.14. This information is important because the resistance offered by the pore structure to various transport phenomena, i.e., permeability, is controlled by the pore throats.

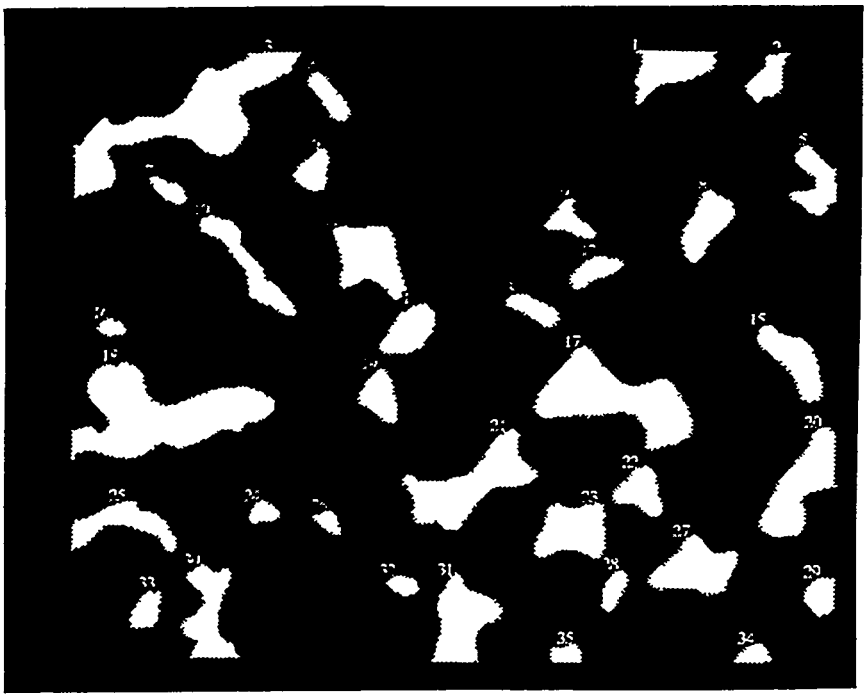

FIG. 5.10a: Computerized analysis of Berea sandstone image shown in Fig. 3.5a display intergranular pore space contours from which hydraulic radius distribution and transport properties (hydraulic and electric) have been calculated. The width of field is 1107 μm.

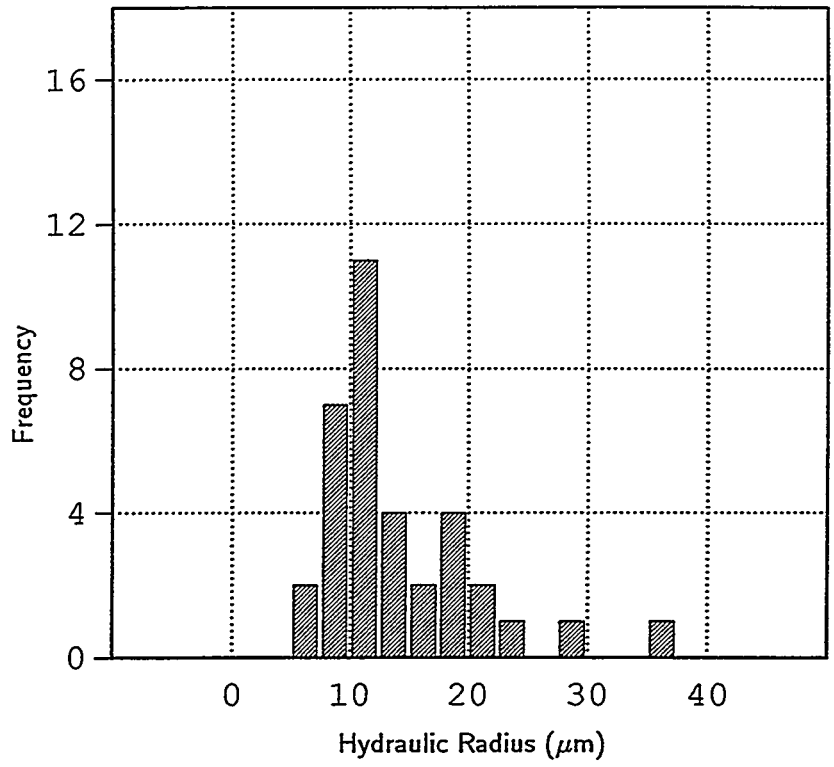

FIG. 5.10b: Pore hydraulic radii frequency distribution of Berea sandstone obtained from pore space contours shown in Fig. 5.10a.

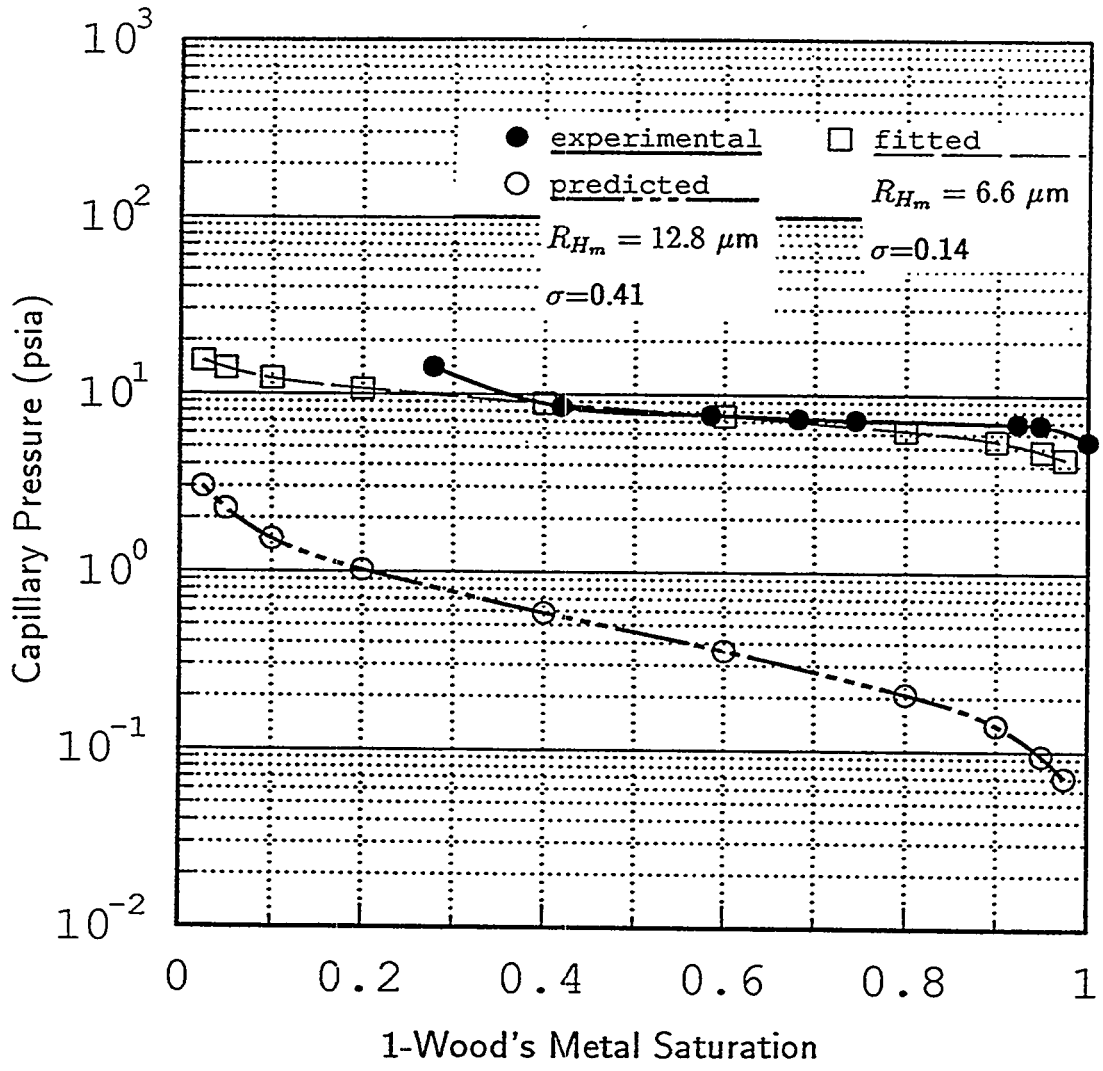

FIG. 5.11: Experimental vs. predicted capillary pressure function of Berea sandstone. The rock has been impregnated with a nonwetting fluid (Wood's metal) at different equilibrium pressures and solidified in place. The procedure allows for direct observation and analysis of the fluid distribution at a fixed pore pressure and saturation level.

Pore-size distributions and pore sizes of rocks have been measured by many researchers using a variety of methods (Dullien and Dhawan, 1974, 1975; Chatzis and Dullien, 1982; Chatzis et al., 1983; Yanuka et al., 1986; Jerauld and Salter, 1990). Most methods require a model of the pore space and simplifying assumptions. Because of these difficulties and the simplified model we use, we have not attempted to determine pore-size distribution precisely but use a simple functional form to determine average pore and throat sizes controlling capillary pressure. We have found that pore throats are smaller than pore bodies; $R_{H_{tm}} = 6.6$ μm and $R_{H_{bm}} = 12.8$ μm with an aspect ratio $R_{H_{tm}}/R_{H_{bm}} = 0.5$. Our result, assuming a lognormal distribution of pore sizes, is consistent with the one obtained by Jerauld and Salter (1990), which uses an exponential pore-size distribution for Berea sandstone, and is similar to that used by Chatzis and Dullien (1982). For example, Jerauld and Salter (1990) found that pore throats are smaller than pore bodies; $r_{t_m} = 11$ μm and $r_{b_m} = 38$ μm (Figure 5.12). It should be noted that the simple concept leading to Eq. (151) has several limitations, so the result is only a first approximation. For instance, we have ignored possible effects from the wetting phase being held by small-scale roughness and adsorptive forces in the pore walls, and we have neglected the effect of clay minerals, which complicates phase occupancy and mobility. Finally, the model does not account for hysteresis effects originated from different pore accessibilities during drying and wetting cycles.

On the basis of our experimental observations of the relationship between microscopic nonwetting fluid occupancy and the fluid distributions and of their effect on capillary pressure of Berea sandstone, we have found that relatively small number of channels connected by large intergranular throats of narrow size distribution are responsible for conducting a relatively large amount of the nonwetting fluid through the medium (at least in the saturation range up to approximately 50%). In fact, we have also found that a large percentage of the permeability of the medium is contributed by a relatively small number of conduits connected by large intergranular throats of narrow size distribution and high hydraulic conductance (Chapter 6).

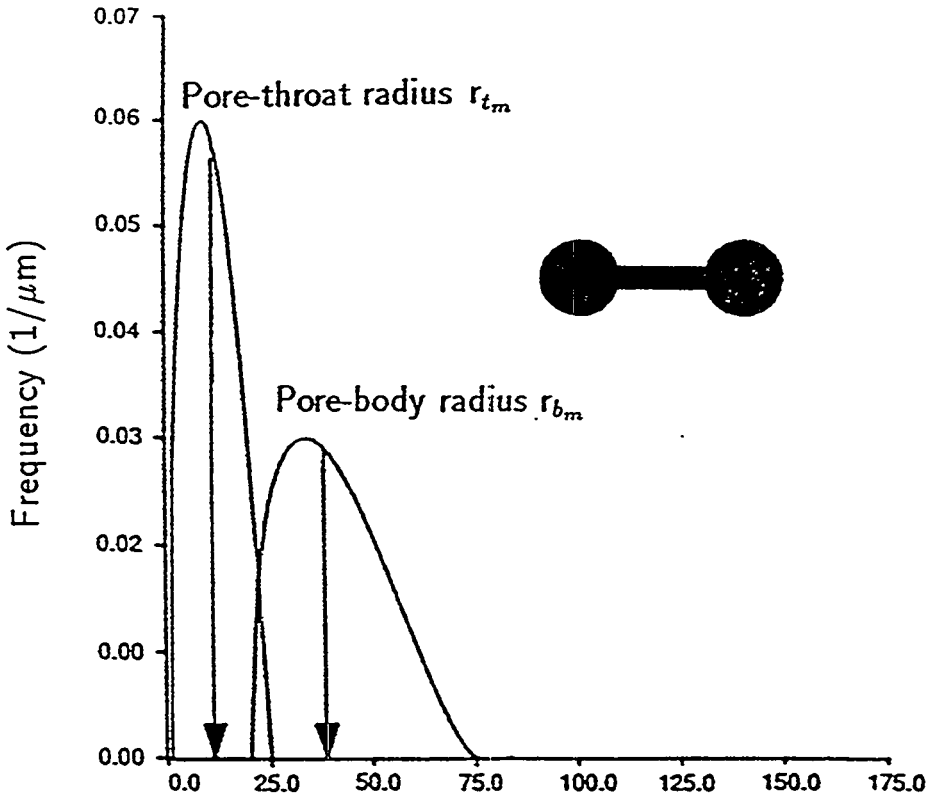

FIG. 5.12: Pore size distribution representative of a consolidated porous medium (Berea sandstone). Pore throats are smaller than pore bodies; $r_{t_m} = 11$ μm, $r_{b_m} = 38$ μm (after Jerauld and Salter, 1990).

6 RELATIVE PERMEABILITY AND THE MICROSCOPIC DISTRIBUTION OF WETTING AND NONWETTING PHASES IN THE PORE SPACE OF BEREA SANDSTONE

Relative permeability and its associated capillary pressure effects are relevant to problems such as enhanced oil recovery and waste remediation and/or isolation. About 50% or more of the original oil-in place is left in a typical U.S. oil reservoir by traditional primary and secondary (i.e., water-flooding) techniques. This unrecovered oil is a large target for enhanced or tertiary oil recovery methods that are being developed. The concept of relative permeability is introduced when extending Darcy's law for single phase flow to the multiphase realm (Scheidegger, 1974). It is generally assumed that relative permeabilities to immiscible fluids are only functions of saturation. A great number of experimental investigations (Hassler et al., 1936; Wyckoff and Botset, 1936; Botset, 1940) substantiate this assumption, within limits. For example, Calhoun (1953) found that the chemical composition of the fluids do not matter much, and that the relative permeability functions are approximately the same for any 'wetting-nonwetting' fluid system. This is a direct consequence of the fact that the microstructure of reservoir rocks strongly influences the mobilization and distribution of fluids in the pore space. Moreover, such factors as (1) fluid/fluid properties-interfacial tension (IFT), viscosity ratio, density difference, phase behavior, and interfacial mass transfer; (2) fluid/solid properties-wettability, ion exchange, adsorption, and interaction; and (3) magnitude of applied pressure gradient, gravity, and aging have been found to play roles in interpreting the motion and distribution of oil in petroleum reservoirs (Dullien, 1979; Stegemeir, 1977).

The relative permeabilities are empirical coefficients which appear in the continuum form of Darcy's law for two-phase flow through porous media:

$$\frac{q_w}{A} = \frac{-k_{rw}k}{\mu_w}\frac{dp_w}{dx} \tag{154}$$

$$\frac{q_{nw}}{A} = \frac{-k_{rnw}k}{\mu_{nw}}\frac{dp_{nw}}{dx} \tag{155}$$

where q_w and q_{nw} are the volumetric flowrates of the wetting and nonwetting phases,

μ_w and μ_{nw} are the viscosities of those phases, dp_w/dx and dp_{nw}/dx are the macroscale pressure gradients in those phases, and A is the cross-sectional area, perpendicular to the flow, of the porous medium. $k_{rw}k$ and $k_{rnw}k$ are the permeabilities to the wetting and nonwetting phases. k is the permeability of the porous medium when only one phase is present, and k_{rw} and k_{rnw} are the wetting and nonwetting phase relative permeabilities. The relative permeabilities depend upon wetting-phase saturation, S_w - the fraction of pore volume occupied by the wetting phase. S_{nw}, the nonwetting phase saturation, is always given by $S_{nw} = 1 - S_w$.

As Eqs. (154) and (155) show, the relative permeability factor is an empirical representation of a well-defined transport process in a highly complex pore space geometry and topology. In spite of this complexity, symplified models of the pore structure have been proposed (Fatt and Dykstra, 1951; Rose and Witherspoon, 1956; Chatzis and Dullien, 1977). However, such parameters as pore body and pore throat distributions, pore coordination numbers and individual fluid-phase coordination numbers as a function of saturation which are implemented in the mathematical models have not been determined experimentally. This is due in part to the lack of good experimental techniques required for visualizing three-dimensional (3-D) microstructures in natural porous media while maintaining the original pore and phase geometry. Therefore, we decided to work on this problem with several main objectives in mind: (1) to further develop an experimental technique initiated by Yadav et al. (1987) that would allow measurement of relative permeability for the full range of saturation, (2) to visualize directly 2-D pore structure and wettabilities for the full range of saturation, (3) to interpret experimental data and fluid distributions qualitatively and quantitatively with respect to pore geometry and topology, (4) to evaluate relative permeability data in terms of microphysics and microchemistry of the processes involved (i.e., effect of clay minerals coating pores), and (5) to compare relative permeability and associated capillary pressure experimental data obtained using conventional methods.

6.1 Apparatus and procedure

The apparatus that was used in this study was designed to measure simultaneously both hydraulic and electrical conductivity (Figure 4.2). The rock core (5 cm in diameter and 5 cm in length) is encased in its rubber jacket and placed in the test cell. The test cell base is connected directly to the bottom of the sample, and a centrally-located orifice is attached to allow fluids to flow through the mounted core. A confining pressure of 50 psi (3.4 atm) is applied using nitrogen gas. Fluid flow through the core is controlled by a syringe pump that provides constant flow rates. The basic procedure used for measuring permeability is first to vacuum saturate each core completely with triple-distilled water. Distilled water is then pumped through the core, and flow is continued for a sufficient time to establish constant pressure readings. It was found that about four pore volumes of water are required to achieve steady state. In our experiments, we used samples of Berea sandstone, which is a homogeneous sedimentary rock used as a reference rock in the petroleum industry. The intrinsic permeability and porosity of a Berea sandstone core are about 600 mD (600×10^{-15} m^2) and 22%, respectively.

6.2 Effect of wetting phase saturation

To determine the effect of partial fluid saturation on permeability, we utilized Berea sandstone samples that had been permeated with triple-distilled water to measure the single phase hydraulic conductivity. This procedure was applied to every sample to find the permeability before paraffin application. The samples were then oven dried. After measuring the permeability, the samples were partially filled with paraffin wax at controlled saturations of 20%, 30%, 40%, 50%, 60%, and 70%. Paraffin wax is a wetting phase composed of a mixture of solid hydrocarbons of high molecular weight with a density of 0.76 g/cm^3, a dynamic viscosity of about 3×10^{-3} Pa·s at 150°C, and a melting point of 56°C. The paraffin is applied at temperatures higher than its melting point in the core axial direction, and until uniform saturation is achieved throughout the sample (Figure 4.3). The paraffin is then solidified in place at ambient temperature conditions. After paraffin application, the rock grain surfaces became hydrophobic. To measure the effective permeability, the rock samples that

TABLE 6.1: Effective (and absolute) permeability data (Case B) - Berea sandstone partially saturated with paraffin wax, with triple-distilled water used as permeant.

Sample	S_w^a (%)	k_{eff}^b (mD)	k_{abs}^c (mD)
1EB4	16	513	282
1EB2	24	553	329
S-1R	24	501	333
1EB3	32	489	376
1EB5	32	473	296
1EB6	41	206	463
1EB1	44	121	288
S-3R	50	54	391
KS15	69	15	—

[a] Paraffin wax saturation.

[b] Effective permeability.

[c] Absolute permeability.

were partially saturated with paraffin were permeated with distilled water. The effective permeability data of the spaces not occupied by the wetting fluid is presented in Figure 6.1 (Case A). Experiments in which electrical conductivity had not been measured previous to paraffin impregnation were repeated on a new and clean set of samples. The result is shown in Figure 6.1 (Case B). In summary, good agreement, within experimental error, was found between the two sets of experiments A and B. Note that the extrapolated value of permeability at zero paraffin saturation from Figure 6.2 - Case B ($\sim$ 600 mD) is higher than the measured value of permeability obtained at the same saturation when using triple-distilled water ($\sim$ 300 to 400 mD) (Table 6.1). A possible explanation of this phenomenon is given in section 6.3.

6.2.1 Effect of pore structure and topology

To understand how pore structure and topology control permeability, the hydraulic conductivity data (Figure 6.4) have been studied in light of the wetting-fluid distributions at each saturation regime (Figures 6.3 to 6.5) with the aid of a complete rock pore cast (Figure 6.6). The rock pore cast was obtained from a rock specimen that had been fully impregnated with Wood's metal alloy and the quartz grains removed by hydrofluoric acid. The rock pore cast clearly reveals that the pore space is composed of grain-contact porosity and intergranular porosity. Paraffin imbibition occurs

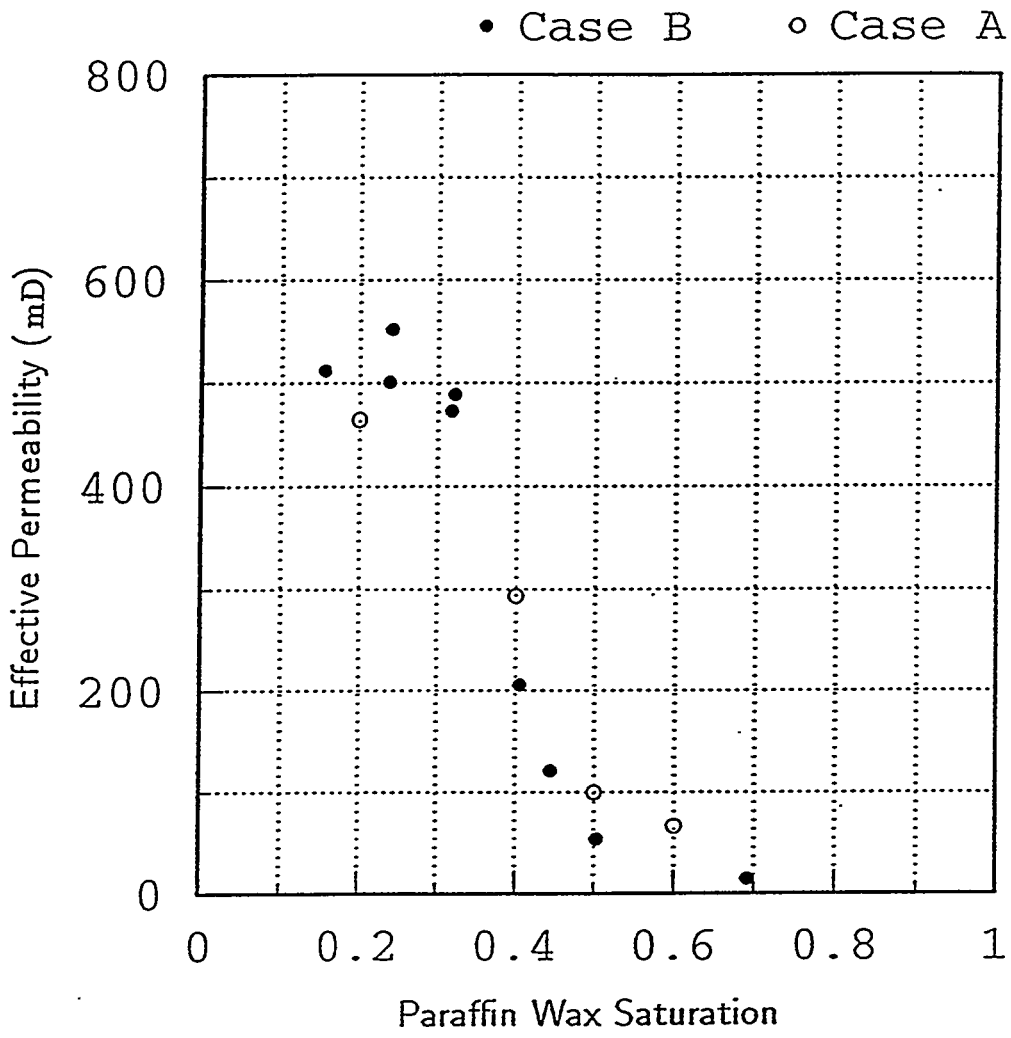

FIG. 6.1: Effective permeability vs. paraffin saturation for Berea sandstone. The pore space was partially saturated with hydrocarbon paraffin. The remaining portion of the pore space was filled with triple-distilled water. Cases A and B correspond to experimental data on samples subjected or not subjected to electrical conductivity measurement before paraffin application, respectively.

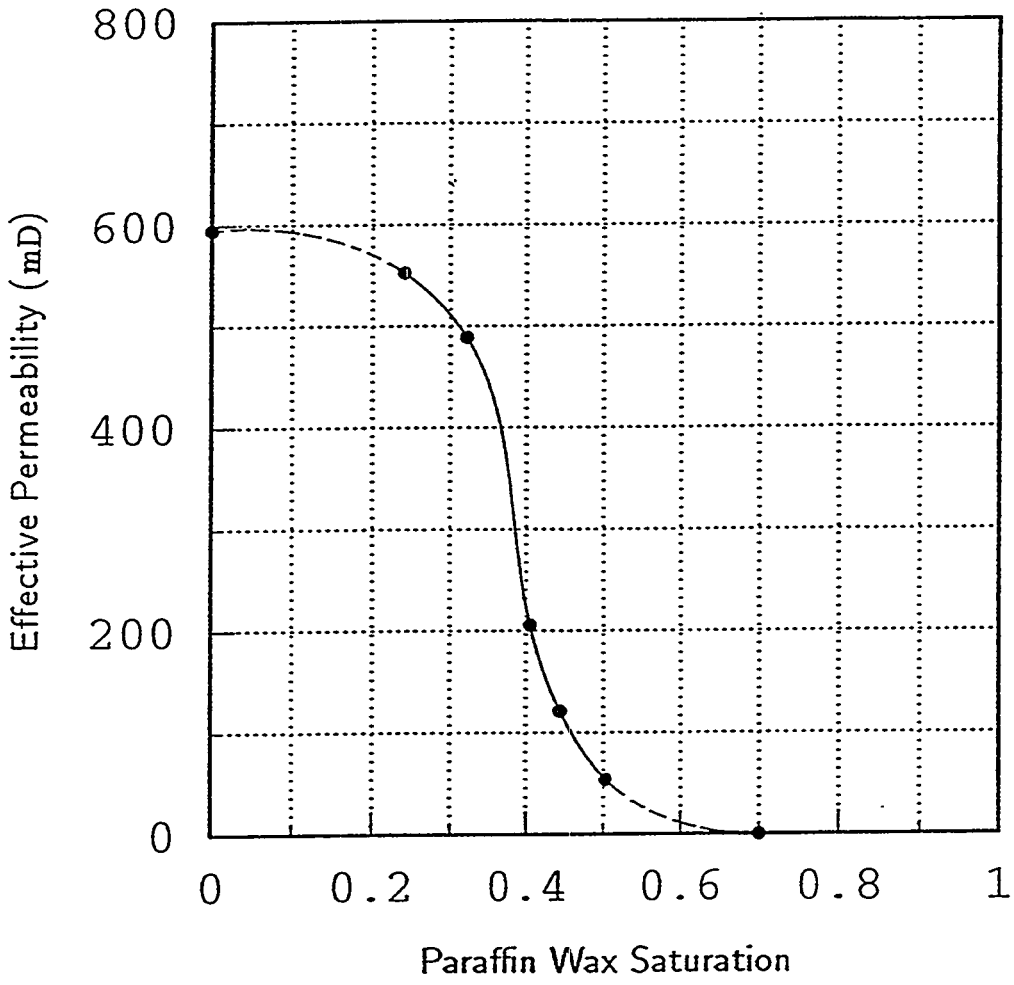

FIG. 6.2: Effective permeability vs. paraffin wax saturation for Berea sandstone (case B). The pore space was partially saturated with hydrocarbon paraffin, with the remainder of the pore space filled with triple-distilled water.

because surface tension effects encourage the displacing fluid to advance. The overall dynamics of the wetting phase imbibition process is as follows: In the grain-contact pore space, in the smaller throats, and in the surface capillary grooves, capillary pressure is high, and the paraffin will advance quickly to the next pore. The pores exert much less capillary pressure, and for a given pressure difference between the phases only the smaller pores will fill. Once a pore is filled, the paraffin will next fill all throats leading from it, again rapidly. A new set of pores will be reached and the process continues. Therefore, during paraffin imbibition the flow dynamics are pore-dominated.

Figure 6.3 shows a scanning electron microscope (SEM) photomicrograph collage of a Berea sandstone specimen that has been partially saturated with approximately 20-30% paraffin. The gray phase corresponds to quartz grains, the white phase corresponds to pores that have been impregnated with paraffin, and the black phase corresponds to the remaining pore space, which was filled with blue epoxy for imaging purposes. Paraffin has invaded grain-contact pore space (i.e., thin sheets and micropores) and intergranular pore space connected by smaller throats, but has only coated the available intergranular channels connected by larger throats. A minor effect on effective permeability is observed (Figure 6.2). Therefore, the fraction of the pore structure connected by smaller constrictions (e.g., grain-contact pore space) do not contribute much to effective permeability. Figure 6.4 shows an SEM photomicrograph collage of a rock specimen partially saturated with approximately 40-50% paraffin. At this stage, we are filling main intergranular conduits connected by the larger throats. A substantial effect on effective permeability is observed. Figure 6.5 shows an SEM photomicrograph collage of a rock specimen partially saturated with approximately 60-70% paraffin. We have filled almost all intergranular conduits connected by larger throats. A few intergranular pores not well connected still remain unfilled. When paraffin saturation is $\sim$ 70%, the whole pore structure behaves as though hydraulically disconnected. Results are summarized in Table 6.2.

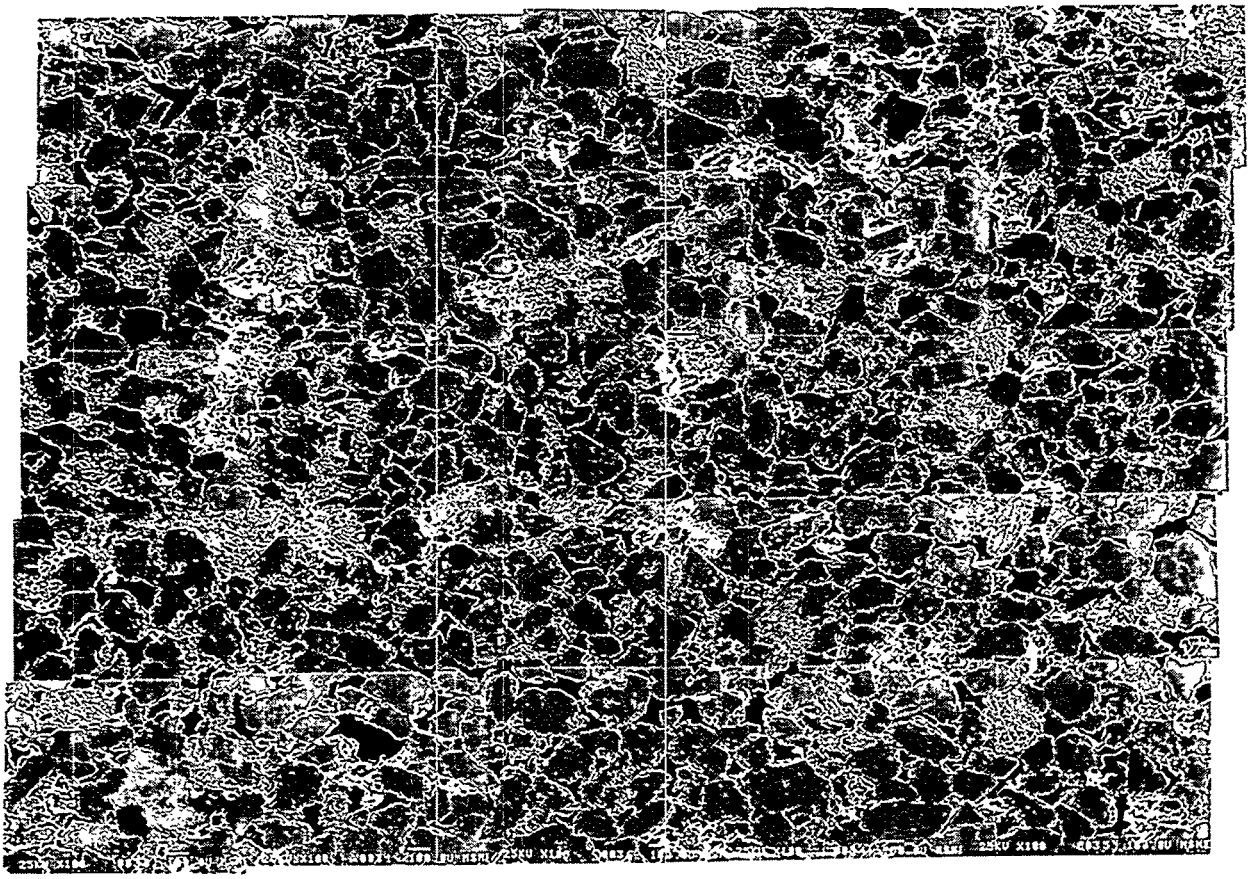

FIG. 6.3: SEM photomicrograph collage of a Berea sandstone specimen impregnated with approximately 20-30% paraffin. The actual width of field is about 6 mm. The gray phase represents quartz grains, the white phase represents pores saturated with paraffin, and the black phase represents remaining pores filled with blue epoxy for imaging purposes.

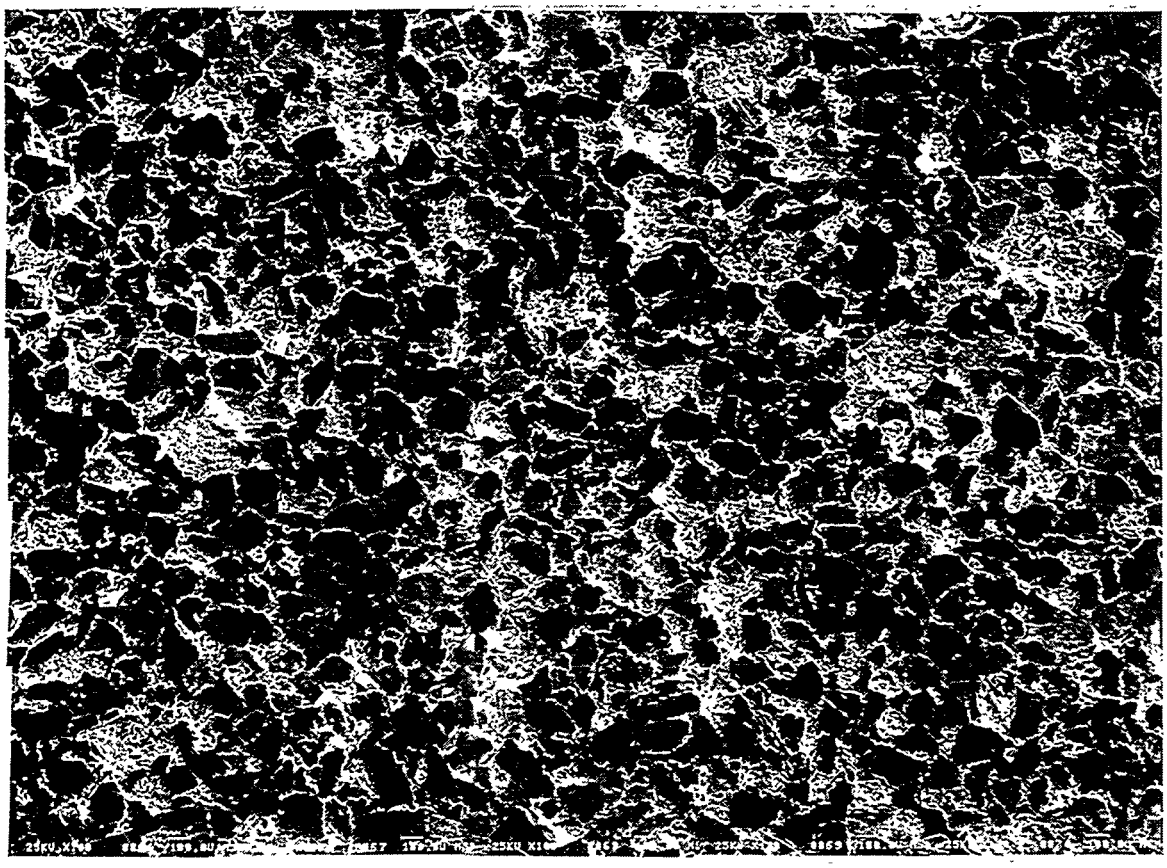

FIG. 6.4: SEM photomicrograph collage of a Berea sandstone specimen impregnated with approximately 40-50% paraffin. Actual width of field is about 6 mm. The gray phase represents quartz grains, the white phase represents pores saturated with paraffin, and the black phase represents remaining pores filled with blue epoxy for imaging purposes.

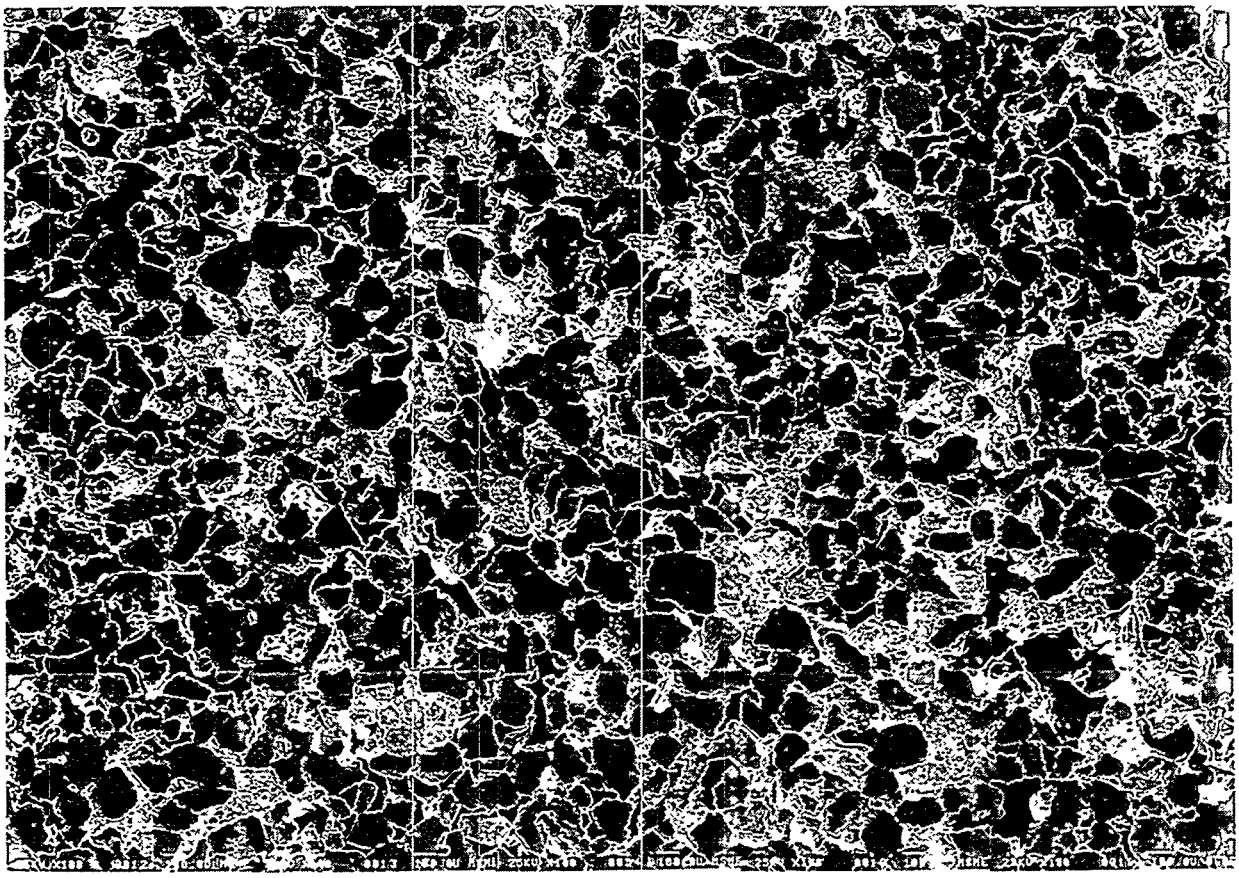

FIG. 6.5: SEM photomicrograph collage of a Berea sandstone specimen impregnated with approximately 60-70% paraffin. Actual width of field is about 6 mm. The gray phase represents quartz grains, the white phase represents pores saturated with paraffin, and the black phase represents remaining pores filled with blue epoxy for imaging purposes.

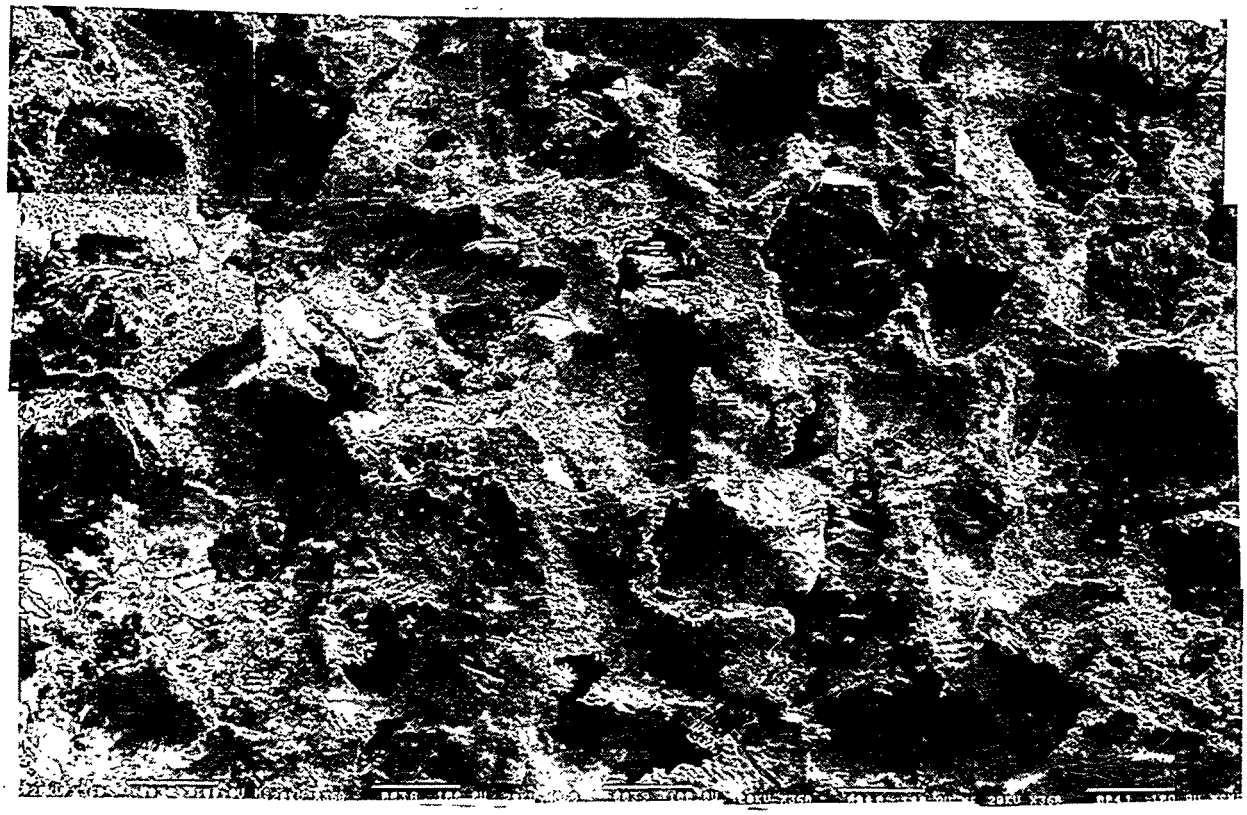

FIG. 6.6: SEM photomicrograph collage of a Berea sandstone pore cast. Actual width of field is about 6 mm. The rock pore space was completely filled with Wood's metal alloy and the quartz grains removed by hydrofluoric acid to allow direct observation of the pore structure.

TABLE 6.2: Wetting fluid invasion and permeability.

- $\mathbf{0.0 \leq S_w \leq 0.3}$
  Wetting fluid fills well-connected grain-contact pore space (e.g., thin sheets and micropores) and intergranular conduits connected by smallest throats, while only coating available intergranular pore space connected by larger throats.

  $\Longrightarrow$ Very small effect on effective permeability.

- $\mathbf{0.3 < S_w \leq 0.5}$
  Wetting fluid fills to partially-fills few intergranular conduits connected by large throats.

  $\Longrightarrow$ Very large effect on effective permeability.

- $\mathbf{0.5 < S_w \leq 0.7}$
  Wetting fluid fills remaining more tortuous intergranular conduits connected by large throats.

  $\Longrightarrow$ Smaller effect on effective permeability.

- $\mathbf{0.7 < S_w \leq 1.0}$
  Structure is disconnected, i.e., nonwetting phase is trapped in disconnected intergranular pore space.

6.2.2 Irreducible wetting phase saturation

Overall, it is observed that that the wetting phase is confined to a continuous network of conduits throughout the porous medium (Figure 6.3). It is composed of clusters of intergranular pores, edges, corners and wedges of intergranular pores, capillary channels present on rough surfaces of pores, and single grain-contact pores. Since the wetting fluid at the 'irreducible saturation' limit forms a hydraulically connected continuum, it is possible to reduce the 'irreducible wetting phase saturation' progressively, at least in principle. Therefore, the 'irreducible wetting phase saturation' is not constant and becomes a function of the externally applied pressure.

Thus, the existence of the 'irreducible wetting phase saturation' in a consolidated rock such as Berea sandstone is due to the fact that (1) grain-contact pores have narrow throats and large surface area, (2) pores have corners (angular cross sections), and (3) the pore surface is rough at the microscopic scale (Figure 6.7).

6.3 Effect of clay minerals

X-ray diffraction studies by Khilar and Fogler (1984), in conjunction with scanning electron microscopy (Figures 6.8 to 6.10) and energy-dispersive x-ray analysis indicate that Berea sandstone contains $\sim$ 8% by weight of dispersable and swelling clays (mainly kaolinite with some illite and smectite). The injection of a fluid such as triple-distilled water whose solution chemistry is not compatible with the porous rock in its natural state can bring significant reductions in the permeability. This is just the manifestation of peptization and flocculation of clay particles in Berea sandstone. Khilar and Fogler (1984) found that when flow is switched from salt water to fresh water, clay particles are released from the pore wall. The particles then migrate in the direction of the flow and are trapped at throats which results in blockage of the pores of the sandstone, decreasing the permeability. For electrolyte solutions with cations of valence 1, at pH = 7, a critical salt concentration (0.07 M for sodium chloride solution at 30°C) has been found below which clay particles are released from Berea sandstone pore walls (Khilar and Fogler, 1984). Particle migration is thought to be the most important mechanism in water-sensitive Berea sandstone due to the fact that the amount of swelling clays is minimal. The peptization and flocculation of

clay particles in Berea sandstone may be explained in terms of double-layer theory. The major forces that hold the clay particles to the pore walls are the London-van der Waals forces of attraction. The forces causing the detachment of the clay particles are the double-layer forces of repulsion and possibly, under conditions of high flow rate, the hydrodynamic shear. Calculations show these two forces of double-layer repulsion and hydrodynamic shear to be the most probable cause for particle release (Mungan, 1968). Experimental observations (Khilar and Fogler, 1984) strongly suggest that the double-layer force of repulsion may be the dominant cause of particle release. These observations include the two most important parameters that govern the stability of the colloidal suspension of clay particles: temperature and type of cation. More importantly, the phenomenon occurs only at relatively low salt concentration, where the double-layer repulsive forces are large.

It is important to recognize that the clay minerals present in the rock have been immobilized by coating pores with hydrocarbon paraffin. Therefore, the permeability extrapolated to paraffin saturation of zero (i.e., no hydrocarbon paraffin) corresponds to either the permeability of the clean rock without clays or the permeability of the rock with clay, but with brine as flowing fluid (with concentration above critical salt concentration if monovalent cations are employed). This hypothesis was verified by partially removing clays in a Berea sandstone core by acid treatment with a mixture of 6% hydrochloric and 1.5% hydrofluoric acids (Suarez-Rivera, personal communication, 1991). After the core was treated and clays flushed out, the permeability was found to be 574 mD, higher than the measured value obtained using triple-distilled water ($\sim$ 300 to 400 mD) (Table 6.1).

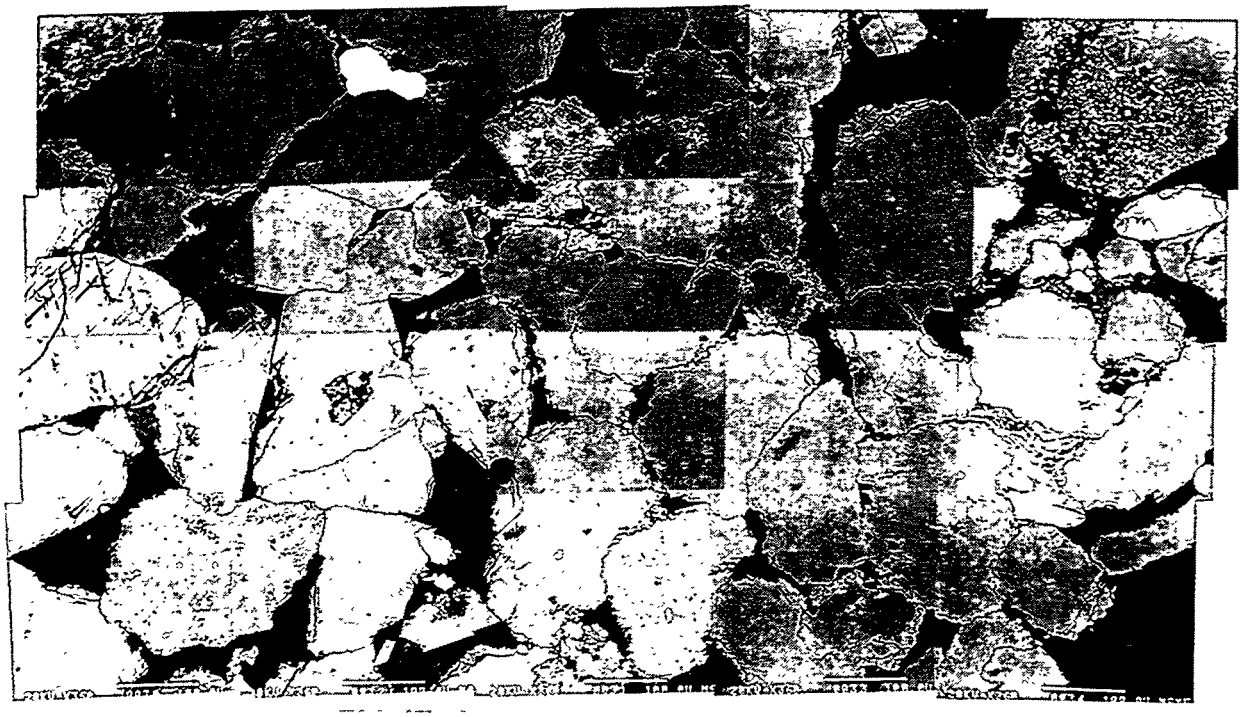

FIG. 6.7: Typical SEM photomicrograph collage of Berea sandstone showing pore-grain interface roughness. The rock is composed mainly of quartz grains (dark gray), feldspar grains (medium gray), and products of grain dissolution (light gray). The pore space is impregnated with Wood's metal alloy (white), and epoxy (black). Actual width of field is about 1.5 mm.

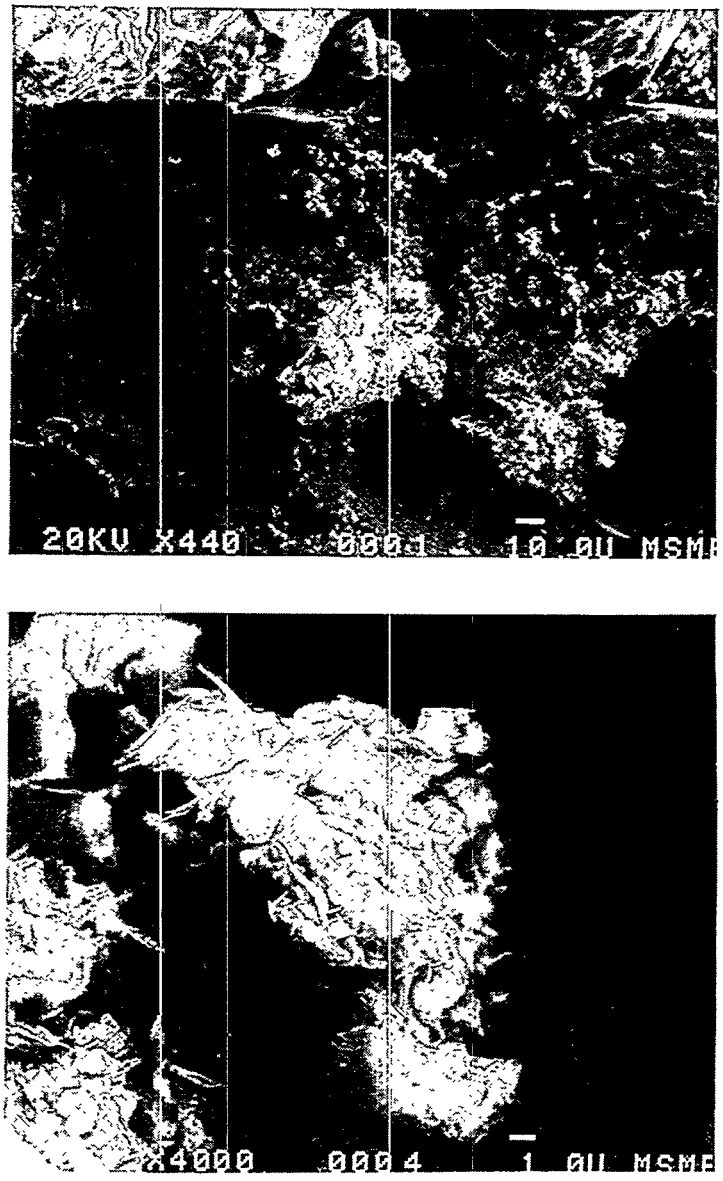

FIG. 6.8: SEM photomicrographs of a Berea sandstone specimen showing the presence of fine-grained clay minerals (mainly kaolinite) partly filling pores between quartz grains.

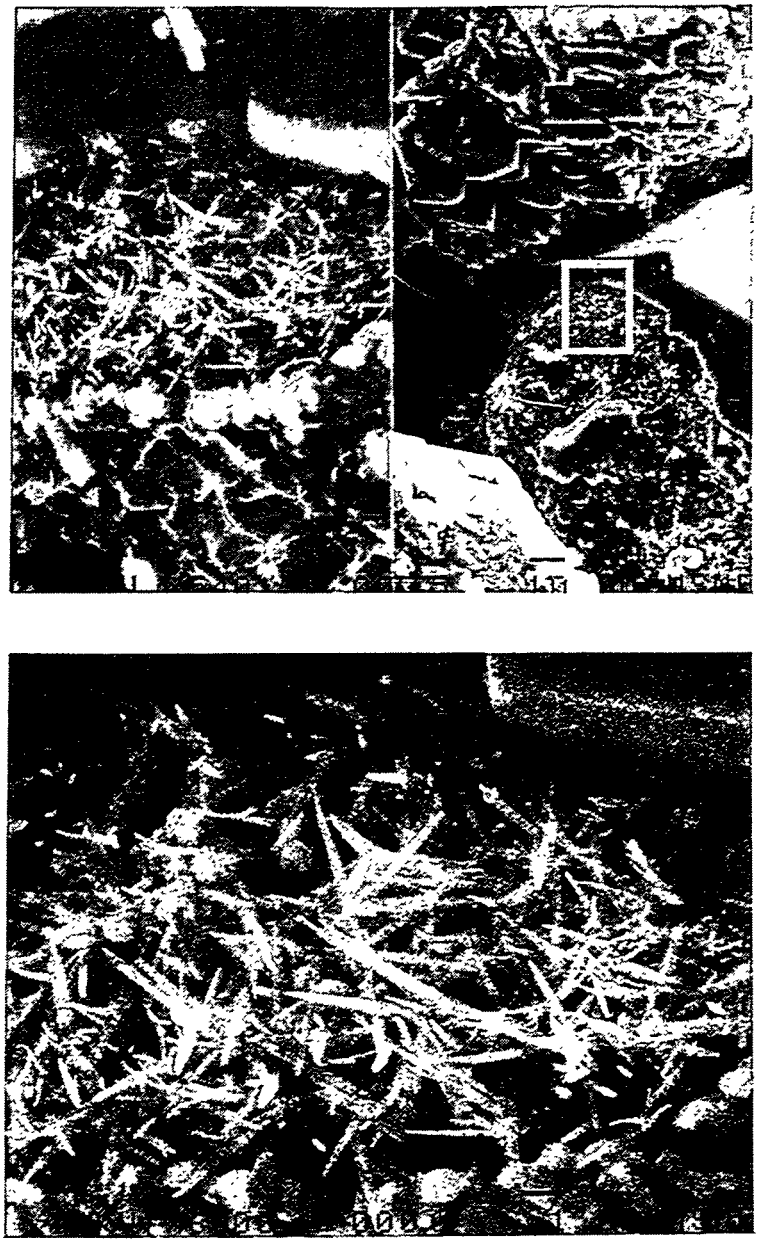

FIG. 6.9: SEM photomicrographs of a Berea sandstone specimen showing the presence of fine-grained clay minerals (mainly illite) partly filling pores between quartz grains.

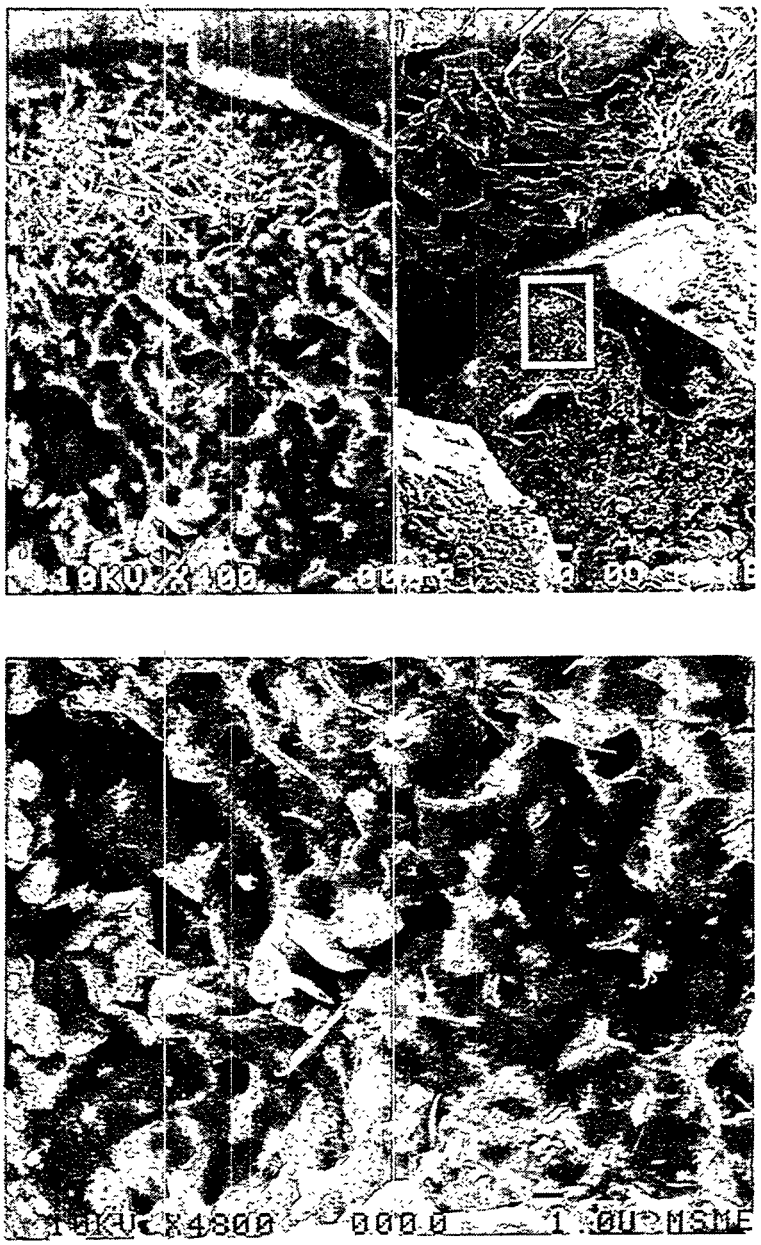

FIG. 6.10: SEM photomicrographs of a Berea sandstone specimen showing the presence of fine-grained clay minerals (mainly montmorillonite) partly filling pores between quartz grains.

6.4 Effect of nonwetting phase saturation

In this experimental investigation, we have sought to examine the relationship between the microscopic pore occupancy by the nonwetting fluid and its effect on effective permeability and capillary pressure.

We have used three-dimensional imbibition of a nonwetting Wood's metal alloy instead of the conventional mercury porosimetry. This technique offers the advantage of allowing analysis of the occupied pore space after the experiment. Wood's metal is an alloy of about 43% Bi, 38% Pb, 11% Sn, and 9% Cd, with a specific gravity of 9.6, a viscosity of about 1.3×10^{-3} Pa·s at 75°C, and a surface tension of about 400 mN/m (Yadav et al., 1987). The apparatus for the three-dimensional imbibition experiments is shown in Figure 5.1. It consists of a metallic container of Wood's metal placed in a metal vacuum chamber provided with a lucite window and surrounded by a heating element to keep the metal molten (melting point varies from about 50°C to 70°C, depending on its composition). A micrometer is attached to the metallic container to determine the pressure at which the Wood's metal first enters the specimen. The 5 cm-long and 5 cm-diameter sandstone sample is first oven-dried, and then immersed in the molten Wood's metal in the metallic container and placed in the metal vacuum chamber. Then the sample is de-aired by applying a full vacuum for about 60 minutes, until no air bubbles are observed through the lucite window. A sub-atmospheric pressure is applied by drawing a partial vacuum, which is maintained at the desired value by a regulating valve until capillary equilibrium is achieved. Each sample was allowed to imbibe at a fixed equilibrium pressure for approximately 90 minutes, at a fixed pressure, until no movement of Wood's metal was noticed through the lucite window. At a pressure of about 5 to 6 psia, the micrometer signaled the first indication of Wood's metal entering the pore space (probably an edge effect on the sample sides). The Wood's metal imbibition experiment was repeated on several samples by applying pressure externally under quasistatic conditions in the range of approximately 6 to 14 psia. The imbibed samples were cut into four axial quarters, each of which had a different saturation. To minimize the effect of gravity (hydrostatic) gradient, we took the top quarter of each imbibed specimen at a particular equilibrium pressure and measured its saturation. Figure 5.2 shows the Wood's metal imbibition curve, in

TABLE 6.3: Effective (and absolute) permeability data - Berea sandstone partially saturated with Wood's metal, with triple-distilled water used as permeant.

Sample	P_c^a (psia)	S_{nw}^b (%)	k_{eff}^c (mD)	k_{abs}^d (mD)
ESB5	6.8	5.2	280	346
EMB3	6.9	7.7	242	388
KBS11	7.2	26	45	386
ESB3	7.3	32	19	345
KBS9	7.7	42	0.71	319

[a] Capillary pressure.

[b] Wood's metal saturation.

[c] Effective permeability.

[d] Absolute permeability.

which the volume of Wood's metal intruded (normalized by the total pore volume) is plotted vs. the applied pressure. Fluid saturation increases rather sharply with a corresponding small increase in capillary pressure in the saturation range from about 10 to 50% (Fig. 5.2). After Wood's metal application, the rock samples were vacuum-saturated and permeated with triple-distilled water to measure the effective permeability (Table 6.3). Figure 6.11 shows the effective permeability curve of the spaces not occupied by the nonwetting fluid, measured at various saturations (in a Berea sandstone of absolute permeability of $\sim$ 600 mD).

6.4.1 Effect of pore structure and topology

To understand how pore structure and topology control the physical property under consideration, we have studied the effective permeability and capillary pressure data in light of the nonwetting fluid distributions observed at each equilibrium pressure. For this purpose, optical and scanning electron microscopic examinations of the tops of samples (after cutting off 3 mm) have provided valuable insights into the pore-level complexity of the natural porous media. In the Wood's metal imbibition process, some external pressure is needed to overcome surface tension and push the Wood's metal through the pores and throats. Large throats, with their comparatively weak capillary pressures, will fill more readily than small throats. Once the fluid reaches a pore, capillary pressure is reduced, and the pore will fill rapidly. In this process, the flow dynamics are mainly controlled by the throats. Isolated regions will occur because a region of large throats surround a region of constricted throats.

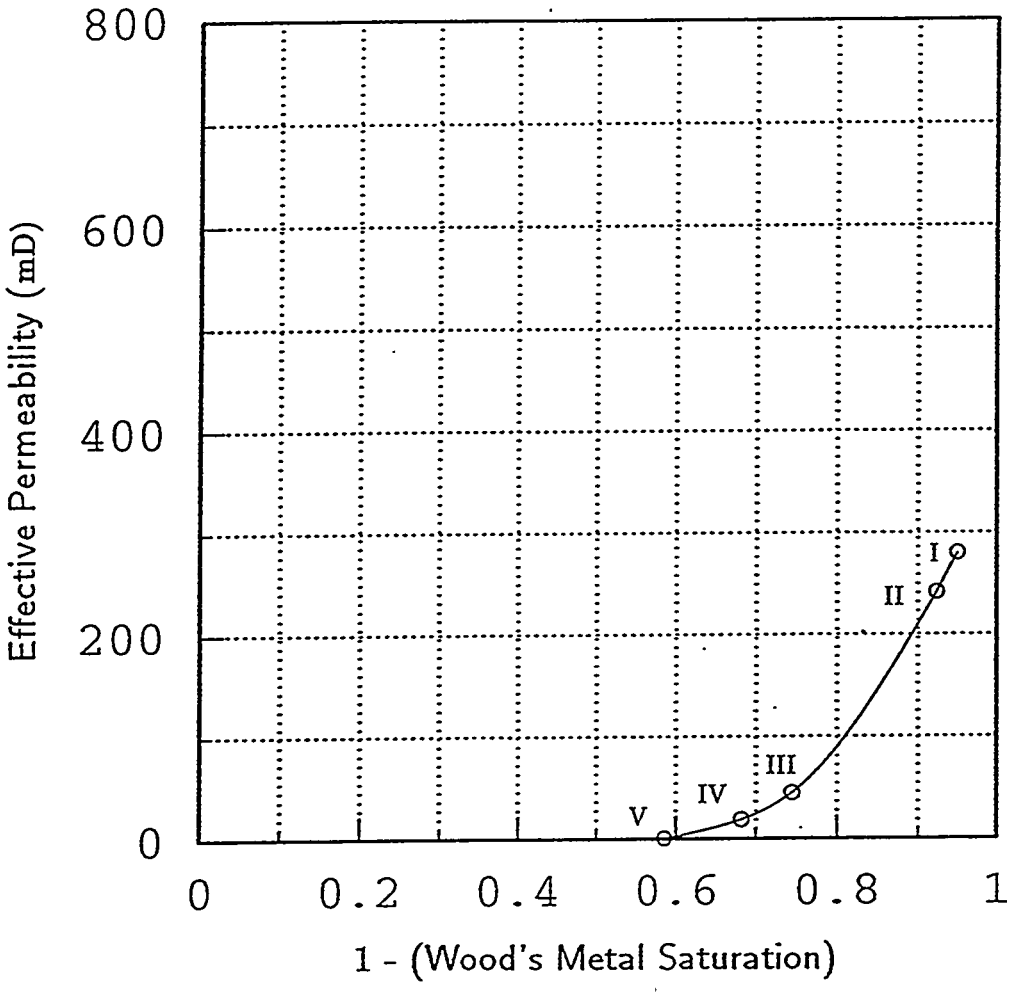

FIG. 6.11: Effective permeability vs. Wood's metal saturation for Berea sandstone. The pore space was partially saturated with Wood's metal at different pressures, with the remainder of the pore space filled with triple-distilled water. The capillary pressures (in psia) for the points on the plot are I = 6.8, II = 6.9, III = 7.2, IV = 7.3, and V = 7.7 psia.

Figure 6.12 shows an optical photograph of the nonwetting fluid distributions obtained in axial quarters in the pressure range 6.8 to 7.7 psia. It is observed that the nonwetting fluid flow network is composed of a set of imbibing clusters correlated in space. At every pressure step, the nonwetting fluid resides in the pores accessible through throats with a radius larger than that corresponding to the current equilibrium capillary pressure. As the pressure increases, the nonwetting phase saturation increases, and the nonwetting fluid invades successively smaller pores and becomes connected to regions which were separated from this phase by small throats. At 6.8 psia (Figure 6.12), the fluid has preferentially penetrated the sample sides. The saturation is greatest near the perimeter of the sample, and least at the center. This observation suggests that pores near the cylindrical surface of the sample are better connected than those towards the center. This interconnection could arise from exposure of pores where they intersect the surface, or from damage adjacent to this surface. At 6.9 psia (Figure 6.12), a saturation gradation is observed in the direction of flow at this pressure (preferentially horizontal). The longer flow paths are connected by smaller constrictions, so fewer flow channels are going to the sample center starting from all available channels at the sample surface. At pressures of 7.2 psia (Figure 6.12) and greater, the nonwetting fluid invades more and more smaller pores, becoming connected to regions that were separated to this phase by smaller pores, and the clusters of nonwetting phase become larger and larger.

Figure 6.13 shows an SEM photomicrograph collage of a 1 in $\times$ 1 in rock specimen saturated with about 30% Wood's metal at 7.2 psia equilibrium pressure. Large percolating clusters have been formed. An SEM photomicrograph collage of an enlarged partial section from the last figure (Figure 6.14) show that there are relatively few intergranular conduits connected by larger throats filled with the nonwetting phase. At this stage, a substantial effect on effective permeability is observed. Figure 5.8 shows an SEM photomicrograph collage of a 1 in $\times$ 1 in rock specimen saturated with approximately 50% of Wood's metal at 8.5 psia equilibrium pressure. Smaller percolating clusters are observed. An SEM photomicrograph collage of an enlarged partial section from the last figure and its associated pore contours areas (Figure 5.9), show that there are still many large (intergranular) pore segments connected by small throats that do not contribute to the flow of the nonwetting phase in the rock. In

addition, the grain-contact pore space (i.e., thin sheets and micropores) does not contribute, either. Furthermore, simple statistical analysis of pore contour areas obtained from Figure 6.14 has shown that relatively few conduits connected by large intergranular throats carry up to about 30% of the nonwetting fluid in the porous media under consideration, producing a clustered structure. At this stage, the effective permeability is low (Table 6.3). Thus, we have found that a large percentage of the permeability of the medium is contributed by a relatively small number of intergranular conduits connected by larger throats of narrow size distribution and of high hydraulic conductance. The effect of nonwetting phase saturation on effective permeability is summarized in Table 6.4.

6.4.2 Irreducible nonwetting phase saturation

In contrast to the previously discussed 'irreducible wetting phase saturation', it is observed that the trapped clusters of a nonwetting fluid are separate entities that are not hydraulically interconnected with each other (Figure 6.5). We have found that when the wetting phase saturation is about 70%, the effective permeability is zero. Thus the nonwetting fluid simply ceases to flow when its saturation falls below the irreducible nonwetting phase saturation limit ($\sim$ 30%) because its continuity breaks down, leaving isolated stranded clusters of disconnected fluid.

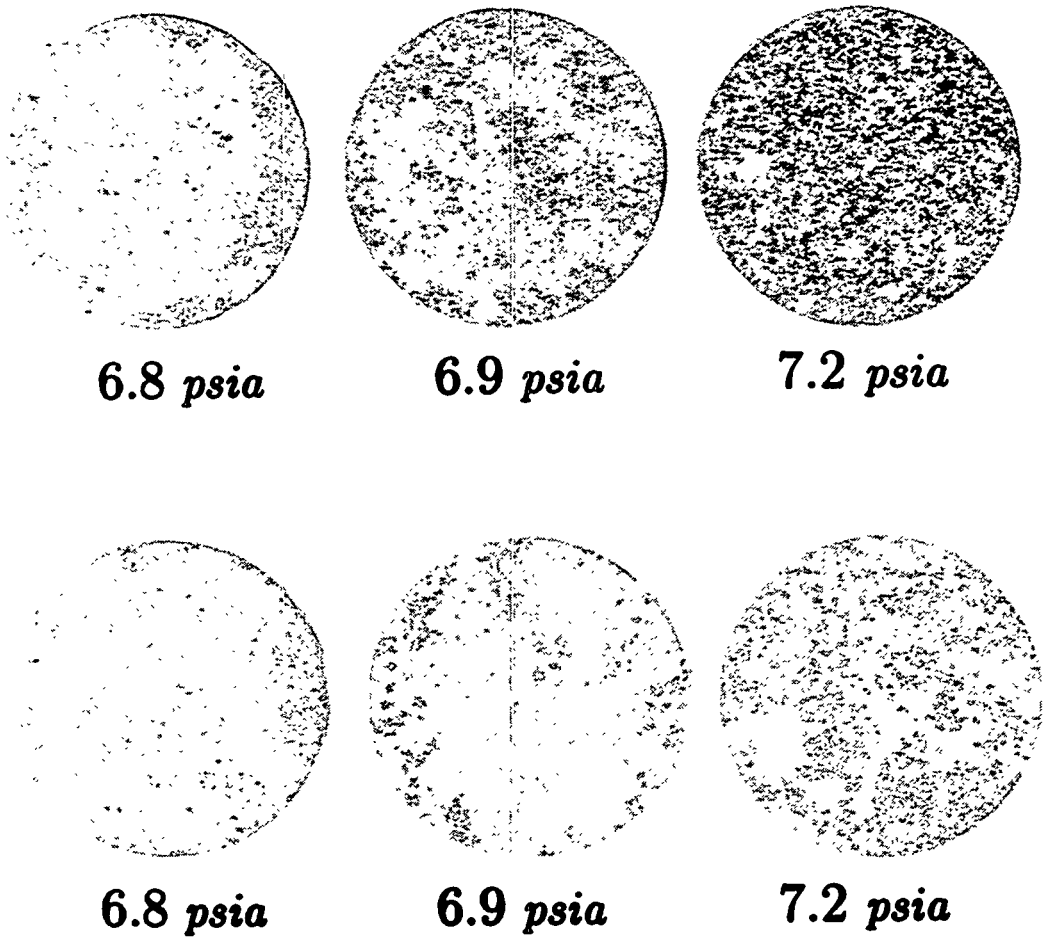

FIG. 6.12: Axial quarter sections of Berea sandstone core partially saturated with a nonwetting fluid (Wood's metal) at different equilibrium pressures, and solidified in place. The procedure allows for direct observation and analysis of the fluid distribution at a fixed pore pressure and saturation level. The sections reveal that the fluid distributions are composed of a set of imbibing clusters correlated in space.

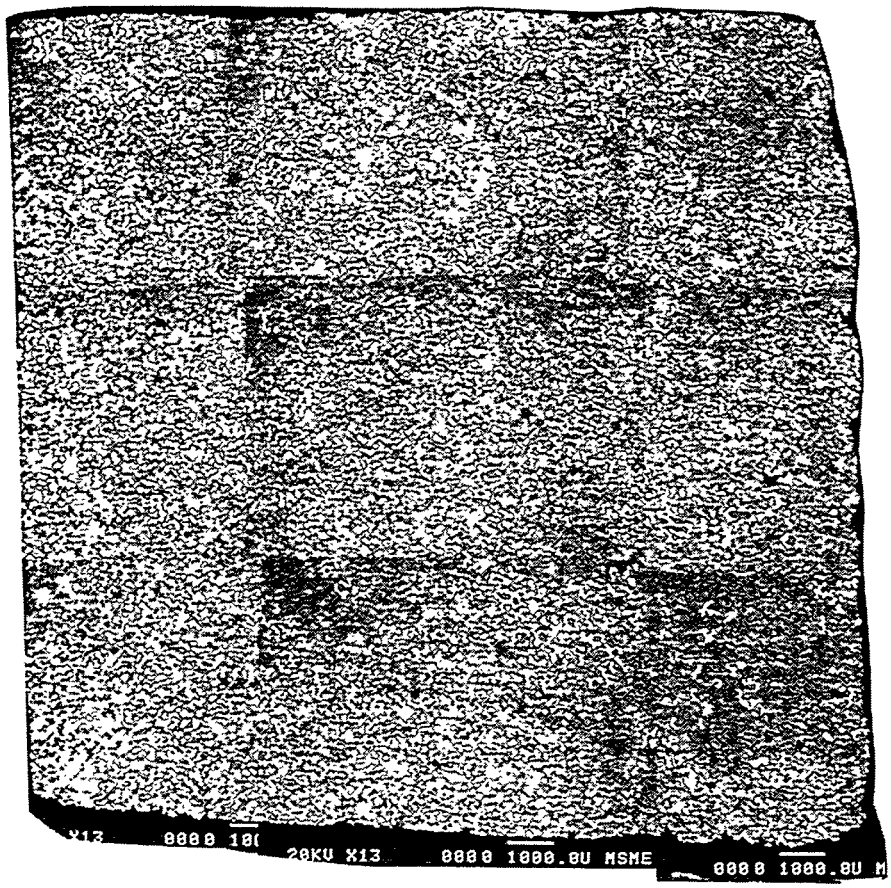

FIG. 6.13: SEM photomicrograph collage of a 1 in × 1 in Berea sandstone specimen partially saturated with approximately 30% Wood's metal at 7.3 psia equilibrium pressure. The rock is composed mainly of quartz grains (gray phase) and pore space that has been impregnated with Wood's metal (white phase) and epoxy (black phase) for imaging purposes.

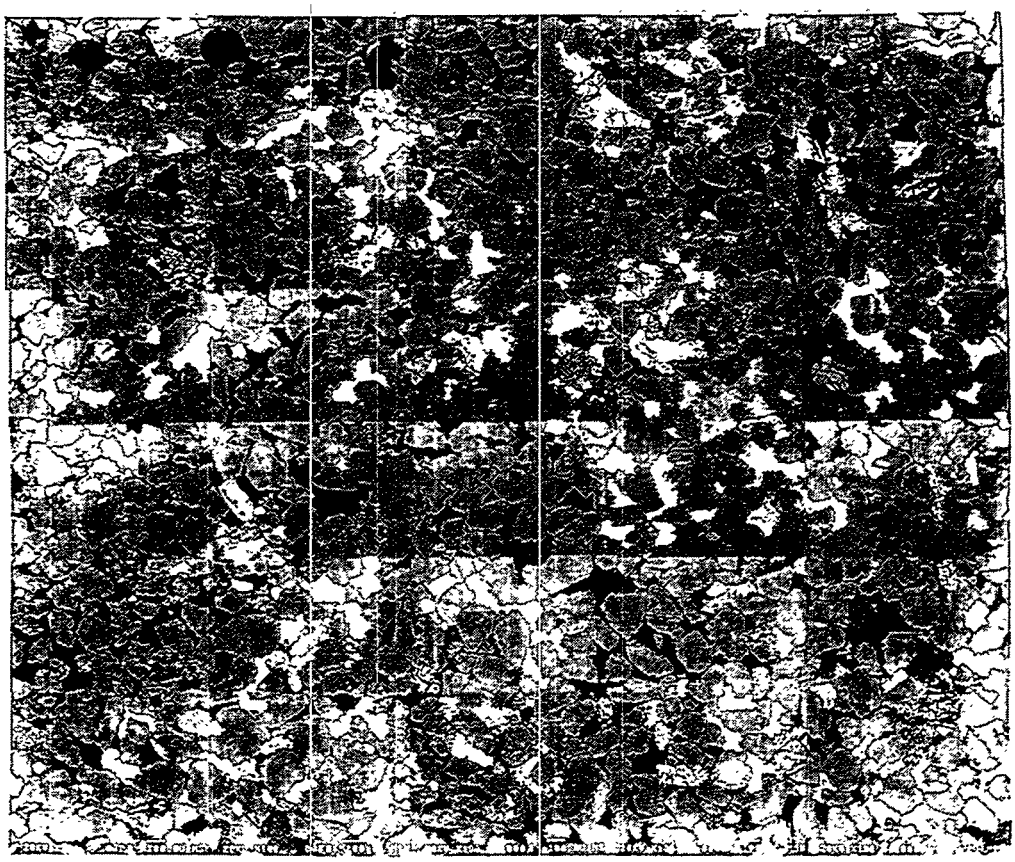

FIG. 6.14: SEM photomicrograph collage of an enlarged partial section obtained from a Berea sandstone sample partially saturated with approximately 30% Wood's metal (white phase) at 7.3 psia pressure shown in Fig. 6.13. Actual width of field is about 5 mm.

TABLE 6.4: Nonwetting fluid invasion and permeability.

- $0.0 \leq S_{nw} \leq 0.2$
  Nonwetting fluid fills few intergranular conduits connected by larger throats of narrow distribution. Large clusters are observed.

  $\Longrightarrow$ Very large effect on effective permeability.

- $0.2 < S_{nw} \leq 0.4$
  Nonwetting fluid fills remaining more tortuous intergranular conduits connected by large throats of narrow distribution. Smaller clusters are observed.

  $\Longrightarrow$ Smaller effect on effective permeability.

- $0.4 < S_{nw} \leq 0.7$
  Nonwetting fluid fills grain-contact and intergranular pore space connected by smallest throats.

  $\Longrightarrow$ Very small effect on effective permeability.

- $0.7 < S_{nw} \leq 1.0$
  When is structure disconnected? i.e., wetting phase is coating connected intergranular pore space filled with the nonwetting phase and is present in intergranular pore space connected by smaller throats as well.

6.5 Results and discussion

Experimental studies have been conducted aimed at studying permeability of a partially saturated rock. For this purpose, the effective permeabilities of the spaces not occupied by the wetting fluid (paraffin wax) or the nonwetting fluid (Wood's metal), respectively, have been measured at various saturations, while solidifying the other phase. The experiments were conducted on Berea sandstone samples of $\sim$ 600 mD absolute permeability. The absolute permeability was extrapolated from the effective permeability curve after partially filling the rock pore space with paraffin. The extrapolated value of permeability at zero paraffin saturation ($\sim$ 600 mD) is higher than the measured value of permeability obtained at the same saturation when using triple-distilled water ($\sim$ 300 to 400 mD). A possible explanation is that the paraffin immobilizes the effect of clay present in the rock pore space (e.g., prevents clay migration, swelling, etc.).

The relative permeabilities, k_r, obtained as a ratio of effective permeability to absolute permeability of the rock, are shown in Figure 6.15. The wetting phase relative permeability is concave upward while the nonwetting phase relative permeability has an S shape. The shape of the nonwetting phase relative permeability in the steep-sloped zone indicates that for a small reduction in nonwetting phase (increase in wetting phase) there is a relatively large decrease in relative permeability. This rapid decrease is due to the occupation of larger pores or flow paths by the wetting phase. The nonwetting relative permeability curve reaches nearly 100% at a nonwetting phase saturation less than a 100% which means that part of the interconnected space composed by smaller pores (e.g., grain-contact) does not contribute to the nonwetting phase relative permeability of the porous medium, but does contribute to electrical conductivity (Chapter 4). The sum of the relative permeabilities is less than unity. One of the reasons is that part of the pore channels available for flow of a fluid may be reduced in size by the other fluid present in the rock. Another reason is that immobilized droplets of one fluid may completely plug some constrictions in a pore channel through which the other fluid would otherwise flow. The laboratory-derived relative permeability data conforms with typical relative permeability curves using oil and gas as the wetting and nonwetting phase, respectively, in Berea sandstone using

conventional methods (Figure 6.16). It is observed that the two curves have similar trends. The relative permeabilities are nearly symmetric within the same range of saturation at which intergranular channels connected by larger throats control effective permeability. This observation then is consistent with fluid flow studies that show that when immiscible fluids flow simultaneously through a porous medium, each fluid follows its own flow path (Honarpour et al., 1986). When Darcy's law is applied to the measurement of relative permeabilities of immiscible fluids, it is assumed that the interfaces are steady, the phases flow through their respective channels as if the other phase were absent, and each fluid phase obeys Darcy's law (Yadav et al., 1987). These conditions are met in the application of this technique. Thus, it is possible to measure the macroscopic properties using only single-phase experiments, while the other phase is frozen in place. It is worth noting that strong phase interference has been found experimentally for the relative permeability function (e.g., $k_{rw} + k_{rnw} << 1$) of a 3-D porous media. Moreover, the fluid phases are allowed to flow together in a rather narrow range of saturation.

The capillary pressure curve obtained when partially saturating the rock with the nonwetting phase (Wood's metal) is presented in Figure 5.2. Our result is consistent with typical capillary pressure curves based on conventional mercury porosimetry saturation for Berea sandstone (Figure 5.3). The initial portion of the curve with positive curvature is interpreted as being associated with surface defects. The rapid rise in the curve occurs when the intruded Wood's metal initially forms a connected cluster. Thereafter, there is a sharp increase in fluid saturation with a corresponding small increase in capillary pressure due to the narrow distribution of pore-throat sizes. In our previous work on Berea sandstone capillary pressure function and its relationship to microgeometry (Chapter 5), we have used a simple functional form to determine average pore and throat sizes controlling capillary pressure and relative permeability. Our result, assuming a lognormal distribution of pore sizes, gave a narrow distribution of intergranular pore throats represented by a hydraulic radius $R_{H_m} = 6.6$ μm, and a standard deviation $\sigma = 0.14$. The corresponding nonwetting fluid distributions are presented in Figure 6.12. It is found that the flow network is composed by spatially correlated percolating clusters. As the nonwetting phase saturation reduces, the network for this phase breaks down and becomes discontinuous

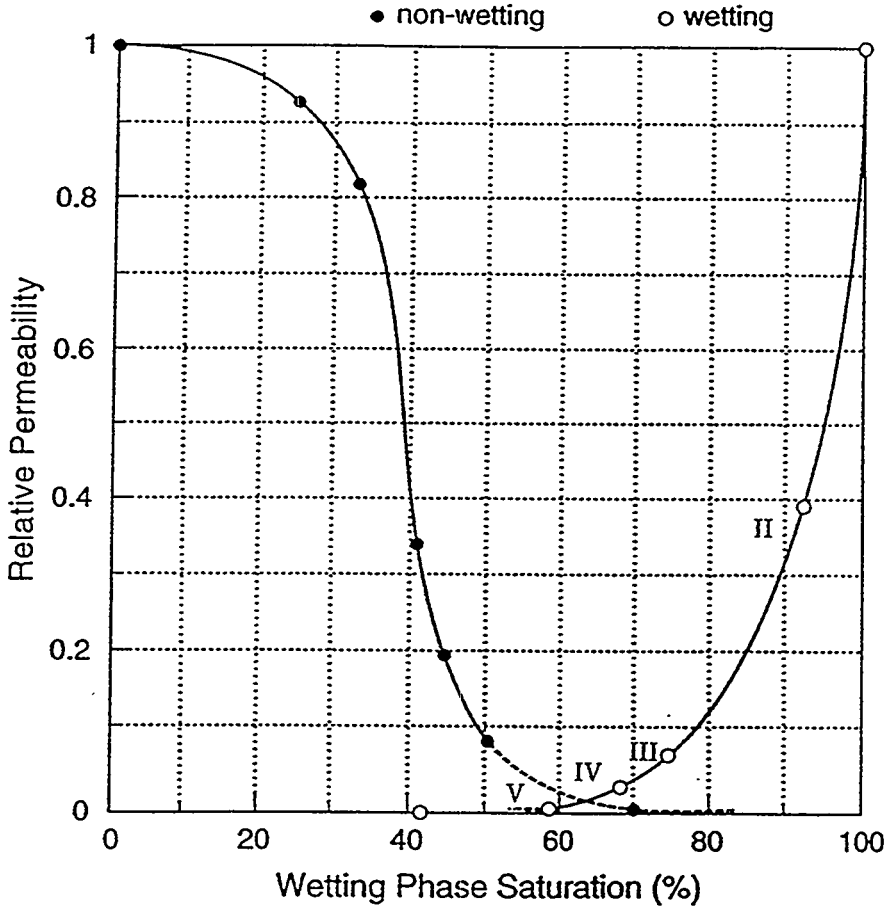

FIG. 6.15: Relative permeability vs. saturation curve for Berea sandstone using two fluids, serving as the wetting and nonwetting phases, that can be frozen in situ, one at a time. The effective permeability of the spaces not occupied by the wetting fluid (paraffin wax) and the nonwetting fluid (Wood's metal), respectively, have been measured at various saturations in Berea sandstone samples of absolute permeability of 600 mD. The capillary pressures (in psia) for the points on the plot are II = 6.9, III = 7.2, IV = 7.3, and V = 7.7 psia.

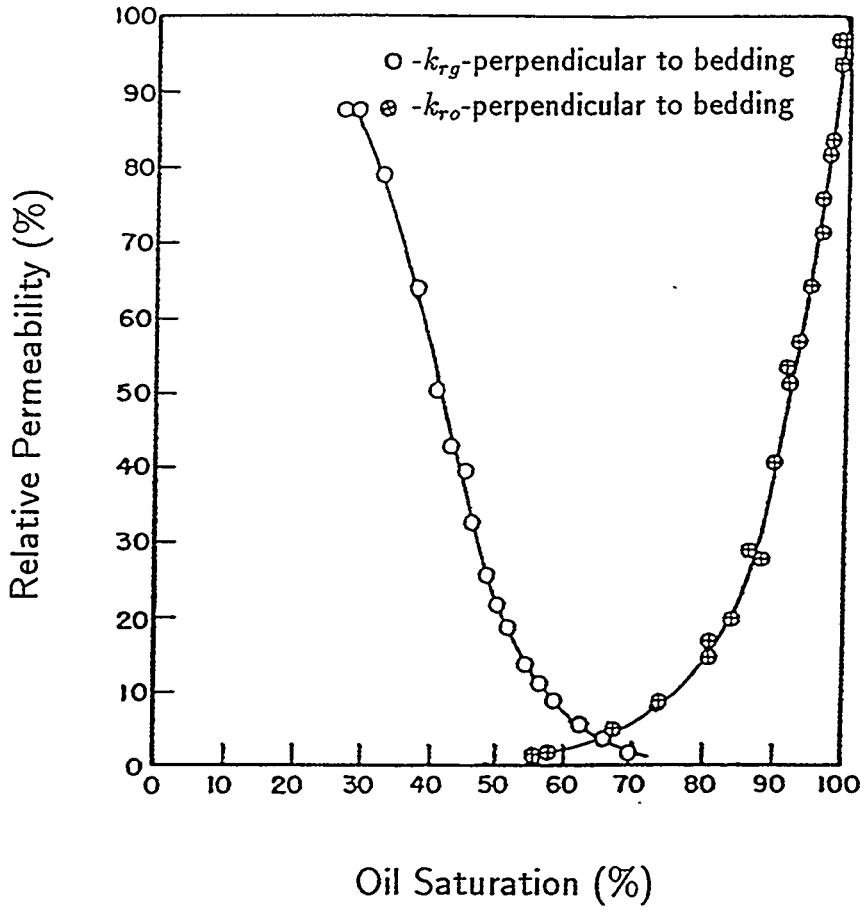

FIG. 6.16: Relative permeability vs. saturation curve for Berea sandstone measured by Corey and Rathjens (1956) using oil and gas.

and hydraulically disconnected. Thus, the irreducible nonwetting phase saturation, S_{rnw}, is found to have a value of about 30% (percolation threshold). In contrast, since the wetting phase constitutes a continuous network even at low wetting phase saturations, the irreducible wetting phase saturation becomes a function of applied external pressure (e.g., $S_{rw} < 30\%$).

The permeability of a partially-saturated rock is controlled by the rock structure and topology as well as the physics and chemistry of mineral-fluid interactions. To understand the relationships, we have measured the effective permeability in the pore spaces not occupied by a wetting fluid (paraffin wax), or a nonwetting fluid, after solidifying the fluid in place. It is important to recognize that when the rock is partially saturated with the hydrocarbon paraffin, the clay minerals present in the rock pore space are immobilized. Thus, permeability extrapolated to paraffin saturation of zero, $k \approx 600$ mD, corresponds to the permeability of the 'clean' rock (e.g., without clay). Effective permeability data have been studied in light of the fluid distributions observed at different saturations with the aid of a complete pore cast and its associated rock section. Our analysis shows that (1) $\sim$ 30% of the pore space consists of grain-contact pores (i.e., thin sheets and micropores) and intergranular pores connected by smaller throats, (2) $\sim$ 40% of the pore space comprises intergranular conduits composed of pores connected by larger throats, and (3) $\sim$ 30% of the intergranular pore space remains hydraulically disconnected. The grain-contact pore space of large surface areas (thin sheets), micropores, and intergranular pores connected by smaller throats provide only minor alternate paths for the fluid to flow to the intergranular conduits connected by larger throats.

On the basis of our experimental observations of the relationship between microscopic nonwetting fluid occupancy and the fluid distributions and of their effect on capillary pressure of Berea sandstone, we have found that relatively small number of intergranular channels connected by large throats of narrow size distribution are responsible for conducting a relatively large amount of the nonwetting fluid through the medium (at least in the saturation range up to approximately 50%). In fact, we have also found that a large percentage of the permeability of the medium is contributed by a relatively small number of conduits connected by large intergranular throats of narrow size distribution and high hydraulic conductance.

7 SUMMARY AND CONCLUSIONS

An attempt to assemble a comprehensive picture of a sedimentary rock based on observation of pore casts, laboratory measurements, and a physically accurate representation of the phenomena has been achieved.

The analytical calculations of transport properties are based on pore microgeometry measurements obtained directly from two-dimensional scanning electron microscope (SEM) photomicrographs of rock sections partially filled with wetting and nonwetting liquids solidified in place. Account has been taken of the fact that the rock cross-sections are randomly oriented with respect to the channel axes. The orientation effect is corrected by means of geometrical and stereological considerations. In addition, account is also taken of possible variation of the cross-sectional area along the length of each tube, i.e., pore throats and pore bodies.

Good agreement was found between measured and predicted analytical calculations of permeability for a variety of sandstones using the cubic lattice-effective medium model of intergranular pore space (discrete approach). It is found that the ratio of average pore throat to pore body ranges from about 0.3 to 0.5 for different sandstones. If a parallel-effective medium or series model is used instead, permeability is overpredicted or underpredicted, respectively, by at least a factor of three. This investigation highlights the importance of pore connectivity in understanding the relationships between pore microstructure and permeability.

A perimeter-area power-law relationship of a smooth representation of the pore space was found for a variety of rocks of different porosities. Examples have been given of how the area-perimeter power-law information together with a pore-size distribution and a classical model of the pore space can be used for making quantitative predictions of permeability (statistical approach). The analysis emphasizes the importance of pore connectivity in understanding the relationship of permeability and rock microstructure.

The region of validity of the Kozeny-Carman permeability formulas for consolidated porous media and their relationship to the microscopic spatial variations of channel dimensions has been established. The permeabilities of most sandstones have

been found to fall in zone II of the conductance envelope. Thus, the permeabilities predicted by the Kozeny-Carman formulas are approximately valid within a factor of three of the observed values. This finding is a direct result of the various sandstones 'principal' pore networks approaching homogeneity in channel dimensions. For highly inhomogeneous rock-pore-space systems falling in zone III of the conductance envelope, the critical path analysis (which focuses on the details of the critical paths along which much of the flow must occur) can be applied within limits to obtain the hydraulic permeability.

Fair-to-good agreement was found between measured and predicted electrical conductivities for a variety of sandstones when using the cubic lattice-effective medium model of the intergranular pore space. In particular, good agreement was found in case of a poorly consolidated rock such as Saint-Gilles sandstone, whereas the agreement was not very good for well-cemented rocks. The possible reason(s) for this effect were investigated experimentally.

In the experimental studies, wetting and nonwetting phases that can be frozen in place have been used one at a time to allow measurement of effective transport properties (hydraulic and electrical) and to allow direct analysis of fluid distributions in the pore space after the experiment. At low wetting phase saturations in Berea sandstone pore space (saturations less than 30%), the wetting fluid preferentially invades grain contact pore space (i.e., thin sheets and micropores) while only coating the intergranular pore space connected by larger throats. A substantial effect on effective formation factor (but a very small effect on effective permeability) is found.

It is observed that there is no unique definition of pore structure and pore-size distribution to model permeability and formation factor, e.g., permeability is strongly controlled by intergranular pore space whereas the formation factor is controlled by both intergranular and grain contact pore spaces. It is found that there is no single characterization of the Archie saturation exponent n, for the full range of saturation. Archie saturation exponents are found to vary from about 3 when mainly grain contact pore space is filled with the wetting fluid, to about 5 when mainly intergranular conduits connected by the larger throats are filled with the wetting fluid, with a critical electrolyte saturation (S_{crit}) of 0.7. The basic intergranular pore space model

that was employed in the analytical calculations of formation factor has to be modified to incorporate relevant geometrical and topological characteristics important for electrical conductivity of consolidated rocks (e.g., grain-contact pore space).

Although the change in trend of Berea sandstone electrical conductivity at low electrolyte concentrations reflects the contribution of surface conduction due to clays, this represents a negligible contribution to formation factor for most practical applications.

Pore microgeometry-based analytical calculations of the capillary pressure vs. saturation function have been conducted. The mathematical expression depends on the distribution of pore hydraulic radii and the area-perimeter power-law relationship. The analytical predictions of capillary pressure are compared to laboratory capillary pressure curves obtained using Wood's metal alloy as the nonwetting phase intead of the conventional mercury porosimetry. This technique allows the examination of the occupied pore space after the experiment. The general shape of our experimental capillary pressure vs. saturation curve for Berea sandstone is consistent with typical capillary pressure curves reported in the literature obtained using mercury porosimetry. The nonwetting fluid in Berea sandstone (in the saturation range up to 50%) invades and fills relatively few intergranular conduits connected by large throats, producing a clustered structure, and controlling capillary pressure within that saturation range. The analytical calculations of Berea sandstone capillary pressure vs. saturation relation together with the analysis of the nonwetting phase fluid distributions in the rock pore space show that the experimental capillary pressure vs. saturation function (in the saturation range up to about 50% saturation) is controlled by relatively few channels connected by large intergranular throats of narrow size distribution, represented by a mean hydraulic radius of approximately 6.6 μm and a standard deviation of 0.14. This analysis confirmed that pore throats are smaller than pore bodies with an average aspect ratio of 0.5 for Berea sandstone.

The experimental relative permeability and capillary pressure data of Berea sandstone has been analyzed in light of the distribution of wetting and nonwetting phases in the rock pore space. The analysis shows that (1) $\sim$ 30% of the pore space consists of grain-contact pores (i.e., thin sheets and micropores) and intergranular pores

connected by smaller throats, (2) $\sim$ 40% of the pore space comprises intergranular conduits composed of pores connected by larger throats, and (3) $\sim$ 30% of the intergranular pore space remains hydraulically disconnected. The grain-contact pore space of large surface areas (thin sheets), micropores, and intergranular pores connected by smaller throats provide only minor alternate paths for the fluid to flow to the intergranular conduits connected by larger throats.

At low wetting phase saturations in Berea sandstone pore space, the wetting fluid preferentially invades grain-contact pore space, coats intergranular pore space connected by larger throats, thus permitting the nonwetting fluid to rapidly invade relatively few intergranular conduits connected by large throats, controlling relative permeability and capillary pressure. Thus, pore geometry and topology establish a hierarchy that governs how wetting and nonwetting fluid invasion processes occur in the pore space, allowing the two processes to be complementary, i.e., each fluid follows its own path.

The laboratory-derived relative permeability data for Berea sandstone conforms well with typical relative permeability curves obtained using conventional methods. Strong phase interference has been found experimentally for the relative permeability function of a 3-D porous media.

The permeability of a partially-saturated rock such as Berea sandstone is controlled by the rock structure and topology as well as the physics and chemistry of mineral-fluid interactions. When the rock is partially saturated with the hydrocarbon paraffin, the clay minerals present in the rock pore space are immobilized. Thus, permeability extrapolated to paraffin saturation of zero, corresponds to the permeability of the 'clean' rock (e.g., without clay).

The experimental relative permeability data of Berea sandstone has been examined near threshold saturation conditions. As the nonwetting phase saturation reduces, the network for this phase breaks down and becomes discontinuous and hydraulically disconnected. Thus, the irreducible nonwetting phase saturation is found to have a value of about 30% (percolation threshold). In contrast, since the wetting phase constitutes a continuous network even at low wetting phase saturations, the irreducible wetting phase saturation becomes a function of applied external pressure reaching a

value less than 30%.

It is clear from this study that the transport properties of porous media (hydraulic and electrical) are strongly controlled by both pore microgeometry and topology as implicit, for example, in constitutive relations expressed by Eqs. (12), (82), (94), and (140).

Finally, the analytical/experimental method can be applied to various extensions. These include (a) to develop a network/percolation model to estimate two-phase relative permeabilities of Berea sandstone from direct measurements of pore microgeometry obtained from 2-D SEM photomicrographs of thin sections, (b) to find constitutive relationships between the area-perimeter power-law relationship of pores and two-phase relative permeabilities, (c) to study the rock void space power-law relationships (i.e., perimeter-area, volume-surface) in light of the law derived by Mandelbrot (1988) for islands whose boundaries are fractal: $P = \epsilon^D A^{D/2}$, where ϵ is some constant that depends on the length of the measuring grid size, and D is the fractal dimension of the pore perimeter, (d) to develop constitutive relations between single and two-phase transport properties (hydraulic and electrical) of unconsolidated porous media to pore microstructure, and to compare these to consolidated porous media, (e) to measure three-phase relative permeabilities of consolidated porous media using multiple fluids that can be solidified in place to allow direct observation and analysis of the fluid distributions in the pore space after the experiment, and (f) to measure single and multiphase transport properties of fractured media and to study their relationship to microstructure and heterogeneity.

References

[1] Ambegaokar, V., Halperin, B.I., and Langer, J.S. 1971. Hopping conductivity in disordered systems. Phys. Rev. B, 4(8), p. 2612.

[2] Anderson, W.G. 1986. Wettability literature survey-Part 3: The effects of wettability on the electrical properties of porous media. J. Pet. Technol., 12, p. 1371.

[3] Archie, G.E. 1942. The electrical resistivity log as an aid in determining some reservoir characteristics. Trans. AIME, 146, p. 54.

[4] Batra, V.K. 1973. An experimental investigation of the structure of porous media and its relation to oil recovery. Ph.D. Thesis. University of Waterloo, Canada.

[5] Berker, R. 1963. Integration des equations du mouvement d'un fluid visqueux incompressible. Handbuch der Physik, 8(2), p. 1. Springer-Verlag, Berlin.

[6] Berryman, J.G., and Blair, S.C. 1987. Kozeny-Carman relations and image processing methods for estimating Darcy's constant. J. Appl. Phys., 62(6), p. 2221.

[7] Beyer, W.H. 1988. CRC Standard Mathematical Tables 28th Edition. CRC Press, Inc. Boca Raton, Florida.

[8] Botset, H.G. 1940. Flow of gas liquid mixtures through consolidated sands. Trans. AIME, 136, p. 91.

[9] Calhoun, J.C. 1953. Fundamentals of Reservoir Engineering. University of Oklahoma Press. Norman, Oklahoma.

[10] Carman, P.C. 1941. Capillary rise and capillary movement of moisture in fine sands. Soil Sci., 52, p. 1.

[11] Caruso, L., Simmons, G., and Wilkens, R. 1985. The physical properties of a set of sandstones-Part I. The samples. J. Rock Mech. Min. Sci. Geomech. Abstr., 22(6), p. 381.

[12] Chatzis, I., and Dullien, F.A.L. 1982. Application of the theory of percolation for a model of drainage in porous media and relative permeability of injected nonwetting liquid. Rev. l'Institut Francais du Petrole, 37, p. 183.

[13] Chatzis, I., Morrow, N.R., and Lim, H.T. 1983. Magnitude and detailed structure of residual oil saturation. SPEJ, April, p. 311.

[14] Chatzis I., and Dullien, F.A.L. 1985. The modeling of mercury porosimetry and the relative permeability of mercury in sandstones using percolation theory. A.I.Ch.E., 25(1), p. 47.

[15] Chatzis, I., and Dullien, F.A.L. 1977. Modelling pore structure by 2-D and 3-D networks with application to sandstones. J. Can. Pet. Technol., 16, p. 97.

[16] Corey, A.T., and Rathjens, C.H. 1956. Effect of stratification on relative permeability. Transactions AIME, 207, p. 358.

[17] Dewan, J.T. 1983. Essentials of Modern Open-Hole Log Interpretation. Penn Well. Tulsa, Oklahoma.

[18] Doyen, P. 1988. Permeability, conductivity, and the geometry of sandstone. J. Geophys. Res., 93(B7), p. 7729.

[19] Dullien, F.A.L., and Dhawan, G.K. 1974. Characterization of pore structure by a combination of quantitative photomicrography and mercury porosimetry. J. Coll. Int. Sci., 47, p. 337.

[20] Dullien, F.A.L. 1979. Porous Media Fluid Transport and Pore Structure. Academic Press.

[21] Efros, A.L. 1986. Physics and Geometry of Disorder. Mir publishers, Moscow.

[22] Falta, R.W., Pruess, K., Javandel, I., and Witherspoon, P.A. 1992. Numerical modeling of steam injection for the removal of nonaqueous phase liquids from the subsurface, 2, code validation and application. Water Resour. Res., 28(2), p. 433.

[23] Fatt, I., and Dykstra, H. 1951. Relative Permeability Studies. Trans. AIME, 192, p. 249.

[24] Fatt, I. 1956a. The network model of porous media: 1. Capillary pressure characteristics. Trans. AIME, 207, p. 144.

[25] Fatt, I. 1956b. The network model of porous media: 2. Dynamic properties of a single size tube network. Trans. AIME, 207, p. 160.

[26] Fatt, I. 1956c. The network model of porous media: 3. Dynamic properties of networks with tube radius distribution. Trans. AIME, 207, p. 164.

[27] Hansen, J.P., and Skjeltorp, A.T. 1988. Fractal pore space and rock permeability implications. Phys. Rev. B, 38(4), p. 2635.

[28] Hassler, G.L., Rice, R.R., and Leeman, E.H. 1936. Investigations of recovery on the oil from sandstones by gas-drive. Transactions AIME, 118, p. 116.

[29] Honarpour, M., Koederitz, L., and Harvey, A.H. 1986. Relative Permeability of Petroleum Reservoirs. CRC Press, Inc. Boca Raton, Florida.

[30] Jerauld, G.R., and Salter, S.J. 1990. The effect of pore structure on hysteresis in relative permeability and capillary pressure: pore-level modeling. Transport in Porous Media, 5, p. 103.

[31] Khilar, K.C., and Fogler, H.S. 1984. The existence of a critical salt concentration for particle release. J. Coll. Int. Sci., 101, p. 214.

[32] Kirkpatrick, S. 1971. Classical transport in disordered media: Scaling and effective-medium theories. Phys. Rev., 27(25), p. 1722.

[33] Kirkpatrick, S. 1973. Percolation and conduction. Rev. Mod. Phys., 45(4), p. 574.

[34] Kirkpatrick, S. 1979. Models of disordered materials. Edité par Roger Balian, Roger Maynard, Gerard Toulouse. La Matière Mal Condensée. Ill-Condensed Matter. North Holland Publishing Company, Amsterdam-New York-Oxford.

[35] Koplik, J., and Lasseter, T.J. 1984. One- and two-phase flow in network models of porous media. Chem. Eng. Commun., 26, p. 285.

[36] Koplik, J., and Lasseter, T.J. 1985. Two-phase flow in random network models of porous media. J. Soc. Pet. Eng., Feb., p. 89.

[37] Koplik, J., Lin, C., and Vermette, M. 1984. Conductivity and permeability from microgeometry. J. of Appl. Phys., 56(11), p. 3127.

[38] Leblanc, M. 1988. Institut Francais du Petrole. Division Géologie. Gaz de France. Direction des Etudes et Techniques Nouvelles. Départment "Réservoirs Souterrains". Nos Réf.: M.D5-LM/DT-G1036.

[39] Lenormand, R., Touboul, E., and Zarcone, C.: Numerical models and experiments on immiscible displacements in porous media. J. Fluid Mech., 189, p.165.

[40] Mandelbrot, B.B. 1982. The Fractal Geometry of Nature. Freeman, San Francisco.

[41] Matheron, G. 1967. Eléments pour une Théorie des Milieux Poreux. Masson, Paris.

[42] Mohanty, K.K., and Salter, S.J. 1982. Multiphase flow in porous media: 2. Pore-level modeling. Paper SPE presented at the 1982 SPE Annual Technical Conference and Exhibition, Sept., New Orleans.

[43] Mungan, N. 1968. Permeability reduction due to salinity changes. Journal of Canadian Petroleum Technology, 7(8), p. 113.

[44] Muskat, M. 1937. The Flow of Homogeneous Fluids through Porous Media. Ann Arbor, Michigan.

[45] Purday, H.F.P. 1949. Streamline Flow. Constable & Company, London.

[46] Råde, L., Westergren, B. 1990. Mathematics Handbook. CRC Press, Boca Raton, Florida.

[47] Reserves of crude oil, natural gas liquids, and natural gas in the U.S. and Canada as of December 31, 1977. American Petroleum Institute, 32, (1978).

[48] Rose, W., and Witherspoon, P.A. 1956. Studies of Waterflood Performance: II. Trapping Oil in a Pore Doublet. Producers Monthly 21(2), p. 32.

[49] Scheidegger, A.E. 1974. The Physics of Flow through Porous Media. University of Toronto Press.

[50] Schultze, K. 1925a. Kapillarität, verdunstung, und auswitterung. Kolloid Ztschr., 36, p. 65.

[51] Schultze, K. 1925b. Kapillarität und benetzung. Kolloid Ztschr., 37, p. 10.

[52] Sokolnikoff, I.S. 1956. Mathematical Theory of Elasticity. Mc.Graw-Hill, New York.

[53] Sposito, G. 1984. The Surface Chemistry of Soils. Oxford University Press, New York.

[54] Stegemeir, G.L. 1977. Mechanism of Entrapment and Mobilization of Oil in Porous Media. Improved Oil Recovery by Surfactant and Polymer Flooding. D.O. Shah and R.S. Schechter (eds.), Academic Press.

[55] Swanson, B.F. 1981. A simple correlation between permeabilities and mercury capillary pressures. JPT, Dec., p. 2498.

[56] Touboul, E., Lenormand, R., and Zarcone, C. 1987. Immiscible displacements in porous media: Testing network simulators by micromodel experiments. Paper SPE 16954 presented at the 1987 SPE Annual Technical Conference and Exhibition, Dallas, Sept.

[57] Underwood, E.E. 1970. Quantitative Stereology. Addison-Wesley, Reading, Massachusetts.

[58] Walsh J.B., and Brace, W.F. 1984. The effect of pressure on porosity and the transport properties of rocks. JGR, 89(11), p. 9425.

[59] Williams, D.J.A., and Williams, K.P. 1978. Electrophoresis and zeta potential of kaolinite. J. Coll. Int. Sci., 65, p. 79.

[60] Wong, P.-z., Koplik, J., and Tomanic, J.P. 1984. Conductivity and permeability of rocks. Phys. Rev. B, 30(11), p. 6606.

[61] Wyllie, M.R.J., and Gardner, G.H.F. 1958. The generalized Kozeny-Carman equation, its application to problems of multi-phase flow in porous media. World Oil, 146, p. 121.

[62] Wyllie, M.R.J. 1963. The Fundamentals of Electric Log Interpretation. Academic Press, Inc., New York.

[63] Wyckoff, R.D. and Botset, H.G. 1936. Flow of gas liquid mixtures through sands. Physics, 7, p. 325.

[64] Yadav, G.D., Dullien, F.A.L., Chatzis, I., and Macdonald, I.F. 1987. Microscopic distribution of wetting and nonwetting phases in sandstones during immiscible displacements. SPE Reservoir Engineering, May, p. 137.

[65] Yanuka, M., Dullien, F.A.L., and Elrick, D.E. 1986. Percolation processes and porous media: I. Geometrical and topological model of porous media using a three-dimensional joint pore size distribution. J. Coll. Int. Sci., 112, p. 24.

APPENDIX A

EXPLORATORY SIMULATIONS OF GAS INJECTION TESTS IN AN UNDERGROUND ROCK LABORATORY

A: EXPLORATORY SIMULATIONS OF GAS INJECTION TESTS IN AN UNDERGROUND ROCK LABORATORY[1]

Abstract

A computational model of a gas injection test in a dual-porosity dual-permeability medium under isothermal conditions was developed. Results from the numerical simulations provide general guidelines for the design of the phase II gas test in the fracture investigation (FRI) zone at Grimsel, Switzerland.

A.1 Introduction

The Nationale Genossenschaft für die Lagerung radioaktiver Abfaelle (NAGRA) of Switzerland is studying the feasibility of disposing low and intermediate level nuclear wastes at an Oberbauenstock mountain site. The corrosion of metals and microbial degradation of the organic materials from a nuclear waste repository are expected to generate large amounts of gas, the main constituent being hydrogen with minor amounts of methane, carbon dioxide, and others (Wiborgh et al.[1]). From the data given by Wiborgh et al.,[1] it can be estimated that due to the expected gas release, pressures in the repository may rise to several hundred bars. The high pressure could endanger the engineered repository structure unless proper venting is installed. Additionally, the influence of gas production on solute transport may produce: 1) a displacement of contaminated water by the gas front, 2) a pumping effect due to pressure variations in the gas front, and/or 3) a mixed flow of contaminated water and gas. Thus it becomes important to study the evolution of a free gas phase (and associated multiphase effects) from waste package corrosion in an initially saturated environment.

[1]This work was jointly supported by the U.S. Department of Energy under Contract No. DE-AC03-76SF00098 and by the Swiss National Cooperative for the Storage of Nuclear Waste (NAGRA).

A.2 Radial flow in a fracture with permeable rock matrix

The evolution of a free gas phase in an initially saturated environment is modeled numerically via the multiphase simulator TOUGH[2], using its air component to model the gas behavior. For an exploratory calculation a dual-porosity, dual-permeability system with only one fracture and one matrix continuum was defined using an idealized radial flow geometry (Figures A-1a and A-1b).

The problem design and parameters for the numerical simulation were provided by Dr. Bob Andrews (memo of September 1, 1988)[3]. The following changes to the specified data were made (Table A-1):

- Corey[4] relative permeability functions instead of Grant[5] relative permeability functions were used, as it is considered that $k_{rg} + k_{rl} \leq 1$ is a more realistic and conservative approach than is $k_{rg} + k_{rl} = 1$[6]; i.e., Corey relative permeability curves give higher pressure and lower saturation versus time curves for well grid block AA-1 (Figures A-2a and A-2b).
- The gas injection rate was reduced one order of magnitude (from 10^{-4} to 10^{-5} kg/s), since pressure at the injection grid block increased to a value larger than 60 bars with the higher injection rate (Figures A-3a and A-3b).
- Gravity was neglected since if a pressure $P = 1$ bar was taken at $z = 0$ m, we would obtain a pressure $P = 0$ bar at $z = 10$ m (i.e., at the top of the matrix grid). Also, gravity effects are minor as compared to the pressure-time response from gas injection tests (Figures A-2b, A-3a, A-3b, and A-3c).
- An initial gas saturation of 1% across the domain was specified to decrease the nonlinear effects associated with the advance of the gas injection front. To avoid unphysical effects from this gas saturation, an irreducible gas saturation of 2% in the fractures and of 10% in the matrix was introduced so that the initial gas is immobile.
- Capillary pressure effects were neglected.

After making the above modifications to the specified data, the desired injection/shut-in schedule was followed yielding the following results (Figure A-4):

Step 1: Gas is injected at 10^{-5} kg/s until about 10% gas saturation is 10 m from the well. This is achieved after approximately 7 days in grid block AA-9 ($R = 6.05$ to 10.05 m). Pressure at the injection grid block AA-1 reaches a value of 19.95 bars after 3.9 days and remains essentialy constant thereafter. Initial pressure buildup is very rapid, reaching 9.9 bars after 7 s, and 16.42 bars after 55 s.

Step 2: Gas injection is stopped at 7.04 days. Subsequent pressure recovery is rapid at first but slows down progressively. About 80% of pressure recovery is reached after 114 days.

Step 3: Gas injection is resumed at 10^{-5} kg/s after 114 days. Gas saturation of 50% at 10 m from the well is reached after $\sim$ 5000 days.

Step 4: Gas injection is stopped again and pressure allowed to recover. The recovery is extremely slow, requiring about 45,000 days for 80% recovery.

The [specified] injection/recovery schedule was terminated at this point due to slow time scales of the flows. Gas saturation response is plotted in Figures A-5a, A-5b, A-5c, and A-5d.

A.3 Discussion and Conclusions

When evaluating the numerical simulation results one has to keep in mind that the test case studied here is of a highly idealized and schematic nature; furthermore, important formation characteristics such as relative permeability and capillary pressure behavior are not known at the present time, and hypothetical assumptions had to be made. The dominant feature seen in the simulations is the very tight nature of the formation into which gas injection is made. Matrix permeability is extremely low, and the higher fracture permeability is available only in a very thin zone. This tightness causes a very strong pressure response to injection, as gas pushes in to displace formation water. Single phase flow of formation water ahead of the gas displacement front is the dominant cause of pressure buildup; additional flow resistance is generated from two-phase relative permeability effects behind the displacement front.

Assuming that the FRI test section at Grimsel is in fact as tight as specified in the simulations, the following recommendations for the phase II gas injection tests

can be made:

1. Use an injection rate of 10^{-5} kg/s so as to avoid excessive pressure buildup at the wellbore. (Pressures up to 60 bars after 7 days may occur at the injection rate of 10^{-4} kg/s).

2. Readjust the [specified] gas testing schedules to a more sensible time frame according to the results obtained.

In order to have more confidence in simulation predictions it may be worthwile to attempt to calibrate the model developed here against data obtained in previous single-phase injection tests. Model parameters should be re-examined and adjusted as needed as soon as gas injection test data become available.

References

[1] Wiborgh, M., Hoglund, L.O., and Pers, K. 1986. Gas formation and gas transport in the host rock. NAGRA Report NTB 85-17.

[2] Pruess, K. 1987. TOUGH User's Guide. Nuclear Regulatory Commission Report NUREG/CR-4645 (also: Lawrence Berkeley Laboratory Report LBL-20700).

[3] Andrews, B. 1988. Design/test calculations for two-phase flow in a dual-porosity, dual-permeabilty medium using TOUGH. Memorandum: September 1, 1988.

[4] Corey, A.T. 1954. The interrelation between gas and oil relative permeabilities. Producers Monthly, p.38.

[5] Grant, M.A. 1977. Permeability reduction factors at Wairakei. Paper 77-HT-52, presented at ASME/AICHE Heat Transfer Conference, Salt Lake City, Utah.

[6] Pruess, K., and Tsang, Y.W. 1989. On relative permeability of rough-walled fractures, Lawrence Berkeley Laboratory Report LBL-26509.

TABLE A-1: Initially specified parameters for the reference case[3].

Formation parameters:

domain	permeability	porosity
Fracture	10 mD (saturated)	50%
Matrix	10^{-4} mD (saturated)	1%

Relative permeability:

(Corey's curves)[4]

liquid phase: $k_{rl} = [S^*]^4$

gas phase: $k_{rg} = (1 - S^*)^2(1 - [S^*]^2)$

where: $S^* = (S_l - S_{lr})/(1 - S_{lr} - S_{gr})$

$S_{lr} = 0.3$

$S_{gr_{fracture}} = 0.02$

$S_{gr_{matrix}} = 0.1$

Air injection rate: $Q = 10^{-5}$ kg/s

Boundary conditions:

bottom:	no flow
top:	no flow
fracture, outer:	specified pressure of 1.0 bar
matrix, outer:	no flow

Initial conditions:

temperature:	10°C
pressure:	1 bar
S_g:	1% across the domain

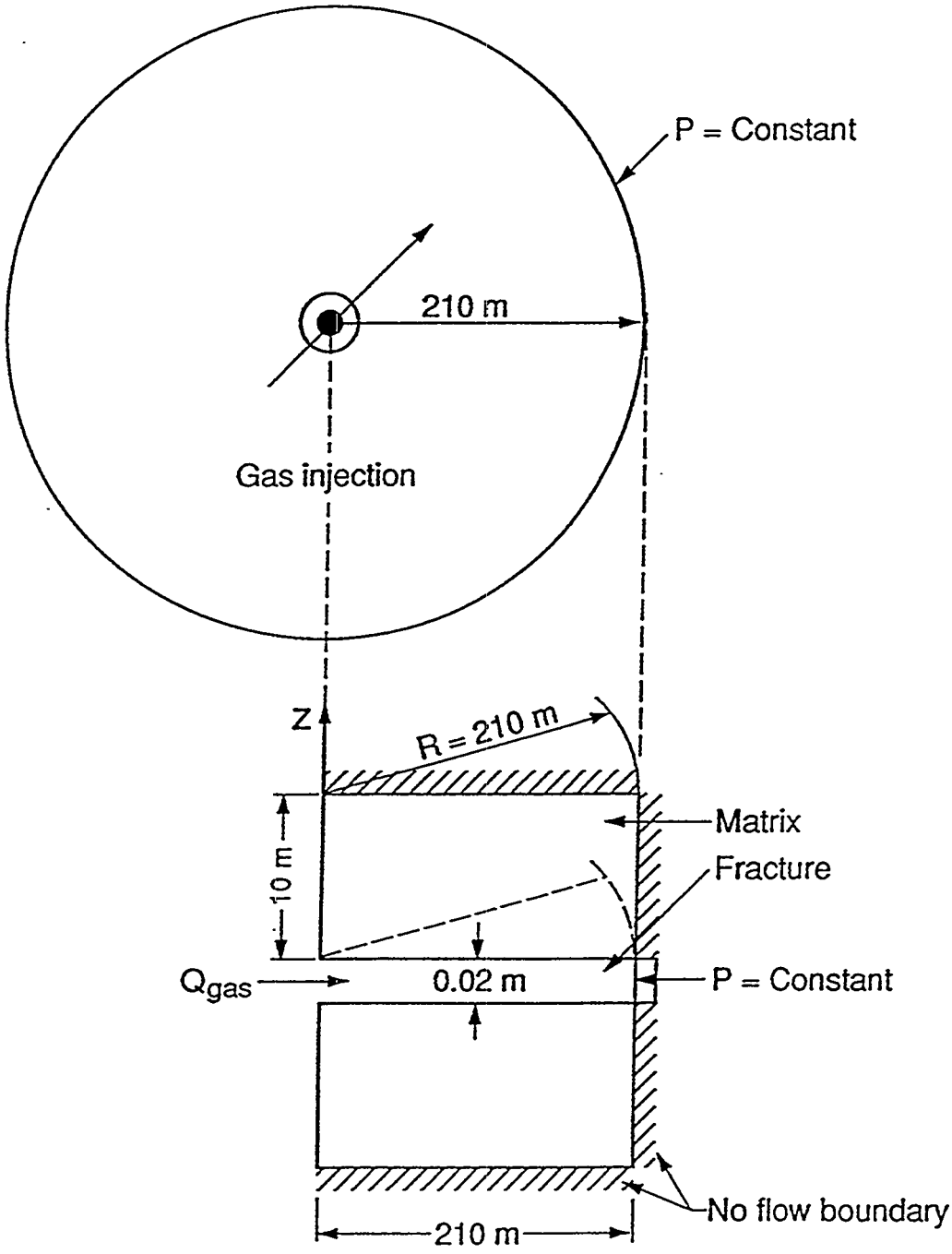

FIG. A-1a: Radial flow domain.

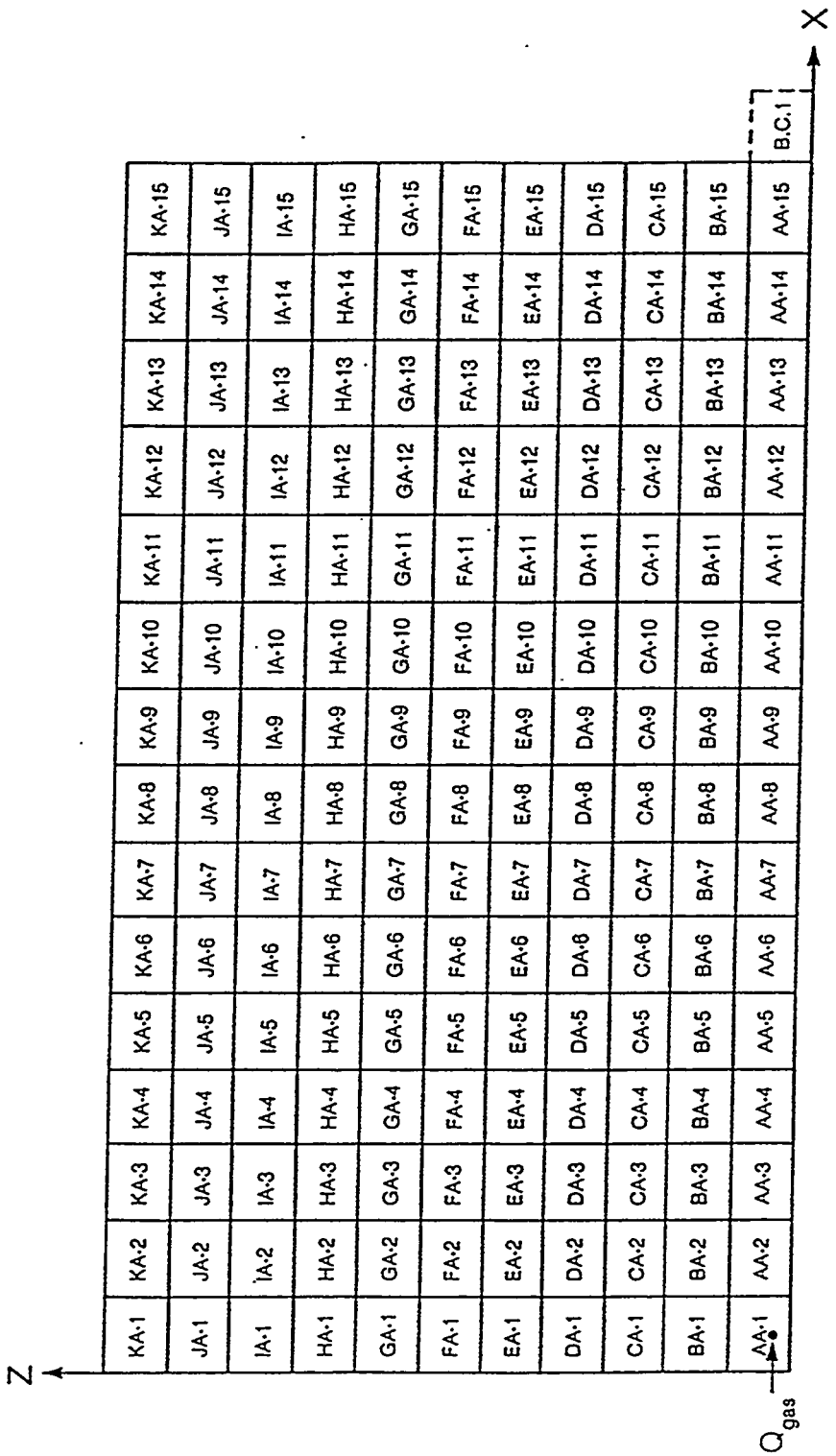

FIG. A-1b: Radial flow griding.

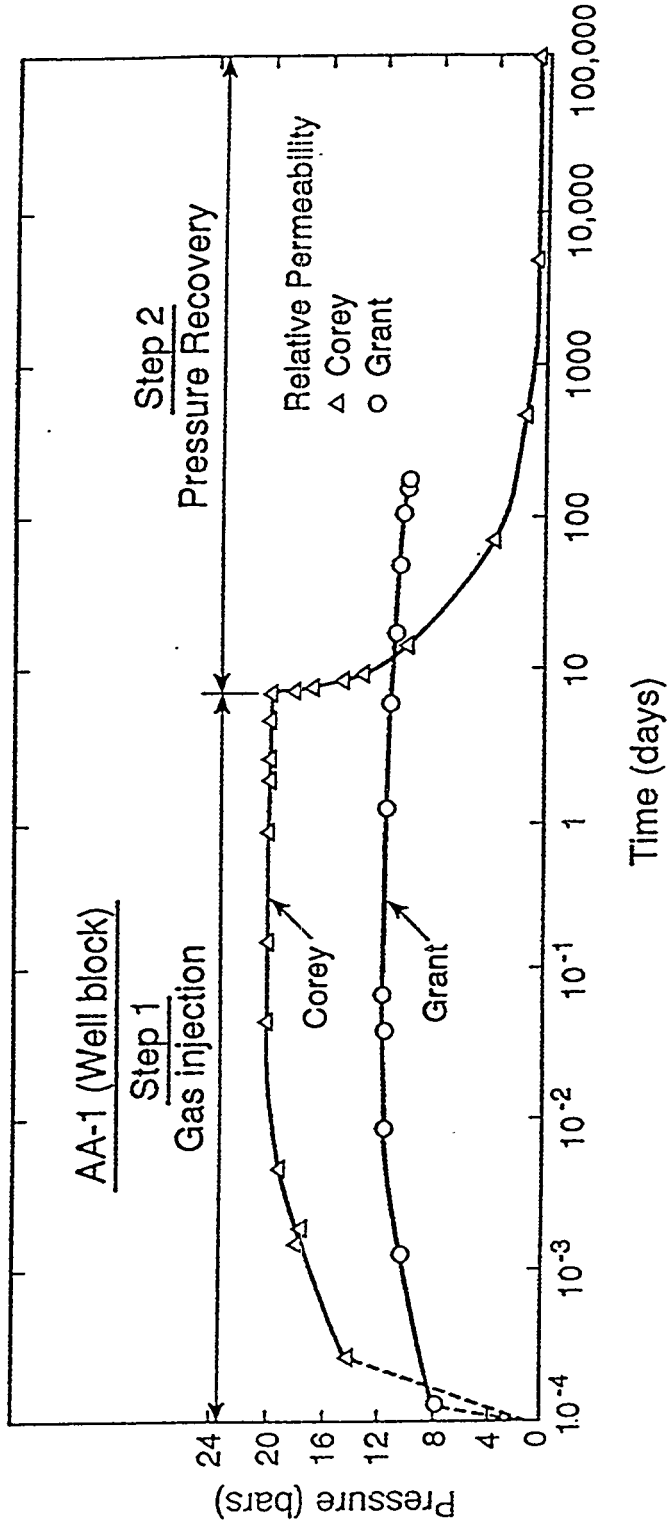

FIG. A-2a: Gas pressure vs. time at wellblock.

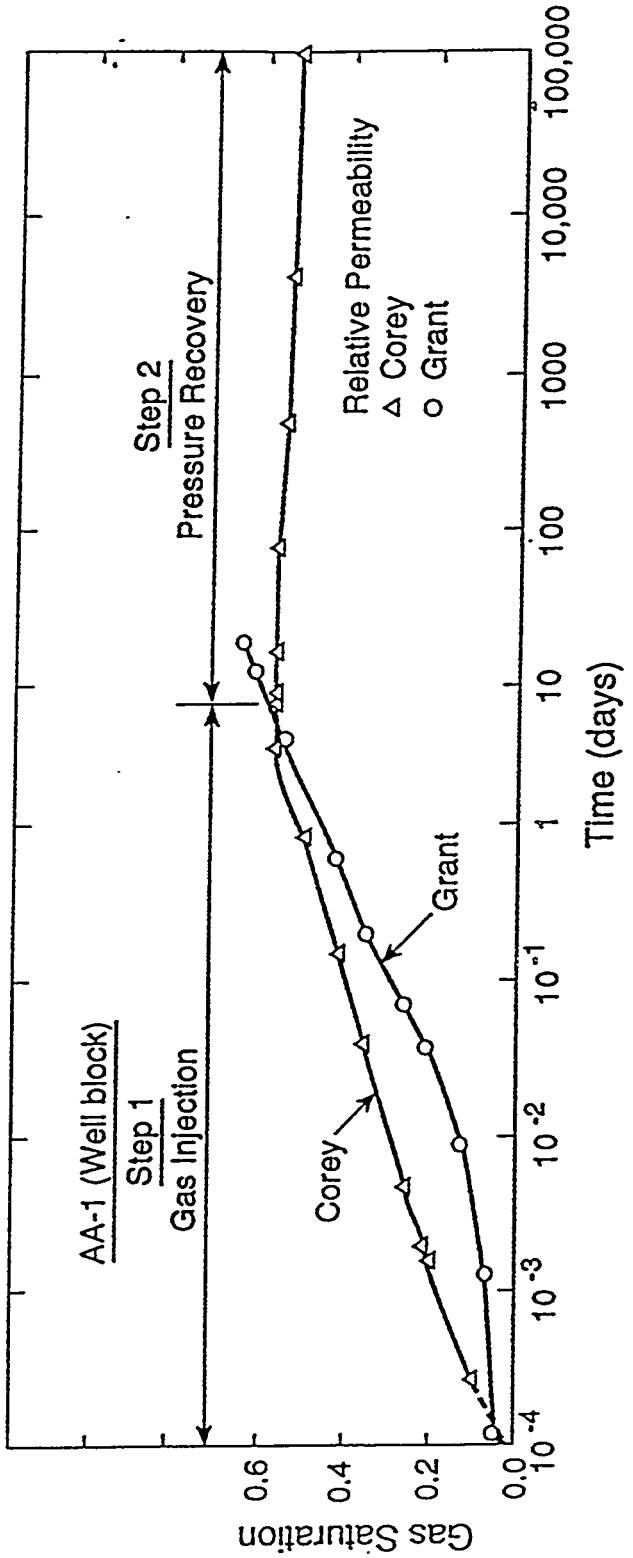

FIG. A-2b: Gas saturation vs. time at wellblock.

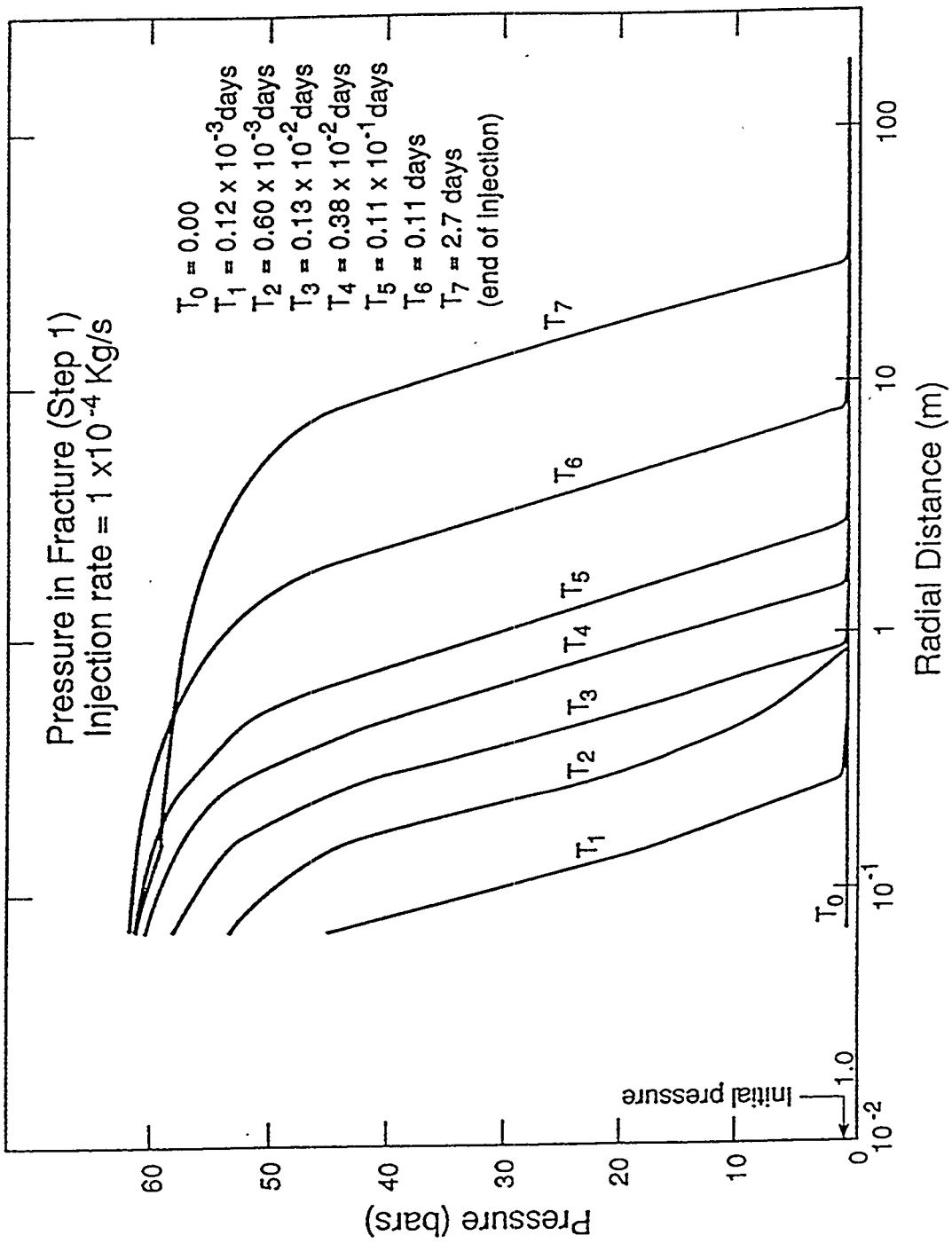

FIG. A-3a: Gas pressure profiles in fracture ($Q = 1 \times 10^{-4}$ kg/s).

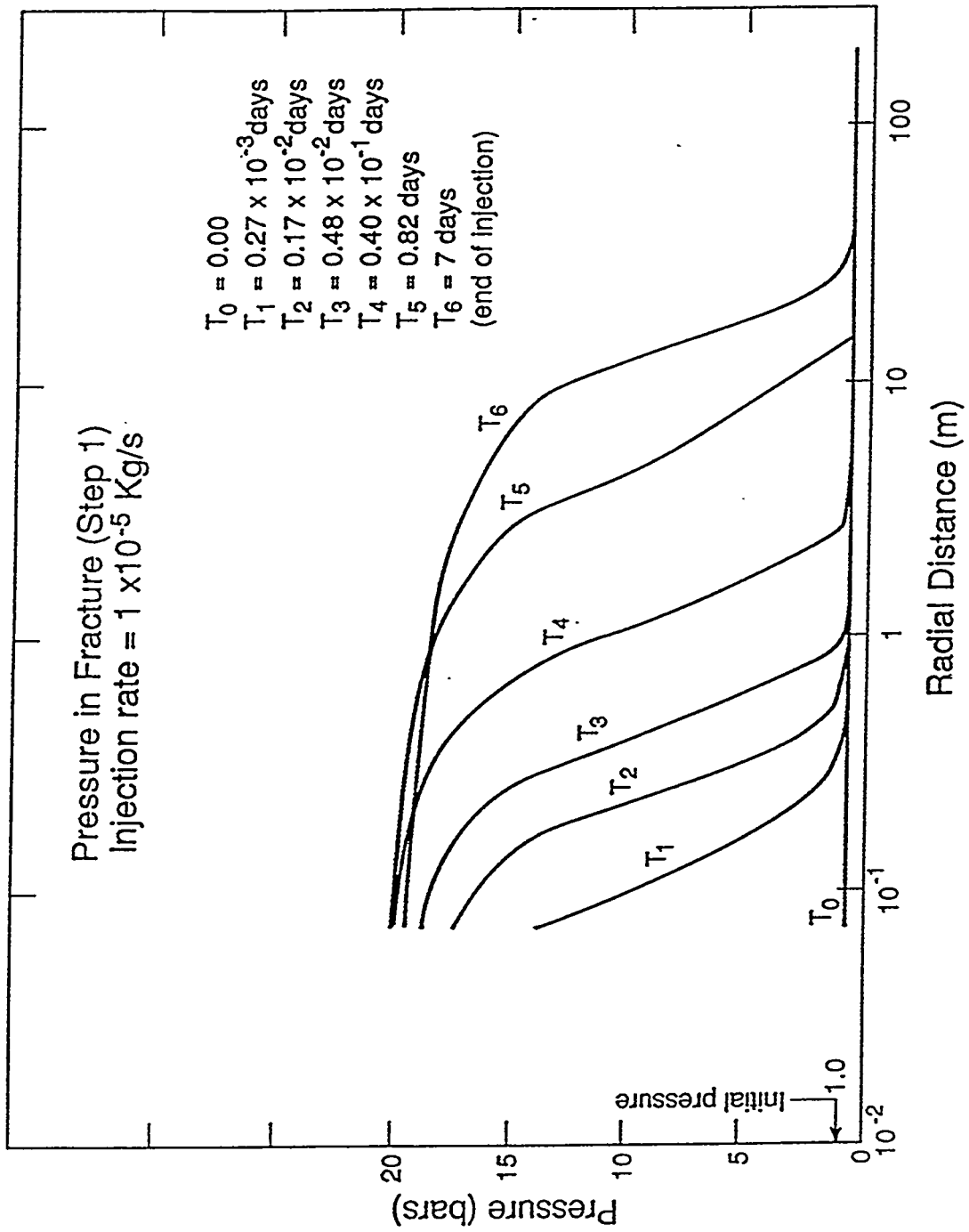

FIG. A-3b.: Gas pressure profiles in fracture ($Q = 1 \times 10^{-5}$ kg/s).

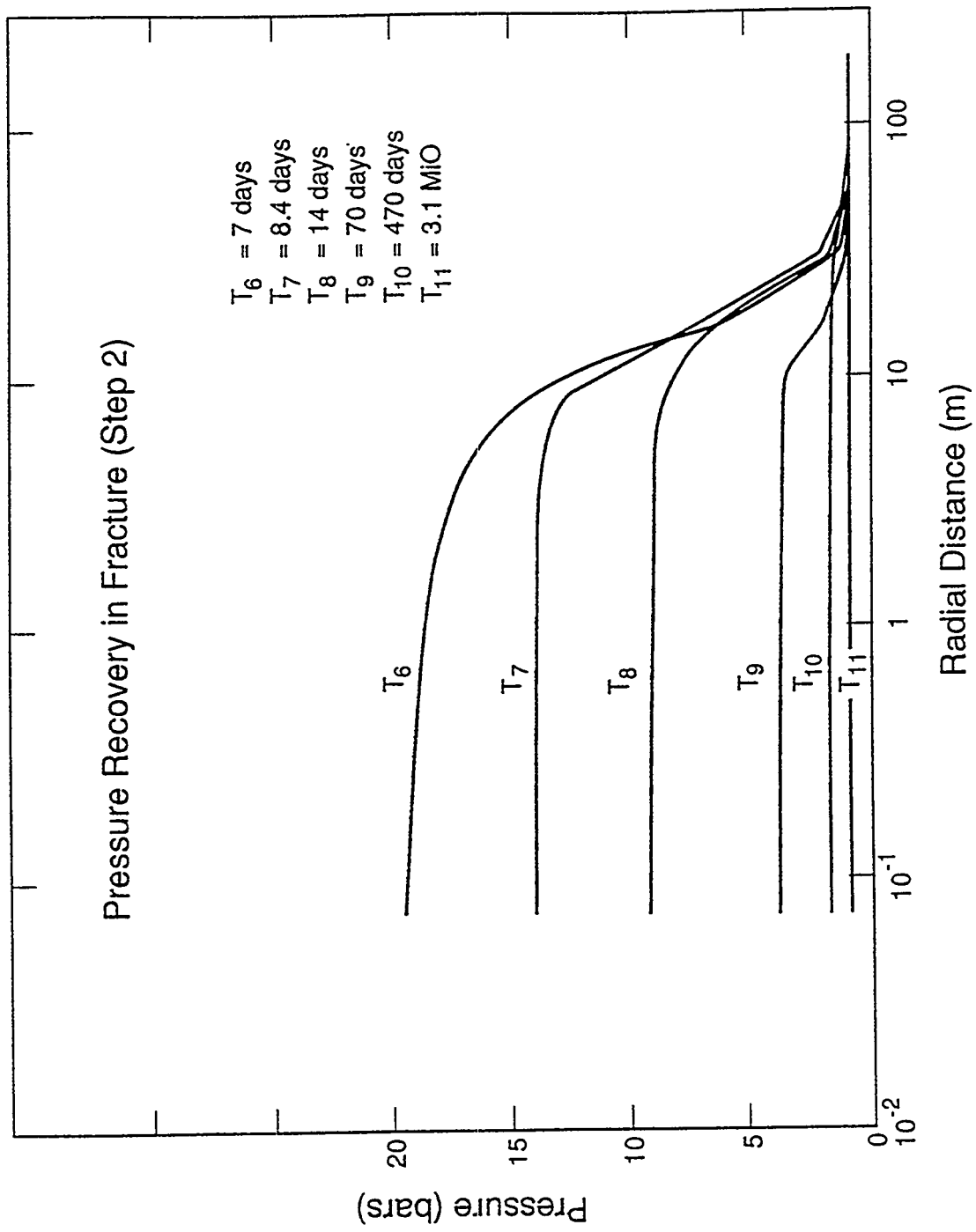

FIG. A-3c: Gas pressure recovery profiles in fracture ($Q = 0 \times 10^{-5}$ kg/s).

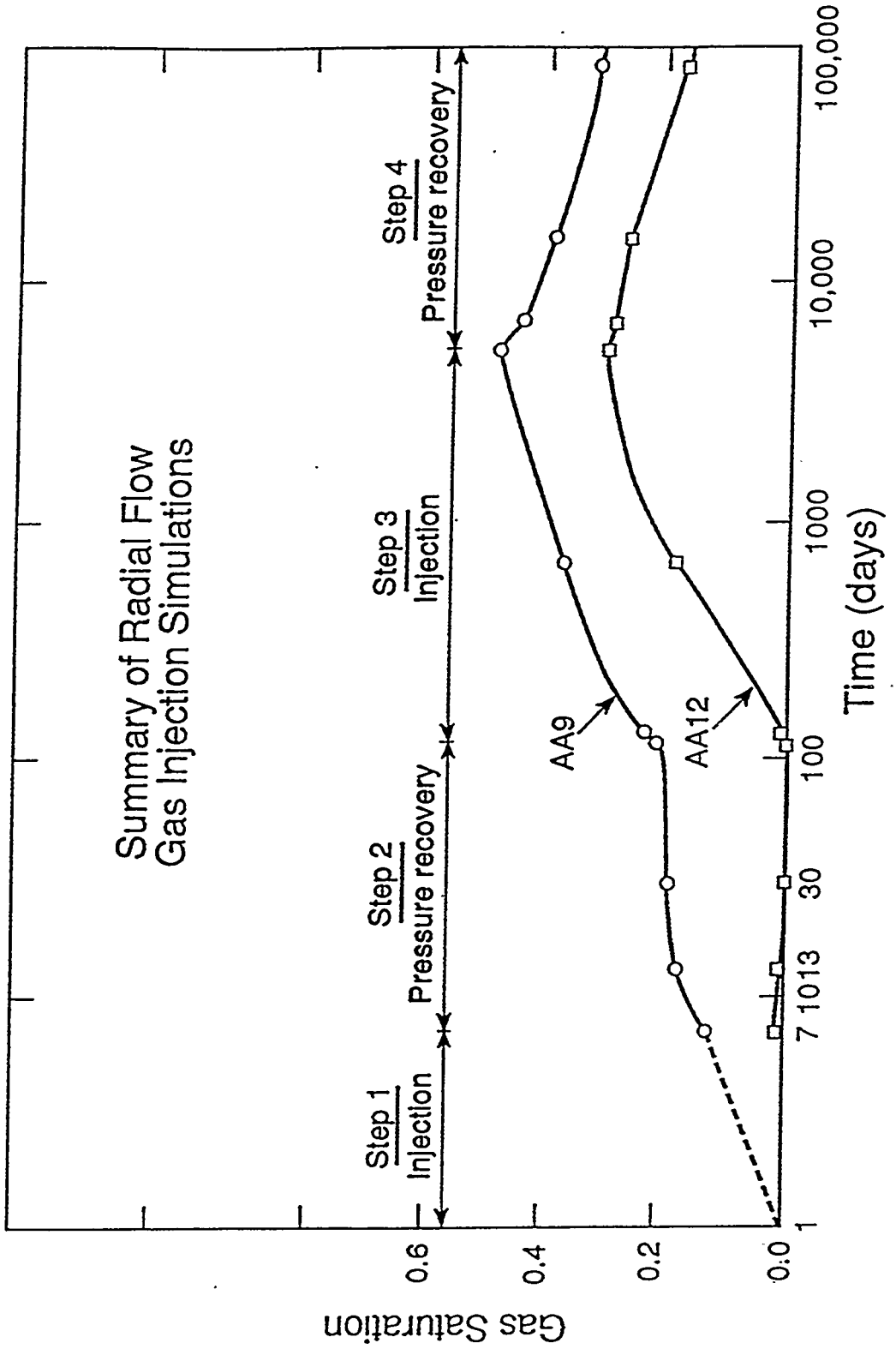

FIG. A-4: Gas saturation vs. time for different injection/recovery periods.

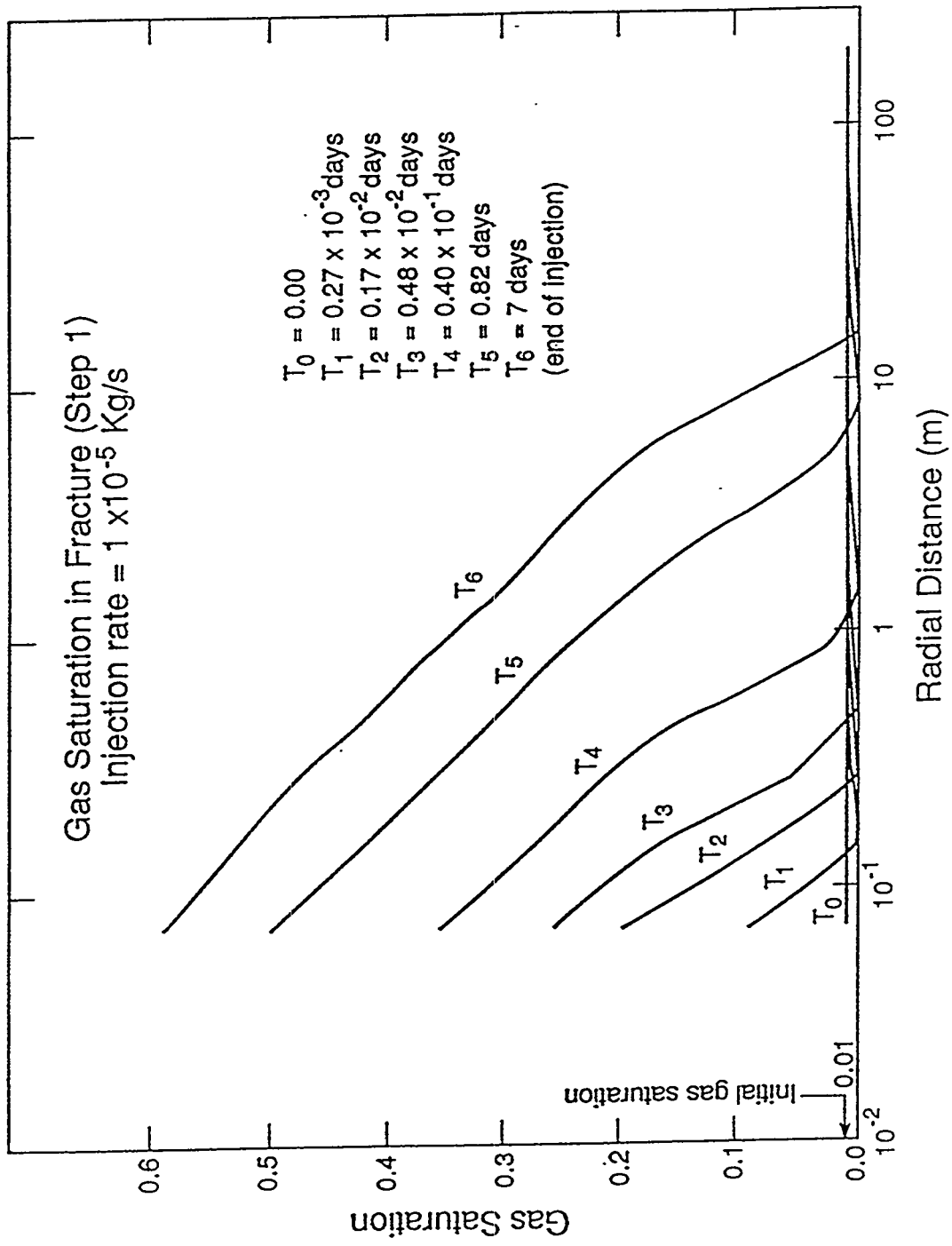

FIG. A-5a: Gas saturation profiles in fracture ($Q = 1 \times 10^{-5}$ kg/s).

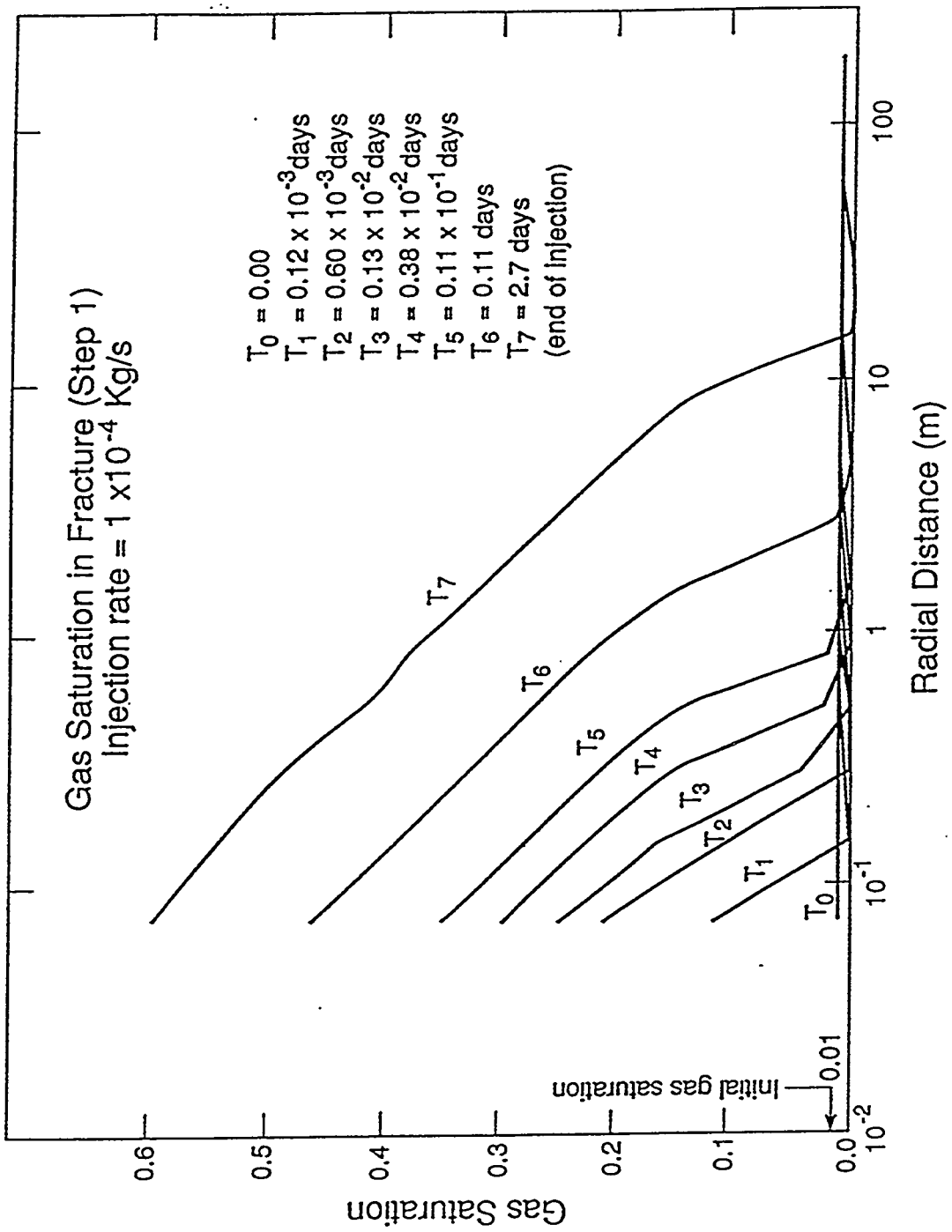

FIG. A-5b: Gas saturation profiles in fracture ($Q = 1 \times 10^{-4}$ kg/s).

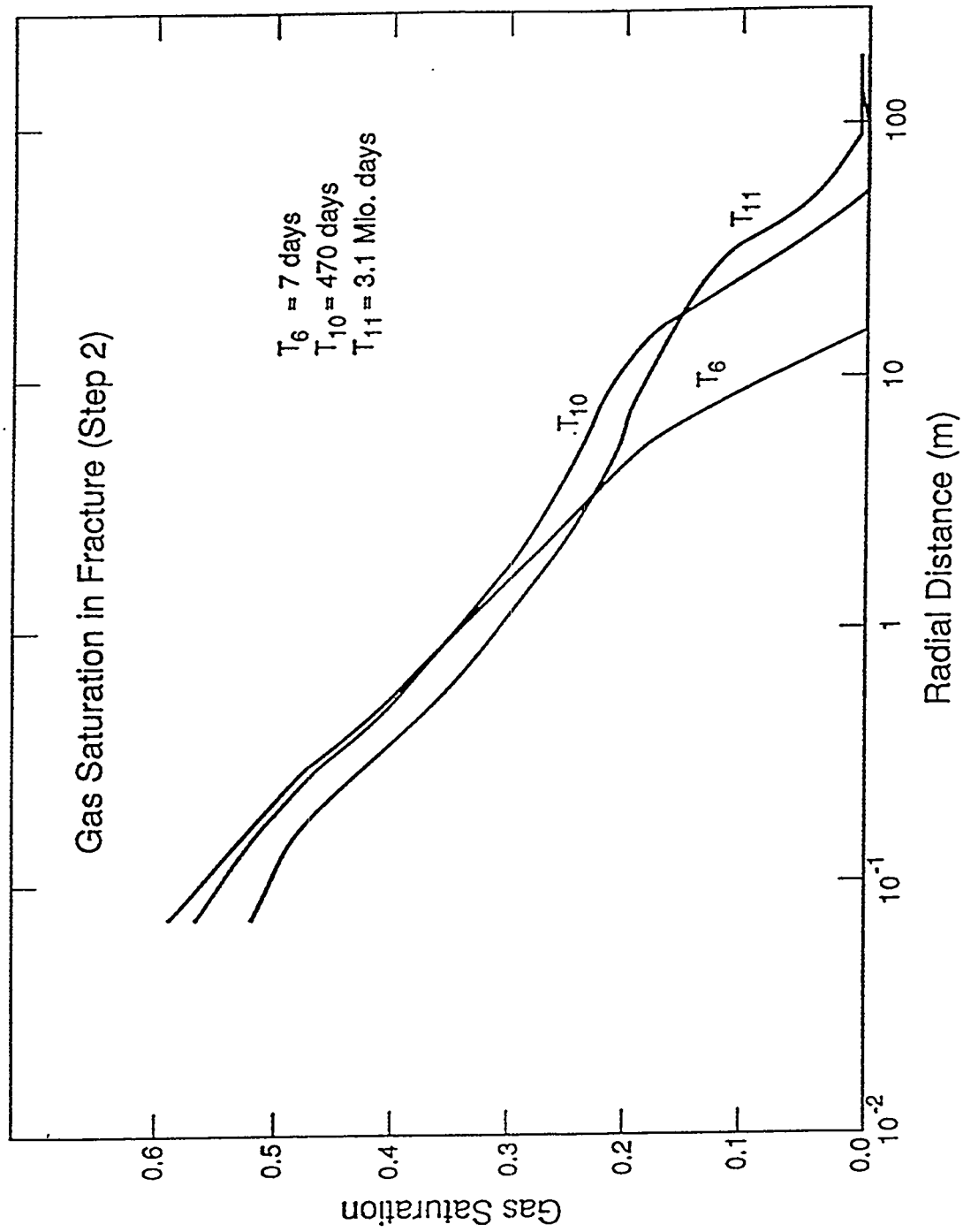

FIG. A-5c: Gas saturation profiles in fracture ($Q = 0 \times 10^{-5}$ kg/s).

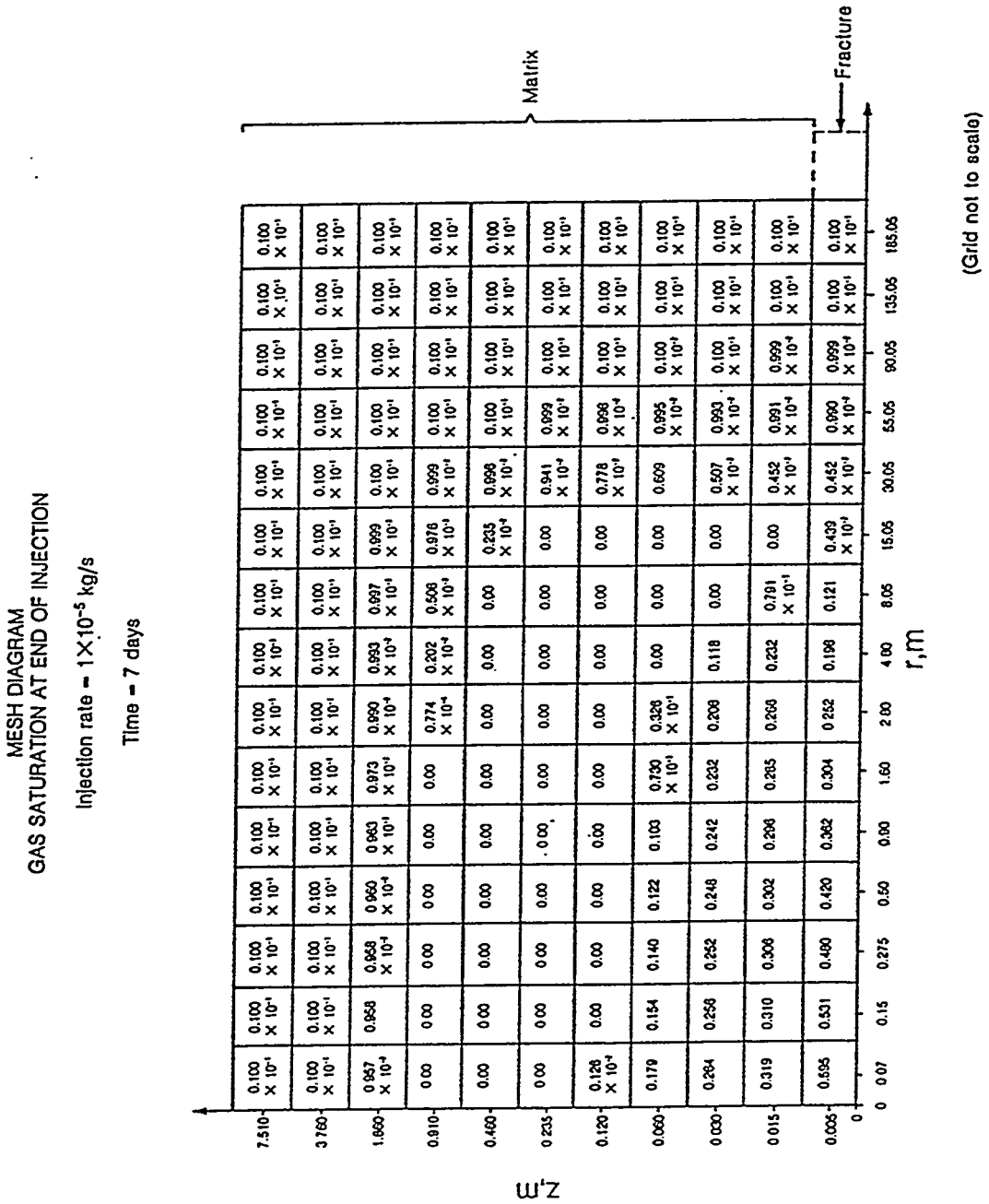

FIG. A-5d: Saturation distribution at 7 days ($Q = 1 \times 10^{-5}$ kg/s).

APPENDIX B

SENSITIVITY STUDIES ON PARAMETERS AFFECTING GAS RELEASE FROM AN UNDERGROUND ROCK CAVERN

B: SENSITIVITY STUDIES ON PARAMETERS AFFECTING GAS RELEASE FROM AN UNDERGROUND ROCK CAVERN[2]

Abstract

A series of numerical simulation experiments is performed to quantify the effects of the release and migration of non-condensible gas in water-saturated fractured rock formations. The relative importance of multiphase parameters such as relative permeability, capillary pressure, intrinsic permeability, and porosity on system behavior is studied.

B.1 Introduction

The Nationale Genossenschaft für die Lagerung Radioaktiver Abfaelle (NAGRA) of Switzerland is studying the feasibility of disposing low and intermediate level nuclear wastes in a geologic repository. The corrosion of metals and microbial degradation of the organic materials from such a repository are expected to generate large amounts of gas, the main constituent being hydrogen, with minor amounts of methane, carbon dioxide, and others[1]. From the data given by Wiborgh et al.[1], it can be estimated that due to the expected gas release pressures in the repository may rise to several hundred bars, unless proper venting is installed. Gas production and migration may also influence the transport of soluble species in groundwater, through displacement of water by the gas front, and/or a mixed flow of contaminated water and gas.

In a previous study two reference cases were developed for evaluating effects of gas release and migration at a potential nuclear waste repository site at Oberbauenstock[2]. The reference cases used alternative conceptualizations of the rock mass as a porous and a fractured-porous medium, respectively, and employed 'best estimates' for the hydrologic parameters applicable at the site. Many important parameters are not well known, however, leading to considerable uncertainty in expected behavior. The present study attempts a broader and more systematic evaluation of gas release effects. We consider an idealized geometric model of the flow system that represents the conditions encountered at Oberbauenstock in a schematic way. Flow effects from

[2]This work was jointly supported by the U.S. Department of Energy under Contract No. DE-AC03-76SF00098 and by the Swiss National Cooperative for the Storage of Nuclear Waste (NAGRA).

gas release are investigated under a variety of conditions of relative permeability, capillary pressure, intrinsic permeability, and porosity. The numerical simulations are performed with the multiphase numerical simulator TOUGH2 using its air component to model the gas behavior[3,4].

B.2 Model domain and computational grid

It is assumed that gas release occurs uniformly over a large area. Ignoring regional-scale boundary effects, the flow system is taken to be a one-dimensional vertical column of 1 m^2 cross-sectional area and 100 m height (Figure B-1). The column is assumed to be water-saturated initially with a hydrostatic gradient, so that initial pressure at the bottom is approximately 10 bars. Pressure is maintained at ambient conditions, i.e., P = 1 bar at the top, while gas is injected at the bottom of the column at a rate of 10^{-8} kg/s $\times$ m^2 (Appendix B.A). For numerical simulation, the section is subdivided into 40 elements spaced at 2.5 m. The parameters for the reference case are similar to those used in the porous medium case of Pruess[2], except that we include a non-zero capillary pressure (Table B-1 and Appendix B.B; Code Listings 1 to 3) (Figures B-2 and B-3).[5,6] The parameter variations considered in the sensitivity studies are summarized in Table B-2 (cases 1 to 8). A sample input file for TOUGH2 is shown in Code Listing 4. Note that, because of the one-dimensional model used in this report, we cannot address issues of formation heterogeneities and (viscous or gravitational) flow instabilities.

B.3 System behavior for the reference case

The gas injected into the porous medium initially dissolves in the water that is present in the injection grid block. However, gas solubility is soon exceeded and a free gas phase forms (Figure B-4). Further gas release leads to an increase in gas saturation accompanied by pressurization, as water is displaced by the growing gas bubble (Figure B-5). At approximately 6×10^6 s (80 days), gas saturation reaches the irreducible limit of 5%, and begins to flow upward. A gas-water displacement front then migrates up the column (Figure B-6). Note that the pressure gradient is smaller behind the displacement front than ahead of it (Figure B-7), due to the much smaller viscosity of the gas phase. In the well block, gas pressure reaches its maximum

(38 bars) at about 7×10^7 s (2.2 years) (Figure B-5). Then it enters into a period of slow decline, with a continued increase in gas saturation. After 6.5×10^8 s (20.6 years) the gas reaches the top of the boundary of the flow domain (Figures B-6 and B-8; Code Listing 5). It is of interest to consider the liquid outflow at the top of the column in response to gas injection at depth (Figure B-9). Due to the small compressibility of liquid water, the pressurization at depth is transmitted rapidly upward. Outflow at the top commences as soon as a free gas phase is formed near the injection point. The outflow rate increases rapidly at first, and more slowly after gas becomes mobile at depth ($\approx 6 \times 10^6$ s). A quasi-steady situation with slowly increasing liquid outflow prevails until about 5×10^8 s. Subsequently, as the gas front approaches the top boundary, liquid outflow is enhanced from the steep pressure gradient ahead of the front (see Figure B-7).

B.4 Sensitivity studies

The hydrologic parameters that characterize fractured rock masses on a large scale are difficult to determine accurately in practice. It is important to evaluate the uncertainty in flow behavior that arises from the parameter uncertainty. In this section we present results of sensitivity studies, which examine the impact on flow behavior of variations in capillary pressures, relative permeabilities, absolute permeability, and porosity. All of these formation parameters are of course interrelated, because they all depend on the geometry of the pore space in which flow takes place. For certain classes of permeable media, such as unconsolidated sands, quantitative relationships between some of these parameters have been found. However, due to the inherent variability of the pore geometry in natural media, there are no generally useful quantitative relationships that would apply to broad classes of media. For example, one expects the permeability of a medium to generally decrease with decreasing porosity. However, in fractured media one often encounters large permeability accompanied by small porosity. Because of the strong inherent variability of flow properties of fractured rock masses, we have adopted the approach of varying the important parameters one at a time, independently of each other. The specifications of the sensitivity studies are given in Table B-2.

B.4.1 Capillary pressure

To explore the sensitivity of system behavior to variations in capillary pressure, case 1 uses a stronger capillary pressure with air entry effects (Figure B-10)[7], while in case 2 capillary effects are neglected. Stronger capillary pressures accelerate and increase gas pressurization at the injection point (Figure B-11), as expected, while slowing and diminishing gas saturation buildup (Figure B-12). Neglect of capillary pressures has the opposite effects. Capillary pressures are generally relatively weak compared to the pressurization from viscous flow resistance, so that their impact in systems response is minor. This can also be seen from the weak retardation of the gas displacement front due to capillary effects (Figure B-13).

B.4.2 Relative permeability

There is considerable uncertainty at present about the relative permeability behavior of fractured rock masses. It has often been postulated or assumed that fracture relative permeabilities should obey the constraint $k_{rl} + k_{rg} = 1$[8,9], while recent theoretical work has suggested that phase interference in fractures may be very strong, with both k_{rl} and k_{rg} being small at intermediate saturations[5]. Here we consider two variations on the reference case, corresponding to the conventional view of fracture relative permeabilities (case 3; Figure B-14) and the recent suggestion of strong phase interference (case 4; Figure B-15, Appendix B.C, and Code Listing 6), respectively. Figures B-16 and B-17 show that relative permeability uncertainty can have a very major effect on predicted fluid pressures and gas saturations. For the Grant curves (case 3), gas flow is facilitated in comparison to the reference case, giving rise to smaller pressure and saturation increases. The strong interference relative permeabilities (case 4) on the other hand, produce a vastly stronger pressure response and much higher gas saturations. Very strong corresponding effects are seen on the advancement of the gas displacement front (Figure B-18).

B.4.3 Absolute permeability

Variation of absolute permeability produces the expected effects (Figures B-19 and B-20). Fluid pressures near the injection point increase (decrease) when permeability is diminished (enhanced). For higher permeability the advance of the gas front is more rapid. It is interesting to note that permeability effects on gas saturation are rather minor (Figure B-21).

B.4.4 Porosity

Effects from porosity variations are somewhat complementary to those from permeability variations (Figures B-22 and B-23). Gas saturation near the injection point increases more rapidly and to higher values for smaller porosity, due to the smaller available pore volume. Pressure response is also more rapid for smaller porosity, but the pressure level maintained during the advancement of the gas displacement front up the column is little affected by porosity. The rate at which the gas front advances is approximately inversely proportional to porosity (Figure B-24).

B.5 Summary of multiphase effects

For the particular process considered here, i.e., displacement of water by gas, the impacts of system parameters on flow behavior can be summarized as follows (Table B-3):

B.5.1 Capillary pressure

Its effects were found to be generally weak, because typical capillary pressures are only of the order of a few bars, while pressure increase from viscous flow resistance in the problem considered here is typically a few tens of bars. Increased capillary pressures will tend to cause increases in gas phase pressurization, while diminishing and slowing gas saturation buildup.

B.5.2 Relative permeability

Interference between liquid and gaseous phases as described by relative permeability functions has an overwhelmingly strong impact on system behavior. Pressurization effects from gas release can increase dramatically when phase interference is strong, i.e., when relative permeabilities are small at intermediate saturations.

B.5.3 Absolute permeability

This parameter has a strong impact on pore pressures and advancement of the gas front, but relatively small impact on fluid saturation.

B.5.4 Porosity

This parameter has a strong impact on the time scale of the flow processes, with things happening faster for smaller porosity. The rate of advancement of the gas front and the rate of saturation buildup are approximately inversely proportional to porosity. Pressure effects are relatively minor.

B.6 Conclusions

Major multiphase system parameters such as relative permeability and capillary pressure of fractured media are poorly understood at the present time. In this report we have attempted to analyze the relative impact of these and other fluid flow parameters such as porosity and intrinsic permeability on a particular two-phase system under isothermal conditions. It is important to note that due to the strong coupling effects in multiphase flow, there is a complex relationship between the input parameters and the output variables. The parameter that was shown to have by far the largest impact is relative permeability. It affects strongly both the gas pressure and the gas front displacement velocity (Table B-3). It is followed in importance by intrinsic permeability that affects more the gas pressure values than the displacement front speed. The parameter that has the least impact, within the range studied here, is capillary pressure. Porosity does not have much influence on gas pressures at the injection point but it strongly affects gas saturation front velocities. On the other

hand, intrinsic permeability has a higher impact on gas pressures than on gas front velocities.

We conclude that relative permeability constitutes a crucial multiphase system parameter. Efforts have to be made to obtain reliable relative permeability functions that would apply to the particular field conditions under consideration. We would like to note that the strong interference relative permeability model is expected to be more applicable to a single fracture viewed as a two-dimensional heterogeneous porous medium rather than to a three-dimensional fracture network. A three-dimensional network would present less interference between the fluid phases because it allows more alternative pathways for the phases to flow.

In our studies, we have assumed immiscible displacement of water by gas in a homogeneous sparsely fractured rock. However, the variation in apertures in any given fracture will mean that gas will tend to follow the widest aperture paths. Hence, it is conceivable that some parts of the medium may never allow gas to flow and will remain saturated with water. It is not clear a-priori to what extent the relative permeability concept being a continuum concept can be applied to flow processes in highly heterogeneous media.

In general, we can state that our sensitivity studies are useful to:

- identify the importance (or lack thereof) of formation parameters;
- identify the most important physical processes;
- quantify the extent and sources of error for prediction;
- serve as a guide for fitting a model to actual data;
- assist in the design of field experiments aimed at reducing uncertainty in system parameters.

References

[1] Wiborgh, M., Hoglund, L.O., and Pers, K. 1986. Gas formation and gas transport in the host rock. NAGRA Report NTB 85-17.

[2] Pruess, K. 1989. Numerical modelling of gas migration at a proposed repository for low and intermediate level nuclear wastes at Oberbauenstock, Switzerland. Lawrence Berkeley Report LBL-25413, NDC-5.

[3] Pruess, K. 1987. TOUGH User's Guide. Nuclear Regulatory Commission, Report NUREG/CR-4645 (also: Lawrence Berkeley Laboratory Report LBL-20700.

[4] Pruess, K. 1990. TOUGH2-A General-Purpose Simulator for Multiphase Non-isothermal Flows, draft manuscript.

[5] Pruess, K., and Tsang, Y.W. 1989. On relative permeability of rough-walled fractures. Lawrence Berkeley Laboratory Report LBL-26509.

[6] Corey, A.T. 1954. The interrelation between gas and oil relative permeabilities. Producers Monthly, p.38.

[7] Narasimhan, T.N., Witherspoon, P.A., and Edwards, A.L. 1978. Numerical model for saturated-unsaturated flow in deformable porous media, Part 2: The algorithm. Water Resour. Res., 14(2), p.255.

[8] Grant, M.A. 1977. Permeability reduction factors at Wairakei, paper 77-HT-52, presented at ASME/AICHE Heat Transfer Conference, Salt Lake City, Utah.

[9] Gilman, J.R., and Kazemi, H. 1983. Improvements in simulation of naturally fractured reservoirs. Soc. Pet. Eng. J., p.695.

APPENDIX B.A: GAS RELEASE RATES

The gas release rate was obtained as follows:

Top surface area of repository is $700 \times 1 = 700$ m^2 .

$Q_g = 3.3 \times 10^{-7}$ kg/s of hydrogen over 700 m^2.[2]

Equivalent Q_g for 1 m^2 $= 3.3 \times 10^{-7}/700 = 4.7 \times 10^{-10}$ kg/s.

To scale for air (same rate on molar or volumetric basis):

From the ideal gas law, $P_g V_g = (m/M)RT$, where P_g is gas pressure, V_g is gas volume, m is moles per molecule, M is molecular weight, R is universal gas constant, and T is temperature.

The molecular weights of hydrogen and air are $M_{H_2} = 2.016$ and $M_{air} = 28.96$, respectively.

Thus

$$Q_{g,eq,air} = (28.96/2.016) \times 4.7 \times 10^{-10} = 6.75 \times 10^{-9} \text{ kg/s} \times \text{m}^2 .$$

The gas rate used was: $Q_g = 10^{-8}$ kg/s $\times$ m^2 .

APPENDIX B.B: CAPILLARY PRESSURE FOR A FRACTURE WITH LOG-NORMAL APERTURE DISTRIBUTION

B.B.1 Function origin

Laboratory measurements of fracture void space geometry have shown that, in many cases, apertures follow a log-normal distribution. Under those conditions, a relationship between liquid saturation and aperture can be obtained in closed form, as follows:[5]

$$S_l = 1/2(1 + erf[(\log(b_p) - \beta)/\sqrt{2\sigma^2}]) , \quad \log(b_p) - \beta > 0 , \qquad (B1)$$

$$S_l = 1/2(1 - erf[(\log(b_p) - \beta)/\sqrt{2\sigma^2}]) , \quad \log(b_p) - \beta < 0 , \qquad (B2)$$

where

$$\beta = \sigma^2 \ln(10) + \log(\bar{b}/e^{(\sigma \ln(10))^2/2}) ,$$

and $S_l \equiv$ liquid saturation ,

$b_p \equiv$ cut-off aperture (apertures $b < b_p$ containing liquid and $b > b_p$ gas) ,

$\sigma \equiv$ variance ,

$\bar{b} \equiv$ mean aperture .

Note that β is the logarithm of the aperture cutoff corresponding to $S_l = 50\%$.

Eqs. (B1) and (B2) can be rewritten as follows:

$$S_l = 1/2(1 + erf[(\log(b_p) - \beta)/\sqrt{2\sigma^2}]) \; . \quad (B3)$$

Thus

$$b_p = 10^{\beta - \sqrt{2\sigma^2} erfi(1-2S_l)} \; , \quad (B4)$$

where $erfi \equiv$ inverse error function.

The capillary pressure is defined by Laplace's equation. Assuming a contact angle of zero, we then have

$$P_c = 2\varsigma/b_p = 2\varsigma 10^{\sqrt{2\sigma^2} erfi(1-2S_l) - \beta} \; , \quad (B5)$$

where $\varsigma \equiv$ air-water surface tension (≈ 0.073 N/m).

B.B.2 Parameter adjustment

The theoretically-based capillary pressure curve for $\sigma = 0.43$ and $\bar{b} = 81.8$ μm as used by Pruess and Tsang[5] is presented in Figure B-25. This curve was fitted with the 'limestone' curve of Wiborgh et al.[1] at $S_l = 50\%$ as follows (Figure B-26):

$P_c = 3.15 \times 10^5$ N/m^2 at $S_l = 50\%$ for 'limestone'.

Thus

$$b_{p_{eq}} = \frac{2\varsigma}{P_c} = \frac{2 \times 0.073 \; N/m}{3.15 \times 10^5 \; N/m^2} = 0.0463 \times 10^{-5} \text{ m} = 0.463 \; \mu\text{m}.$$

Then it follows that

$$\beta = \log(b_{p_{eq}}) = \log(0.463) = -0.3344.$$

From Eq. (B49) (with $\sigma = 0.43$) we obtain

$$\beta = -0.3344 = (0.43)^2 \ln(10) + \log(\bar{b}/e^{(0.43 \ln 10)^2/2}) \, .$$

Hence

$$\bar{b} \approx 0.2836 \ \mu\text{m}.$$

Thus the parameters of the capillary pressure for the reference case are (Figure B-25):

$$\sigma = 0.43 \, , \quad \bar{b} = 0.2836 \ \mu\text{m} \, , \quad \beta = -0.3344 \, .$$

B.B.3 Numerical implementation

Capillary pressure must be calculated as a function of saturation to be used in the TOUGH2 simulator. This involves inversion of the relationships Eqs. (B1) and (B2) or Eq. (B3).

The programming was executed in two alternative ways:

1. Using Eqs. (B1) and (B2) (Code Listing 1).
2. Using Eq. (B3) (Code Listing 2).

1. Inverse error function

As it is presented in Eqs. (B4) and (B5), the expression that relates aperture size or capillary pressure with liquid saturation contains the inverse error function (Figure B-27). The error function analytical inversion is not a trivial operation. A Cray-IMSLSFUN mathematical library function erfi(x), was implemented in TOUGH2 to calculate the inverse error function.

Restrictions of erfi(x):

- $-1 < x < 1$.
- data may be real or double precision if the double precision version derfi(x) is used. Results of derfi(x) are accurate to less than one half precision if the absolute value of the argument is too large (Terrie Dickson (LLNL), private communication).

2. Access procedure of erfi(x) on the Cray (see Code Listing 3)

3. Treatment of singularities

As it is shown in Figure B-27, erfi(+1) is not defined. Also, erfi(-1) = -erfi(1) is not defined either. From formula (B5), it is obvious that at values of saturation $S_l = 0$ and $S_l = 1$; $erfi(x) = erfi(+1)$ and $erfi(x) = erfi(-1)$, respectively. Therefore, a special treatment is required for the mathematical singularities at $S_l = 0, 1$ (Fig. B-2).

Study first how the function P_c vs. S_l behaves for:

- Increasingly small S_l values: (e.g., $S_l \rightarrow 0$; Table B-4a).
- Increasingly large S_l values: (e.g., $S_l \rightarrow 1$; Table B-4b).

From the observed behavior ($S_l \rightarrow 0$, $P_c \rightarrow \infty$; $S_l \rightarrow 1$, $P_c \rightarrow 0$), the following solution was proposed. For small liquid saturation, we impose a cutoff:

- For $S_l \leq 10^{-5}$: $P_c = P_{c_b}$, where $P_{c_b} \equiv P_c$ at $S_l = 10^{-5}$; while for large liquid saturation we perform a linear interpolation.
- For $S_l \geq 1 - 10^{-5}$: $P_c = P_{c_t}(1 - S_l)/10^{-5}$, where $P_{c_t} \equiv P_c$ at $S_l = 1 - 10^{-5}$. (Note that at $S_l = 1$, $P_c = 0$).

4. Test cases

Test cases were performed to study:

1. Performance of erfi(x).
2. Comparison of analytical solution using the probability table with the numerical solution proposed (Table B-5). (Pick cut-off aperture b_p and calculate liquid saturation S_l and capillary pressure $P_{c_{[anal.]}}$. Then, use the code with S_l to calculate $P_{c_{[num.]}}$ and compare the two capillary pressure values thus obtained).
3. Handling at the boundaries $S_l \rightarrow 0$ and $S_l \rightarrow 1$.
4. Comparison of codings using either Eqs. (B1) and (B2) or Eq. (B3).

5. Comments:

- noted that erfi(x) is very accurate.
- the analytical solution checks against the numerical solution.
- the boundaries behave well numerically.
- codings using either Eqs. (B1) and (B2) or Eq. (B3) are both correct.

5. P_c vs. S_l functions for different σ and $\bar{b}$

- Constant $\sigma = 0.43$ and varying $\bar{b}$ (Figure B-25)

  $\bar{b_1} = 81.8$ μm

  $\bar{b_2} = 0.2836$ μm

  Note that the curve simply translates vertically parallel to the capillary pressure axis since the range of apertures is scaled by a common factor, e.g., $P_c \approx 1/b$. The theoretically-based capillary pressure-saturation relation depends only on the variance of the lognormal distribution and the ratio of the most probable aperture to the cut-off aperture. Therefore, the relationship between capillary pressure and saturation for fractures with lognormal aperture distribution for fixed standard deviation has the same functional form independently of the magnitude of the most probable aperture. If all apertures are scaled by a common factor, the capillary pressure at a given saturation will scale by the inverse of that factor.

- Constant $\bar{b} = 0.2836$ μm and varying σ (Figure B-28)

  $\sigma_1 = 0.23$

  $\sigma_2 = 0.43$

  $\sigma_3 = 0.63$

  Note that there is leftward rotation and flattening of the curves with decreasing variance.

APPENDIX B.C: STRONG INTERFERENCE RELATIVE PERMEABILITY FUNCTIONS

The strong interference relative permeability functions used in this studies were described by the following polynomials:

$$k_{r_l} = (S_1^*)^4 ,$$

$$k_{r_g} = (S_2^*)^4 ,$$

$$S_1^* = (S_l - S_{l_r})/(1 - S_{l_r}) ,$$

$$S_2^* = (S_g - S_{s_r})/(1 - S_{s_r}) ,$$

where $k_{r_l} \equiv$ liquid relative permeability ,
$k_{r_g} \equiv$ gas relative permeability ,
$S_{l_r} \equiv$ liquid irreducible saturation ,
$S_{s_r} \equiv$ gas irreducible saturation .

These functions as coded in TOUGH2 are presented in Code Listing 6 and plotted in Figure B-15.

APPENDIX B.D: CODE LISTINGS

B.D.1: FORTRAN source code for calculating fracture capillary pressure (version 1).

B.D.2: FORTRAN source code for calculating fracture capillary pressure (version 2).

B.D.3: Access procedure for inverse error function from IMSLSFUN library.

B.D.4: Coding for identifying the position of the gas saturation front.

B.D.5: Coding for relative permeability function with strong phase interference.

B.D.6: Sample TOUGH2-input file for reference case.

CODE LISTING B.D.1: FORTRAN source code for calculating fracture capillary pressure (version 1).

```
      IF(SL.GT.CP(2,NMAT)) SS=(SL-CP(2,NMAT))/(1.-CP(2,NMAT))
      OSS=1.-SS
      F=1.417*OSS-2.120*OSS**2+1.263*OSS**3
      CALL SIGMA(T,ST)
      PC=-CP(1,NMAT)*ST*F
      RETURN
   16 CONTINUE
C-----CAPILLARY FUNCTION OF VAN GENUCHTEN, SOIL SCI. SOC. AM. J. 44,
C     PP.892-898, 1980.
C
      IF(SL.NE.1.)GO TO 160
      PC=0.
      RETURN
C
  160 SLX=SL
      IF(SLX.GE.CP(5,NMAT)) GOTO 161
      IF(CP(4,NMAT).EQ.0.)SLX=AMAX1(SL,1.001*CP(2,NMAT))
      PC=-ABS(CP(4,NMAT))
      IF(SLX.GT.CP(2,NMAT))
     XPC=-1./ABS(CP(3,NMAT))*(((SL-CP(2,NMAT))/(CP(5,NMAT)-CP(2,NMAT)))
     X**(-1./CP(1,NMAT))-1.)**(1.-CP(1,NMAT))
      IF(CP(4,NMAT).NE.0.) PC=AMAX1(PC,-ABS(CP(4,NMAT)))
      IF(SL.GT..999) PC=PC*(1.-SL)/.001
      RETURN
  161 PC=0.
      RETURN
   17 CONTINUE
C
C-----CAPILLARY FUNCTION FROM LOG-NORMAL APERTURE DISTRIBUTION, EMS.
C
        SLX=SL
        IF(SLX.GE.(1.-1.E-5)) SLX=1.-1.E-5
        IF(SLX.LE.1.E-5) SLX=1.E-5
        B0=CP(1,NMAT)/EXP(((CP(2,NMAT)*ALOG(10.))**2)/2.)
C       WRITE(6,300) B0
C 300   FORMAT('B0 =',1X,E12.5)
        BETA=CP(2,NMAT)**2*ALOG(10.)+ALOG10(B0)
C       WRITE(6,500) BETA
C 500   FORMAT('BETA =',1X,E12.5)
        BP=10**(BETA-SQRT(2.)*CP(2,NMAT)*ERFI(1.-2.*SLX))
C       XYZ=ERFI(1.-2.*SLX)
C       WRITE(6,600) SLX,XYZ,CP(2,NMAT),BP
C 600   FORMAT('SLX =',E12.5,2X,'XYZ =',E12.5,2X,'CP(2,NMAT) =',
C    &  E12.5,2X,'BP =',E12.5)
C       DO 999 I=1,5
C       X=0.01+I*0.02
C       Y=ERF(X)
C       Z=ERFI(Y)
C       WRITE(6,900) X,Y,Z
C 900   FORMAT('X =',E12.5,3X,'Y =',E12.5,3X,'Z =',E12.5)
  999   CONTINUE
        IF((ALOG10(BP)-BETA)/CP(2,NMAT).LE.0.) THEN
        PC=(2*CP(3,NMAT)*10**6)/BP
        ELSE
          BP=10**(BETA+SQRT(2.)*CP(2,NMAT)*ERFI(2.*SLX-1.))
C         XYZ=ERFI(2.*SLX-1.)
C         WRITE(6,800) SLX,XYZ,CP(2,NMAT),BP
C 800     FORMAT('SLX =',E12.5,2X,'XYZ =',E12.5,2X,'CP(2,NMAT) =',
C    &    E12.5,2X,'BP =',E12.5)
          IF((ALOG10(BP)-BETA)/CP(2,NMAT).GT.0.) THEN
```

```
              PC=(2*CP(3,NMAT)*10**6)/BP
            ELSE
              WRITE(6,400)
  400         FORMAT('STOP-400, ERROR IN BP CALCULATION')
              STOP
            END IF
          END IF
        PC=-PC
        IF(SL.GE.(1.-1.E-5)) PC=PC*(1.-SL)/CP(4,NMAT)
        RETURN
C
        END
        SUBROUTINE SIGMA(T,ST)
C
C-----COMPUTE SURFACE TENSION OF WATER, USING THE
C     "INTERNATIONAL REPRESENTATION OF THE SURFACE TENSION OF
C                                                WATER SUBSTANCE" (1975).
C
        IF(T.GE.374.15) GOTO 1
        ST=1.-0.625*(374.15-T)/647.3
        ST=ST*.2358*((374.15-T)/647.3)**1.256
        RETURN
C
      1 ST=0.
        RETURN
        END
        SUBROUTINE OUT
C
C-----THIS SUBROUTINE GENERATES PRINTOUT.
C
C
C$$$$$$$$$ COMMON BLOCKS FOR ELEMENTS $$$$$$$$$$$$$$$$$$$$$$$$$$$$$$$$
C
C     THESE BLOCKS HAVE A LENGTH OF NEL (= NUMBER OF ELEMENTS)
C
        COMMON/E1/ELEM(1)
        COMMON/E2/MATX(1)
        COMMON/E3/EVOL(1)
        COMMON/E4/PHI(1)
        COMMON/E5/P(1)
        COMMON/E6/T(1)
C
C$$$$$$$$$$$$$$$$$$$$$$$$$$$$$$$$$$$$$$$$$$$$$$$$$$$$$$$$$$$$$$$$$$$$$$
C
C$$$$$$$$$ COMMON BLOCKS FOR PRIMARY VARIABLES $$$$$$$$$$$$$$$$$$$$$$$
C
C     THESE BLOCKS HAVE A LENGTH OF 3*NEL
C
        COMMON/P1/X(1)
        COMMON/P2/DX(1)
        COMMON/P3/DELX(1)
        COMMON/P4/R(1)
        COMMON/P5/DOLD(1)
C
C$$$$$$$$$$$$$$$$$$$$$$$$$$$$$$$$$$$$$$$$$$$$$$$$$$$$$$$$$$$$$$$$$$$$$$
C
C
C$$$$$$$$$ COMMON BLOCKS FOR CONNECTIONS $$$$$$$$$$$$$$$$$$$$$$$$$$$C
C
        COMMON/C1/NEX1(1)
```

CODE LISTING B.D.2: FORTRAN source code for calculating fracture capillary pressure (version 2).

```
C     WATER RES. RES., VOL. 18 NO.3 (JUNE 1982), PP. 489-498.
C
      IF(SL-CP(1,NMAT).GE..371) GOTO 130
      SLX=AMAX1(SL,1.001*CP(1,NMAT))
      EX=(0.371/(SLX-CP(1,NMAT))-1.)**.25
      EX=2.26*EX-2.
      PC=-9.7783E3*10.**EX
      RETURN
C
  130 PC=-97.783
      RETURN
   14 CONTINUE
   15 CONTINUE
C-----LEVERETTOS J-FUNCTION.
      SS=0.
      IF(SL.GT.CP(2,NMAT)) SS=(SL-CP(2,NMAT))/(1.-CP(2,NMAT))
      OSS=1.-SS
      F=1.417*OSS-2.120*OSS**2+1.263*OSS**3
      CALL SIGMA(T,ST)
      PC=-CP(1,NMAT)*ST*F
      RETURN
   16 CONTINUE
C-----CAPILLARY FUNCTION OF VAN GENUCHTEN, SOIL SCI. SOC. AM. J. 44,
C     PP.892-898, 1980.
C
      IF(SL.NE.1.)GO TO 160
      PC=0.
      RETURN
C
  160 SLX=SL
      IF(SLX.GE.CP(5,NMAT)) GOTO 161
      IF(CP(4,NMAT).EQ.0.)SLX=AMAX1(SL,1.001*CP(2,NMAT))
      PC=-ABS(CP(4,NMAT))
      IF(SLX.GT.CP(2,NMAT))
     XPC=-1./ABS(CP(3,NMAT))*(((SL-CP(2,NMAT))/(CP(5,NMAT)-CP(2,NWAT)))
     X**(-1./CP(1,NMAT))-1.)**(1.-CP(1,NMAT))
      IF(CP(4,NMAT).NE.0.) PC=AMAX1(PC,-ABS(CP(4,NMAT)))
      IF(SL.GT..999) PC=PC*(1.-SL)/.001
      RETURN
  161 PC=0.
      RETURN
   17 CONTINUE
      IF(ICALL.GT.1.) GO TO 1000
C
C-----CAPILLARY FUNCTION FROM LOG-NORMAL APERTURE DISTRIBUTION, EMS
C
      B0=CP(1,NMAT)/EXP(((CP(2,NMAT)*ALOG(10.))**2)/2.)
      BETA=CP(2,NMAT)**2*ALOG(10.)+ALOG10(B0)
 1000 CONTINUE
      SLX=SL
      IF(SLX.GE.(1.-CP(4,NMAT))) SLX=1.-CP(4,NMAT)
      IF(SLX.LE.CP(4,NMAT)) SLX=CP(4,NMAT)
      BP=10**(BETA+SQRT(2.)*CP(2,NMAT)*ERFI(2.*SLX-1.))
C     DO 999 I=1,5
C     X=0.01+I*0.02
C     Y=ERF(X)
C     Z=ERFI(Y)
C     WRITE(6,900) X,Y,Z
C 900 FORMAT('X =',E12.5,3X,'Y =',E12.5,3X,'Z =',E12.5)
  999 CONTINUE
```

```
      PC=(2*CP(3,NMAT)*10**6)/BP
      PC=-PC
      IF(SL.GE.(1.-CP(4,NMAT))) PC=PC*(1.-SL)/CP(4,NMAT)
      RETURN
C
      END
      SUBROUTINE SIGMA(T,ST)
C
C-----COMPUTE SURFACE TENSION OF WATER, USING THE
C     "INTERNATIONAL REPRESENTATION OF THE SURFACE TENSION OF
C                                                WATER SUBSTANCE" (1975).
C
      IF(T.GE.374.15) GOTO 1
      ST=1.-0.625*(374.15-T)/647.3
      ST=ST*.2358*((374.15-T)/647.3)**1.256
      RETURN
C
    1 ST=0.
      RETURN
      END
      SUBROUTINE OUT
C
C-----THIS SUBROUTINE GENERATES PRINTOUT.
C
C
C$$$$$$$$$$ COMMON BLOCKS FOR ELEMENTS $$$$$$$$$$$$$$$$$$$$$$$$$$$$$$$$$$
C
C     THESE BLOCKS HAVE A LENGTH OF NEL (= NUMBER OF ELEMENTS)
C
      COMMON/E1/ELEM(1)
      COMMON/E2/MATX(1)
      COMMON/E3/EVOL(1)
      COMMON/E4/PHI(1)
      COMMON/E5/P(1)
      COMMON/E6/T(1)
C
C$$$$$$$$$$$$$$$$$$$$$$$$$$$$$$$$$$$$$$$$$$$$$$$$$$$$$$$$$$$$$$$$$$$$$$$$$
C
C$$$$$$$$$$ COMMON BLOCKS FOR PRIMARY VARIABLES $$$$$$$$$$$$$$$$$$$$$$$$$$
C
C     THESE BLOCKS HAVE A LENGTH OF 3*NEL
C
      COMMON/P1/X(1)
      COMMON/P2/DX(1)
      COMMON/P3/DELX(1)
      COMMON/P4/R(1)
      COMMON/P5/DOLD(1)
C
C$$$$$$$$$$$$$$$$$$$$$$$$$$$$$$$$$$$$$$$$$$$$$$$$$$$$$$$$$$$$$$$$$$$$$$$$$
C
C
C$$$$$$$$$$ COMMON BLOCKS FOR CONNECTIONS $$$$$$$$$$$$$$$$$$$$$$$$$$$$$C
C
      COMMON/C1/NEX1(1)
      COMMON/C2/NEX2(1)
      COMMON/C3/DEL1(1)
      COMMON/C4/DEL2(1)
      COMMON/C5/AREA(1)
      COMMON/C6/BETA(1)
      COMMON/C7/ISOX(1)
```

CODE LISTING B.D.3: Access procedure for inverse error function from IMSLSFUN library.

```
b=(bmulkm,bgasic,bmulkz,bnrce3c7,bma28),lib=imslsfun,x=xtc7
*** warning - module MULTI            in file bgasic will be used
*** warning - copy in file bmulkz will be ignored
*** warning - module CONVER           in file bgasic will be used
*** warning - copy in file bmulkz will be ignored
*** warning - module OUT              in file bgasic will be used
*** warning - copy in file bnrce3c7 will be ignored


                                        cray1 loader -   11/03/89

time and date of load is - 18:56:50  02/18/90 , machine is e

program length is 01432144

transfer address = 0001205700a

loader size = 240364.


unrestricted memory management heap is at 00000312,size is 00011504
stack is at 00002451,   size is 00003217

following is a list of relocatable binaries specified for this load.
they will be referred to by their ordinal elsewhere in this load map.

ordinal      name

    1   bmulkm
    2   bgasic
    3   bmulkz
    4   bnrce3c7
    5   bma28
    6   imslsfun
    7   imslcore
    8   fortlib
    9   mathlib
   10   omnilib
   11   stacklib
   12   baselib

            libraries used

library          updated                created          used

    6        04/21/89 13:58:32     09/16/88 10:46:47   yes
    7        04/21/89 13:48:45     09/16/88 10:47:57   yes
    8        11/13/89 11:08:38     10/20/89 14:14:53   yes
    9        02/12/90 11:47:57     11/13/89 13:28:39   yes
   10        08/28/89 12:03:32     11/25/85 14:17:09   no
   11        04/21/89 16:16:29     01/09/84 15:32:44   yes
   12        12/12/89 11:41:19     12/12/89 11:41:19   yes
```

CODE LISTING B.D.4: Coding for identifying the position of the gas saturation front.

```
     1  'DX2',9X,'DX3',8X,'K(GAS)      K(LIQ.)      H(GAS)       H(LIQ.)')
 5031 FORMAT(110X,'(J/KG)       (J/KG)'/)
 1000 FORMAT(A1,'ELEM.  INDEX      P',11X,'T',10X,'SG',10X,'SL',7X,
     1  'XAIRG',7X,'XAIRL',8X,'tmob',8X,'PCAP',10X,'DG',10X,'DL')
 1001 FORMAT(17X,'(PA)       (DEG-C)',53X,'     ',8X,'(PA)',7X,
     1  '(KG/M**3)    (KG/M**3)'/)
 5040 FORMAT(1X,A5,I6,10(E11.4,1X))
 5060 FORMAT(A1,2X,'ELEM1  ELEM2  INDEX     FLOH',A6,'FLOH/FLOF',7X,
     1  'FLOF',7X,'FLO(GAS)      FLO(LIQ.)    VOL(GAS)      VOL(LIQ.)',
     2'     VOL')
 5061 FORMAT(26X,'(W)',8X,'(J/KG)',8X,'(KG/S)',7X,'(KG/S)',7X,
     1  '(KG/S)       (m**3/s)',5x,'(m**3/s)',5x,'(m**3/s)'/)
 5070 FORMAT(3x,2A7,I4,(10(1X,E12.4)))
 5120 FORMAT(A1,'ELEMENT SOURCE INDEX       GENERATION RATE',
     1  '      ENTHALPY    FF(GAS)       FF(LIQ.)       P(WB)')
 5121 FORMAT(29X,'(KG/S) OR (W)      (J/KG)',33X,'(PA)'/)
 5130 FORMAT(2X,A5,3X,A5,3X,I2,10X,E12.5,2X,6(1X,E12.5))
 5140 FORMAT('0',131('0')/A1)
C
      END
      SUBROUTINE CONVER
C
C-----THIS SUBROUTINE IS CALLED AFTER SUCCESFULL COMPLETION OF
C     A TIME STEP.
C     IT UPDATES PRIMARY VARIABLES, AND DEFINES THE NEXT TIME STEP.
C
C
      COMMON/SECOND/PAR(1)
      COMMON/E1/ELEM(1)
      COMMON/E2/MATX(1)
      COMMON/E4/PHI(1)
      COMMON/E5/P(1)
      COMMON/E6/T(1)
      COMMON/P1/X(1)
      COMMON/P2/DX(1)
C
      COMMON/G4/ELEG(30),SOURCE(30),LTABG(30),G(30),EG(30),NEXG(30)
     A,SDENS(30),SSAT(30),ITABG(30),NGIND(30),LCOM(30)
      COMMON/G6/PI(30),PWB(30),GVOL(30),HG(30)
C
      COMMON/SOLI/COM(27),EXPAN(27),CDRY(27),TORT(27)
      COMMON/KC/KC
      COMMON/DFM/TIMAX,REDLT
      COMMON/SVZ/NOITE,MOP(24)
      COMMON/DM/DELTEN,DELTEX,FOR,FORD
      COMMON/NN/NEL,NCON,NOGN,NK,NEQ,NPH,NB,NK1,NEQ1,NBK,NSEC,NFLUX
      COMMON/DLT/NDLT,DLT(100)
      COMMON/KONIT/KON,DELT,IGOOD
      COMMON/CYC/KCYC,ITER,ITERC,TIMIN,SUMTIM,GF,TIMOUT
      COMMON/TIMES/ITI,DELAF,ITPR,TIS(100),ITCOUNT,NOWTIM,DELTMX
C
      DIMENSION DXM(10)
C
      DO10 K=1,NK1
   10 DXM(K)=0.
C
      NGAS=0.
      DO3 N=1,NEL
      SGAS=PAR(NLOC2+1)
      IF(SGAS.EQ.0..OR.NGAS.NE.0) GO TO 1
```

```
      NGAS=N-1.
      SGAS0=SGAS
      PRES=X((NGAS-1)*3+1)
    1 CONTINUE
      NLOC=(N-1)*NK1
      NLOC2=(N-1)*NSEC*NEQ1
C-----COMPUTE CHANGES IN POROSITY.
      PHIN=PHI(N)
      NMAT=MATX(N)
      DPHI=PHIN*(COM(NMAT)*DX(NLOC+1)+EXPAN(NMAT)*(PAR(NLOC2+NSEC-1)
     A-T(N)))
      PHI(N)=PHIN+DPHI
C
C-----UPDATE ELEMENT PRESSURES AND TEMPERATURES.
      P(N)=X(NLOC+1)+DX(NLOC+1)
      T(N)=PAR(NLOC2+NSEC-1)
C
C-----INCREMENT PRIMARY VARIABLES.
      DO3 M=1,NEQ
      NLM=NLOC+M
      X(NLM)=X(NLM)+DX(NLM)
      DXM(M)=AMAX1(DXM(M),ABS(DX(NLM)))
    3 CONTINUE
      PRINT 600,ELEM(NGAS),NGAS,SGAS0,PRES
  600 FORMAT(1X,A5,I6,2X,'SGAS =',E12.5,2X,'PRES=',E12.5)
C
C-----FOR PERCENTAGE INJECTION, ASSIGN INJECTION RATE FOR NEXT
C     TIME STEP.
      DO 30 N=1,NOGN
      IF(LCOM(N).NE.NEQ+4) GOTO 30
      G(N)=-HG(N)*G(N-1)
   30 CONTINUE
C
C
      SUMTIM=SUMTIM+DELTEX
      IF(TIMAX.NE.0..AND.TIMAX.EQ.SUMTIM) NOWTIM=1
C-----AFTER CONVERGENCE UPDATE TOTAL TIME AND ASSIGN NEW TIME STEP.
      IF(NDLT.EQ.0) GOTO20
      IF(KC+1.GT.8*NDLT.OR.DLT(KC+1).EQ.0.) GOTO20
C-----IF NO FURTHER TIME STEP INSTRUCTIONS ARE PROVIDED, KEEP
C     GOING WITH LAST TIME STEP.
C-----COME HERE FOR NEW TIME STEP ASSIGNMENT.
      DELT=DLT(KC+1)
      GOTO 22
   20 DELT=DELTEX
      IF(ITER.LE.MOP(16)) DELT=2.*DELTEX
   22 IF(TIMAX.NE.0.) DELT=AMIN1(DELT,TIMAX-SUMTIM)
      IF(DELTMX.NE.0.) DELT=AMIN1(DELT,DELTMX)
C
      RETURN
      END
```

CODE LISTING B.D.5: Coding for relative permeability function with strong phase interference.

```
      REPL=0.
      REPG=1.
  102 CONTINUE
      IF (IRP(NMAT).EQ.4) REPG=1.-REPL
      RETURN
C
   13 CONTINUE
C-----BOTH PHASES ARE PERFECTLY MOBILE.
C
      REPL=1.
      REPG=1.
C
      RETURN
   14 CONTINUE
C-----RELATIVE PERMEABILITIES OF FATT AND KLIKOFF (1959), AS REPORTED
C     BY K. UDELL (BERKELEY, 1982).
C
      SS=0.
      IF (SL.GT.RP(1,NMAT)) SS=(SL-RP(1,NMAT))/(1.-RP(1,NMAT))
      REPL=SS**3
      REPG=(1.-SS)**3
      RETURN
C
C
   15 CONTINUE
C-----RELATIVE PERMEABILITY OF VAN GENUCHTEN, SOIL SCI. SOC. AM. J. 44,
C     PP. 892-898, 1980.
C
      IF (SL.GE.RP(3,NMAT)) GO TO 150
      SS=(SL-RP(2,NMAT))/(RP(3,NMAT)-RP(2,NMAT))
      REPL=0.
      IF (SS.GT.0.)
     1   REPL=SQRT(SS)*(1.-(1.-SS**(1./RP(1,NMAT)))**RP(1,NMAT))**2
      REPG=1.-REPL
      RETURN
C
  150 REPL=1.
      REPG=0.
      RETURN
C
   16 CONTINUE
C     RELATIVE PERMEABILITIES AS MEASURED BY VERMA ET AL. IN
C     LABORATORY FLOW EXPERIMENTS FOR STEAM-WATER MIXTURES
C
      SS=(SL-RP(1,NMAT))/(RP(2,NMAT)-RP(1,NMAT))
      IF(SS.GT.1.) SS=1.
      IF(SS.LT.0.) SS=0.
      REPL=SS**3
      REPG=RP(3,NMAT)+RP(4,NMAT)*SS+RP(5,NMAT)*SS*SS
      IF(REPG.GT.1.) REPG=1.
      IF(REPG.LT.0.) REPG=0.
      RETURN
C
   17 CONTINUE
C     STRONG PHASE INTERFERENCE RELATIVE PERMEABILITIES, EMS
C
      SSTAR1=0.
      IF(SL.GT.RP(1,NMAT)) SSTAR1=(SL-RP(1,NMAT))/(1.-RP(1,NMAT))
      REPL=SSTAR1**4
      IF(SL.LE.RP(1,NMAT)) REPL=0.
```

```
      SSTAR2=0.
      IF(SG.GT.RP(2,NMAT)) SSTAR2=(SG-RP(2,NMAT))/(1.-RP(2,NMAT))
      REPG=SSTAR2**4
      IF(SG.LE.RP(2,NMAT)) REPG=0.
      RETURN
C
      END
      SUBROUTINE PCAP(SL,T,PC,NMAT)
C
C-----THIS ROUTINE COMPUTES CAPILLARY PRESSURE AS FUNCTION OF LIQUID
C     SATURATION SL AND TEMPERATURE T.
C
      DATA ICALL/0/
      ICALL=ICALL+1
      COMMON/RPCAP/IRP(27),RP(7,27),ICP(27),CP(7,27),IRPD,RPD(7),
     XICPD,CPD(7)
C
      GOTO(10,11,12,13,14,15,16,17),ICP(NMAT)
C
   10 CONTINUE
C-----LINEAR FUNCTION.
      PC=-CP(1,NMAT)*(CP(3,NMAT)-SL)/(CP(3,NMAT)-CP(2,NMAT))
      IF(SL.GE.CP(3,NMAT)) PC=0.
      IF(SL.LE.CP(2,NMAT)) PC=-CP(1,NMAT)
      RETURN
   11 CONTINUE
C-----CAPILLARY PRESSURE FUNCTION OF PICKENS ET AL, AS GIVEN IN
C     J. HYDROLOGY 40, 243-264, 1979.
C
      SLX=AMAX1(SL,1.001*CP(2,NMAT))
      IF(SLX.GT..999*CP(3,NMAT)) SLX=.999*CP(3,NMAT)
      A=(1.+SLX/CP(3,NMAT))*(CP(3,NMAT)-CP(2,NMAT))/
     X(CP(3,NMAT)+CP(2,NMAT))
      B=(1.-SLX/CP(3,NMAT))
      PC=-CP(1,NMAT)*ALOG(A*(1.+SQRT(1.-B*B/(A*A)))/B)**
     X(1./CP(4,NMAT))
      IF(SL.GT..999*CP(3,NMAT)) PC=PC*(1.-SL)/.001
      RETURN
C
C
   12 CONTINUE
C-----CAPILLARY PRESSURE FUNCTION AS USED IN THE TRUST-PROGRAM, WHICH
C     WAS DEVELOPED BY T.N. NARASIMHAN AT LAWRENCE BERKELEY LABORATORY.
C
      IF(SL.NE.1) GOTO 120
      PC=0.
      RETURN
C
  120 SLX=SL
      IF(CP(5,NMAT).EQ.0.)SLX=AMAX1(SL,1.001*CP(2,NMAT))
      PC=-ABS(CP(5,NMAT))
      IF(SLX.GT.CP(2,NMAT))
     XPC=-CP(4,NMAT)-CP(1,NMAT)*((1.-SLX)/(SLX-CP(2,NMAT)))
     X**(1./CP(3,NMAT))
      IF(CP(5,NMAT).NE.0.)PC=AMAX1(PC,-ABS(CP(5,NMAT)))
      IF(SL.GT..999) PC=PC*(1.-SL)/.001
      RETURN
C
   13 CONTINUE
C-----CAPILLARY PRESSURE OF YOLO CLAY AFTER CHRIS MILLY,
```

CODE LISTING B.D.6: Sample TOUGH2-input file for reference case.

```
•cycl14• SENSITIVITY STUDIES - REFERENCE CASE (GRAVITY)
ROCKS
FRACT    2      2600.        .01     1.E-17                              2.1   1000.
    1.e-10
    3             0.3        .05
    8            .2836       .43       .073      1.e-5
BOUND    2      2600.        .01     1.E-17                              2.1    1.E4
    1.e-10
    5
    1             0.0        0.0         1.

START
MULTI
    2    2    2    6
PARAM
   2 150      150000030100000020370000000
                  -1.                    V  40        +9.80665
      2.E6
     1.E-5
                 1.E5                    0.                 .      10.
TIMES
    6    6
     .36E8     .294E9      .45E9      .55E9      .60E9    .6735E9
ELEME
V   1   39     1FRACT        2.5
B   1           BOUND      1.E30

CONNE
V   1V   2   38    1    1    1       1.25       1.25         1.          1.
B   1V   1                   1     1.E-10       1.25         1.          1.

INCON
V   1             0.10000012e-01
 0.1122557464220e+06 0.1765930404651e-06 0.1000000000000e+02
V   2             0.10000037e-01
 0.1367674525159e+06 0.1925489430222e-08 0.1000000000000e+02
V   3             0.10000061e-01
 0.1612794432601e+06 0.2099353498015e-10 0.1000000000000e+02
V   4             0.10000086e-01
 0.1857917187122e+06 0.2300230425667e-12 0.1000000000000e+02
V   5             0.10000110e-01
 0.2103042791347e+06 0.2559756193228e-14 0.1000000000000e+02
V   6             0.10000135e-01
 0.2348171245779e+06 0.                  0.1000000000000e+02
V   7             0.10000159e-01
 0.2593302556216e+06 0.                  0.1000000000000e+02
V   8             0.10000184e-01
 0.2838436724648e+06 0.                  0.1000000000000e+02
V   9             0.10000208e-01
 0.3083573746549e+06 0.                  0.1000000000000e+02
V  10             0.10000233e-01
 0.3328713631771e+06 0.1406125628500e-14 0.1000000000000e+02
V  11             0.10000257e-01
 0.3573856375797e+06 0.1450031897742e-14 0.1000000000000e+02
V  12             0.10000282e-01
 0.3819001980844e+06 0.1420207585712e-16 0.1000000000000e+02
V  13             0.10000306e-01
 0.4064150453006e+06 0.                  0.1000000000000e+02
V  14             0.10000331e-01
 0.4309301787973e+06 0.                  0.1000000000000e+02
```

```
V  15            0.10000355e-01
 0.4554455996198e+06 0.                    0.1000000000000e+02
V  16            0.10000380e-01
 0.4799613071994e+06 0.                    0.1000000000000e+02
V  17            0.10000404e-01
 0.5044773025021e+06 0.                    0.1000000000000e+02
V  18            0.10000429e-01
 0.5289935845343e+06 0.                    0.1000000000000e+02
V  19            0.10000454e-01
 0.5535101541519e+06 0.                    0.1000000000000e+02
V  20            0.10000478e-01
 0.5780270118187e+06 0.                    0.1000000000000e+02
V  21            0.10000503e-01
 0.6025441570685e+06 0.                    0.1000000000000e+02
V  22            0.10000527e-01
 0.6270615904687e+06 0.                    0.1000000000000e+02
V  23            0.10000552e-01
 0.6515793123895e+06 0.                    0.1000000000000e+02
V  24            0.10000576e-01
 0.6760973221617e+06 0.                    0.1000000000000e+02
V  25            0.10000601e-01
 0.7006156213184e+06 0.                    0.1000000000000e+02
V  26            0.10000625e-01
 0.7251342081822e+06 0.                    0.1000000000000e+02
V  27            0.10000650e-01
 0.7496530832087e+06 0.                    0.1000000000000e+02
V  28            0.10000674e-01
 0.7741722478876e+06 0.                    0.1000000000000e+02
V  29            0.10000699e-01
 0.7986917006109e+06 0.                    0.1000000000000e+02
V  30            0.10000723e-01
 0.8232114428660e+06 0.4057354985448e-14   0.1000000000000e+02
V  31            0.10000748e-01
 0.8477314748554e+06 0.7423652773043e-14   0.1000000000000e+02
V  32            0.10000772e-01
 0.8722517950499e+06 0.6587215970874e-16   0.1000000000000e+02
V  33            0.10000797e-01
 0.8967724048514e+06 0.5273578149481e-18   0.1000000000000e+02
V  34            0.10000821e-01
 0.9212933036854e+06 0.2825857613270e-14   0.1000000000000e+02
V  35            0.10000846e-01
 0.9458144919453e+06 0.1747186698946e-16   0.1000000000000e+02
V  36            0.10000870e-01
 0.9703359698576e+06 0.9132897765051e-19   0.1000000000000e+02
V  37            0.10000895e-01
 0.9948577367295e+06 0.                    0.1000000000000e+02
V  38            0.10000919e-01
 0.1019379793928e+07 0.                    0.1000000000000e+02
V  39            0.10000944e-01
 0.1043902139969e+07 0.                    0.1000000000000e+02
V  40            0.10000968e-01
 0.1068424775061e+07 0.                    0.1000000000000e+02
B   1            0.10000000e-01
 0.1000000000000e+06 0.1050000000000e+02   0.1000000000000e+02

GENER
V  40AIR                          AIR       1.E-8       0.0

ENDCY
```

TABLE B-1: Parameters for the reference case.

Formation parameters:

permeability	porosity	compressibility
10^{-17} m^2	1%	10^{-10} (Pa)$^{-1}$

Relative permeability:

(Corey's Curves[6]; see Figure B-3)

liquid phase: $k_{rl} = [S^*]^4$

gas phase: $k_{rg} = (1 - S^*)^2(1 - [S^*]^2)$

where: $S^* = (S_l - S_{lr})/(1 - S_{lr} - S_{gr})$

$S_{lr} = 0.3$

$S_{gr} = 0.05$

Capillary pressure:

Fracture capillary pressure as derived for a lognormal aperture distribution by Pruess and Tsang[5]; see Appendix B.B and Figure B-2.

$P_c = 2\varsigma 10^{(\sqrt{2\sigma^2} erfi(1-2S_l)-\beta)}$

$\gamma = 0.073$ N/m

$\beta = -0.3344$

$\sigma = 0.43$

$b_{ave} = 0.2836$ μm

Boundary conditions:

bottom: air injection rate: 10^{-8} kg/s

top: $P_g = P_l = 10^5$ Pa $\equiv$ 1 bar

$(P_{cap} = 0)$

Initial conditions:

temperature: 10°C

pressure: hydrostatic pressure gradient

gas saturation: no air present

TABLE B-2: Sensitivity studies.

Case	Variation
1	stronger capillary pressure, with air entry effects (Narasimhan et al.[7]; see Figure B-10) parameters: $ICP = 3$, $P_o = 5 \times 10^5$ Pa, $S_{lr} = 0.3$, $\nu = 1.0$, $P_e = 2 \times 10^5$ Pa
2	no capillary pressure $P_c = 0$
3	Grant's relative permeabilities (Grant[8]; see Figure B-14) parameters: $IRP = 4$; other specifications as in reference case
4	strong interference relative permeabilities (see Appendix B.C and Figure B-15) parameters: $IRP = 9$; other specifications as in reference case
5	intrinsic permeability $k = 2 \times k_{ref}$; other specifications as in reference case
6	intrinsic permeability $k = 0.5 \times k_{ref}$; other specifications as in reference case
7	porosity $\phi = 2 \times \phi_{ref}$; other specifications as in reference case
8	porosity $\phi = 0.5 \times \phi_{ref}$; other specifications as in reference case

TABLE B-3: Results of sensitivity studies.

Case	$P_{g_{max}}$ (bars)	time (seconds)	Gas breakthrough time (seconds)
reference	37.98	0.72×10^8	0.67×10^9
1	39.38	0.93×10^8	0.69×10^9
2	37.21	0.72×10^8	0.66×10^9
3	35.18	0.29×10^8	0.19×10^9
4	93.55	59×10^8	3.8×10^9
5	28.96	0.36×10^8	0.49×10^9
6	50.79	1.00×10^8	0.94×10^9
7	37.88	1.8×10^8	1.3×10^9
8	37.95	0.36×10^8	0.34×10^9

TABLE B-4a: Behavior of fracture capillary pressure for $S_l \rightarrow 0$.

S_l	P_c (Pa)
10^{-4}	-0.1253×10^8
10^{-5}	-0.2151×10^8
10^{-6}	-0.3489×10^8

TABLE B-4b: Behavior of fracture capillary pressure for $S_l \rightarrow 1$.

S_l	P_c (Pa)
$1 - 10^{-4}$	-0.7936×10^4
$1 - 10^{-5}$	-0.4622×10^4
$1 - 10^{-6}$	-0.2850×10^4

TABLE B-5: Numerical check of fracture capillary pressure function.

b_p (μm)	$\frac{\log(b_p)-\beta}{\sigma\sqrt{2}}$	$erf\left(\frac{\log(b_p)-\beta}{\sigma\sqrt{2}}\right)$	$S_l(b_p)$	$P_{c_{[anal.]}}(b_p)$ (Pa)	$P_{c_{[num.]}}(b_p)$ (Pa)
.05	-1.5902	.97546	.0123	-2.9×10^6	-2.945×10^6
.1	-1.0952	.87851	.0607	-1.5×10^6	-1.457×10^6
.2	$-.6002$	.60543	.197	-7.3×10^5	-7.328×10^5
.332	$-.2382$	.26357	.367	-4.4×10^5	-4.411×10^5
.6	.1844	.20530	.592	-2.4×10^5	-2.503×10^5
.8	.3899	.41874	.695	-1.8×10^5	-1.902×10^5
1.0	.5492	.56249	.781	-1.5×10^5	-1.462×10^5
2.0	1.044	.86017	.930	-7.3×10^4	-7.309×10^4
3.0	1.334	.94097	.971	-4.9×10^4	-4.895×10^4

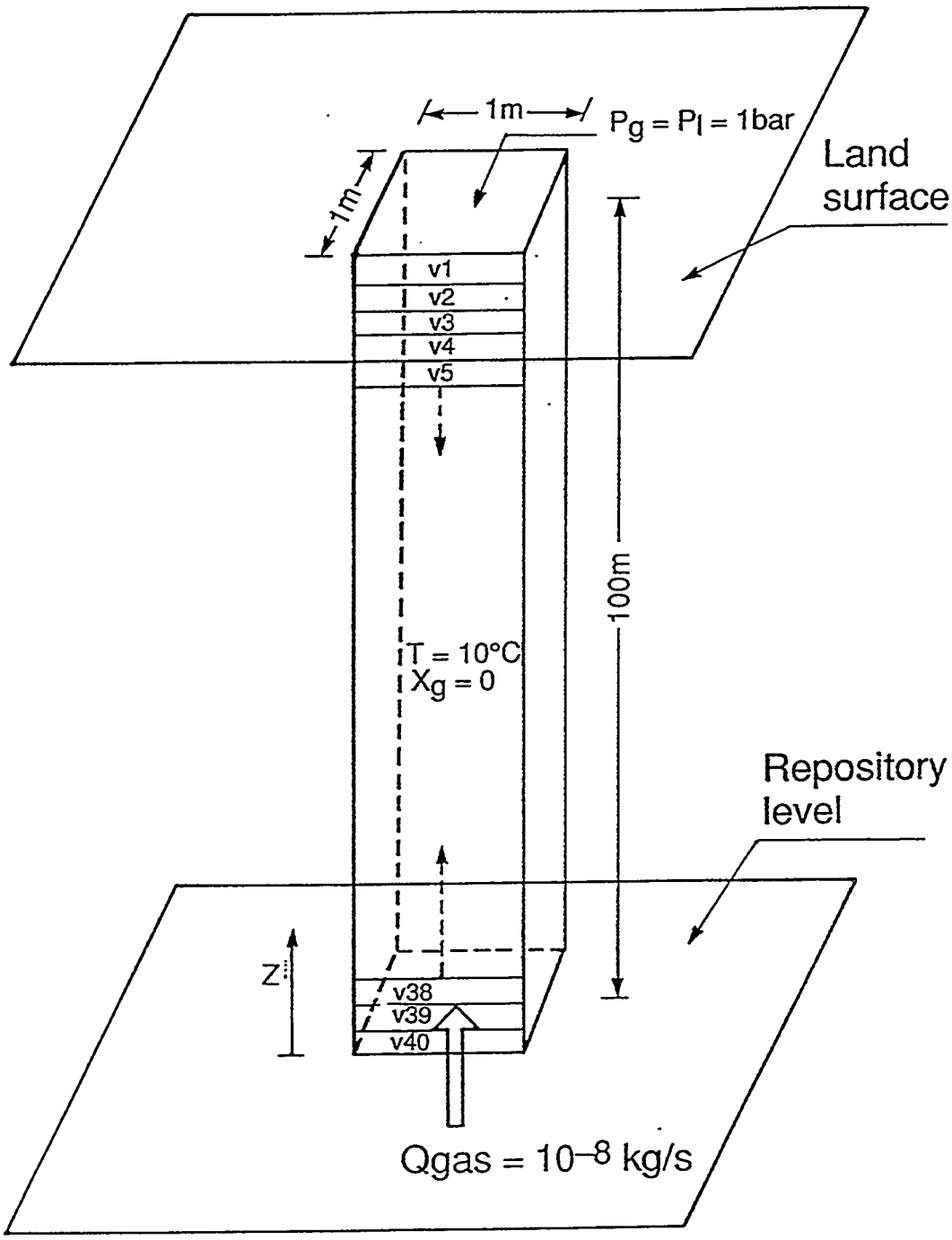

FIG. B-1: Schematic of flow system for gas migration studies.

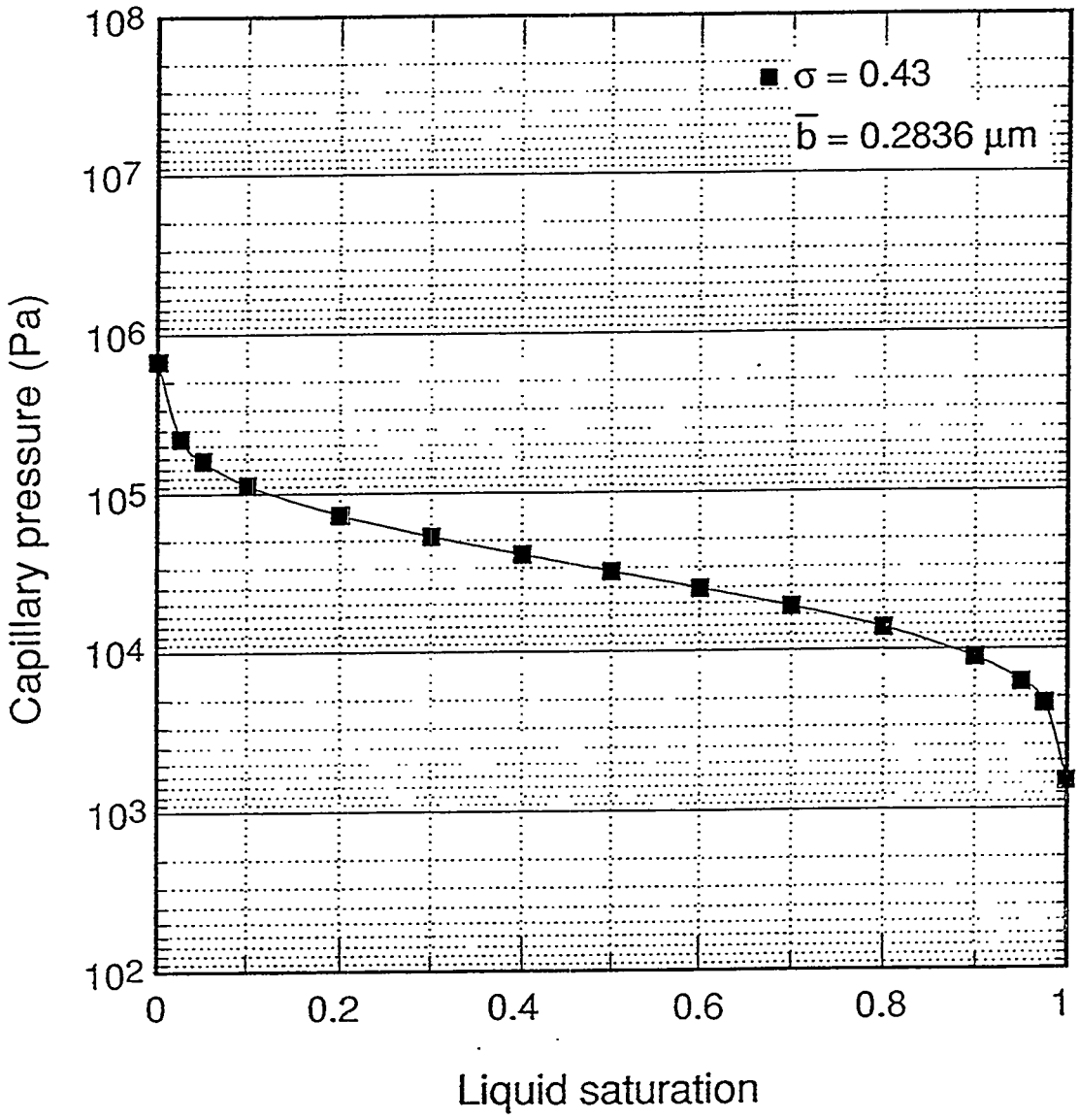

FIG. B-2: Capillary pressure of rough-walled fractures with log-normal aperture distribution.

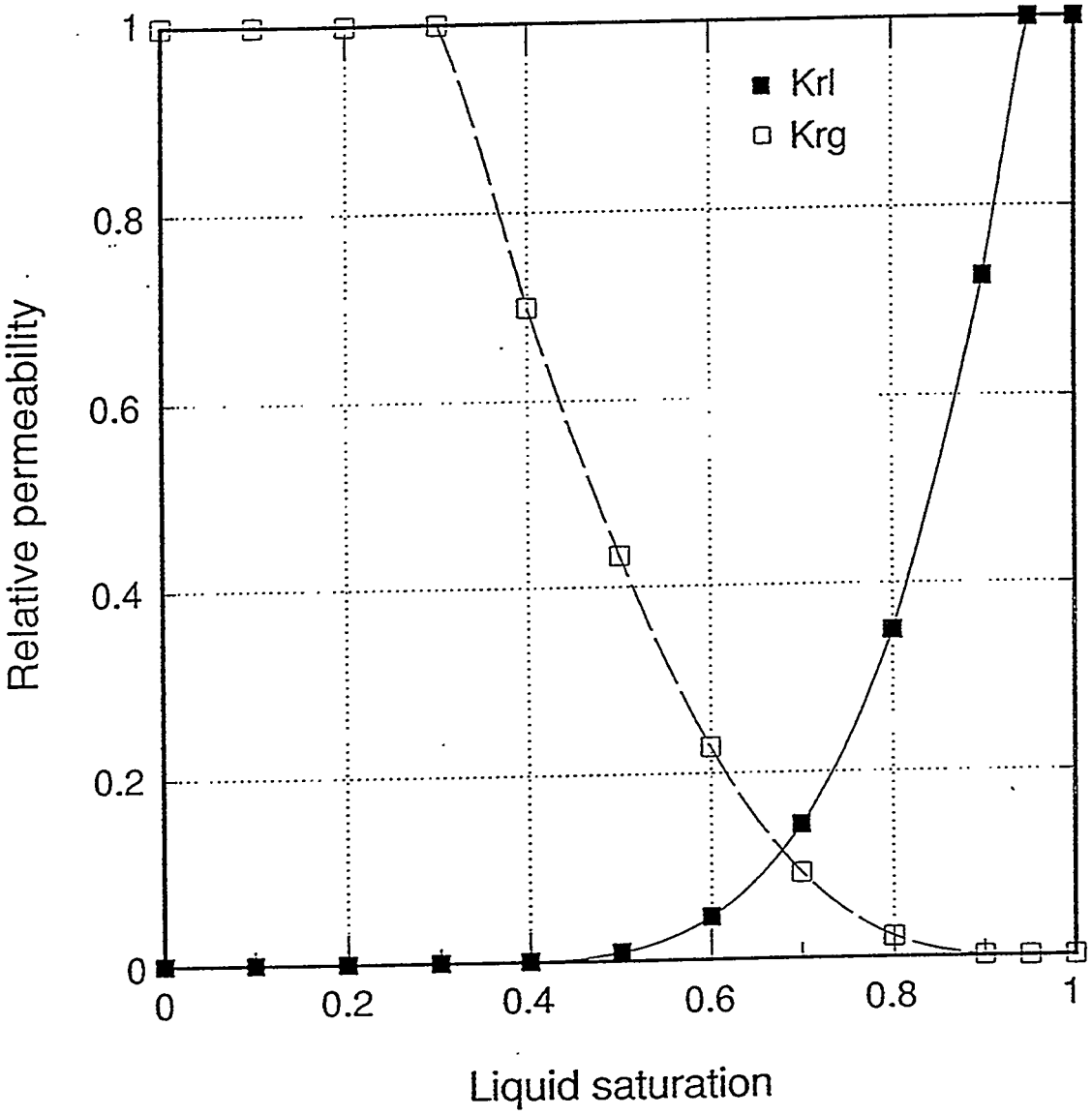

FIG. B-3: Two-phase relative permeability curves (after Corey, 1954).

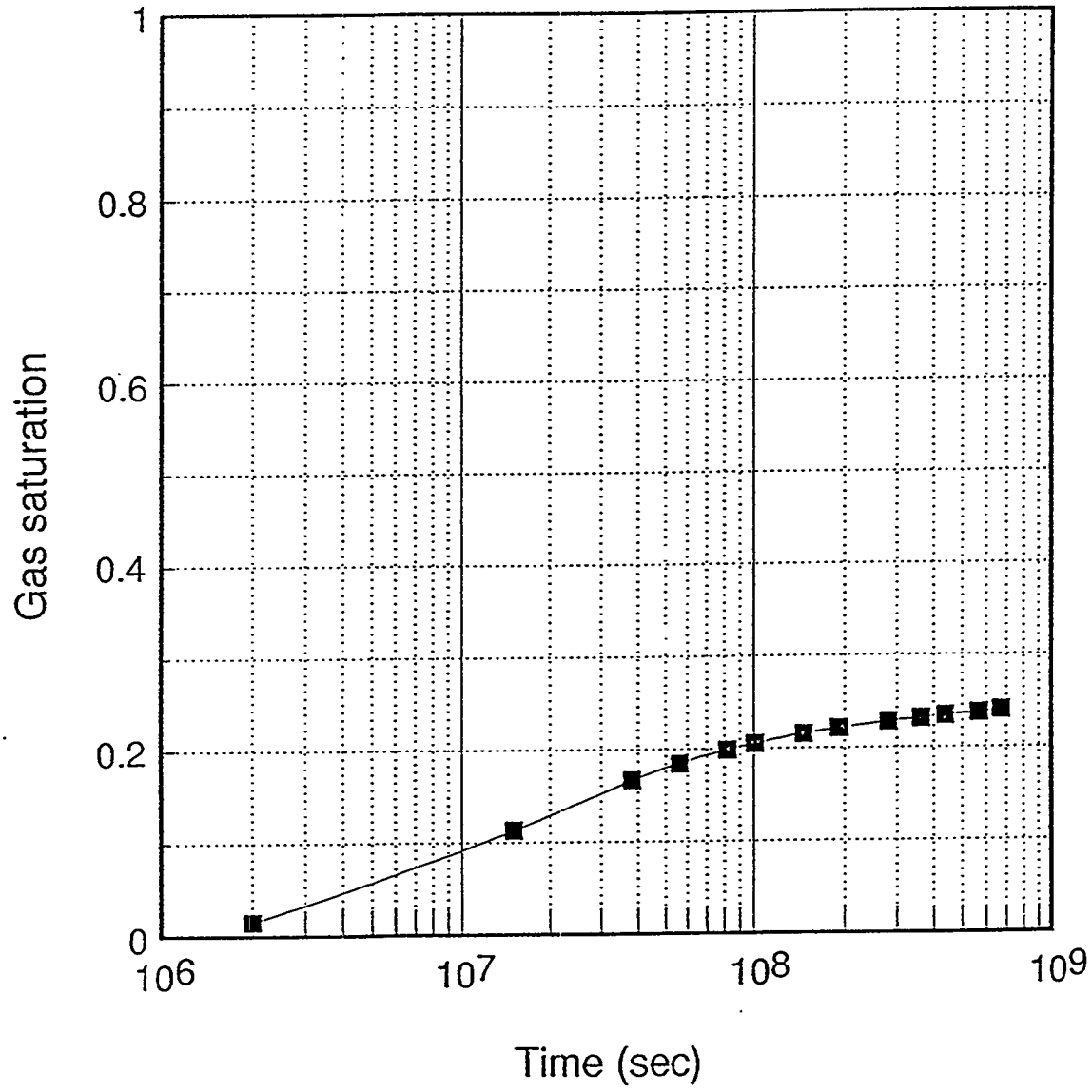

FIG. B-4: Simulated gas saturation in injection grid block for reference case.

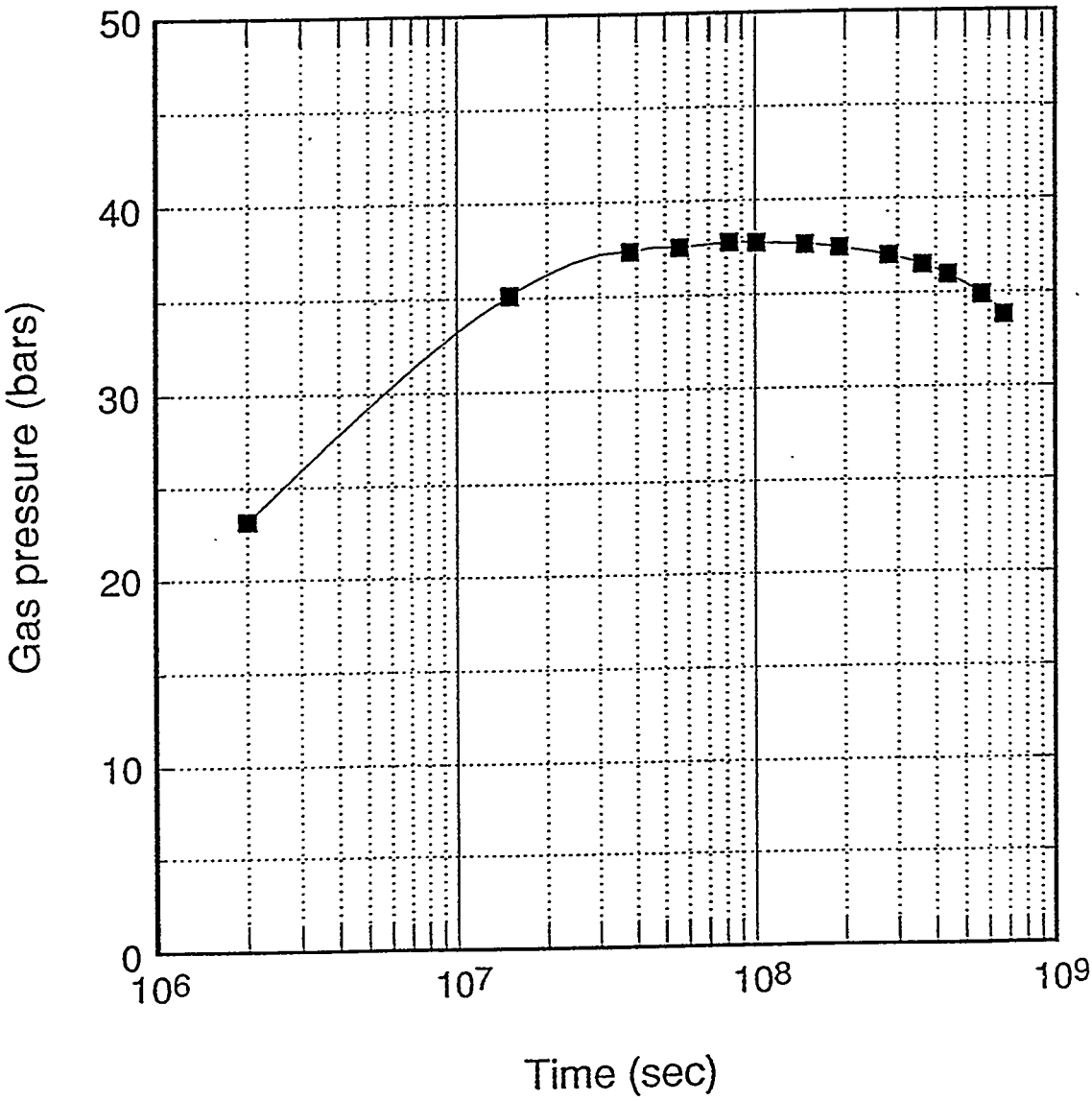

FIG. B-5: Simulated gas pressure in injection grid block for reference case.

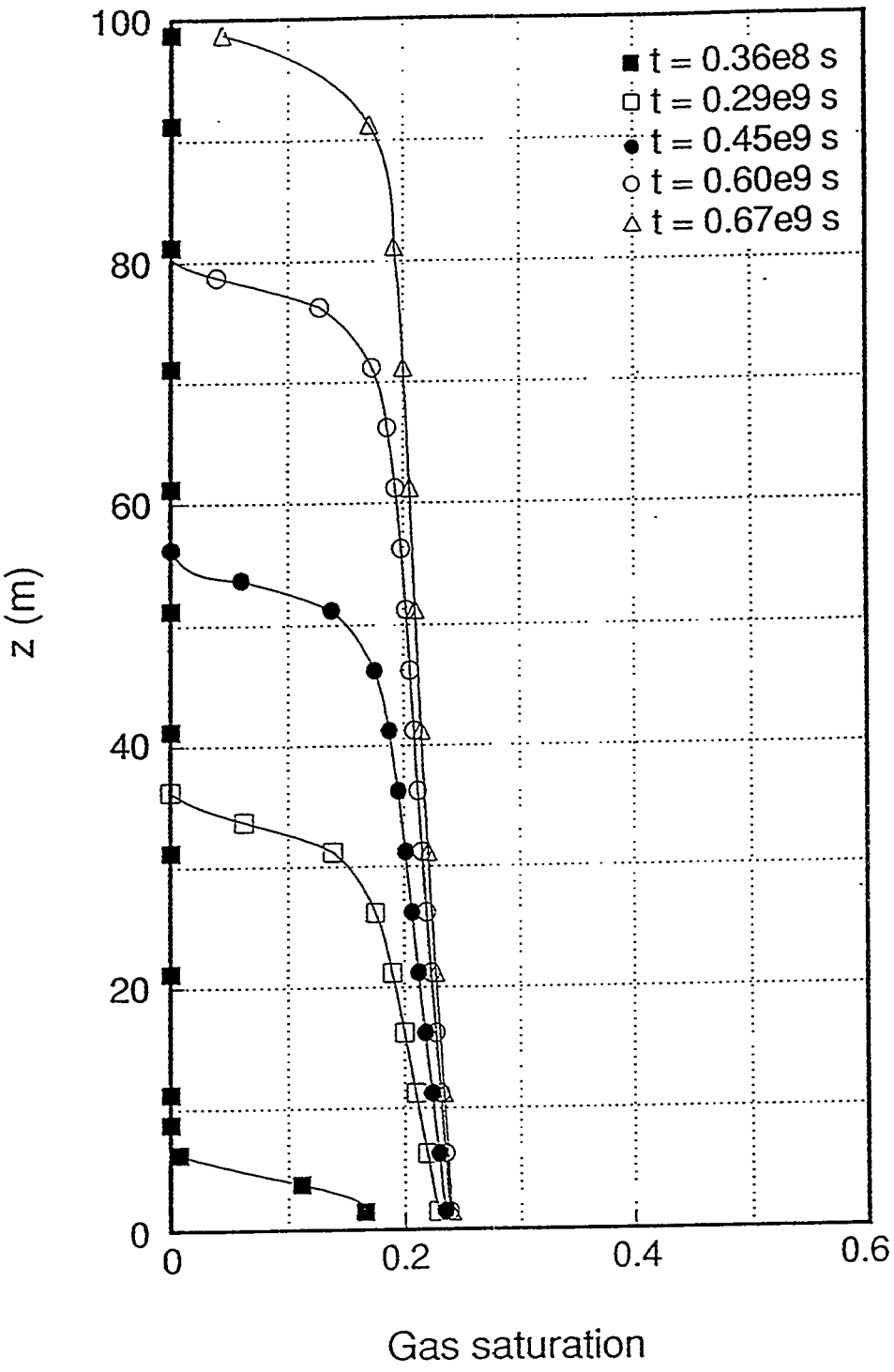

FIG. B-6: Simulated gas saturation profiles for the reference case at different times.

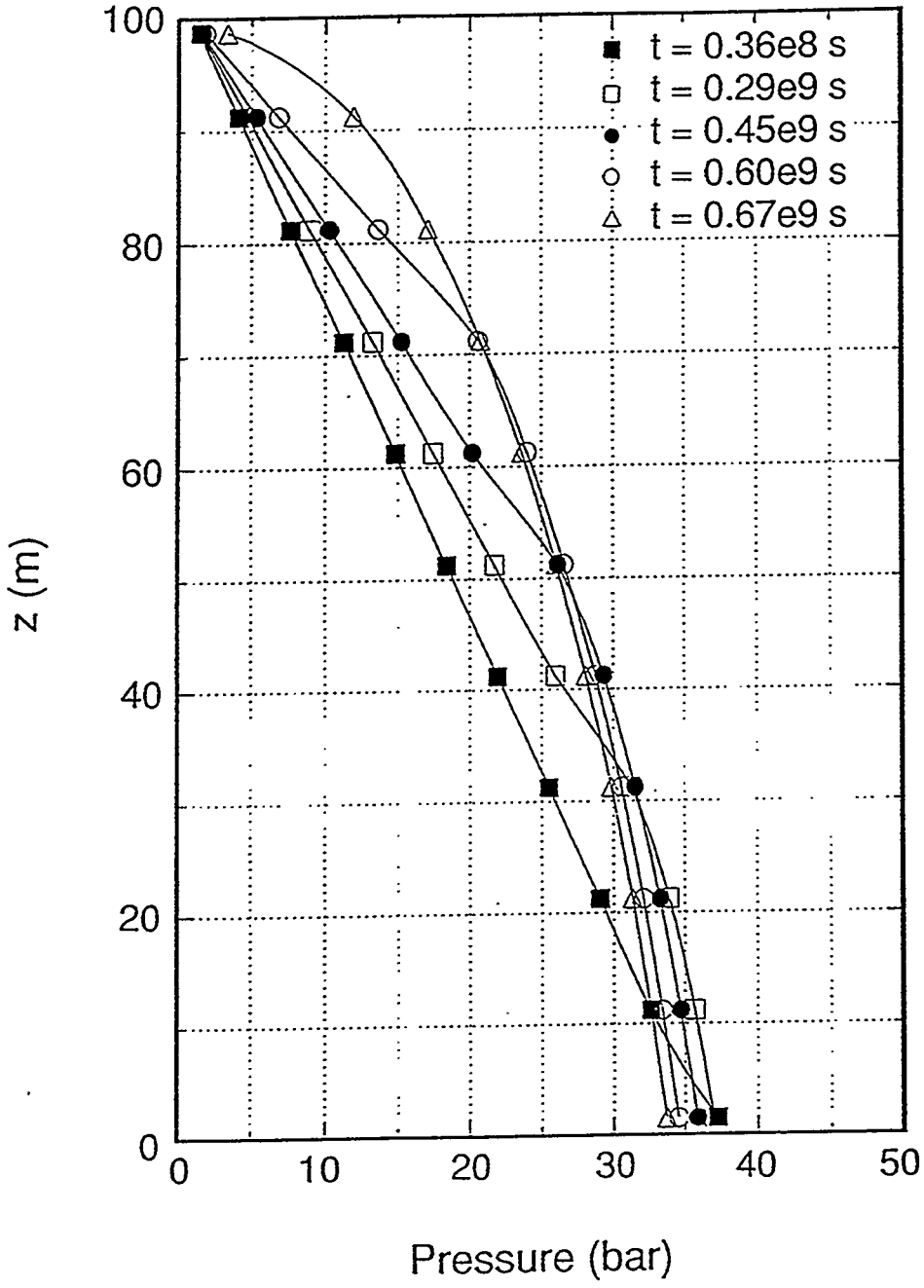

FIG. B-7: Gas pressure profiles for the reference case at different times.

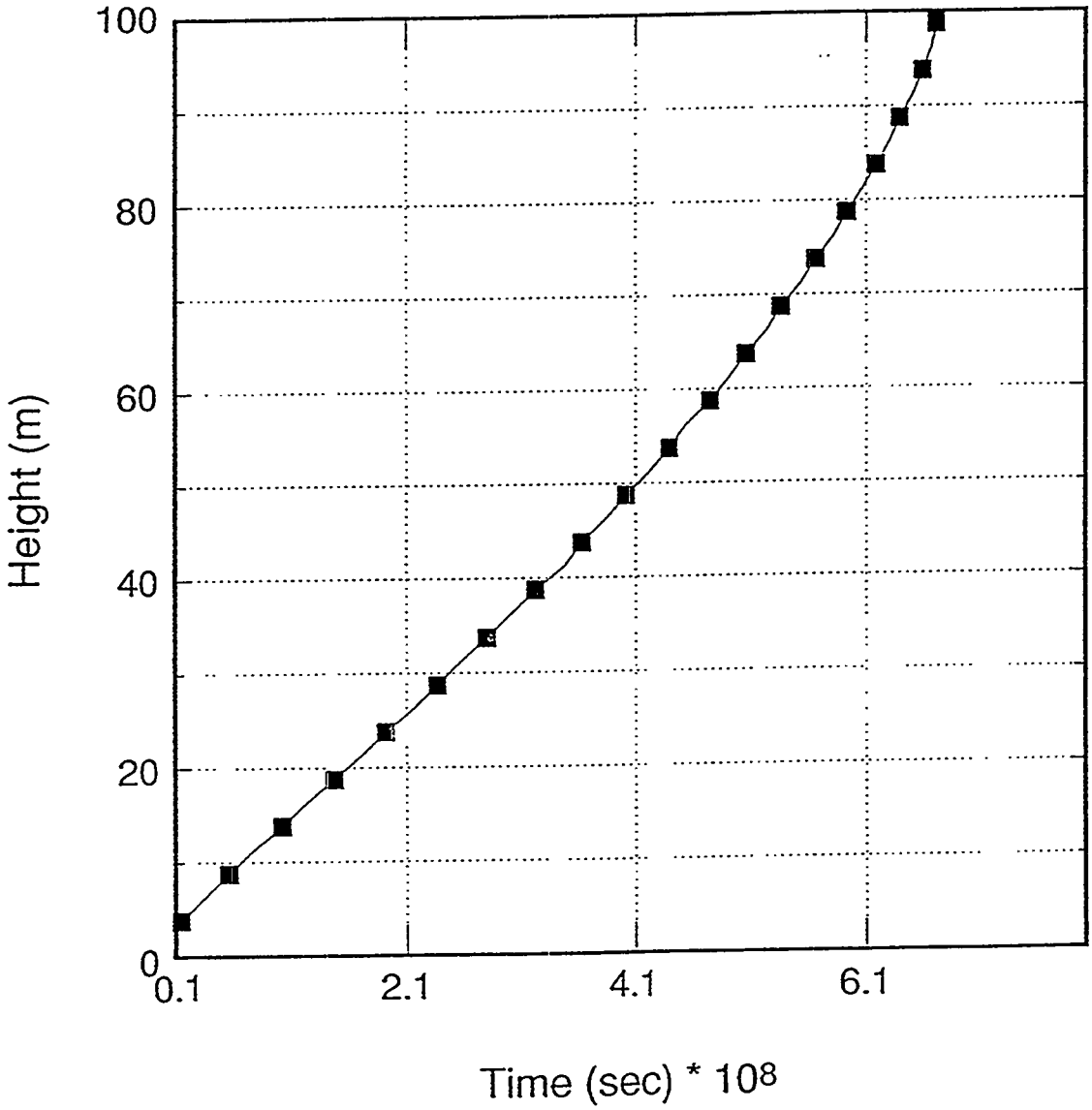

FIG. B-8: Simulated advance of the gas front for the reference case.

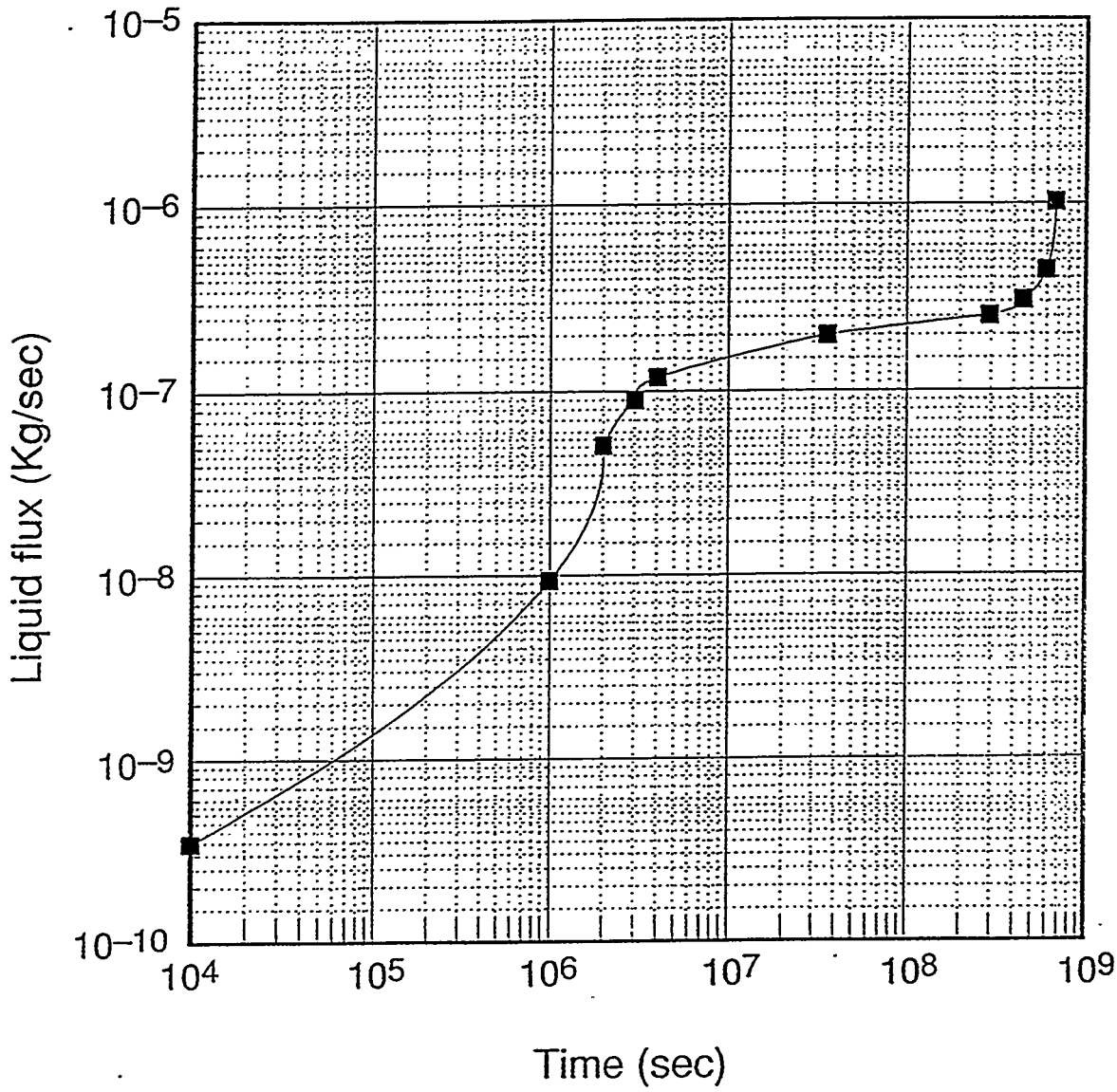

FIG. B-9: Simulated rate of liquid outflow at the top of the column.

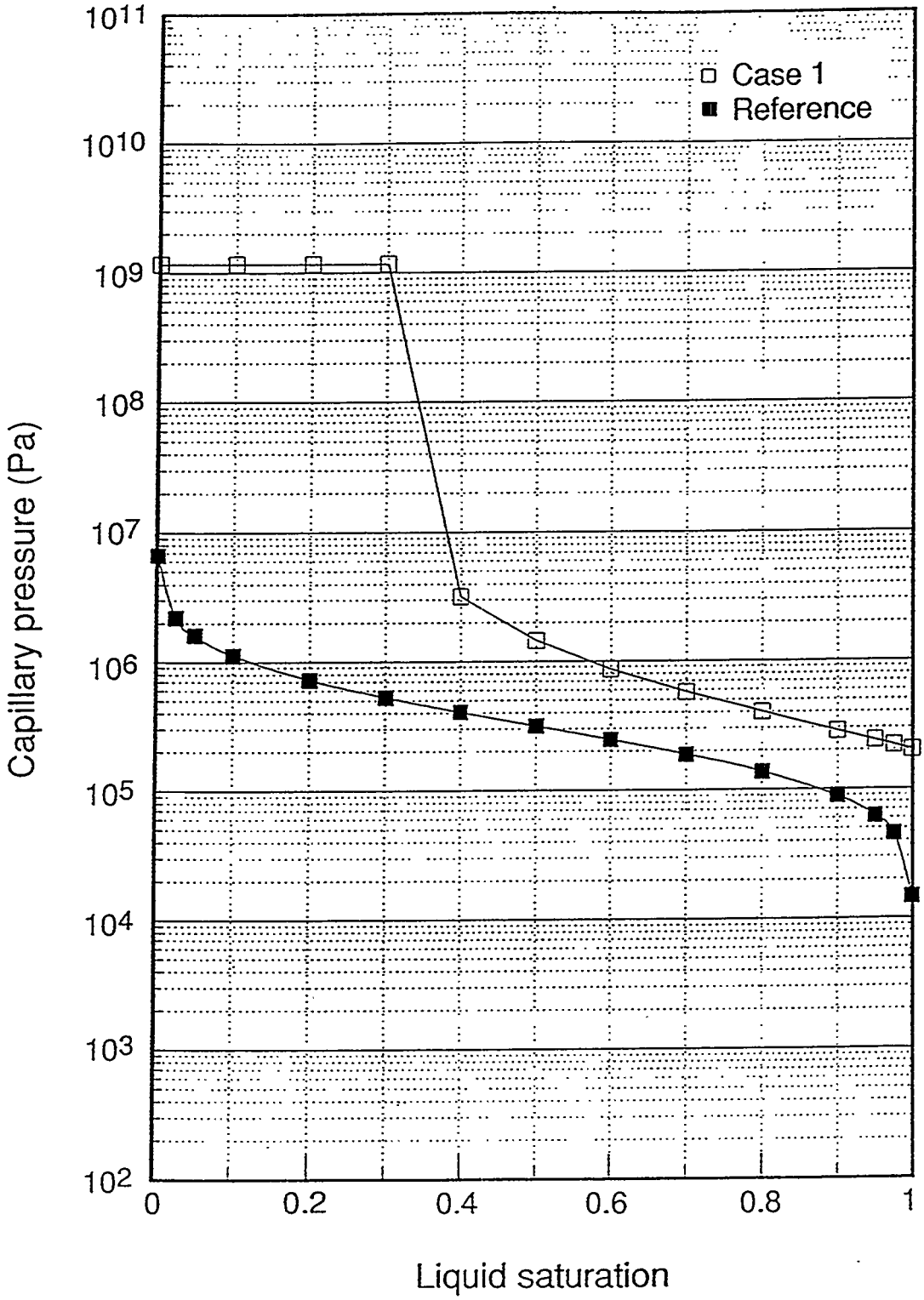

FIG. B-10: Capillary pressure functions used in sensitivity studies.

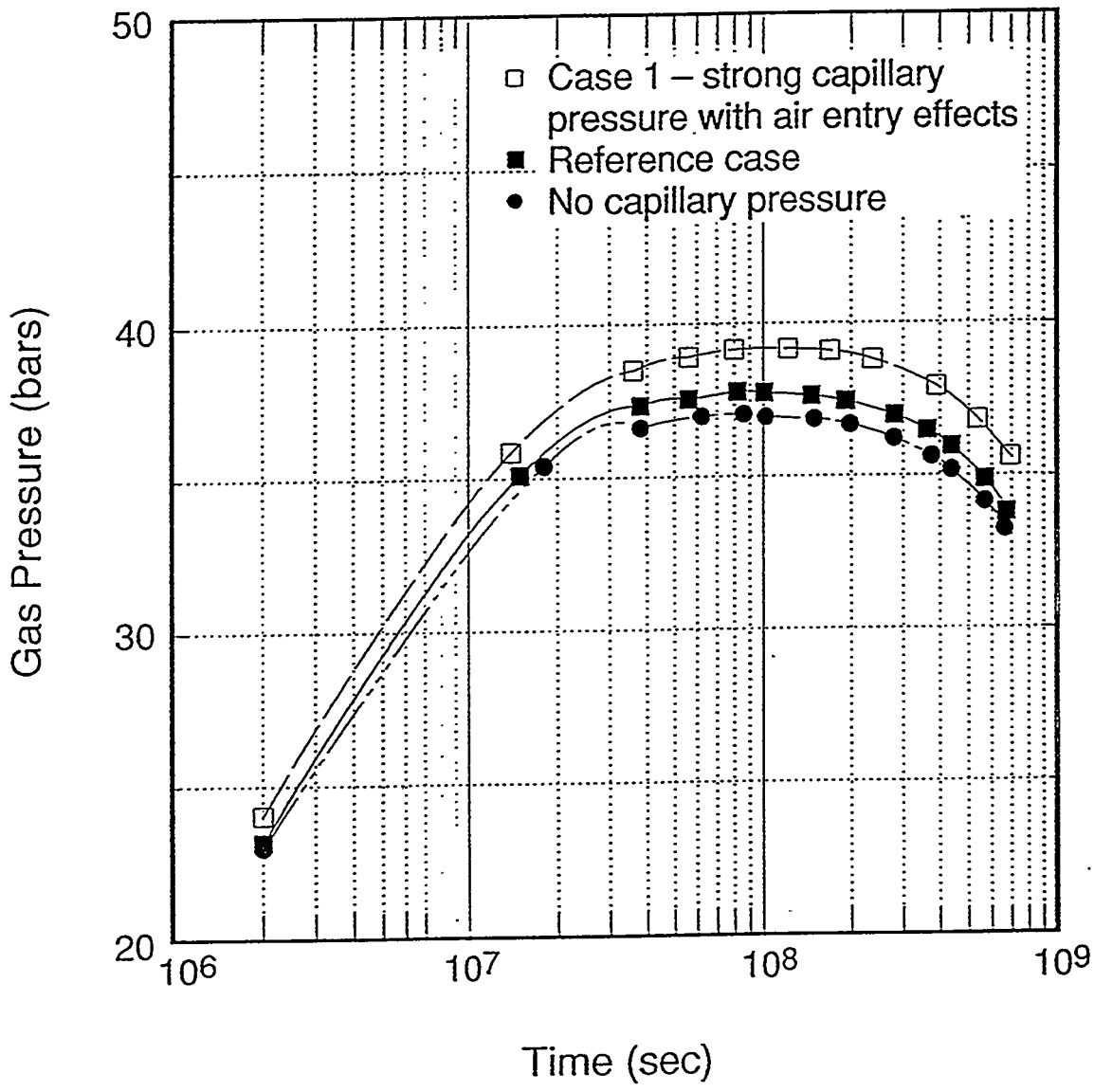

FIG. B-11: Sensitivity of gas pressures in injection block to variations in capillary pressure.

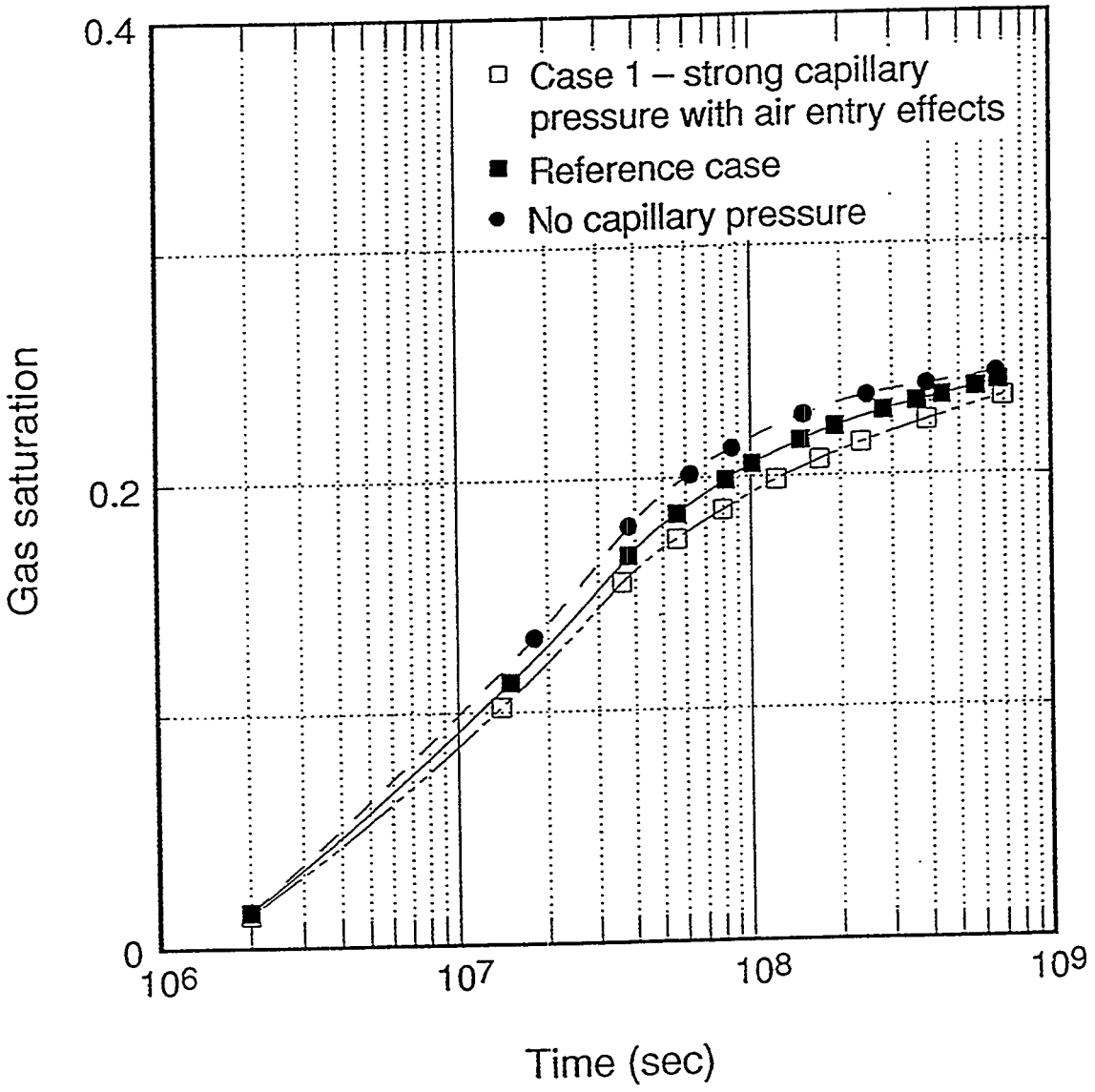

FIG. B-12: Sensitivity of gas saturation in injection block to variations in capillary pressure.

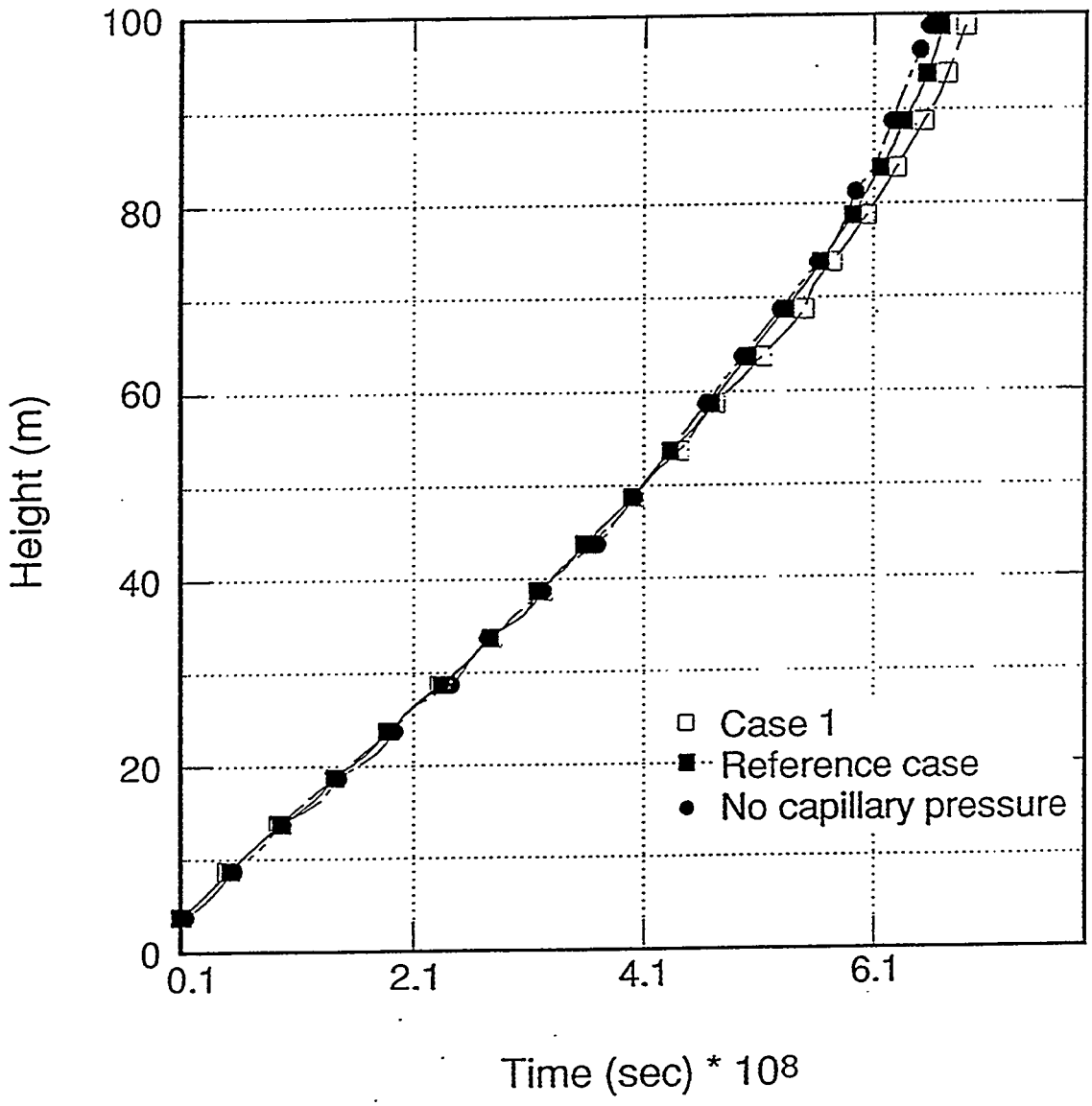

FIG. B-13: Advance of gas displacement front for different capillary pressures.

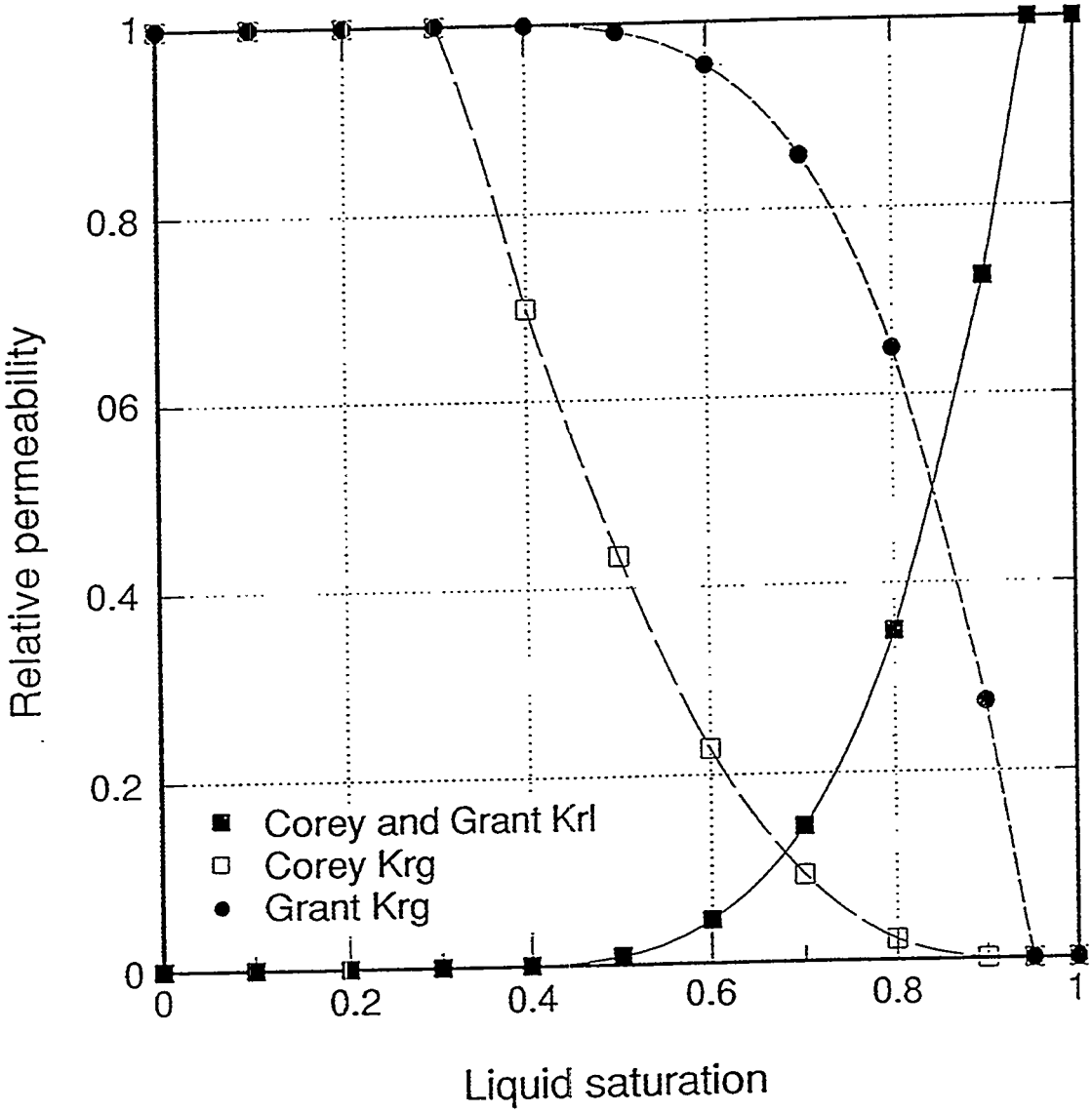

FIG. B-14: Grant's relative permeabilities compared with Corey's curves used for the reference case.

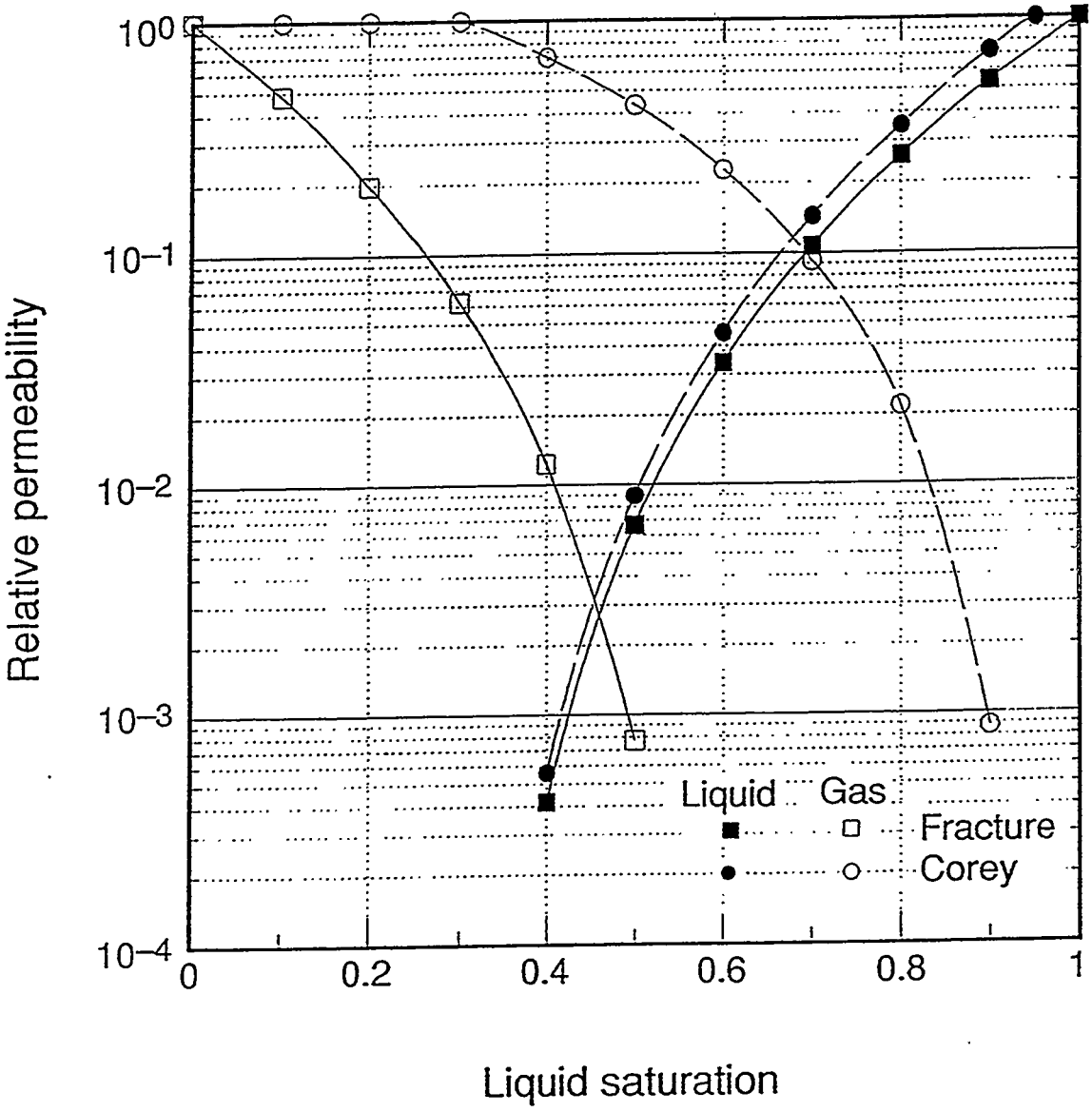

FIG. B-15: Relative permeabilities with strong phase interference compared with Corey's curves. Note the logarithmic scale.

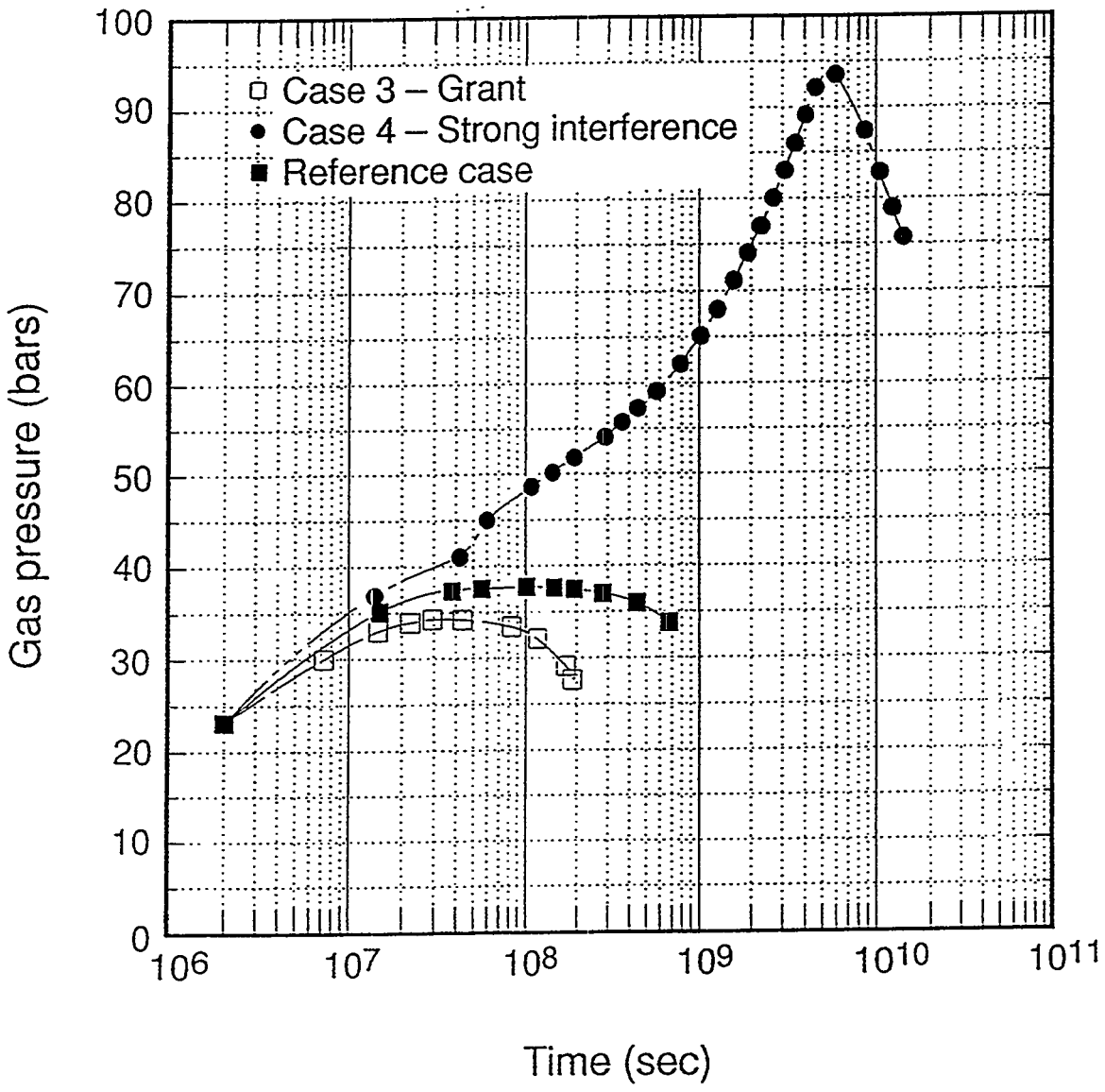

FIG. B-16: Sensitivity of gas pressures in injection block to variations in relative permeability.

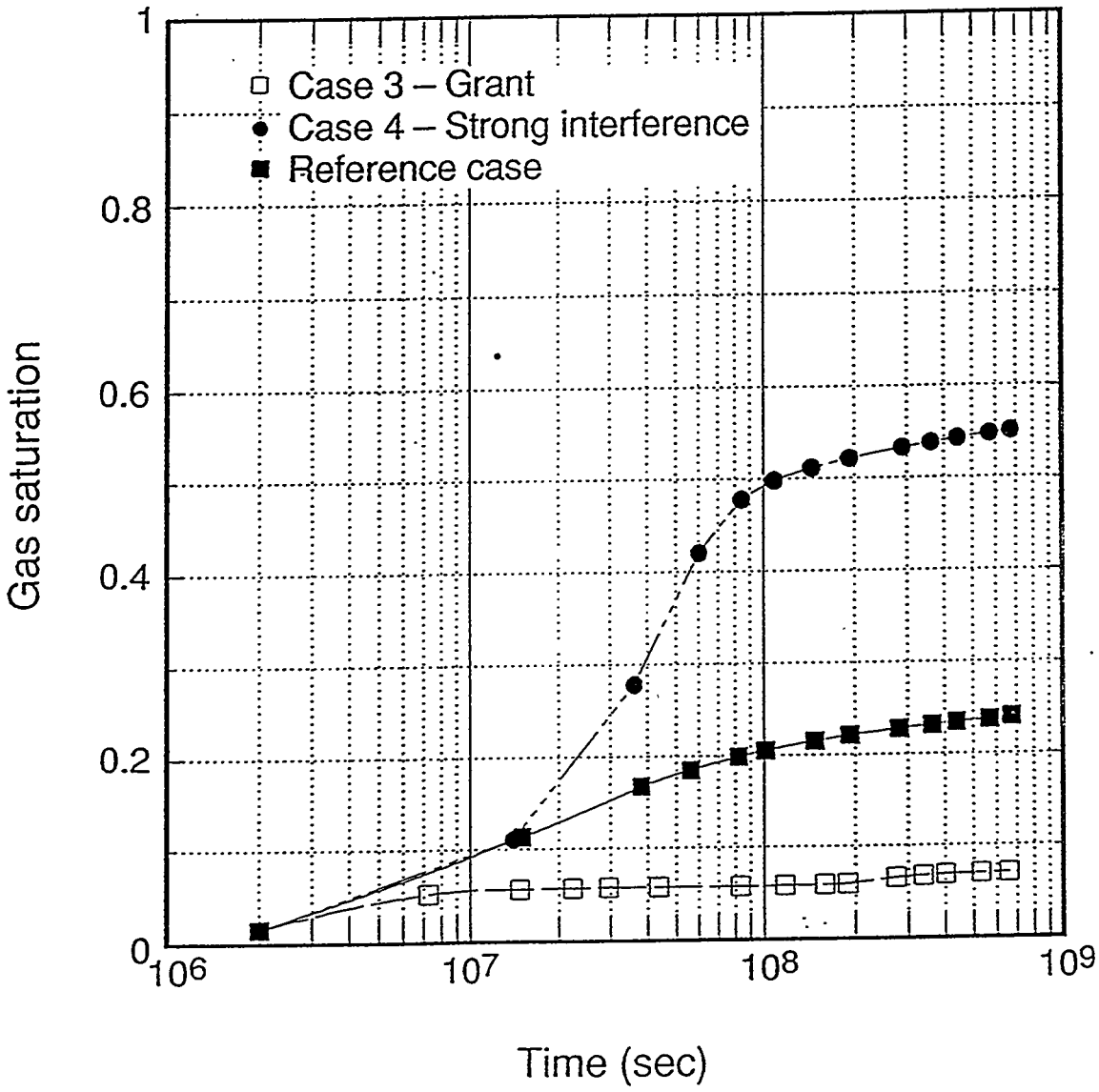

FIG. B-17: Sensitivity of gas saturations in injection block to variations in relative permeability.

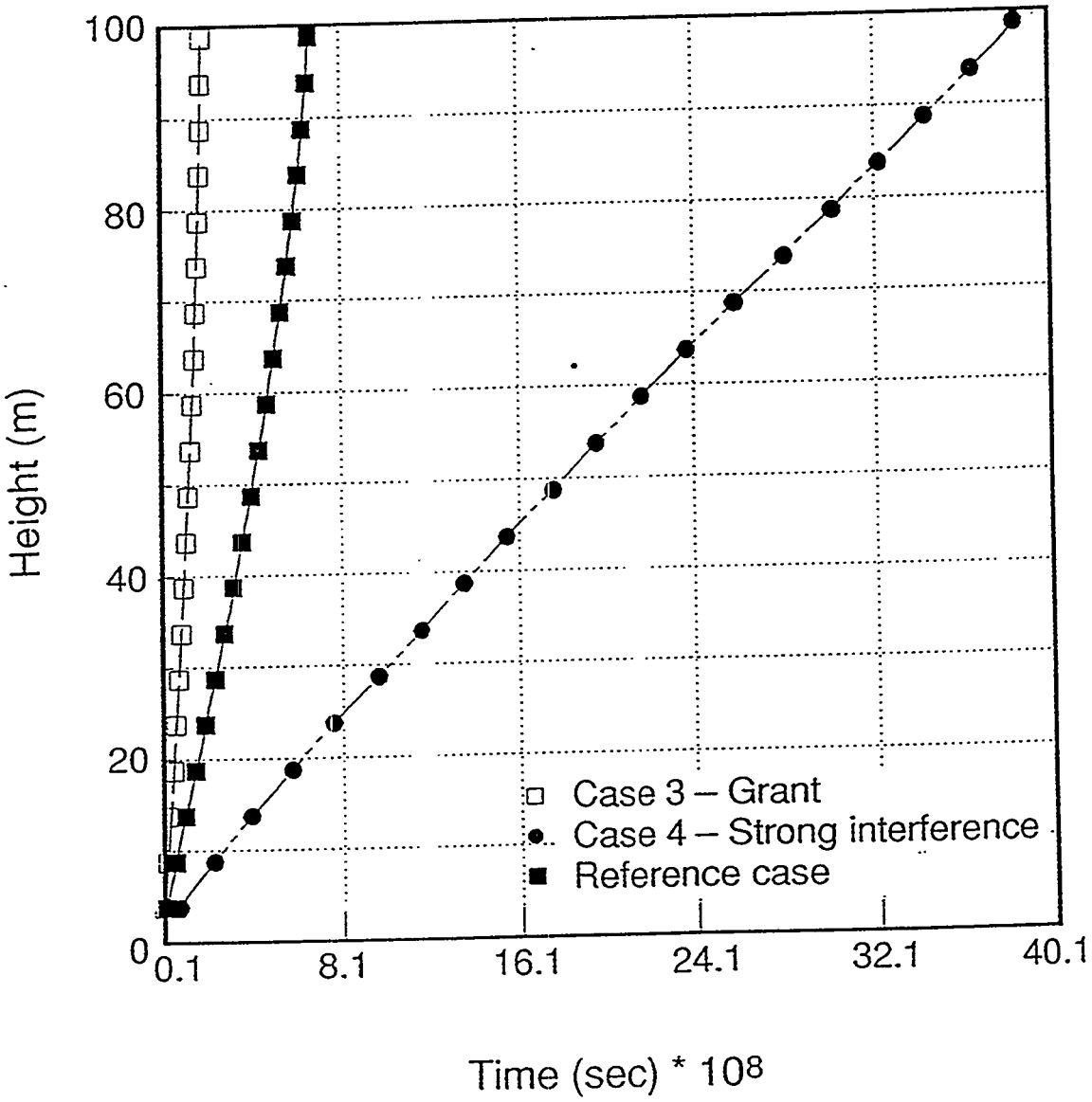

FIG. B-18: Sensitivity of gas front advance to variations in relative permeability.

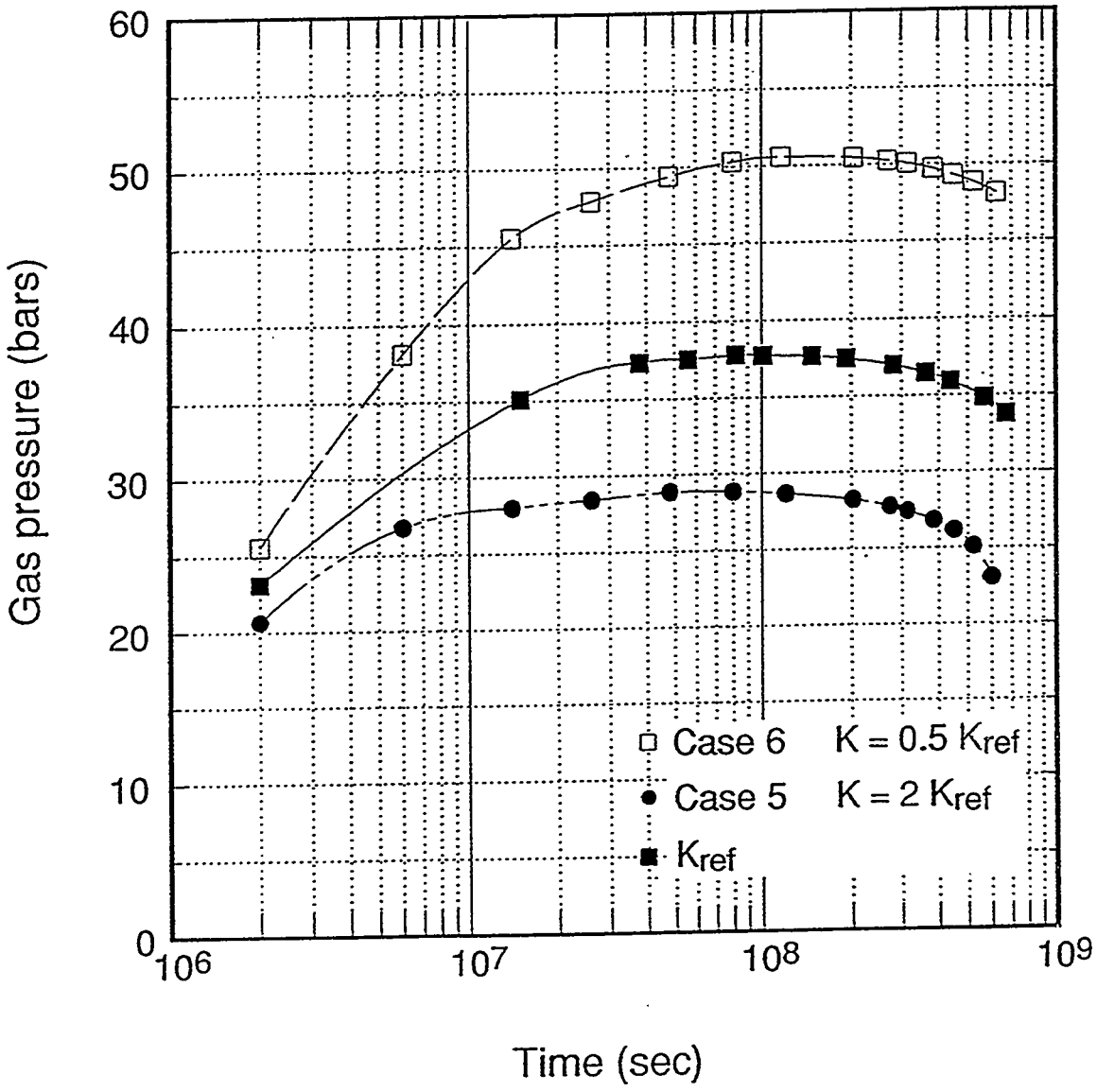

FIG. B-19: Sensitivity of gas pressures in injection block to variations in absolute permeability.

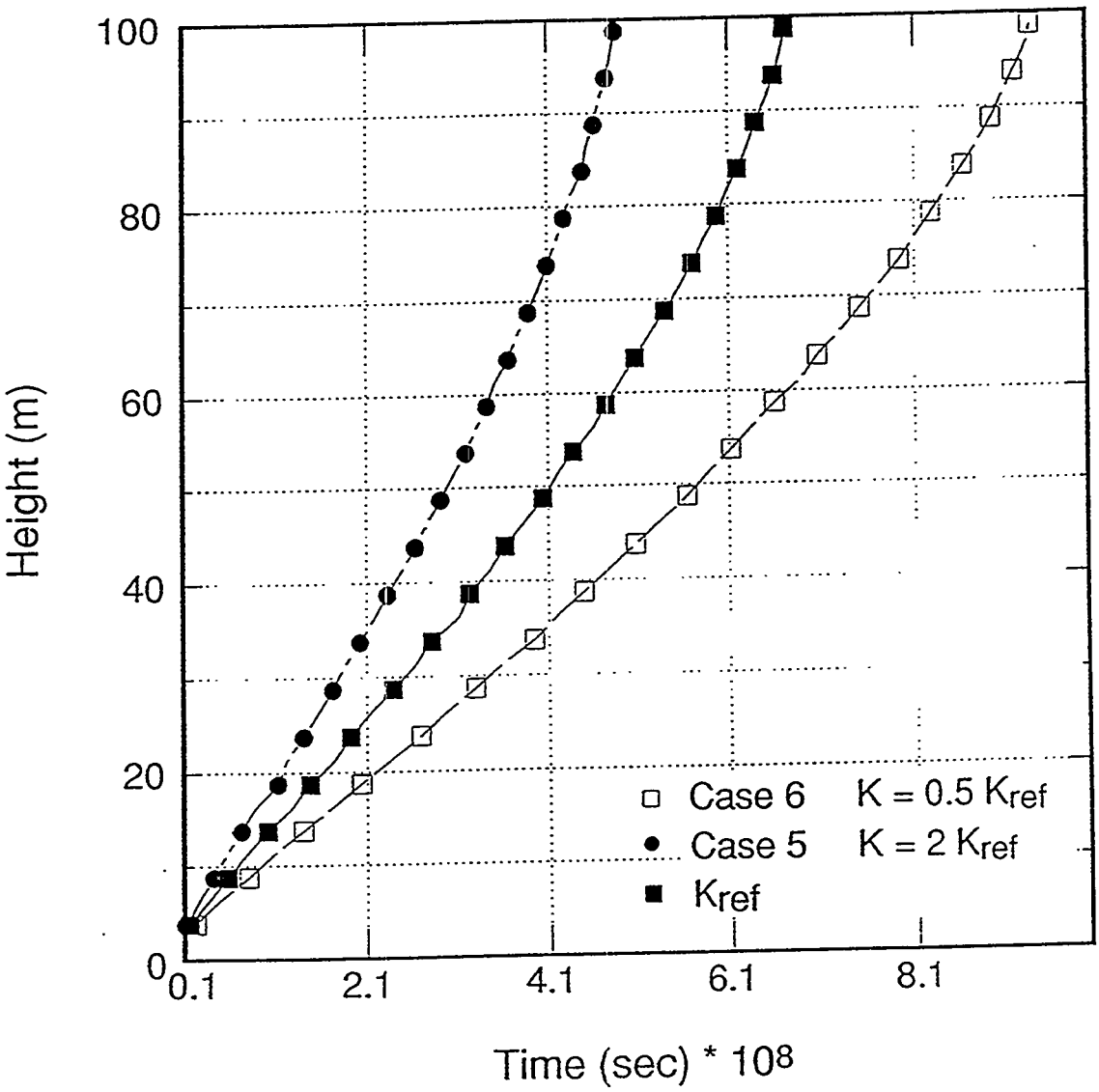

FIG. B-20: Sensitivity of gas front advance to variations in absolute permeability.

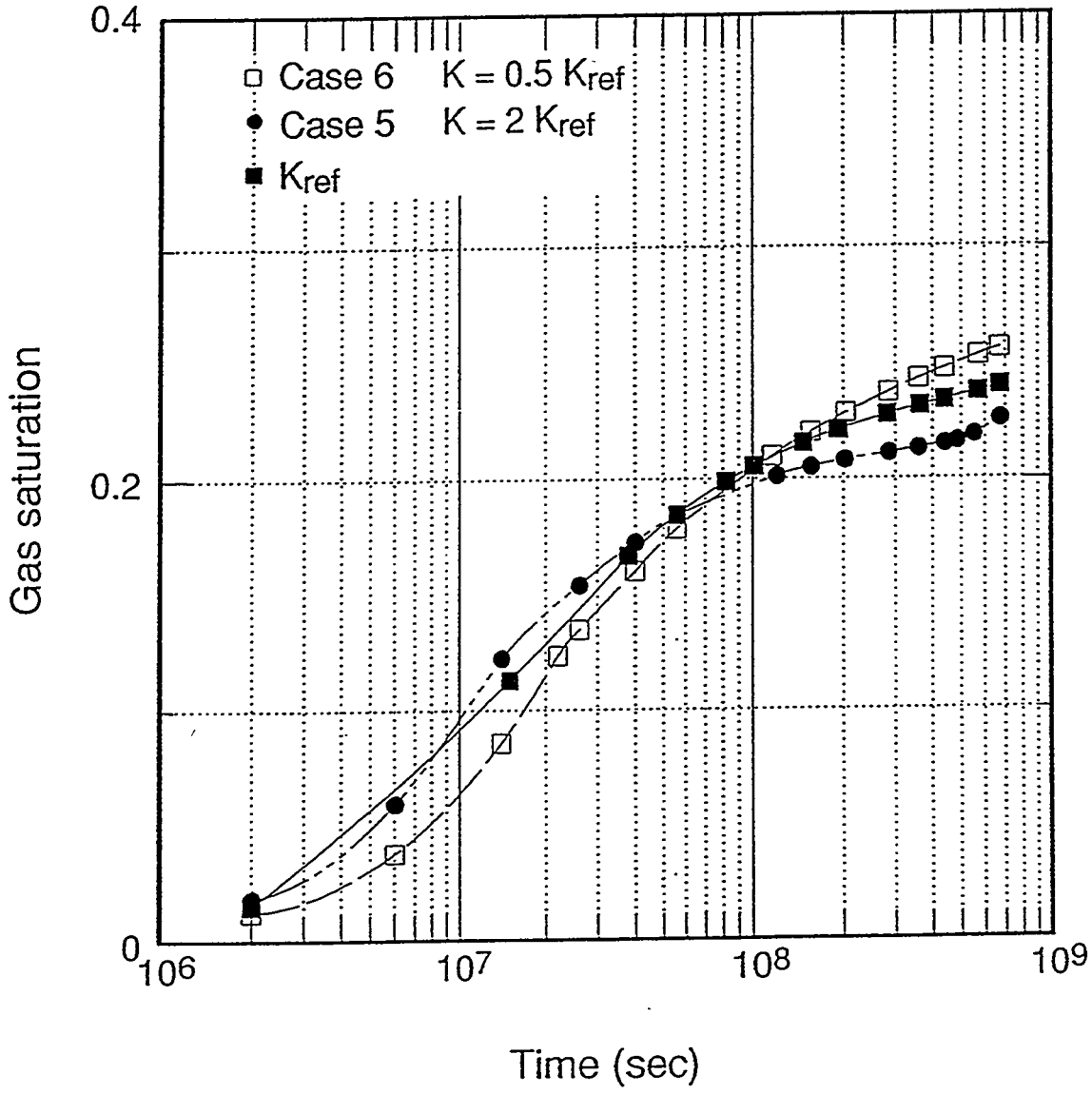

FIG. B-21: Sensitivity of gas saturations in injection block to variations in absolute permeability.

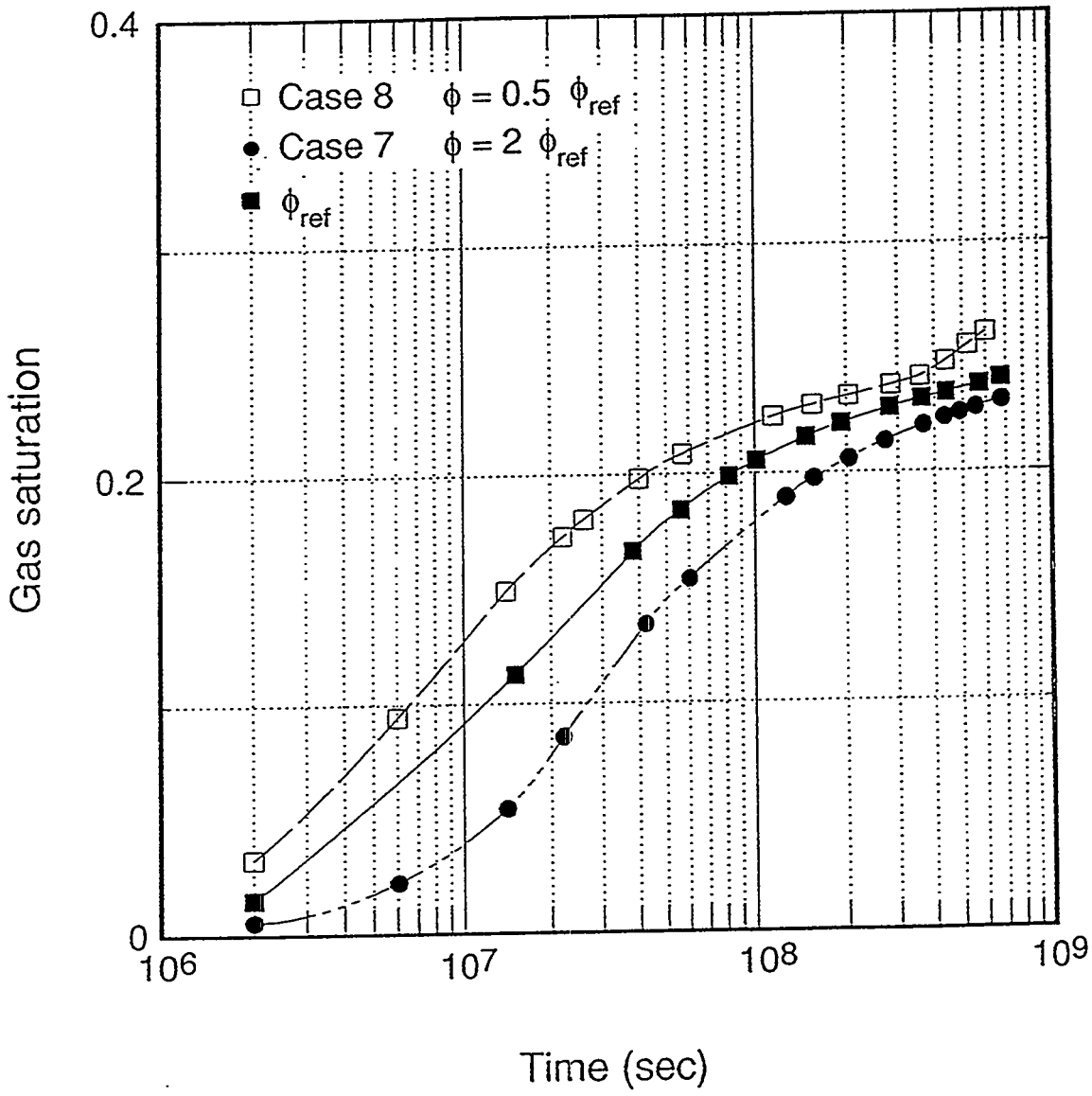

FIG. B-22: Sensitivity of gas saturations in injection block to variations in porosity.

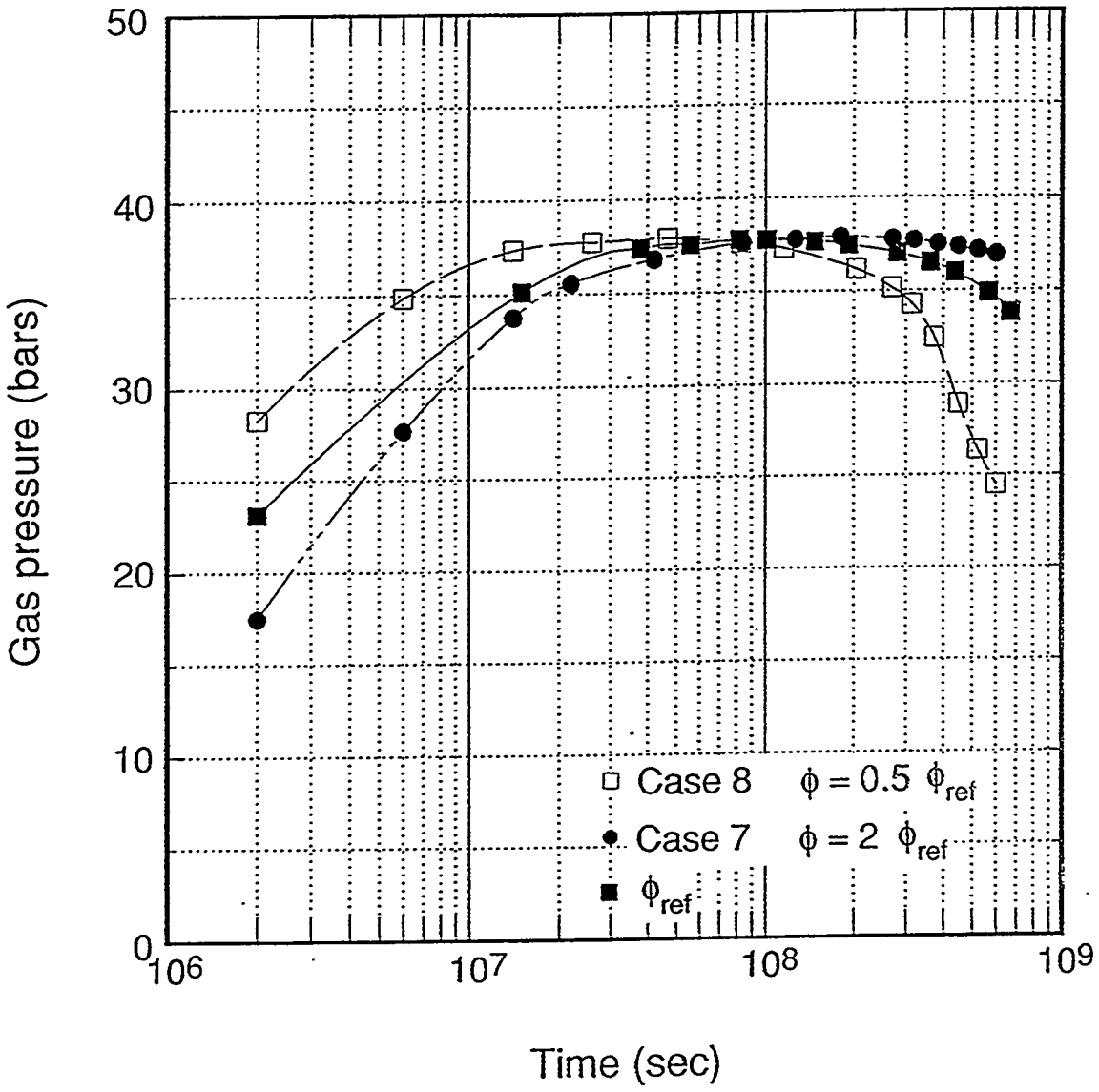

FIG. B-23: Sensitivity of gas pressures in injection block to variations in porosity.

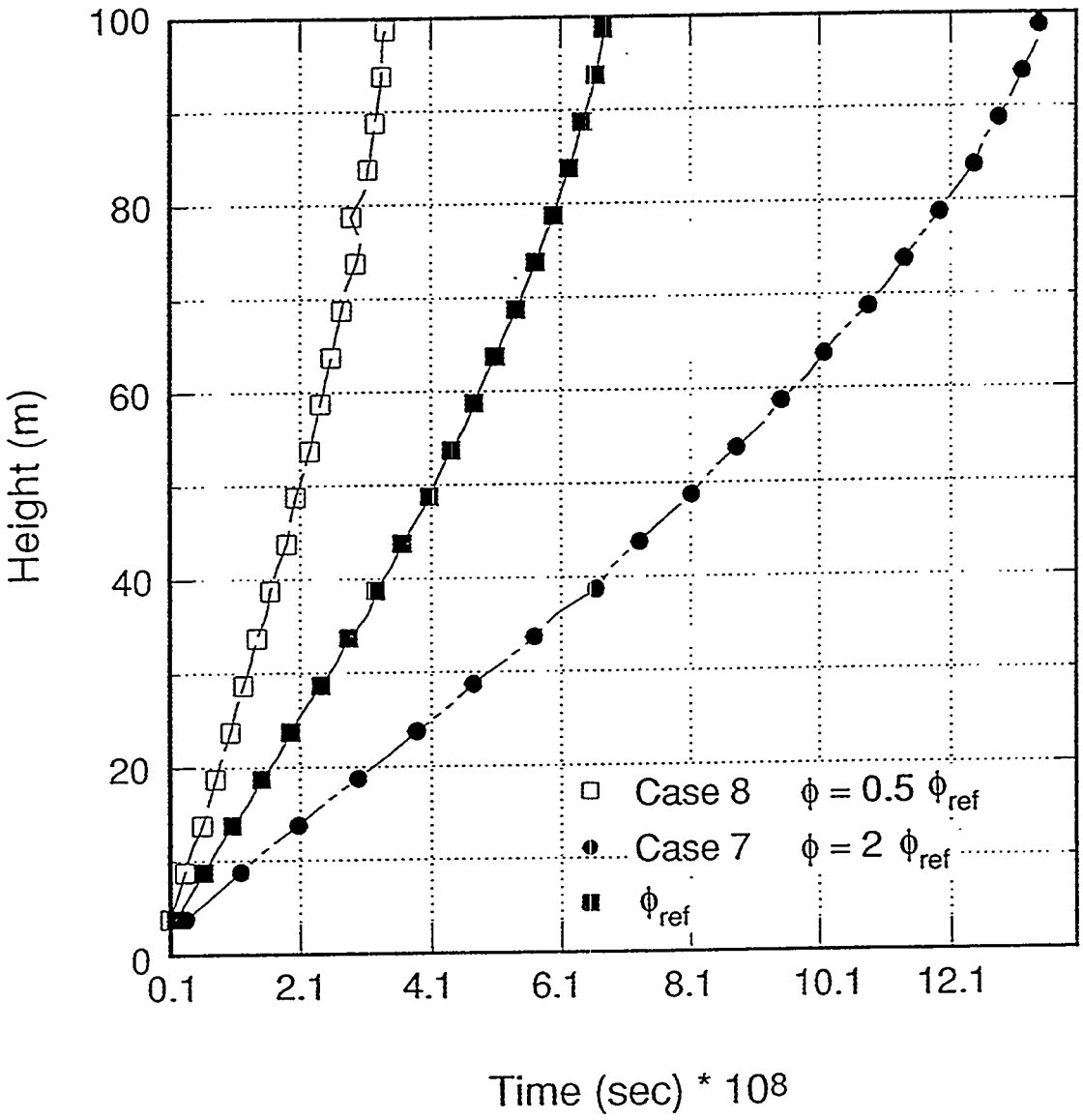

FIG. B-24: Sensitivity of gas front advance to variations in porosity.

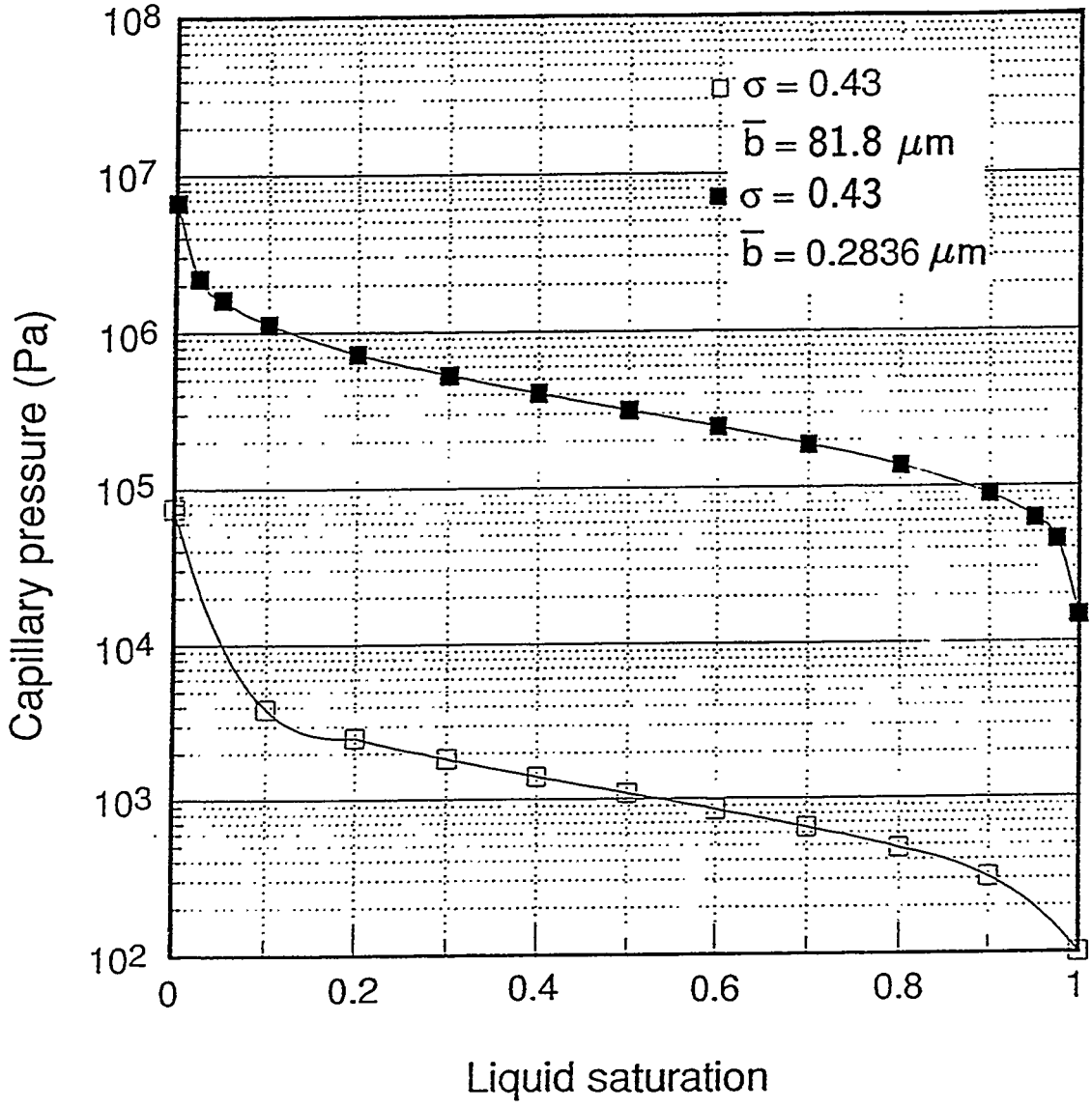

FIG. B-25: Fracture capillary pressures for log-normal aperture distribution.

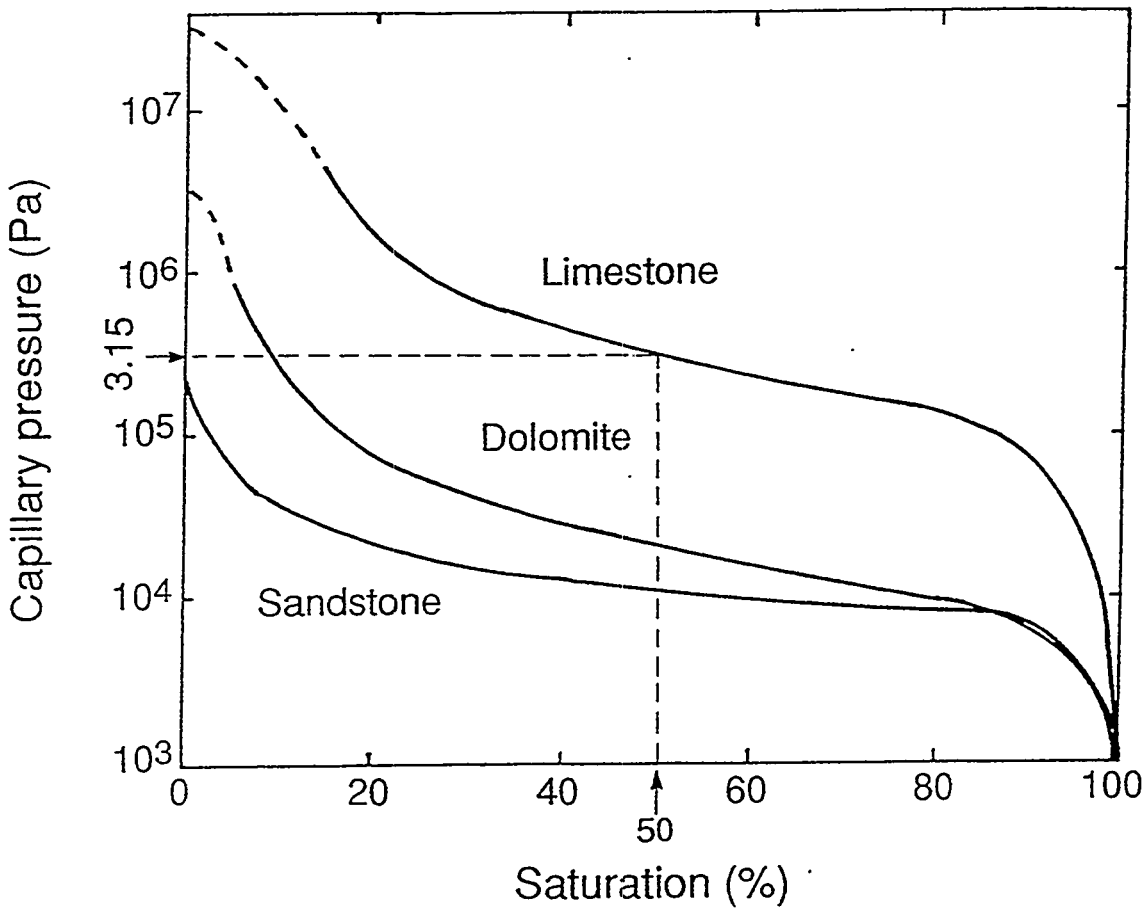

FIG. B-26: Capillary pressure functions for three geologic media (after Wiborgh et al., 1986).

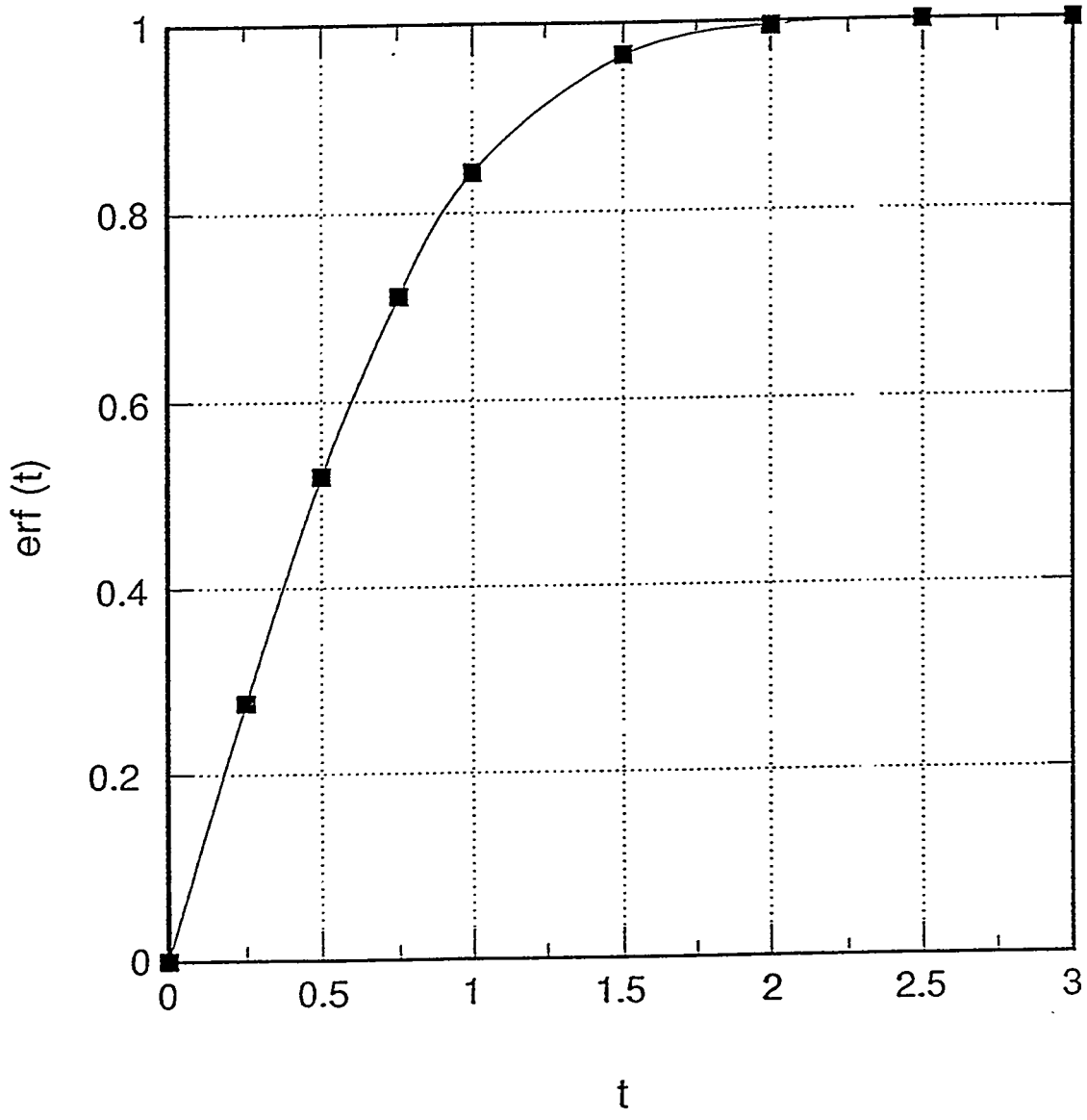

FIG. B-27: The error function.

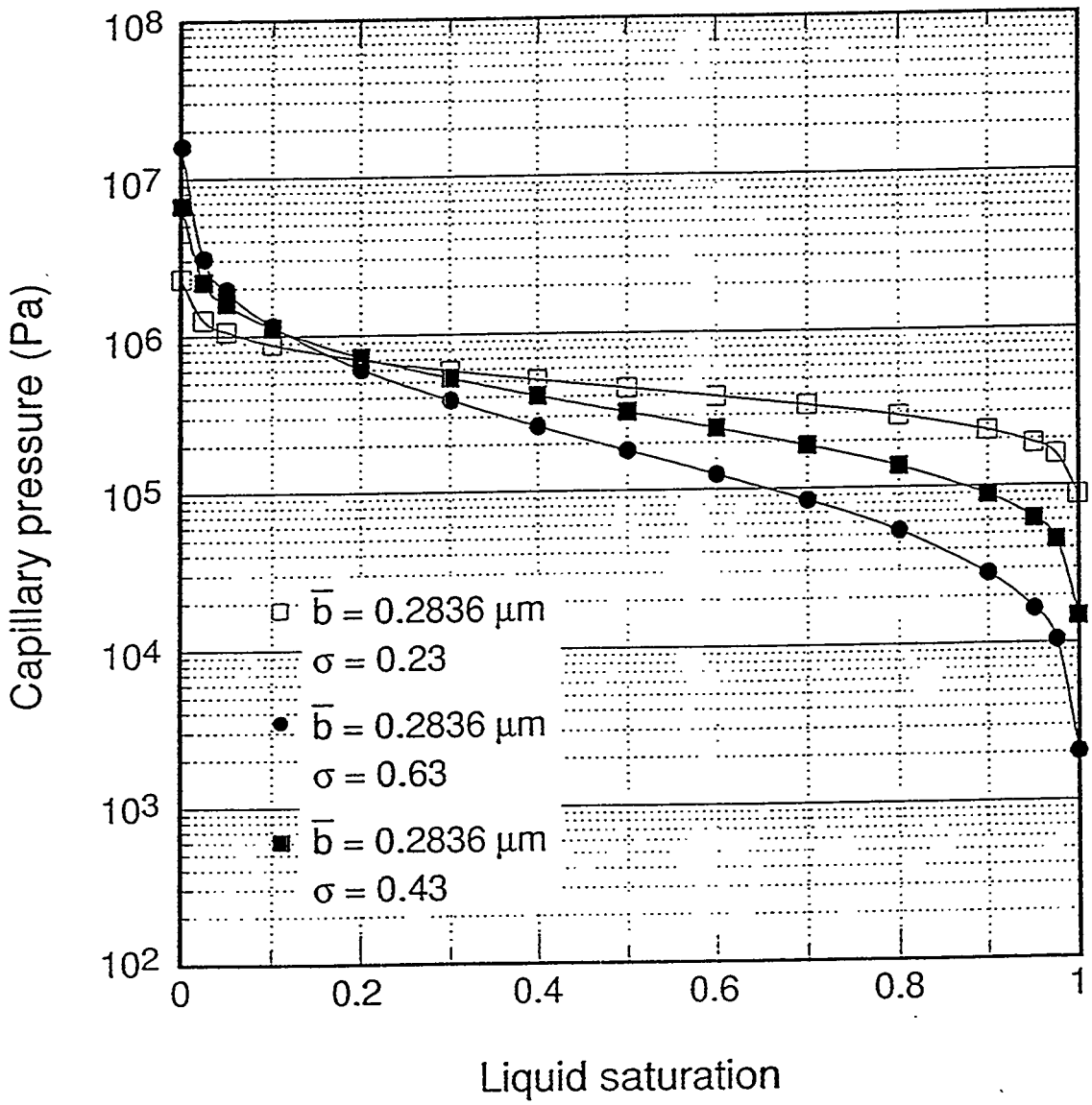

FIG. B-28: Fracture capillary pressures for different values of variance σ.